Rapid Decompression of Dense Particle Beds

by

Heather Anne Zunino

A Thesis Presented in Partial Fulfillment

of the Requirements for the Degree

Doctor of Philosophy

Approved April 2019 by the
Graduate Supervisory Committee:

Ronald Adrian, Chair
Amanda Clarke
Marcus Herrmann
Kangping Chen
Huei-Ping Huang

ARIZONA STATE UNIVERSITY

MAY 2019

ABSTRACT

Rapid expansion of dense beds of fine, spherical particles subjected to rapid depressurization is studied in a vertical shock tube. As the particle bed is unloaded, a high-speed video camera captures the dramatic evolution of the particle bed structure. Pressure transducers are used to measure the dynamic pressure changes during the particle bed expansion process. Image processing, signal processing, and Particle Image Velocimetry techniques, are used to examine the relationships between particle size, initial bed height, bed expansion rate, and gas velocities.

The gas-particle interface and the particle bed as a whole expand and evolve in stages. First, the bed swells nearly homogeneously for a very brief period of time (< 2ms). Shortly afterward, the interface begins to develop instabilities as it continues to rise, with particles nearest the wall rising more quickly. Meanwhile, the bed fractures into layers and then breaks down further into cellular-like structures. The rate at which the structural evolution occurs is shown to be dependent on particle size. Additionally, the rate of the overall bed expansion is shown to be dependent on particle size and initial bed height.

Taller particle beds and beds composed of smaller-diameter particles are found to be associated with faster bed-expansion rates, as measured by the velocity of the gas-particle interface. However, the expansion wave travels more slowly through these same beds. It was also found that higher gas velocities above the the gas-particle interface measured *via* Particle Image Velocimetry or PIV, were associated with particle beds composed of larger-diameter particles. The gas dilation between the shocktube diaphragm and the particle bed interface is more dramatic when the distance between the gas-particle interface and the diaphragm is decreased—as is the case for taller beds.

To further elucidate the complexities of this multiphase compressible flow, simple OpenFOAM[32] simulations of the shocktube experiment were performed and compared to bed expansion rates, pressure fluctuations, and gas velocities. In all cases, the trends and relationships between bed height, particle diameter, with expansion rates, pressure fluctuations and gas velocities matched well between experiments and simulations. In most cases, the experimentally-measured bed rise rates and the simulated bed rise rates matched reasonably well in early times. The trends and overall values of the pressure fluctuations and gas velocities matched well between the experiments and simulations; shedding light on the effects each parameter has on the overall flow.

DEDICATION

To my wonderful parents, Ben and Mary Zunino.

By being life-long teachers, you've instilled in me the love of being a life-long learner.

You are the heroes of heroes in academia and in life.

ACKNOWLEDGMENTS

Firstly, I would like to express my sincerest gratitude to all my family members and friends who have supported me in my academic journey to obtaining this degree. Time and time again, I sought advisement from my family and close friends, and I always felt immensely supported and loved from each one of them. Thank you to my incredible parents, Ben and Mary Zunino. I owe all my success in academia and life to you and all of the wonderful things you each have taught me over the years.

I would like to thank my brilliant and exceptional advisor and committee chair, Dr. Ronald Adrian. Thank you for your unending patience, mentorship, and expert teaching. Your dedication to performing excellent research and experience in science and engineering have inspired me greatly. I have enjoyed our interesting and exciting conversations over the years about all aspects of science, research, and academia. Thank you for your kindness and patience in teaching me the complexities of engineering and fluid mechanics. I would also like to acknowledge the members of my advisory committee Dr. Marcus Herrmann, Dr. H.P. Huang, Dr. K.P. Chen, and Dr. Amanda Clarke. Thank you all for your exceptional classes and instruction. Additionally, thank you to Dr. Clarke for allowing me to work in the Experimental Volcanology Laboratory and for all of the guidance and help you gave me over the years.

I would like to acknowledge and express my deepest gratitude to all of the graduate students and colleagues who have helped me immensely during this research. I would especially like to thank Dr. Liuyang Ding and Dr. Rafeed Chaudhury for all of their assistance and support during my time at ASU. Their expertise and knowledge in science and engineering paired with their desire to help and teach others impacted me greatly and I am forever grateful.

I would also like to acknowledge the several groups and organizations that provided funding for this research; including the U.S. Department of Energy, National Nuclear Security Administration, Advanced Simulation and Computing Program, as a Cooperative Agreement under the Predictive Science and Academic Alliance Program, under Contract No. DE-NA0002378, Los Alamos National Laboratory and Dr. Kathy Prestridge's Extreme Fluids Team; and the School of Matter, Transport and Energy Engineering at Arizona State University.

TABLE OF CONTENTS

LIST OF TABLES

Table Page

LIST OF FIGURES

Figure Page

1 INTRODUCTION

1.1 Problem Statement and Goals

Sold-gas multiphase flows are pervasive throughout both engineering and science. They are present in explosions, mining, erosion, atmospheric flows, and volcanic eruptions. These examples in which solid particles are contained within gases have the added complexity of compressibility, thermal effects, and possibly turbulence. Modeling and numerically simulating these flows is extraordinarily demanding. The fluid-particle interaction is complex because of the thermodynamic conditions and the enormous number of solid particles involved. It is difficult to study these flows inside a laboratory; being compressible and energetic, they are difficult to contain and typically run for very short periods of time—requiring expensive, high-speed measurements. Additionally, due to the immense complexity, particle-by-particle simulations of this type of flow are outside of modern computing capabilities.

The Center for Compressible Multiphase Turbulence (CCMT) at the University of Florida, which is part of the Predictive Science Academic Alliance Program (PSAAP), is working on developing the science and technology to be able to simulate highly-complex flows, specifically exploding charges. The goal is to be able to predictively simulate several dominate processes and flow structures of an exploding cylindrical charge experiment performed at Eglin Airforce Base, located just outside Valparaiso, Florida. The simulation code aims to predict shock characteristics, expansion wave characteristics, gas velocities, particle velocities, dynamic pressure changes, and general flow structures. In order to do this, researchers at CCMT need to develop not only the simulation, but the associated physics and the computing technology as well.

There is a great need for a simple experiment that can be used for early-stage code validation for these massive simulations. If the simulation is able to accurately predict the outcome of a simpler experiment, code developers can be confident that the physics applied to a more complex flow are correct. The capstone experiment of the exploding cylindrical charge has been broken down into several smaller and simpler experiments designed to study specific processes. Experiments performed at Arizona State University (ASU) were designed to study the expansion wave as it travels down into the dense granular material of the exploding charge. Experiments performed at Sandia National Lab examine particulate and gas behavior when a shock passes through a dense particle curtain [2]. Additional experiments are performed at Eglin Airforce Base to study projectiles

accelerated by explosions [6].

1.2 Brief Outline of Experiment

In the Experimental Volcanology Laboratory at Arizona State University, a vertical shocktube designed after the one used in the Chojnicki *et. al* experiments in [1], was used to examine rapidly decompressed particle beds and the particles' effect on gas flows. Figure 1 is a simple diagram showing the shocktube dimensions and the location of the pressure transducers along the axial coordinate $\boldsymbol{z}$. Also shown is the location of the diaphragm, a thin piece of adhesive polypropylene placed over a nichrome wire, which creates a physical barrier between the initial pressures $p_4 =$ 101,325Pa and $p_1 =$ 5,000Pa. Once the initial conditions are set, including pouring a dense particle bed composed of glass spheres in the bottom of the shocktube in atmospheric pressure, a current is produced by a current generator and sent through the nichrome wire, which heats rapidly. The wire burns through the edges of the polypropylene very quickly, causing a rapid decompression of the high-pressure region below the diaphragm and a shockwave to propagate upward and away from the diaphragm to the top of the shocktube. This process is shown in Figure 2.

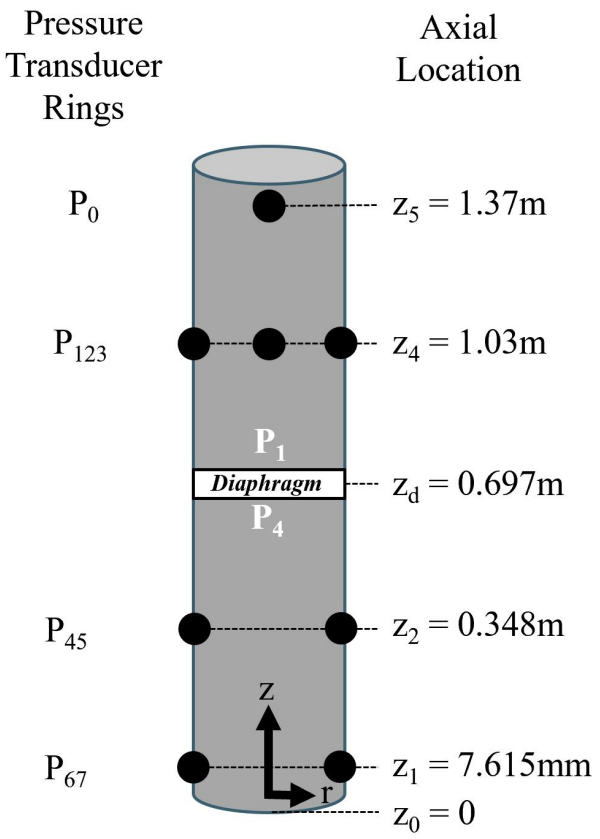

Figure 1: Nearly All the Data Presented Was Obtained from Using the Vertical Shocktube in the Setup Shown. This Setup Is Termed The *Standard* Setup with Two Sets of Pressure Transducers above the Diaphragm and Two Sets of Pressure Transducers below the Diaphragm. The Pressure Transducer Naming Convention Starts with P0 at the Top of the Shocktube, But z_0 Is at the Very Bottom of the Shocktube. With the Current Naming Conventions, Pressure Transducers Can Be Added below (for Possible Future Experiments) along with More Glass Segments and the Naming Convention Will Not Need to Be Changed. A More In-depth Description of the Shocktube Setup Is Discussed in Chapter 2.

Once the diaphragm is ruptured and the shockwave propagates upward past pressure transducers 1, 2, and 3, the data collection system is triggered. This includes data from a high-speed camera capturing the evolution of the particle bed and all eight pressure transducers measuring dynamic changes in gas pressure. Both the pressure readings and the imaging system have a 0.01s buffer of data, which is saved with additional data captured after the triggering event. In total, one second of data is captured from each realization, although the majority of the studied events occur on the millisecond time-scale. The late time data was saved for further studies involving the particle

bed evolution and gas motions at late-times.

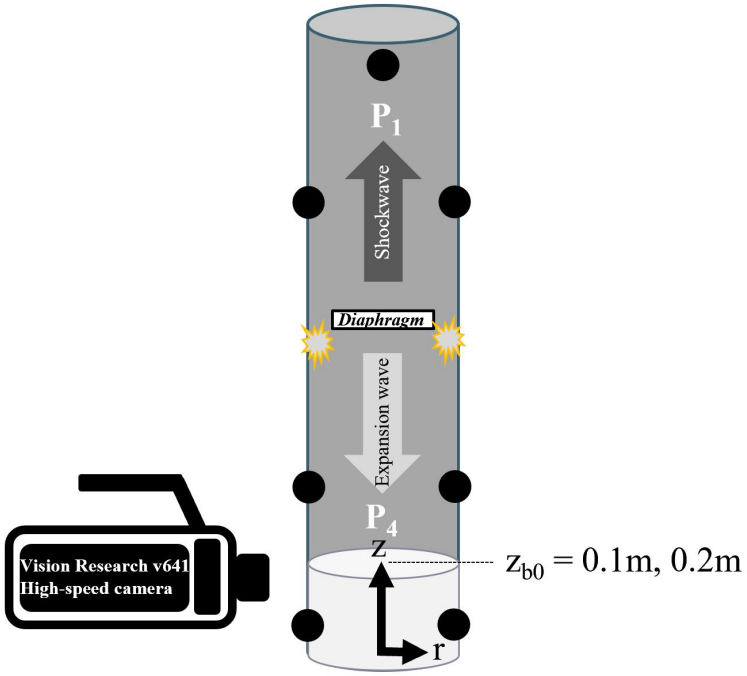

Figure 2: Depicted Is a Simple Flow Diagram Showing an Upward-moving ($+z$) Shockwave and a Downward-moving ($-z$) Expansion Wave Which Form Once the Diaphragm Is Ruptured by a Heated Nichrome Wire. Once the Perimeter of the Diaphragm Burns Completely Through along the Inlaid Nichrome Wire, It Becomes Detached from the Rest of the Shocktube and Is Rapidly Forced Upward from the Large Pressure Gradient Across Its Boundary.

Once the expansion wave impinges on the gas-particle interface at the top of the bed, the particle bed begins to deform as the high-pressure (atmospheric pressure) gases begin to expand and rapidly move in the $+z$ direction. Interestingly, the bed swells homogeneously only briefly. After this brief swelling stage, the bed begins to break down into horizontal slabs, and then further into a cellular-like pattern of particle-vacant regions. The specific evolution including the size of the particle-vacant regions and the timescales depend on the particle diameters. This is discussed in detail in Chapter 6.

Shown in Figure 3 are a few snapshots showing the evolution of a rapidly decompressed particle bed. The bed swells seemingly-homogeneously briefly for a few milliseconds before horizontal layers begin to appear along the edges. These layers form at progressively lower z values, eventually

reaching the bottom of the particle bed. As each layer is deformed by the gas expansion and motion in occurring between layers, the bed is further broken down into a semi-regular cellular-like pattern. Also notice the deformation of the gas-particle interface. As the gases below the surface expand, the top layers of particles are accelerated upwards, beginning with the perimeter near the wall. The gas-particle interface deformation and wall effects are discussed in Chapter 4.

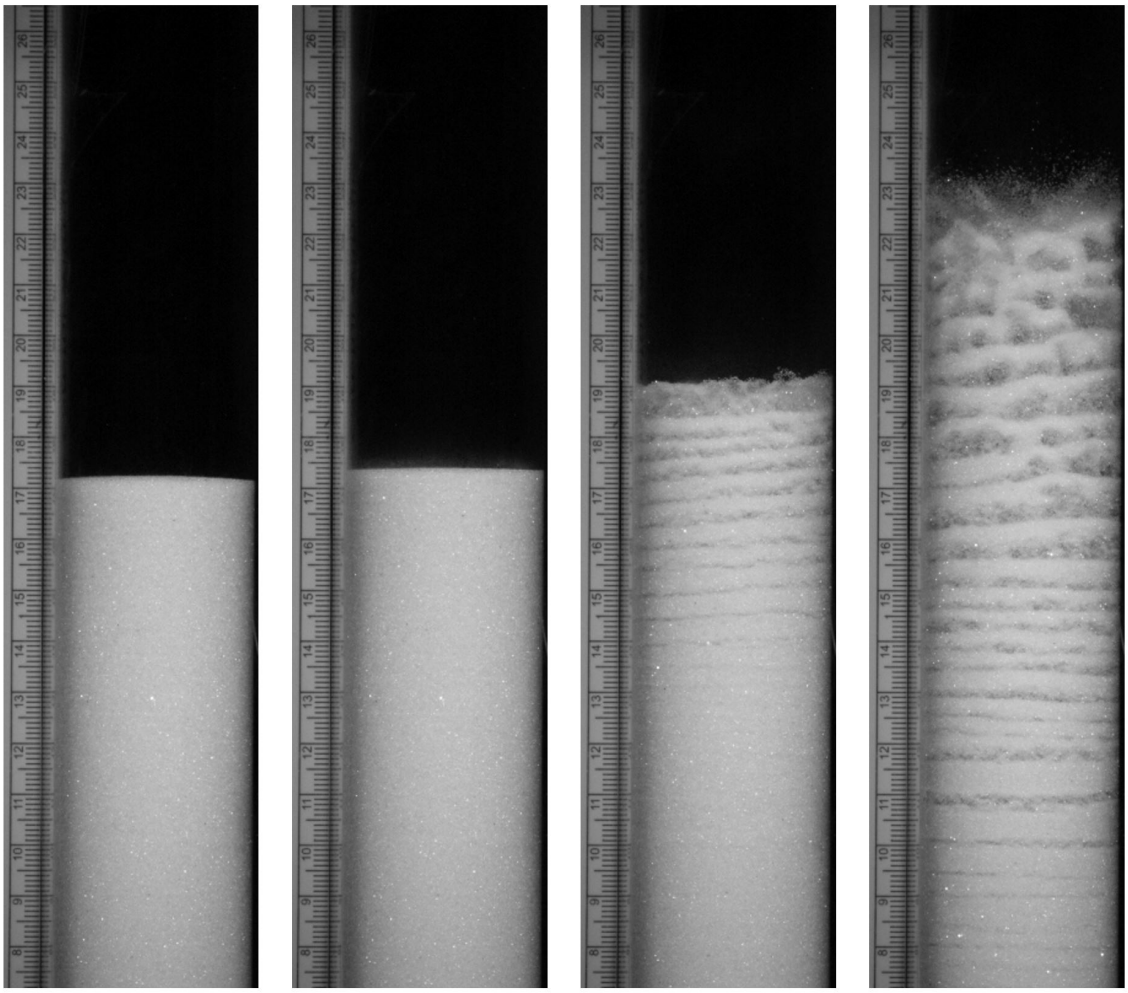

Figure 3: Shown Are a Few Snapshots of a Particle Bed Evolution. Here, the Particle Bed Is Composed of Small Glass Spheres with a Particle Diameter d_p Ranging Between 212μm and 297μm and Has an Initial Bed Height Of 0.2m. The Ruler along the Side of the Snapshots Does Not Fit down to the Level of the Bottom of the Particle Bed, Therefore It Is Used as a Measure of Displacement and Not Absolute Bed Height. Particular Features of Interest in the Particle Bed Evolution Is the Brief Period of Swelling Seen for Approximately the First 2.8ms of the Expansion, the Breakdown of the Bed into Horizontal Layers, and the Further Breakdown into a Cellular-like Pattern. The File Names Associated with these Images are 111617_1(-9, 19, 50, 100).

1.3 Fluidized Beds

Figure 3 looks somewhat reminiscent of a fluidized bed experiment. Fluidized beds are dense beds composed of small-diameter particles, which are then typically aerated from below.

Fluidized beds, though they are composed of individual granular particles, act very much like a liquid—even to the point of having waves and splashing against sidewalls. Objects with lower density than the density of the fluidized bed may float due to to liquid-like nature of the bed and Archimedes' Principle. Fluidized beds have many applications, mostly within two categories—physical or mechanical applications and chemical applications. Physical applications include heating, cooling, fine powder mixing, and transport. The fluidization process maximizes the surface contact between the particles and gas. Because of this, fluidized beds are also very useful for chemical processes, as they can increase the efficiency of chemical reactions [18].

A fluidized particle bed has a lower overall solid volume fraction than the same bed at rest. The gases injected from below the particle bed, typically through a distributor plate—a plate with many holes drilled into it, suspends the particles in such a way that the bed, as a whole, can be considered to be a heterogeneous mixture with a single bulk density. When the gas velocity within a particle bed reaches what's called the minimum fluidization velocity $\boldsymbol{u_{mf}}$, the drag force equals the weight of the particles—at which point the bed is considered fluidized. As the velocity increases further, particle-vacant regions begin to form and the bed is considered a *bubbling* fluidized bed. When gas velocities are increased even further, the diameter of the particle-vacant regions near the diameter of the particle bed, causing the bed to briefly form thick layers called slugs[18]. Figure 4 shows several of the different fluidized bed regimes based on varied gas velocities, including beds associated with very high gas velocities.

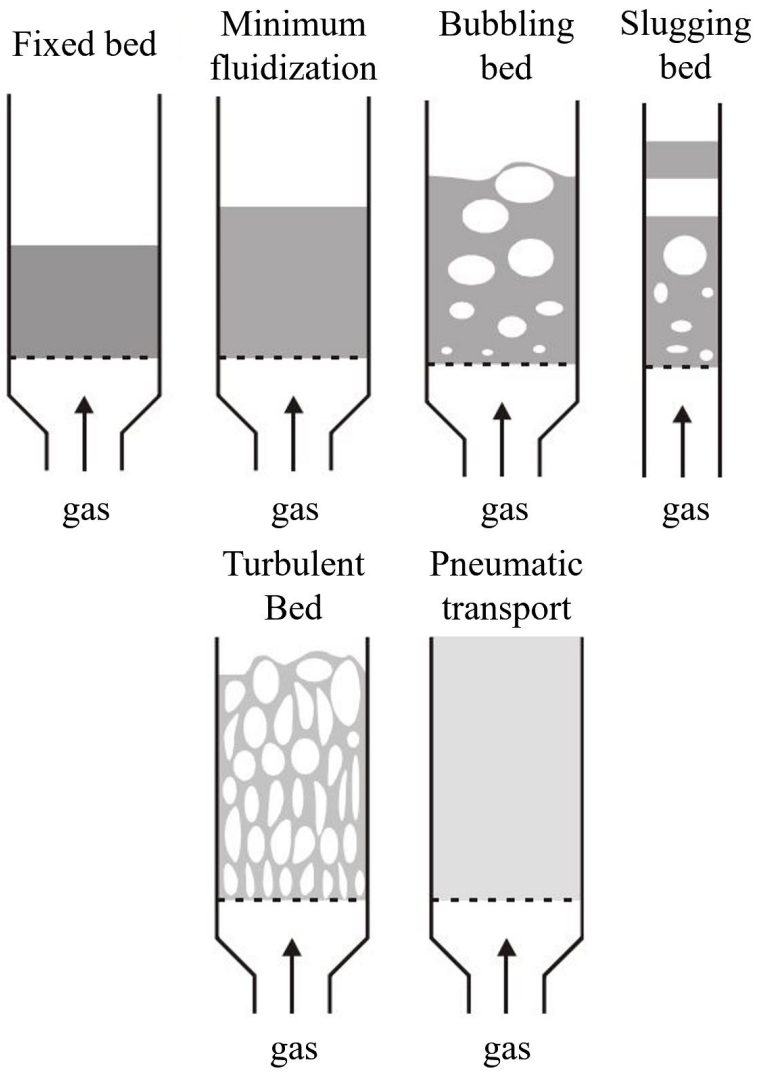

Figure 4: Shown Is a Sketch Characterizing Different Regimes of Fluidization of Particle Beds. The Transition Between Fluidization Regimes Is Caused by Changing the Input Gas Velocity at the Bottom of the Particle Bed. *Courtesy: Dechsiri, 2004.*

An important difference to note between the fluidized beds described and shown in Figure 4 and the beds shown in Figure 3 is that the fluidized beds are created by adding mass to the enclosed system; whereas the particle-vacant regions created from the rapid decompression experiments performed at ASU are formed due to the forces created by the expansion from the gases already contained within the bed. Additionally, the pattern of particle-vacant regions from the

rapidly decompressed bed initially forms at the top of the bed and grows downward toward the base of the bed. The particle-vacancies seen in the bubbling fluidized beds start at the bottom of the particle bed and travel upward, looking very reminiscent of boiling water. In 1952, Ergun derived equations to describe the friction inside a column of granular particles. The equation, known as the Ergun equation, is as follows [19]

Given:

f_p = friction factor in a particle bed [unitless]
Gr_p = modified Reynolds number [unitless]
Δp = the pressure drop across the particle bed [kPa]
D_p = the diameter of the particles [μm]
ρ_g = the density of the gas [$\frac{kg}{m^3}$]
ϕ_p = solid volume fraction [unitless]
ρ_p = the density of the particle [$\frac{kg}{m^3}$]
ρ_b = the bulk density of the particle bed [$\frac{kg}{m^3}$]
μ_g = the dynamic viscosity of the gas [$\frac{kg}{ms}$]
$\Re_{mf}$ = the minimum fluidization Reynolds number [unitless]
$\boldsymbol{u}$ = velocity of the gas [$\frac{m}{s}$]
$\boldsymbol{u_s}$ = superficial gas velocity [$\frac{m}{s}$]
ϵ_b = the void fraction of the particle bed, also called porosity [unitless]
ϵ_{mf} = the void fraction of the particle bed at minimum fluidization [unitless]
z_b = height of the particle bed [m]
Φ_s = sphericity of the particles [unitless]
ϕ_p = solid volume fraction [unitless]
$\mathbf{g}$ = gravitational acceleration [$\frac{m}{s^2}$]

Table 1: Fluidized Bed-related Quantities

$$f_p = \frac{150}{Gr_p} + 1.75 \tag{1}$$

where

$$Gr_p = \frac{\rho_g \boldsymbol{u_s} D_p}{(1-\epsilon_b)\mu_g} \tag{2}$$

Here $\mathbf{u}_s$ is called the *superficial velocity* of the gas, which is the hypothetical velocity at which the gas would flow through the same volume if the particles were not present. The superficial velocity can be calculated by

$$\boldsymbol{u_s} = \frac{\text{volume flow rate of the gas}}{\text{cross sectional area of the particle bed}} \tag{3}$$

or by using the void fraction of the bed [14]

$$\boldsymbol{u} = \frac{\boldsymbol{u_s}}{\epsilon_b} \tag{4}$$

Note that ϵ_b is equal to 1 - ϕ_p, where ϕ_p is the solid volume fraction of the particles. The void fraction of the particle bed can be calculated by

$$\epsilon_b = 1 - \frac{\rho_b}{\rho_p} \tag{5}$$

The mass contribution from the gases mixed in with a particle bed is very low, therefore it is neglected in (5). When applied specifically to the incipient fluidization of a particle bed, the following relationship applies [14] [21].

$$\frac{\Delta P}{z_b} = 150\frac{(1-\epsilon_{mf})^2}{\epsilon_{mf}^3}\frac{\mu_g \boldsymbol{u_{mf}}}{(\Phi_s D_p)^2} + 1.75\frac{(1-\epsilon_{mf})}{\epsilon_{mf}^3}\frac{\rho_g \boldsymbol{u_{mf}^2}}{\Phi_s D_p} \tag{6}$$

In (6), the minimum fluidization voidage is needed. In 1966, Wen and Yu[21] found an approximate relationship for the voidage in a particle bed based on studies of a range of particle sizes.

$$\begin{aligned} \frac{1-\epsilon_{mf}}{\Phi_s^2 \epsilon_{mf}^3} &\approx 11 \\ \frac{1}{\Phi_s \epsilon_{mf}^3} &\approx 14 \end{aligned} \tag{7}$$

where

$$\Phi_s = \frac{\text{Surface area of a volume equivalent sphere}}{\text{surface area of the particle}} \tag{8}$$

Combining these relationships the relationship for the minimum fluidization Reynolds number can be derived

$$Re_{mf} = \frac{D_p \boldsymbol{u_{mf}} \rho_g}{\mu_g} = \sqrt{33.7^2 + 0.0408 \frac{D_p^2 \rho_g (\rho_s - \rho_g) \boldsymbol{g}}{\mu_g^2}} - 33.7 \tag{9}$$

The particle diameter D_p can have dramatic effects on the fluidization of particle beds, as noted by Geldart in 1972 [16]. Four specific groups of particles are shown in Figure 5. The grouping depends both on the mean average particle diameter and the difference between the density of the particle and the density of the fluid. Starting from the left side of the Geldart Scale, Group C contains particles with the smallest diameters ranging from 1μm to approximately 150μm and are described as behaving in a very "cohesive" manner and that, "the interparticle forces are greater than the fluid can exert on the particle." This causes the particles to lift up together as plugs, forcing the gases to travel through the bed through "rat-holes" or small-diameter tubes. Because the injected gases travel through these channels, instead of permeating through the bulk of the bed, there is very little contact between the particles and the gas. In general, particles in Group C do not work well for many fluidized bed applications, especially those that require good mixing or heat transport. Interestingly, Geldart found that any particle with a mean particle diameter of 20μm or less, regardless of the density difference between the solid phase and the fluid phase, behaves in this way.

The next group, as ordered by particle size is Group A. Group A contains particles with diameters between 20μm and 600μm. Particles in Group A create fluidized beds that promote rapid mixing, achieve gross circulation, and readily exchange gases between the "bubbles" and the bulk of the particle bed. These bubbles travel upwards, away from the distribution plate, at a rate of approximately $0.3ms^{-1}$ - $0.4ms^{-1}$, which is faster than the interstitial gas velocity. As the superficial gas velocity is increased through slugging beds composed of particles from Group A, Geldart quotes Kehoe and Davidson's finding that the slugs tends to break down into "tongues of fluid darting in a zig-zag fashion up the bed"[20]. Geldart also noted that necessary gas velocity required to reach this

state decreases with decreasing particle diameter.

The particles used in the shocktube experiments performed at Arizona State University are mostly categorized as being in Group A. The density of the particles used is 2,500$kg \cdot m^{-3}$ or 2.5 $g \cdot cm^{-3}$, making difference between densities of the particles and the fluidizing gas (air) just over 2.498$g \cdot cm^{-3}$. Three particle sizes were used [44, 90]μm, [150,212]μm, and [212,297]μm. The smallest size range and the mid-size range of particles used at ASU are in Group B, while the largest size range of particles used at ASU are in Group C.

Particles in Group B range in size from 50μm to 1,000μm. Particles used for fluidized beds in this size range may resemble sand (in contrast to powder) when being poured and manipulated. Bubbles in fluidized beds composed of particles from Group B form just as the gas velocity reaches the fluidization condition. In general, the particles do not tend to mix except when disturbed by the rising bubbles. The vertical velocity of the bubbles increased linearly with the particle bed height as the bed expands. Gas exchange between the bubbles and the rest of the bed was found to be relatively low compared to the fluidized beds composed of particles from Group A. Geldart found no evidence of the slugs breaking down into turbulent flow for beds composed of particles in this group.

Particles in Group D, the largest sizes categorized by Geldart, are 400μm to over 2,000μm in diameter. There are not many fluidization experiments performed with particles nearing the large end of this range in diameters. The interstitial gases move more rapidly than any bubbles that form—as the gases move into the bottom of a bubble and out through the top of the bubble. In fluidized beds composed of particles in Group D, mixing tends to be quite poor [16].

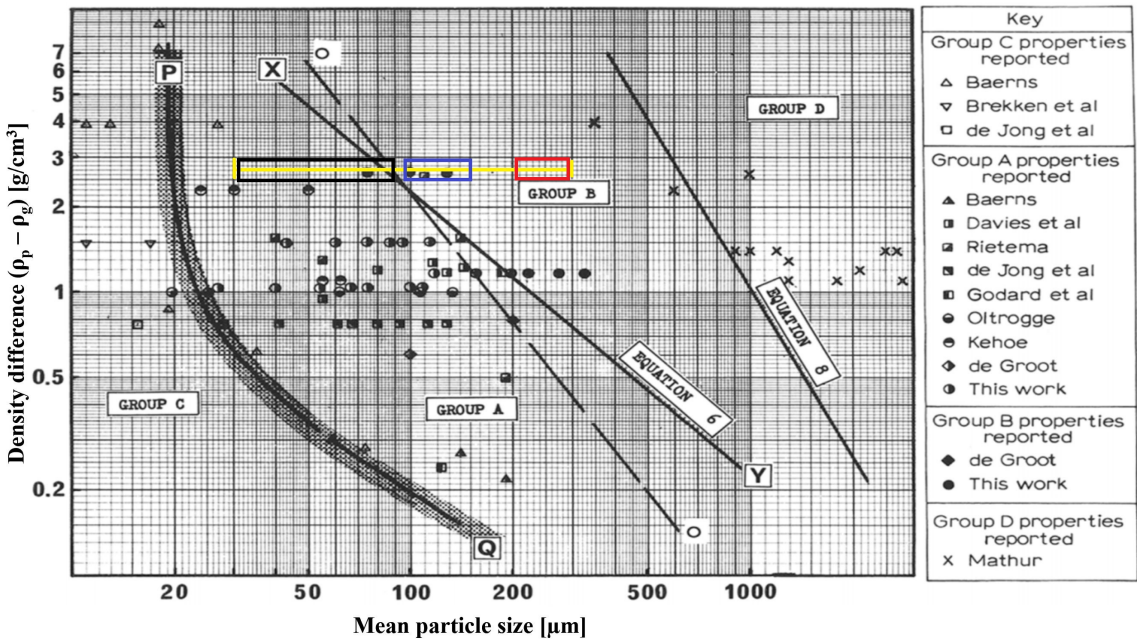

Figure 5: Shown Is the Geldart Scale Separating Particles into Four Different Groups Relating to the Observed Behaviors of Fluidized Beds Composed of Each of These Particle Groups. The Experiments Performed in the Vertical Shocktube at ASU Used Particles in Group a and Group B. The List along the Right Side of the Figure Denotes Which Data Sets Go along with Which Symbols Plotted. The Black Box Shows Where the Smallest Particles Used at ASU $[44, 90]\mu$m Are Located on This Plot. The Blue Box Shows the Mid-sized Particles Used at ASU $[150, 212]\mu$m. The Red Box Denotes the Largest Particles Used at ASU $[212, 297]\mu$m. *Courtesy: Geldart, 1973.*

Geldart also found a relatively linear correlation between the minimum bubbling velocity and the mean particle diameter shown as a solid line in Figure 6. He determined the slope of the linear relation between particle size and the minimum bubbling velocity, a coefficient called K_{MB} with units of s^{-1}, to be simply 100; such that the minimum bubbling velocity $\boldsymbol{u_{MB}} = K_{MB}D_p = 100D_p$. Also shown in dashed lines is the minimum fluidization velocity for particles in air with the density differences noted on the plotted lines.

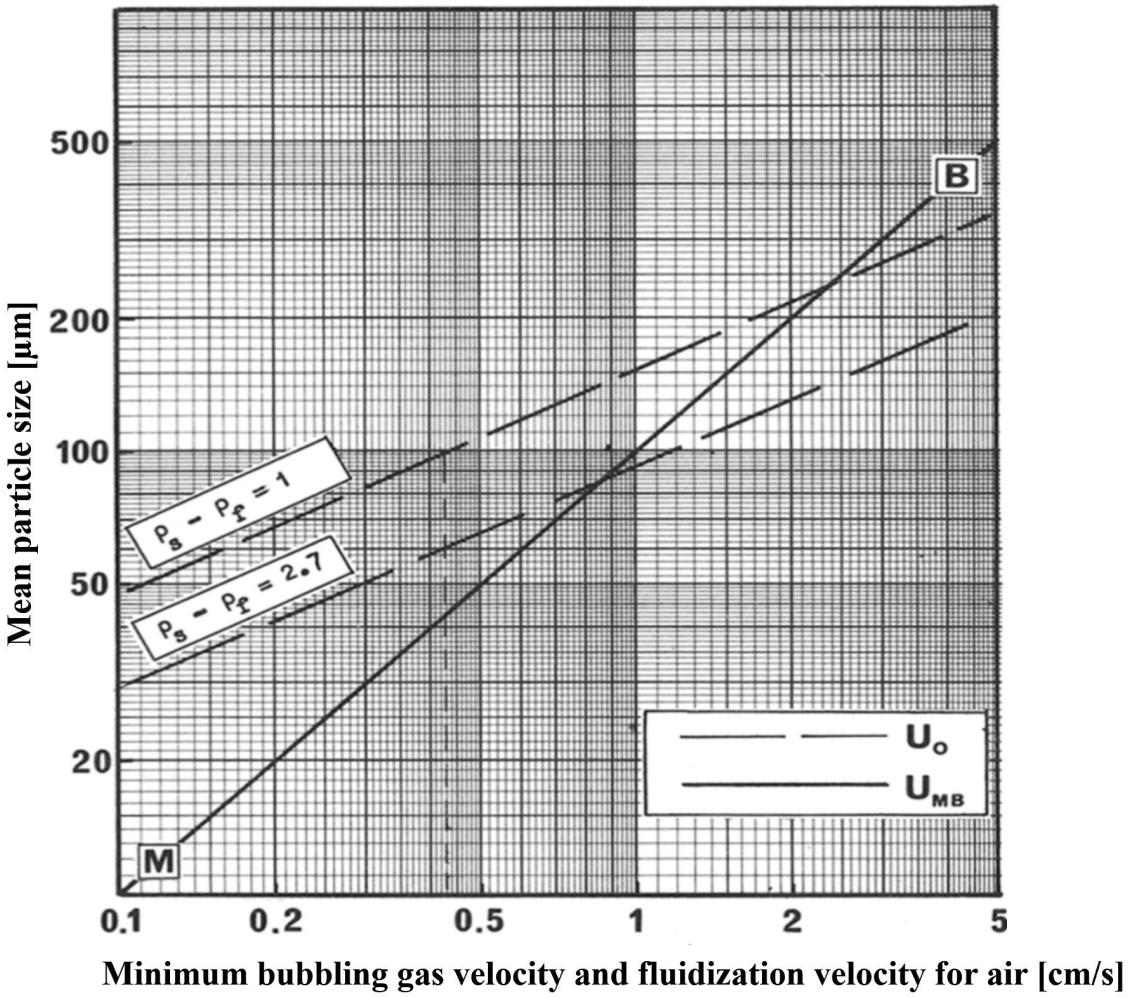

Figure 6: Minimum Bubbling Gas Velocity *Courtesy: Geldart, 1973.*

Though the cases shown in Geldart's paper from 1973 have gas velocities much slower ($u_g < 1m \cdot s^{-1}$) than the rapid decompression experiments, which have gas velocities ranging from $0 \geq u_g < 55m \cdot s^{-1}$ as measured above the bed, there are still some interesting findings relating to the differences in fluidization and particle size that may be very relevant to the this research. Noted in later chapters, the particle diameter does have an effect on the layering and particle-vacant region sizes during decompression. It may or may not be the case that in a compressible regime, the scale shown in Figure 5 may require slight adjustments. In 1986, Geldart is somewhat famously quoted as saying, "The arrival time of a space probe traveling to Saturn can be predicted more accurately

than the behavior of a fluidized bed chemical reactor!" This remains true today, as scientists and engineers are still working hard to improve predictive capabilities of complex compressible multiphase turbulent fluid flows.

1.4 Previous Research on the Motion of Particle Beds Driven by Gas Expansion

The capstone experiment for the CCMT simulation project was designed after experiments performed by Frost in 2012 [3]. Frost lined explosives with a particle bed composed of an inner layer of 120μm spherical glass particles and an outer layer of 200μm spherical steel beads. Two experimental cases were studied, beds composed of dry and wet particles, see Figure 7. Both experiments yielded a dramatic semi-regular spike-like jetting pattern of glass particles. The frequency of the jet pattern from the wetted bed is approximately ten times higher than the pattern from the dry bed. After the initial particle bed compaction phase from the shockwave traveling radially outward, Frost describes the formation of the jets as originating from the expansion wave traveling into the particle bed after it reflects from the outwardly transmitted blast wave. Citing Milne *et al.* [5] and Grady [4], Frost notes that "the fracturing of the compacted particle bed may involve a dynamic balance of surface energy and local kinetic energy."

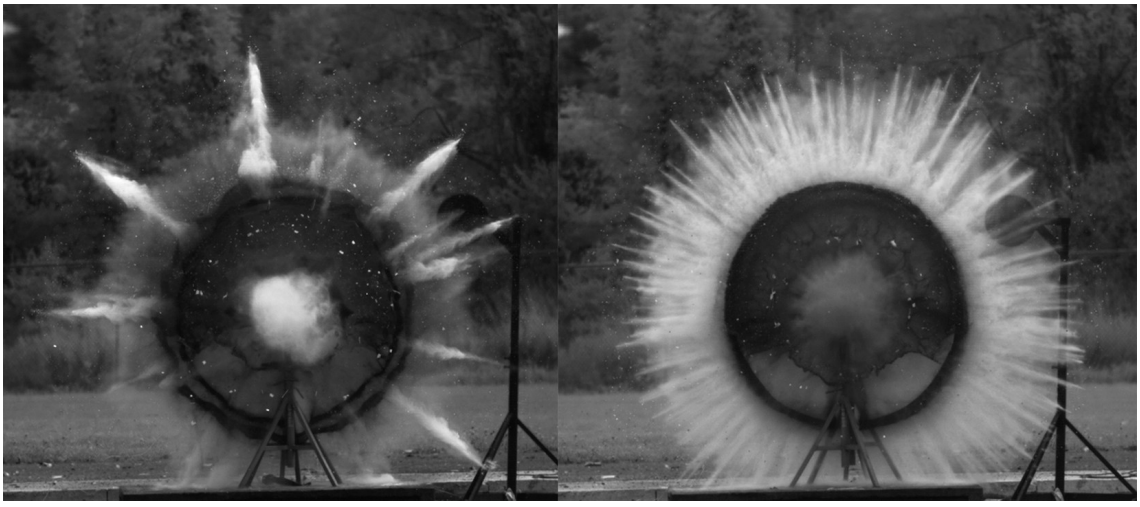

Figure 7: Shown Are Two Images Taken 12ms after Detonation. On the Left, a Dry Particle Bed Was Layered over the Explosive. The Experiment Shown on the Right Used a Thoroughly Wetted Particle Bed. *Used with Permission from the Author Frost, 2012.*

In 1989, Anilkumar decompressed beds of small-diameter spherical glass particles in a vertical shock tube [7]. In these experiments, the particle bed was initially pressurized higher than atmospheric pressure and the particle bed was unloaded *via* diaphragm rupture placed well above the particle bed interface. Anilkumar found average accelerations and velocities of the small glass particles for two different driving pressures (P_4). For P_4 = 310kPa ($\frac{P_4}{P_1} = 3.06$), the average particle acceleration was 275g and the average particle velocity was $15m \cdot s^{-1}$. For P_4 = 200kPa ($\frac{P_4}{P_1} = 1.97$), the average particle acceleration was 150g and the average particle velocity was $7.5m \cdot s^{-1}$. Several interesting features were noted in the particle bed evolution, including the development of horizontal layers which eventually broke down into a "honeycomb pattern" of particle-vacant regions. See Figure 8. Anilkumar stated the honeycomb pattern developed from particles raining down from the bottom surfaces of the horizontal slabs, analogous to Rayleigh-Taylor instabilities. While the honeycomb pattern of particle-vacant regions was observed in present experiments performed at Arizona State University, the specific effect of particles raining down from the horizontal slabs was not. It was also stated in Anilkumar (1989) [7], that there was an absence of wall effects during the rapid depressurization experiments. The experiments at ASU found that there were significant wall effects (to be discussed later) in the very early stages of the bed expansion. This discrepancy may be due to the improvement of high-speed imaging technology since this Anilkumar's Doctoral Dissertation was written.

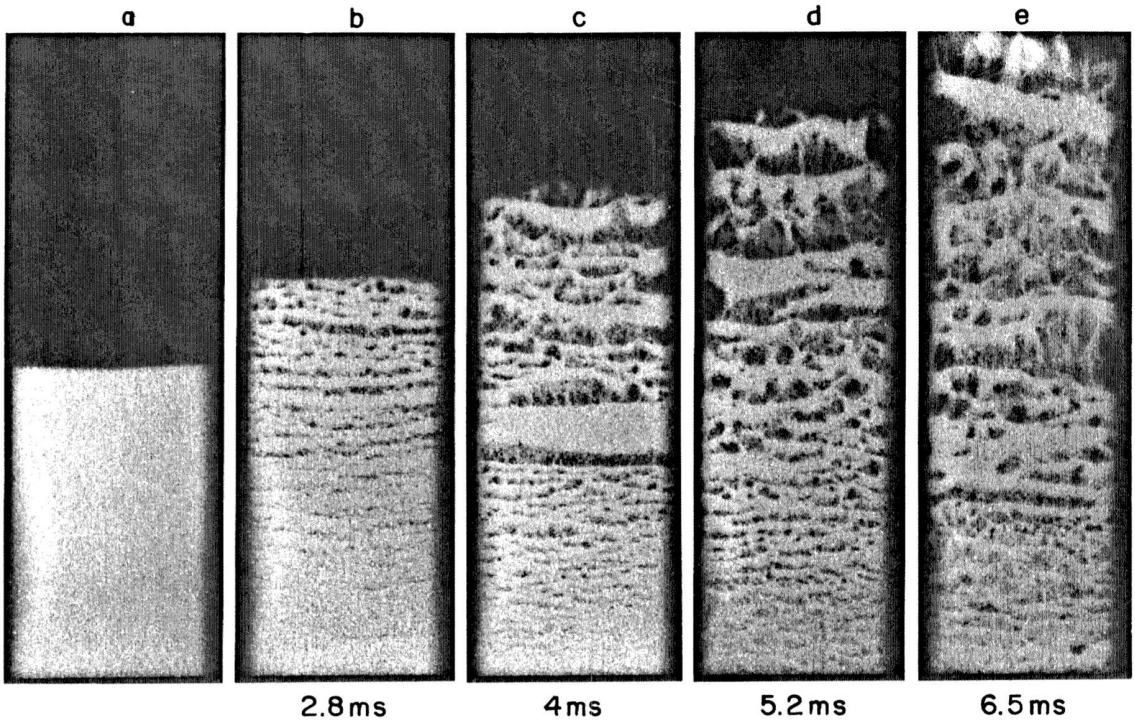

Figure 8: Shown Are Images from One of Anilkumar's Dusty Gas Experiments with $P_4 = 310$kPa ($\frac{P_4}{P_4} = 3.06$). Each Image Shown Was Captured *via* Single-flash Photographs. As Described by Anilkumar, the Images *a* and *b* Show the Horizontal Fractures That Arise Due to the Inherent Instabilities That Exist in High-density Particle Beds. In the Images *c*, *d*, and *e*, Anilkumar Describes the Particles Transitioning into an "Acceleration Phase" Where Particles Rain down from the Bottom of the Horizontal Slabs and the Honeycomb Pattern Emerges. *Used with Permission from the Author Anilkumar, 1989.*

Cagnoli *et al.* [8] also performed experiments decompressing dense particle beds composed of small-diameter glass spheres in a vertical shock tube with the motivation of better understanding explosive volcanic eruptions [8]. The rapid decompression of a dense particle bed can be compared to the rapid decompression of volcanic material that occurs within a volcanic conduit after the volcanic cap is ruptured. Cagnoli [8] described the evolution of the decompressing particle bed as being "reminiscent" of fluidization experiments. See Figure 9. Two different expansion regimes were noted—expansion without "bubbles" and expansion with "bubbles." *NOTE*: Cagnoli refers to the particle-vacant regions as bubbles. As the term *bubble* is typically used to describe well-defined gas pockets in liquid, it is recommended that these features be referred to as particle voids or

particle-vacant regions. In addition to highly irregular flow fronts, Cagnoli noted jetting effects both near the rapidly rising particle bed interface and within the bulk of the particle bed. Interestingly, the jets appeared to project in opposing directions along the longitudinal axis. It was also noted that under certain decompression conditions, the particle voids may oscillate vertically. This effect was not observed in the experiments performed at ASU.

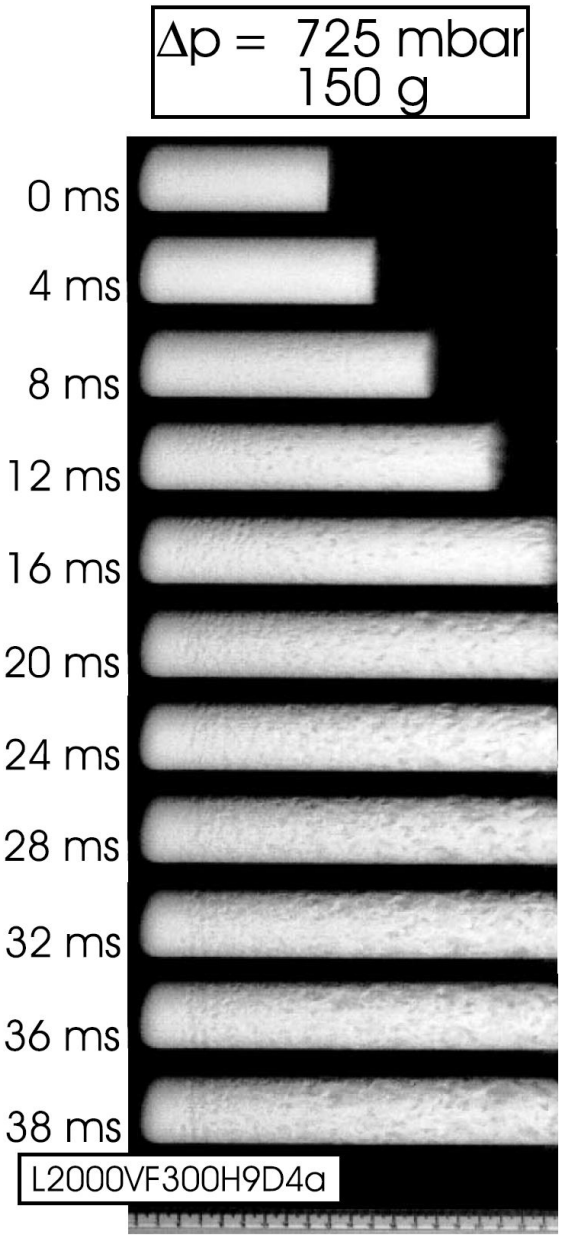

Figure 9: Shown Is a Timeseries of Images Taken by Cagnoli *et al.*. The Evolution of the Particle Bed Expansion Is Shown, Including the Development of Particle Voids. *Used with Permission from the Author Cagnoli, 2002.*

Chojnicki[1] investigated the effects of the particle bed on shock strength and velocity. It was determined that the shock velocity was reduced by 30-40% and the shock strength was reduced

by nearly 60% when a particle bed was present. The apparatus used by Chojnicki was specifically designed to examine a dense particle bed (see Figure 10).

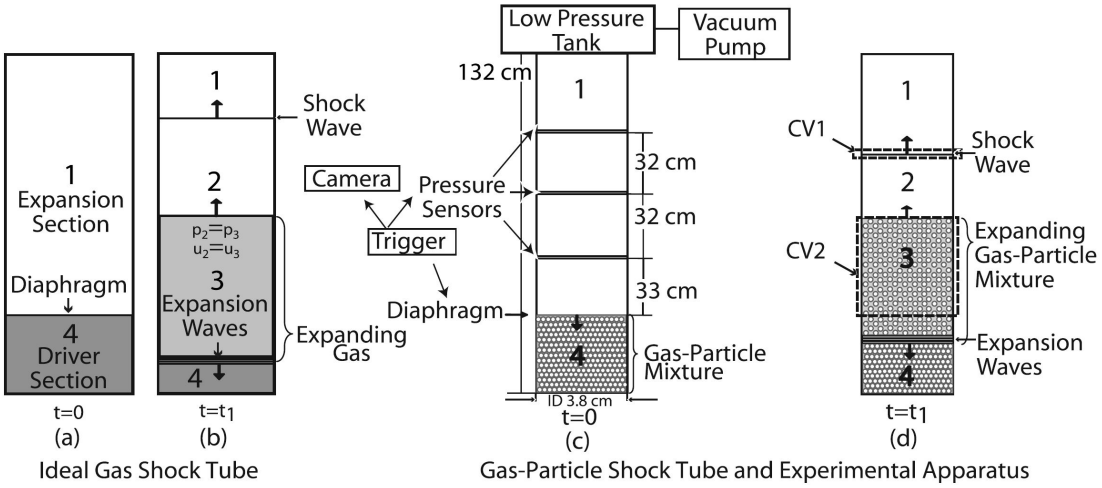

Figure 10: Shown Is the Sketch of the Experimental Setup Used by Chojnicki at the University of Bristol. This Experimental Setup Was Modified to Acquire Data in the Present Research. *Courtesy: Chojnicki, 2006.*

In the context of these previous experiments, the small glass spheres were used to mimic the volcanic material underneath the volcanic cap, after fragmentation has already occurred. Once the pressure inside the underground volcanic conduit reaches a level high enough to rupture the cap, the material inside the conduit is decompressed and is energetically discharged out the vent and into the atmosphere, where the pressure is much lower. As with the experiments performed by Anilkumar, it was observed during these experiments that the bed does not break apart homogeneously. It is not well-understood why this occurs. The rapid decompression inside the volcanic conduit is similar to the decompression that occurs in an exploding charge, in that the two phases may move independently exchanging energy and together as a pseudofluid. The particles can have significant effects on the air flow, causing turbulence or other complex flows.

1.5 Background

Starting from the conservation of mass, momentum, and energy, equations, the basic shock tube equation (for gas only) can be derived. In 2011, this was neatly laid out in Cantwell's

book, *Fundamentals of Compressible Flow* [9] and described below. The various important features and phases of the classic shock tube experiment are shown in Figure 11.

Given:

$\mathbf{U}_{1,\,2,\,3,\,4}$ = Gas velocity in regions 1, 2, 3, 4
$\mathbf{U}'_{1,\,2,\,3,\,4}$ = Gas velocity with respect to the moving shock
$\mathbf{U}_{p}$ = Gas piston velocity
$P_{1,\,2,\,3,\,4}$ = Pressure in regions 1, 2, 3, 4
$T_{1,\,2,\,3,\,4}$ = Temperature in regions 1, 2, 3, 4
$Ma_{1,\,2,\,3,\,4}$ = Gas mach number in regions 1, 2, 3, 4
Ma_{s} = Mach number of the propagating shock
c_{s} = velocity of the propagating shock
$\gamma_{1,\,2,\,3,\,4}$ = Ratio of specific heats in regions 1, 2, 3, 4

Table 2: Quantities Associated with 1D Shocktube Calculations

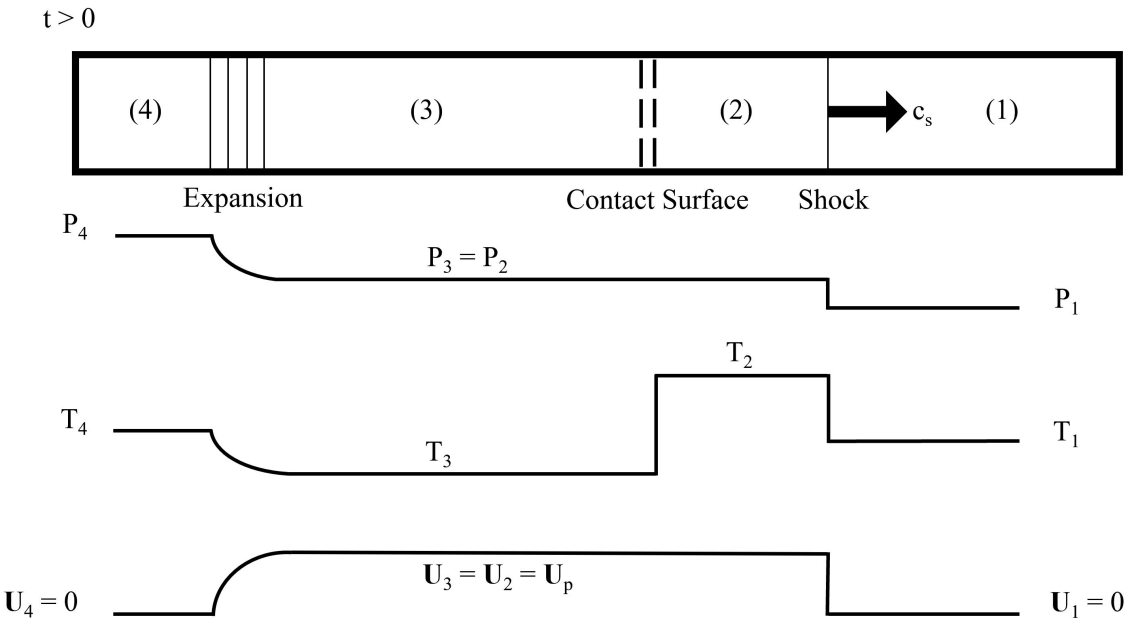

Figure 11: Depicted Are the Pressure, Temperature, and Velocity, of the Gases in the Classic Shocktube Experiment (t <0, Where the Diaphragm is Intact) and the Flows Resulting from the Diaphragm Burst (t >0) [9].

Starting with the boundary conditions of the contact surface within the shock tube

$$P_2 = P_3$$
$$and \tag{10}$$
$$U_2 = U_3 = U_p$$

$\mathbf{U}_\mathrm{p}$ is the so-called piston velocity in the shock tube. It derives its name from the similarity between a shock tube and a piston—cylinder setup. In these cases, $\mathbf{U}_\mathrm{p}$ would be the velocity of the slug of gas moving due to the diaphragm rupture in a shock tube and the velocity of a piston being extracted from a cylinder, respectively. The gas velocities $\mathbf{U}$ measured in the reference frame moving with the shock, traveling at a speed of $\mathrm{c_s}$ are denoted with a prime superscript.

$$U_1^{'} = -c_s$$
$$and \tag{11}$$
$$U_2^{'} = -c_s + U_p$$

The shock is defined as a discontinuity, meaning jump conditions are required to accurately describe the flow mathematically. By dividing the gas two velocities in 11, the jump conditions are as follows

$$\frac{U_2^{'}}{U_1^{'}} = \frac{1 + \frac{\gamma_1 - 1}{2} Ma_1^2}{(\frac{\gamma_1 + 1}{2}) Ma_1^2}$$
$$and \tag{12}$$
$$\frac{P_2}{P_1} = \frac{\gamma_1 Ma_1^2 - \frac{\gamma_1 - 1}{2}}{\frac{\gamma_1 + 1}{2}}$$

Here $\mathrm{Ma_1} = \mathrm{c_s} \ / \ \mathrm{a_1} = \text{-}\mathrm{U}^{'}{}_1 \ / \ \mathrm{a_1}$. From 12

$$U_p = U_2^{'} - U_1^{'} = U_1^{'} \left(\frac{1 - Ma_1^2}{(\frac{\gamma_1 + 1}{2}) Ma_1 (-\frac{U_1^{'}}{a_1})} \right) = a_1 \left(\frac{Ma_1^2 - 1}{(\frac{\gamma_1 + 1}{2}) Ma_1} \right) \tag{13}$$

Again using 11 in addition to 13, a useful equation for U_p can be expressed

$$U_p = a_1 \left(\frac{P_2}{P_1} - 1\right) \left(\frac{\frac{2}{\gamma_1}}{(\gamma_1 + 1)(\frac{P_2}{P_1}) + (\gamma_1 - 1)}\right)^{\frac{1}{2}} \tag{14}$$

Assuming an adiabatic and reversible process, isentropic theory allows

$$U_3 = U_p = \frac{2a_4}{\gamma_4 - 1} \left(1 - \left(\frac{P_3}{P_4}\right)^{\frac{\gamma_4 - 1}{2\gamma_4}}\right) \tag{15}$$

By plugging 14 into 15 and using the following pressure relationships

$$\frac{P_4}{P_1} = \left(\frac{P_3}{P_2}\right)\left(\frac{P_2}{P_1}\right)\left(\frac{P_1}{P_4}\right) \tag{16}$$

$$Note: \frac{P_3}{P_2} = 1$$

the basic shock equation can be written as

$$\frac{P_4}{P_1} = \frac{P_2}{P_1} \left(1 - \frac{(\gamma_4 - 1)(\frac{a_1}{a_4})(\frac{P_2}{P_1} - 1)}{\sqrt{1\gamma_1}\sqrt{2\gamma_1 + (\gamma_1 + 1)(\frac{P_2}{P_1} - 1)}}\right)^{-\frac{2\gamma_4}{\gamma_4 - 1}} \tag{17}$$

Equation 17 is very useful for describing the pressure flows through an experiment. A few other equations that help describe and interpret data from shock tube experiments are

Shock strength equation

$$\frac{P_2}{P_1} = \frac{2\gamma_1}{\gamma_1 + 1} M a_s^2 - \left(\frac{\gamma_1 - 1}{\gamma_1 + 1}\right) \tag{18}$$

Mach number equation

$$Ma_s = \left(\frac{\gamma_1 + 1}{2\gamma_1}\right)^{\frac{1}{2}} \left(\frac{P_2}{P_1} + \frac{\gamma_1 - 1}{\gamma_1 + 1}\right)^{\frac{1}{2}} \tag{19}$$

Temperature ratio between regions 3 and 4

$$\frac{T_3}{T_4} = \left(\frac{P_3}{P_4}\right)^{\frac{\gamma-1}{\gamma}} \tag{20}$$

The goal of the Center for Multiphase Flow is to be able to simulate the shock tube experiment at ASU predictively. To do that, they are using the following versions of the general conservation equations to describe the gas flow [10] [11]

Given:

p = gas pressure[kPa]	M_p = mass of particle [kg]
E = total energy of the gas per unit mass $[\frac{J}{kg}]$	τ_p = particle response time [s]
ϕ_g = gas volume fraction [unitless]	$\phi_\mathrm{p} = (1 - \phi_\mathrm{g})$
a = local speed of sound$[\frac{m}{s}]$	= solid volume fraction [unitless]
ρ_g = gas density $[\frac{kg}{m^3}]$	ρ_p = particle density $[\frac{kg}{m^3}]$
$\boldsymbol{u} = (u_\mathrm{x}, u_\mathrm{y}, u_\mathrm{z})$	$\boldsymbol{v} = (v_\mathrm{x}, v_\mathrm{y}, v_\mathrm{z})$
= Eulerian gas velocity $[\frac{m}{s}]$	= Eulerian particle velocity$[\frac{m}{s}]$
$\boldsymbol{u}_m = \phi_\mathrm{g}\boldsymbol{u} - \phi_\mathrm{p}\boldsymbol{v}$	D_p = particle diameter [m]
= gas-particle mixture velocity $[\frac{m}{s}]$	g_{pg} = work done by coupling force [J]
μ_g = gas dynamic viscosity $[\frac{kg}{ms}]$	$\mathrm{V_p}$ = particle volume $[m^3]$
γ = ratio of specific heats [unitless]	q_{gp} = gas-particle heat exchange [J]
R = specific gas constant $[\frac{J}{mol \cdot K}]$	$\boldsymbol{f}_{gp}$ = gas-particle coupling force[N]
e = internal energy of the gas [J/kg]	T_g = gas temperature [K]

Table 3: Gas and Particle-related Quantities

Conservation of Mass for the gas phase

$$\frac{\partial}{\partial t}(\phi_g \rho_g) + \nabla \cdot (\phi_g \rho_g \boldsymbol{u}) = 0 \tag{21}$$

Conservation of Momentum for the gas phase

$$\frac{\partial}{\partial t}(\phi_g \rho_g \boldsymbol{u}) + \nabla \cdot (\phi_g \rho_g \boldsymbol{u}\boldsymbol{u} - \phi_g p \boldsymbol{I}) = p \nabla \phi_g + \boldsymbol{f}_{gp} \tag{22}$$

Conservation of Energy for the gas phase

$$\frac{\partial}{\partial t}(\phi_g \rho_g E) + \nabla \cdot (\phi_g \rho_g \boldsymbol{u} E + p \boldsymbol{u}_m) = g_{gp} + q_{gp} \tag{23}$$

Additionally, a calorically perfect ideal gas was assumed and can be written as

$$p = \rho_{\mathrm{g}}(\gamma - 1)e = \rho_{\mathrm{g}} R T_g \tag{24}$$

where $e = E - \frac{1}{2}|\boldsymbol{u}|^2$. The governing equations [10][11] [12] for the particles are as follows

Given:

$\mathbf{X}$ = Lagrangian particle position
$\mathbf{V}$ = Lagrangian particle velocity
$\mathbf{F}_{\mathrm{qs}}$ = quasi-steady force
$\mathbf{F}_{\mathrm{un}}$ = undisturbed flow forces
$\mathbf{F}_{\mathrm{b}}$ = external body force applied to each particle
$\mathbf{F}_{\mathrm{c}}$ = net collisional force on particle from neighboring particles and walls

Table 4: Force Definitions

Particle velocity

$$\frac{d\boldsymbol{X}}{dt} = \boldsymbol{V} \tag{25}$$

Conservation of Momentum for the solid phase

$$M_p \frac{d\boldsymbol{V}}{dt} = \boldsymbol{F_{qs}} + \boldsymbol{F_{un}} + \boldsymbol{F_b} + \boldsymbol{F_c} \tag{26}$$

where $\mathbf{F}_{\mathrm{qs}} + \mathbf{F}_{\mathrm{un}}$ = total hydrodynamic force. The quasi-steady force used for the simulations being performed at CCMT is

$$\boldsymbol{F_{qs}} = \beta V_{\mathrm{p}} (\boldsymbol{U} - \boldsymbol{V}) \tag{27}$$

β is an based on an empirical fit and is defined as [13] [15]

$$\beta = \begin{cases} 150 \frac{\phi_{\mathrm{p}}}{\phi_{\mathrm{g}}} \frac{\mu_{\mathrm{g}}}{D^2{}_{\mathrm{p}}} + 1.75 \frac{\rho_{\mathrm{g}}}{D_{\mathrm{p}}} |\mathbf{U} - \mathbf{V}| & \phi_{\mathrm{p}} > 0.2 \\ 0.75 {C_{\mathrm{D}}}^* \frac{D_{\mathrm{p}}}{\rho_{\mathrm{g}}} |\mathbf{U} - \mathbf{V}| {\phi_{\mathrm{g}}}^{-2.65} & \phi_{\mathrm{p}} \leq 0.2 \end{cases} \tag{28}$$

The drag coefficient ${\mathrm{C_D}}^*$

$${C_{\mathrm{D}}}^* = \begin{cases} \frac{24}{Re_p^*} (1 + 0.15 ({Re_{\mathrm{p}}}^*)^{0.687}) & Re_p^* \leq 10^3 \\ 0.44 & {Re_{\mathrm{p}}}^* > 10^3 \end{cases} \tag{29}$$

is dependent on the volume-weighted Reynolds number

$${Re_{\mathrm{p}}}^* = \phi_{\mathrm{g}} Re_{\mathrm{p}} \tag{30}$$

where

$$Re_{\mathrm{p}} = |\boldsymbol{U} - \boldsymbol{V}| \rho_{\mathrm{g}} \frac{D_{\mathrm{p}}}{\mu_{\mathrm{g}}} \tag{31}$$

The particle Mach number is defined as

$$Ma_{\mathrm{p}} = \frac{1}{a}|\boldsymbol{U} - \boldsymbol{V}| \tag{32}$$

The undisturbed force is dependent on the gas pressure gradient at each particle location ∇ P and is defined as

$$\boldsymbol{F_{un}} = -V_p \nabla P \tag{33}$$

The body force acting on each particle is dependent on gravitational acceleration **g**

$$\boldsymbol{F_b} = M_p \boldsymbol{g} \tag{34}$$

In the simulation, to model collisional forces between particle i and particle j, a soft-sphere spring dashpot was used [17]

$$\boldsymbol{F_{c,i,j}} = -k_c \delta_{\mathrm{ij}} \boldsymbol{n}_{\mathrm{ij}} - \eta \boldsymbol{V_{ij}} \tag{35}$$

where $\boldsymbol{n_{ij}}$ is the unit vector from the center of the ith particle to the jth particle and k_c is the stiffness parameter in that direction, δ_{ij} is the relative overlap between particles, η is the normal damping coefficient; which is a function of k_c, M_p, and the coefficient of restitution e_n. $\boldsymbol{V_{ij}}$ is the relative velocity between particle i and particle j. For the cases where a particle collides with a wall, the wall is considered to be an infinitely massive particle j with $D_p = 0$.

Combining both the gas and particle equations, CCMT was able to produce the following simulation of the pressure field changing over the first few layers of glass particles in the particle bed in the very early stage of the expansion while the particles remain motionless (see Figures 12 and 13). In this preliminary simulation, the particles are stationary, just as they would be before the forces from the expanding gases overcome the inertia of the glass particles. An interesting feature is the

pressure pockets maintained on the sides of the particles as the expansion wave passes over them.

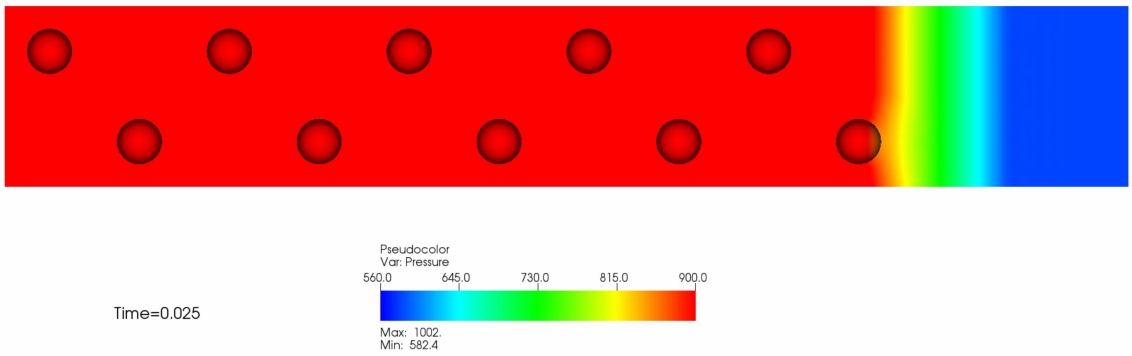

Figure 12: Pictured Is the Pressure Field in the Initial Moment in the Simulation When the Expansion Wave First Impinges on the Particle Bed. *Used with Permission from CCMT [28].*

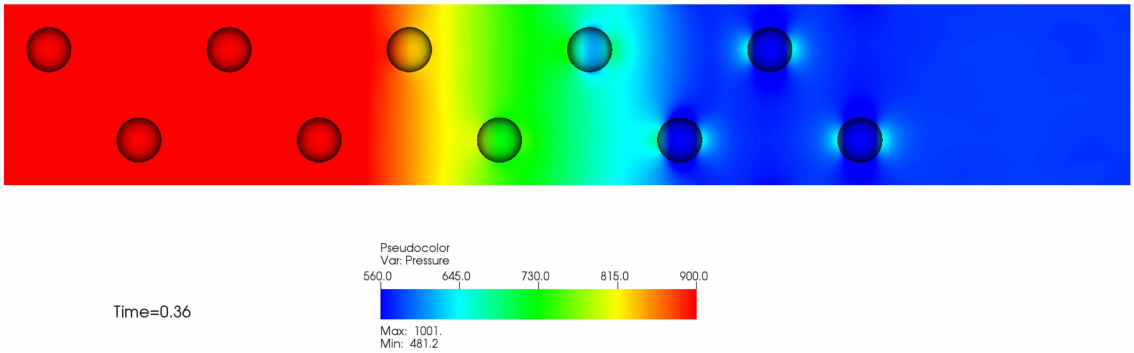

Figure 13: Pictured Is the Pressure Field When the Expansion Wave Has Traveled Midway Through the Particle Bed. *Used with permission from CCMT [28].*

Figure 14 shows the most recent simulation of the Arizona State University shocktube experiment from the CCMT at the University of Florida. The pressure ratio is relatively low, $\frac{p_4}{p_1} = 1.42$, compared to the experiments performed at ASU with $\frac{p_4}{p_1} \approx 20$. Nonetheless, there are several important features which resemble the physical experiments, including a top layer of the particles separating from the bulk of the bed and accelerating upward. Additionally, several particle-vacant regions, or voids, form during the simulated bed expansion. However, the pattern of particle-vacant regions seen in the simulation differ from those seen in the experiments performed at ASU. In the rapid decompression experiments, the particle bed broke down into semi-regular layers and then

further broke down into a semi-regular void pattern, or a "honeycomb pattern" as described by Anilkumar in [7].

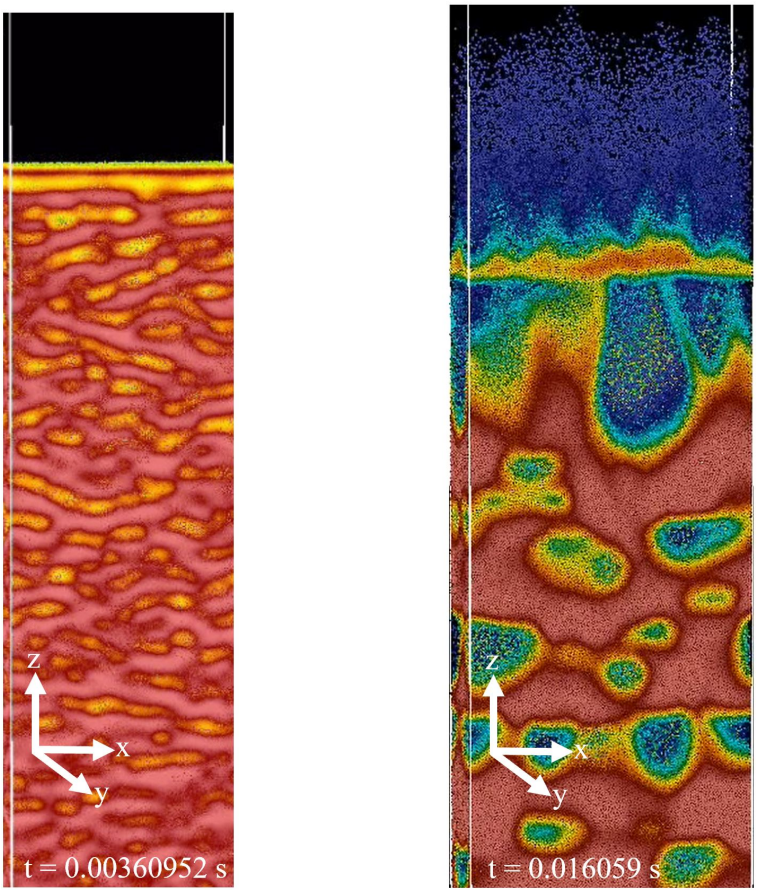

Figure 14: Pictured Is the Most Recent (February 2019) Simulation of an Expanding Particle Bed at t = 3.6ms and t = 16.1 Ms after the Diaphragm Ruptured. The Initial Height of the Particle Bed Is 95mm and the Total Length of the Driving Section Is 0.23m. The Color Scale Denotes the Local Particle Volume Fraction, with Red Indicating High Particle Volume Fraction and Blue Indicating Low Particle Volume Fraction. The d_p of the Simulated Particles Is 95μm and the Initial Pressure Ratio $\frac{P_4}{P_1}$ Across the Diaphragm Is 1.42. *Used with Permission from CCMT [28].*

It may or may not be the case that the differences seen in the void patterns were caused by using a much lower pressure ratio in the simulation compared to the experiments. The simulated particle bed deformation seems somewhat reminiscent of the particle bed deformation seen in the experiments where there was a leak in the diaphragm prior to the main rupture. This caused a much more irregular pattern, including particle-vacant regions of varying sizes. In Figures 15 and

16 the transition between a slow decompression and rapid decompression in a single experimental realization is shown. In Figure 15, a leak in the diaphragm has allowed a small pressure drop across the boundary between Region 1 and Region 4. This relatively small decompression event causes the particle bed to break down into irregularly-sized particle-vacant regions without first breaking down into horizontal layers or slabs. Once the diaphragm fully ruptures as shown in Figure 16, the particle bed is rapidly decompressed. In-between the large particle-vacant regions (formed during the slow decompression) a tight pattern of much smaller and more uniformly-sized voids form. This progression demonstrates how the pressure gradient can dramatically affect the evolution of the particle bed.

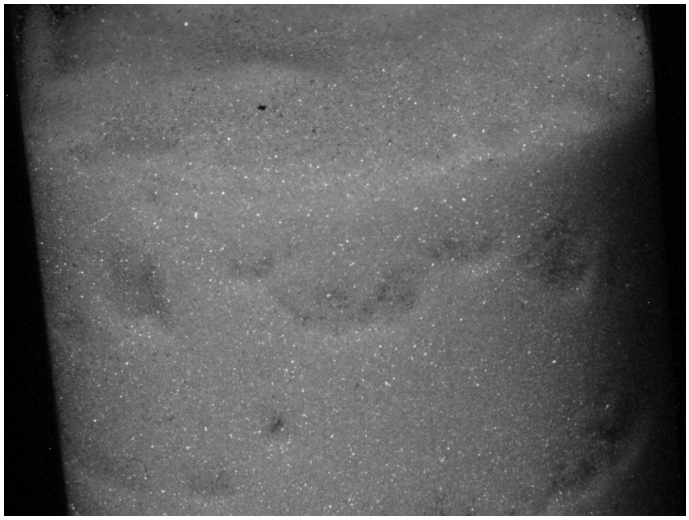

Figure 15: Shown Is a Zoomed-in Snapshot of a Particle Bed During a Period of Irregular Expansion Caused by a Leak in the Diaphragm. The Leak Caused a Small Pressure Gradient Across the Interface of the Particle Bed. Particularly Important Features to Note Are the Irregularly-sized and Irregularly-spaced Particle-vacant Regions and the Absence of Horizontal Layers or Slabs. It Is Also of Interest That the Gas-particle Interface Has Very Little Visible Deformation Compared to the Bulk of the Particle Bed Below. The File Name Associated with this Image is ASU_1(-7670).

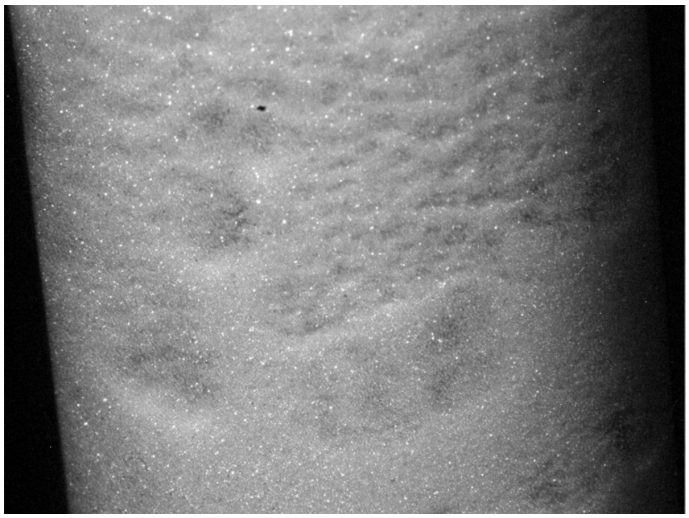

Figure 16: Shown Is an Image Just after the Image from the Experimental Realization Shown in Figure 15. In This Figure, the Diaphragm Has Fully Ruptured after Leaking. This Large Rupturing Event Allowed for a Strong Expansion Wave to Travel Downward Toward the Bed and Rapidly Decompress the Already-slightly Decompressed Particle Bed. Once the Rapid Decompression Commences, the Familiar Cellular Pattern of Particle-vacant Regions Appears. The Pattern Is Disrupted by the Large Bubble-like Features Created During the Slow Decompression Period in This Realization. The File Name Associated with this Image is ASU_1(-7206).

1.6 Research Objectives

The present research was performed with the following primary goals in mind:

1. Provide validation data for the CCMT team's complex multiphase simulation
2. Better understand the physics of multiphase media during a rapid decompression event, such as an explosion or volcanic eruption
3. Given a specific pressure unloading across a particle bed, to examine the very early gas motion prior to particle motion, the bed motion during early expansion periods, the bulk motion of the particle bed, the induced pressure fluctuations, the deformation and evolution of the particle bed interface, and the velocities of the gases as they escape the particle bed.

There are many gas and particle quantities in the rapid decompression experiments that could not be measured, including but not limited to the motion of the particles near the interior of the bed, interstitial gas motion, and temperature. However, the quantities that could be measured provide valuable insight into the true physics involved in this experiment. These measurements include particle bed interface motion, the motion and evolution of the exterior particle-vacant regions, the

dynamic pressure changes, and gas velocities escaping the particle bed during early expansion. The experimental setups designed to measure these quantities are described in Chapter 2.

2 EXPERIMENTAL SETUP

2.1 Components and Connections

The basic components of the vertical shock tube at ASU are four glass cylinders with a length of approximately 0.32m, the data acquisition system, the diaphragm, the vacuum pump, and the particle bed. The four cylinders are $\frac{1}{8}$ inch thick and are connected end-to-end vertically with Teflon joints and metal clamps below a large vacuum tank. A schematic diagram of the shocktube in the standard configuration, including the data collection system connections is shown in Figure 18. Other configurations, such as those designed to measure shock velocities or diaphragm rupture timings will be discussed in the chapters associated with the data collected from those experiments. These glass segments and joints are rearrangeable, which allows for the diaphragm to be moved to four different locations. With this flexibility, experiments with different objectives can be performed on the same apparatus with minimal take-down and setup time. When the particle bed is emplaced, it is necessary for the bottom glass segment to be closed on one end. For the experiments where no particle bed is required, the bottom segment can be closed or left open.

There are two data collection subsystems installed on the vertical shocktube used to measure particle velocities, gas velocities, shock velocities, expansion wave velocities, and other dynamic pressure changes. The first subsystem is used to capture video data of the particle bed expanding upward in the $+\boldsymbol{z}$ direction. The high-speed camera used is a Vision Research v641. For the data presented regarding the particle bed expansion, the frame rate used is 10,000 fps. This specific frame rate was chosen because it was fast enough to be able to track the large particles (the smaller particles cannot be resolved well enough to see individual particles and still have a large enough field of view to track the bed interface rise over a useful period of time) and still allow for reasonable resolution 208($\mathbf{X}$)x800($\mathbf{Y}$) in order to view the bed rise over an appropriate period of time (on the order of milliseconds, but specifically depending on initial bed height $\boldsymbol{z_{b0}}$). Used with the high-speed camera is a Zeiss zoom lens and two high-power LED arrays from Vision Research, each with an output of 7,700 lumens, which allows for very clear and high-quality imaging. The software used to control the camera is designed by Vision Research and is called Phantom Camera Control or PCC. The video recording is triggered by the shockwave interacting with the second data acquisition subsystem.

There is an additional imaging subsystem used for the Particle Image Velocimetry experiments. Briefly described, the configuration is a somewhat standard Particle Image Velocimetry (PIV) setup. A planar laser light sheet is used to illuminate gas flow seeded with 2μ m oil droplets. Image data is collected *via* a TSI PowerView Plus 11MP camera placed in a vertical (z-r) plane located just above the particle bed when the expansion fan impinges on the gas-particle interface. The triggering mechanism for the PIV experiments is identical to the triggering mechanism used for the experiments using the standard shocktube configuration. However, the signal from a different pressure transducer is used to send the hardware trigger through the NI 1073 chassis. The expansion wave traveling downward is used, as opposed to using the upward moving shock. This PIV configuration is discussed further in Chapter 8.

The second subsystem collects dynamic pressure data and triggers the entire data acquisition system. It contains a series of eight PCB 11328B pressure transducers (See Table 5 for a list of the transducers associated properties), a National Instruments PXIe-1073 chassis that connects the data digitization cards to the computer using an integrated MXI-Express controller, a National Instruments PXIe-4492 card which digitizes the analog voltage data into digital data, a National Instruments PXIe-6341 card which is a PXI Multifunction I/O Module used to output a trigger, a BNC 2120 breakout board which is a Shielded Connector Block that allows for specialized connections to be made to the PXIe-6341 card, and a BNC 565 Pulse/Delay generator. The National Instruments chassis and cards are controlled using LabVIEW software. Each of the eight analog pressure transducers is simultaneously sampled-and-held at 200kHz and is digitized into 16-bit words. These are connected *via* BNC cabling to the NI PXIe-4492 card installed in the NI 1073 chassis. There is a hardware connection along the back of the NI 1073 chassis connecting the NI 4492 card and the NI 6341 card. When the shock passes by a predetermined pressure transducer, a signal is automatically sent through this hardware trigger line to the NI 6341 card along the back of the NI 1073 chassis (*Note: this trigger is discussed further in Chapter 3.2*). The NI 6341 card has an output line, which is connected to the BNC 2120 breakout board. Ideally, the PF I/O line on the BNC 2120 breakout board would be connected to the trigger port on the camera. However, the pulse sent out by the BNC 2120 is only 20ns long. This signal is not long enough for the camera to recognize. Therefore, the PF I/O line from the BNC 2120 breakout board is intermediately connected to the

EXT/Gate port on the BNC 565 Pulse/Delay generator. The BNC 565 is set to send out a 5μs pulse from one of the output channels as soon as the 20ns pulse is recognized from the EXT/Gate line. A BNC cable goes from the output channel on the BNC 565 to the trigger port on the camera and initiates the high-speed video recording. The triggering system initiates the recording and saving of both the pressure transducer data and the high-speed video data. This includes one tenth of a second of buffer data, captured prior to the triggering event.

Transducer name	Serial Number	Ring	Port Position in Ring	Calibration mV\kPa
Ai0	LW33447	P0	Middle	14.36
Ai1	LW33446	P123	Left	14.31
Ai2	LW33439	P123	Middle	14.77
Ai3	LW33438	P123	Right	14.70
Ai4	LW33367	P45	Left	15.19
Ai5	LW33442	P45	Right	14.71
Ai6	LW33441	P56	Left	14.73
Ai7	LW33440	P56	Right	14.40

Table 5: Shown is a Table of the 8 PCB 113b28 Pressure Transducers Used and Their Associated Properties.

The pressure transducers are installed in the Teflon joints that connect the glass cylinders together. Two of the Teflon joints have two pressure transducer ports, one of the Teflon joints has three pressure transducer ports (jointly called the *triple pressure transducer* as it is very important and is referenced frequently), and one of the Teflon joints has a single pressure transducer port. The schematic diagram in Figure 18 shows what's called the *standard* configuration. In this configuration, the joint with the sole pressure transducer port is placed in-between the top of the vertical shocktube and the large-diameter vacuum tank. It is used primarily to measure shock velocity between the triple pressure transducer and the top of the shocktube before the shock reflects downward back towards the diaphragm. The triple pressure transducer is placed one glass cylinder above the Teflon joint containing the diaphragm. Its purpose is to measure the shock and determine whether the shock is axisymmetric. The angle between each of the individual pressure transducers installed on this piece is 59°. The angle between the pressure transducers on the joints with only two pressure transducers is 118°. These joints are both placed in between the glass cylinders below the diaphragm. Two detailed schematics created by the technicians working in the machine shop at Arizona State

University are shown of the triple pressure transducer joint and the joint with two pressure transducer ports in Figures 19 and 20, respectively.

The pressure transducer at the top of the vertical shocktube is placed in the center of the Teflon ring P_0, as the other pressure transducers are and the glass cylinder underneath connects as all the other cylinders connect to the other Teflon rings. However, the connection between ring P_0 and the vacuum tank is irregular. Shown in Figure 17 is a schematic of the top joint connection. Notice the inner diameter of the tube connecting the tube to the vacuum tank is smaller than the inner diameter of the glass cylinder and the ring P_0. This causes the shock to reflect in this corner and the pressure transducer reads the increased pressure from the reflected shock approximately 0.1ms from the initial shockwave passes by.

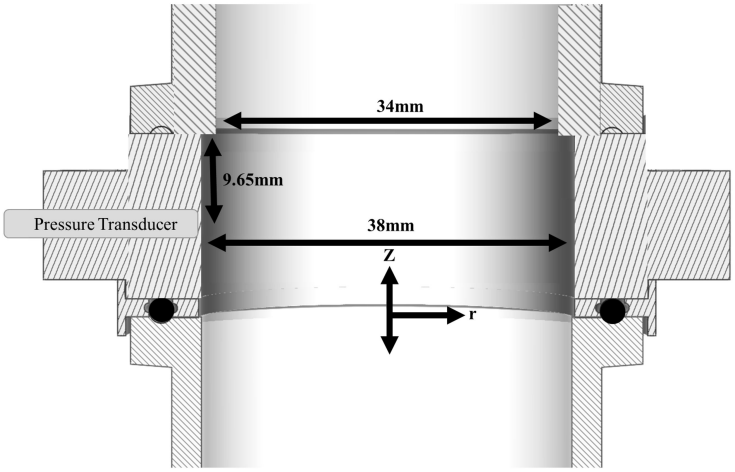

Figure 17: Shown Is a Sketch of the Joint Connecting Teflon Ring p_0 at the Top of the Shocktube with the Vacuum Tank. Note That the Inner Diameters Between the Pieces Do Not Match. This Causes the Shock to Partially Reflect in This Corner. This Reflection Is Read by the Pressure Transducer Located in Ring p_0 Approximately 0.1ms after the Initial Shockwave Passes By. *Used with Permission from Brian Ipema and the Instrument Design and Fabrication Shop at Arizona State University.*

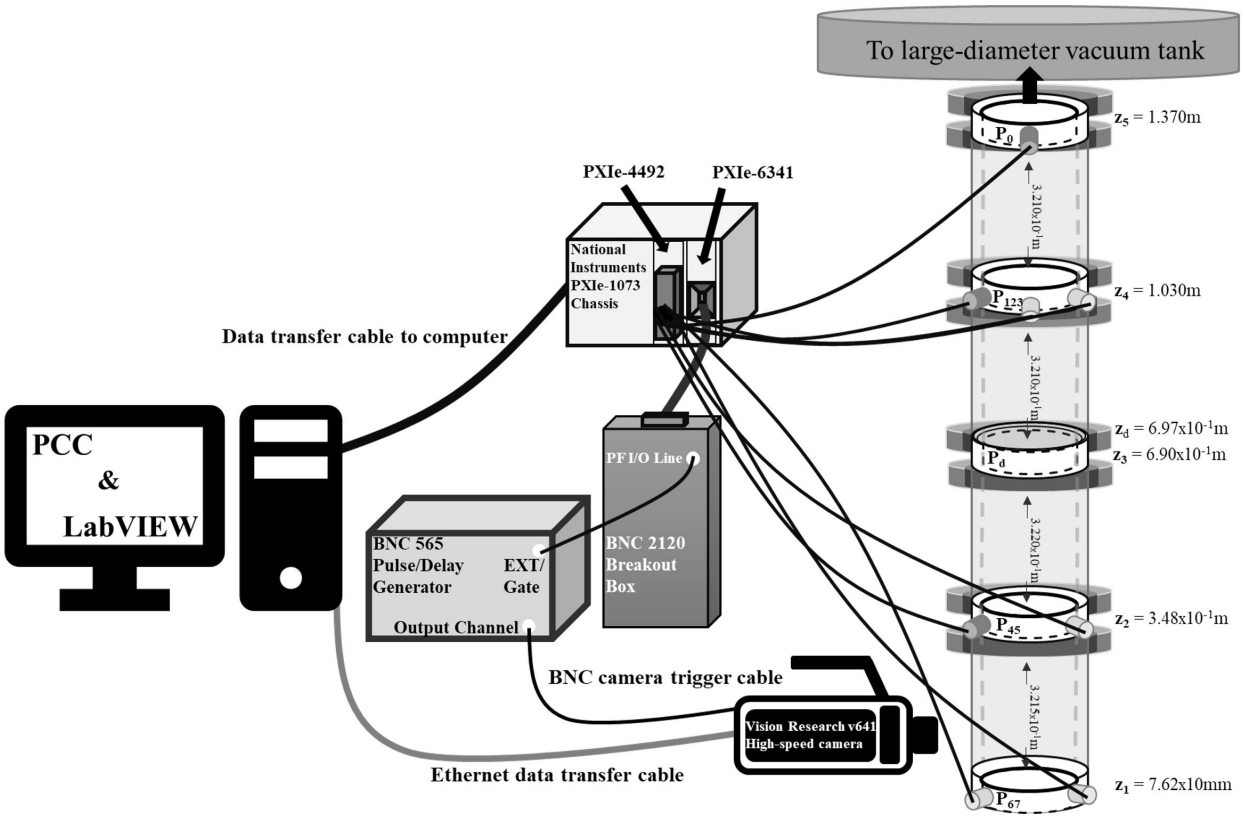

Figure 18: Shown Is a Detailed Schematic of the Vertical Shocktube in the Standard Setup. The Standard Setup Includes the Diaphragm Joint Two Segments up from the Bottom of the Shocktube and the Triple Pressure Transducer One Segment above the Diaphragm. Not Shown Is the Particle Bed in the Bottom of the Shocktube. In Experiments, the Particle Bed Rests on the Bottom of the Shocktube, Which Is Sealed with Many Layers of Polypropylene Tape, with a Height Varying Between 0.1m And 0.2m, Depending on the Specific Experiment. The Pressure Transducers Used to Trigger the Data Acquisition Are Colored Yellow. The Dark Transducer on Ring p_{123} Located at $\boldsymbol{z_4}$ Is Used to Trigger the Data Acquisition System. The Dark Transducer on Ring p_{45} Located at $\boldsymbol{z_2}$ Is Used to Trigger the Data Acquisition When the Experiment Is Configured to Capture PIV Data (Note: The Bottom of the Shocktube Is Open to the Atmosphere for the Diaphragm Timing Configuration). The Dark Transducer on Ring p_0 Located at $\boldsymbol{z_5}$ Is Used to Trigger the Data Acquisition When the Experiment Is Configured to Capture Shock Velocity Data.

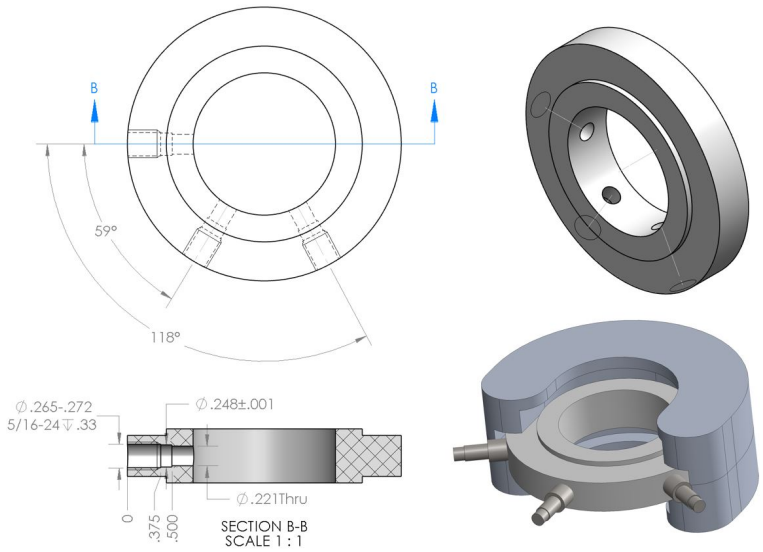

Figure 19: Shown Is a Sketch and Model of the Triple Pressure Transducer Created by the Technicians in the Machine Shop at Arizona State University. Also Depicted Are the Metal Clamps Used to Hold the Joint In-between the Glass Cylinders and Ensure an Air-tight Fit. *Used with Permission from Brian Ipema and the Instrument Design and Fabrication Shop at Arizona State University.*

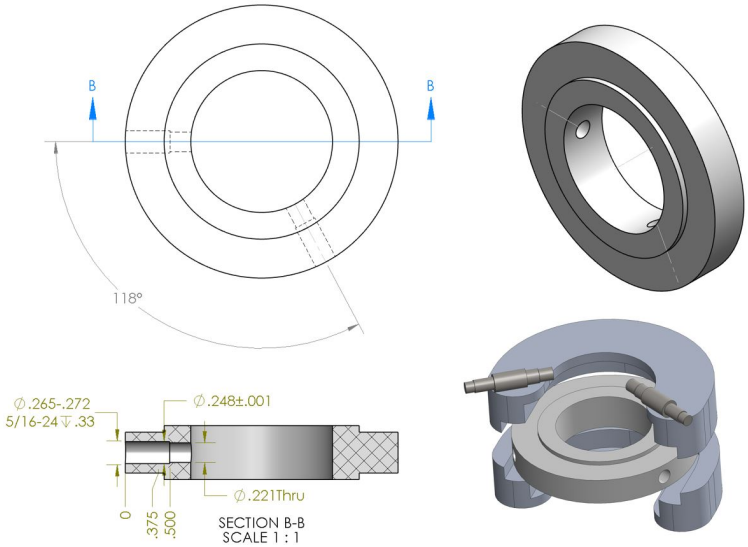

Figure 20: Shown Is a Sketch and Model of a Joint with Two Pressure Transducer Ports Created by the Technicians in the Machine Shop at Arizona State University. Note the Image in the Bottom Right Is Displayed as an Exploded View to Show How the Pieces Fit Together. The Pieces of the Triple Pressure Transducer Shown in Figure 19 Fit Together Identically. *Used with Permission from Brian Ipema and the Instrument Design and Fabrication Shop at Arizona State University.*

Besides the standard configuration, as shown in Figure 18, three other configurations were used to collect the data presented. Shown in Figure 21 is a comparison between the different configurations. The location of the triggering pressure transducer in each configuration is marked with a yellow star. Figure 22 depicts the timing between events during the experiment.

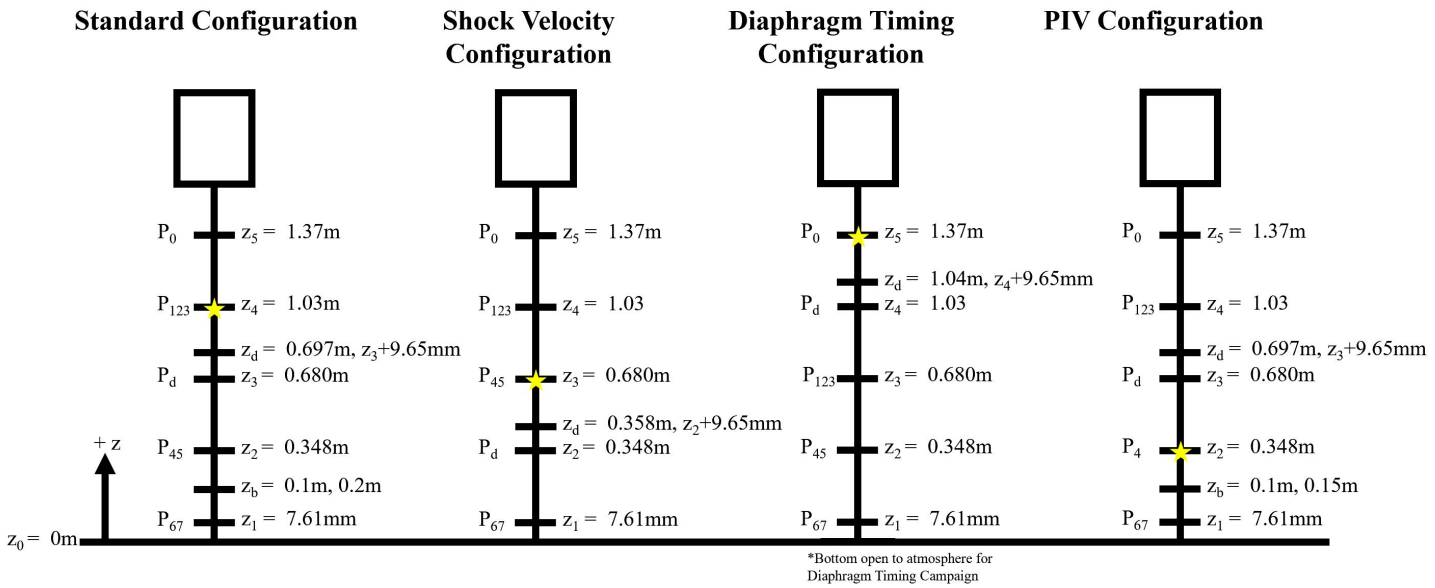

Figure 21: Shown Is a Comparison of the Four Different Vertical Shocktube Configurations Used to Collect the Data Presented.

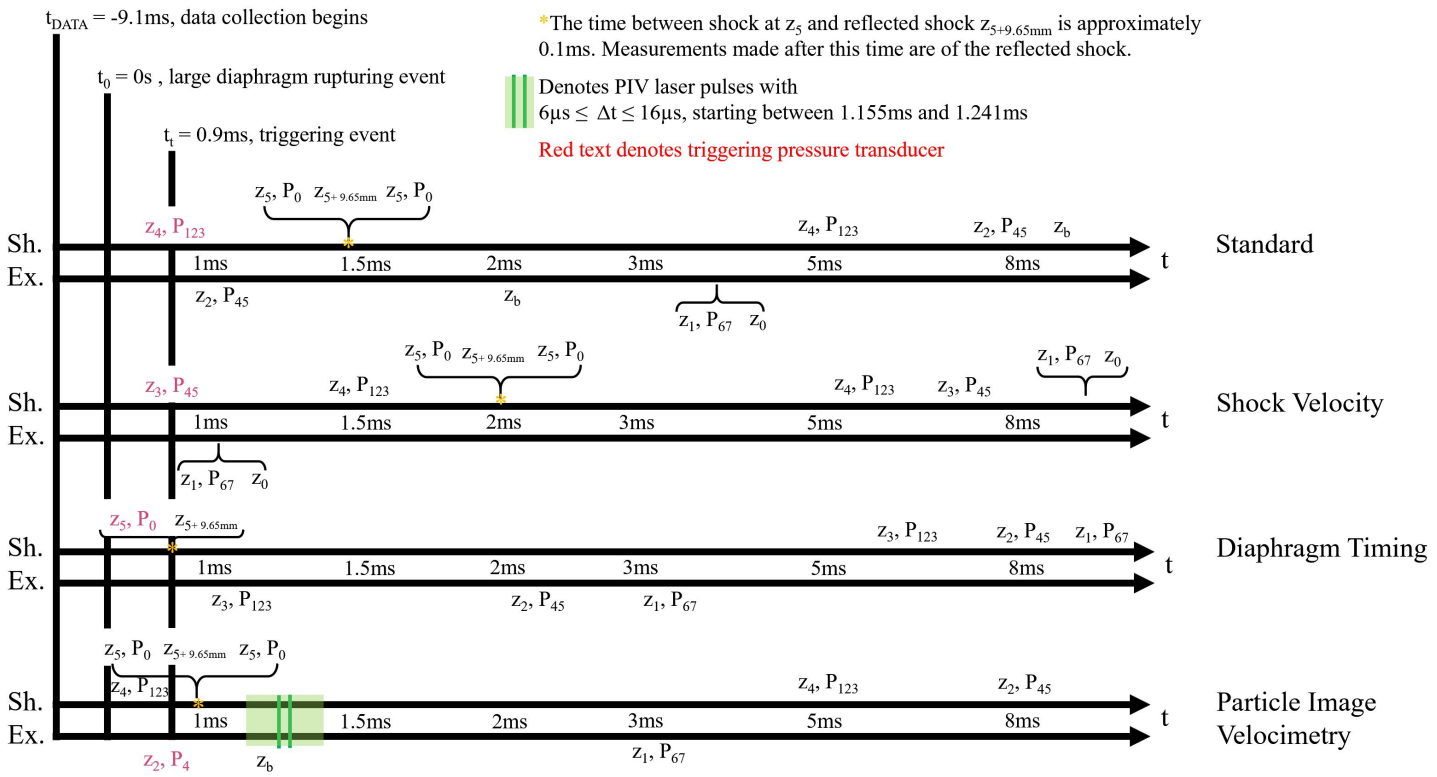

Figure 22: Shown Are the Timing Diagrams Associated with the Four Experimental Configurations. The Lines Marked with "Sh." Are the Lines Associated with the Shockwave. The Lines Marked with "Ex." Are the Lines Associated with the Expansion Wave. The Time Axes Are Not Linear in This Diagram. They Have Been Stretched in Early times to Include All the Events Which Occur Within the First 2ms. The z Locations Are Shown When the Waves Have Reached That Location. If a $p_{\#}$ Is Included, Denoting Which Ring Is Located at That Specific z Location, It Means There Was an Actual Measurement Made at This Point in Time by the Pressure Transducers Indicated by the Ring Number.

The diaphragm is a critical component of the shocktube setup, as it creates a physical barrier between the two initial pressures, $P_1 \approx 5$kPa in the driven region and $P_4 \approx 101$kPa in the driving region at $t < 0$s. Once this barrier is removed at $t = 0$, the experiment begins. The diaphragm is a thin piece of polypropylene tape and is placed over a Nichrome wire inlaid into one of the Teflon joints as shown in Figure 23. The wire, which exits the Teflon joint through two small through holes, is connected *via* alligator clips to a Sorensen XPF 35-10 Dual 35V 10A DC Power Supply, which sends current through the Nichrome. See Figure 24 for a closeup image of the diaphragm flexing under the dramatic pressure gradient ($\frac{P_4}{P_1} \approx 20$). Once the experiment is completely setup, the current generator is triggered manually and 2.15A is sent through the Nichrome wire. Nichrome has a very high resistivity of 1.0-1.5x10$^{-6}\Omega$m. This causes it to heat rapidly and burn through the polypropylene tape. When 2A of current is sent through the Nichrome wire, it heats to over 200°C. Typically the tape burns through in a small region first, as seen in Figure 25, and then the pressure differential across the tape cause it to rip quickly along the perimeter and fly upward toward the vacuum tank. This is the large rupturing event, which initiates the gas flow in the experiment and is used as t = 0. The large diaphragm rupturing event has a duration of approximately 5x10^{-4}s. The timing of the diaphragm rupture is discussed in more detail in Chapter 3.

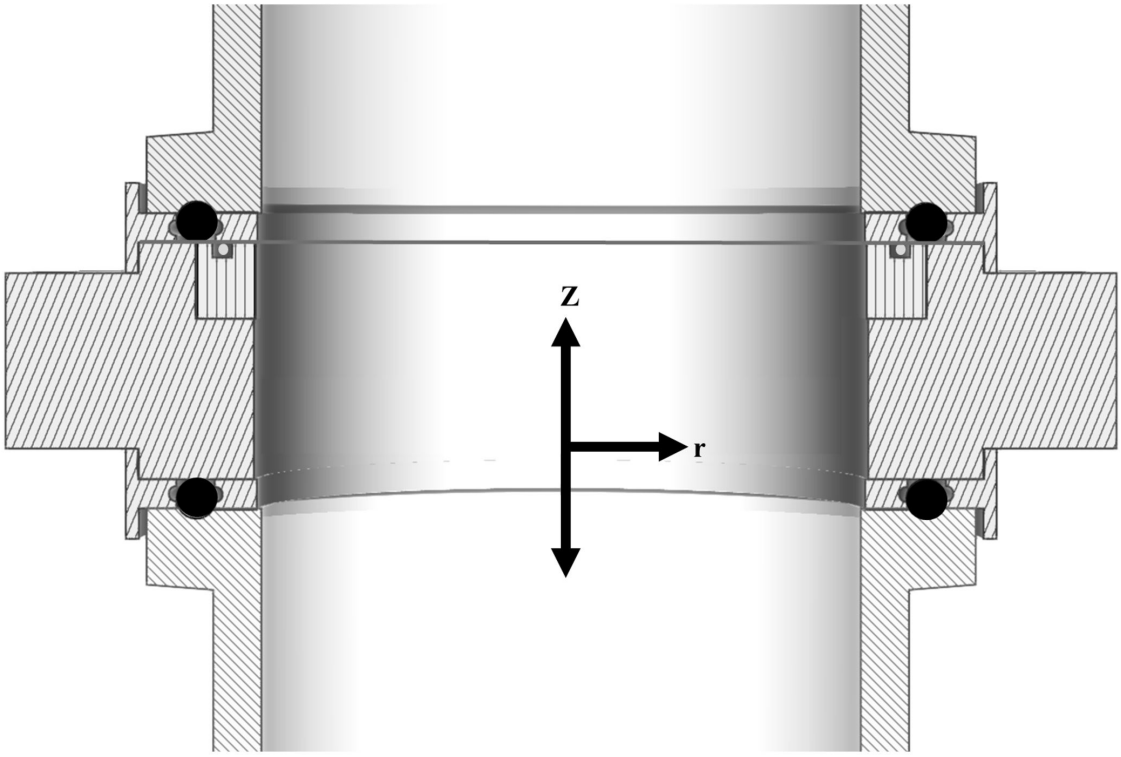

Figure 23: Shown Is a Detailed Schematic of the Diaphragm Joint Assembly. The Slot in the Teflon Joint for the Nichrome Wire Has a Ceramic Insert to Protect the Teflon from the Heat Created When 2A Is Sent Through the Wire. Rubber O-rings Are Used In-between the Glass Cylinders and the Nichrome Wire. The O-rings Are Held into Place by Two White Plastic Rings. Note That the Polypropylene Tape Rests on Top of the Nichrome Wire. The Joint Assembly on Shown Between the Bottom Class Tube and the Diaphragm Ring Is Identical to All Other Joint Assemblies Used in the Shocktube, Except for the Very Top Joint Connecting the Shocktube to the Vacuum Tank. *Used with Permission from Brian Ipema and the Instrument Design and Fabrication Shop at Arizona State University.*

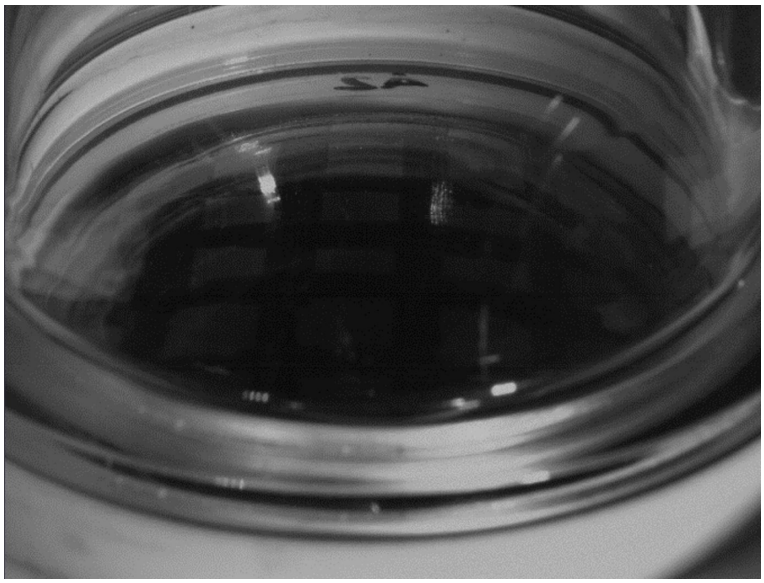

Figure 24: Shown Is a Closeup of the Diaphragm. The Top of the Diaphragm Has Been Marked with a Dark Grid to Show the Dramatic Flexion and to Better Identify the Location of the Diaphragm, as It Is Difficult to See the Clear Polypropylene Material.

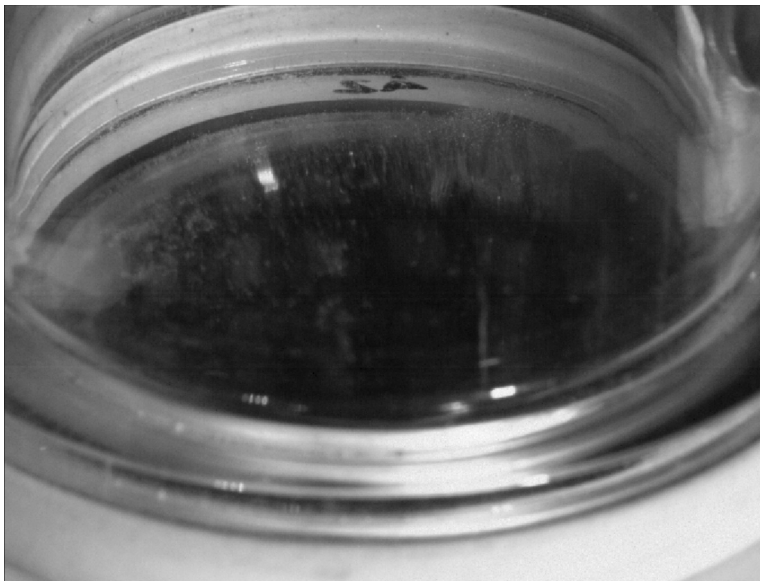

Figure 25: Shown Is an Image Taken a Few Ten-thousandths of a Second after the Image Shown in Figure 24. Visible in the Upper Right Portion of the Diaphragm (Approximately 1 O'clock in Clock Position), Is the Initial Tear That Occurs as the Nichrome Melts Through the Polypropylene. Several Particles Are Visible Flying Upward Away from That Region as Evidence That Gas Flow Is Present and the Diaphragm Is about to Rupture Completely—Called the Large Rupture Event.

The vacuum pump reduces the pressure in the driven region down to approximately 5kPa in the experiments presented. Manual valves are utilized to block any backflow back through the pump when it is turned off. An Omega pressure gauge installed on the vacuum line, which connects the vacuum pump to the vacuum tank, is used to determine the static vacuum pressure P_1 prior to the diaphragm rupture. The reading on this gauge just before the diaphragm ruptures is the value recorded as P_1. The topmost joint on the vertical shocktube connects the glass cylinder assembly to the bottom of the large-diameter vacuum tank. The connection, however, is slightly imperfect and a reflected shock is seen in the pressure traces presented. This is further discussed in Chapter 3.2.

The final component of the experimental setup is the particle bed. The particle beds are composed of small-diameter glass spheres. These particles are Ballotini purchased from Potters Beds. Presented are experiments with three different size ranges of glass particles, 44 - 90μ m, 150 - 212μ m, and 212 - 297μ m. Table 6 shows the calculated particle characteristics for given particle diameters. The diameter distribution among each of these size ranges is Gaussian. Prior to pouring

the particle bed into the bottom of the shock tube, the mass is measured carefully. The particle bed is then emplaced in the bottom of the shock tube using a funnel and the bed height is measured. These steps are very important, because pouring the particles in different ways (i.e. tilting the funnel in differently or pouring the particles at a faster rate) results in different bed heights, as the solid volume fraction ϕ_p varies. The mass of the particle bed and the height of the particle bed has very little variability for all realizations of an experiment, so that the average density of the bed is the same for each size range of particles used. The range of the varying volume over the varying mass within a single experiment has been limited to 0.0006 to 0.002. The majority of the experiments are in the lower end of that range due to the purchase of a new scale partway through the data collection process.

D_p [μm]	ρ_p [kg/m^3]	τ_{cutoff} [s]	Mean settling velocity [m/s]	$\mathrm{Re_p}$
44	2.50E+03	3.94E-02	3.41E-01	9.77E-01
90	2.50E+03	1.65E-01	9.33E-01	5.47E00
150	2.50E+03	4.58E-01	1.44E00	1.41E+01
212	2.50E+03	9.16E-01	1.79E00	2.47E+01
297	2.50E+03	1.80E00	2.04E00	3.96E+01
*0.1	9.97E+02	8.15E-07	8.04E-06	1.05E-07

Table 6: Shown Is a Table of the Calculated Particle Characteristics for Particles at the Boundaries of Each Particle Diameter Range. Note the Starred Particle Row Refers to a Condensation Nuclei Drop to Be Discussed in Chapter 3.2.

In Table 6, the mean settling velocity and the particle slip Reynolds number $\mathrm{Re_p}$ are calculated by [23]

$$\boldsymbol{u} - \boldsymbol{v} = \frac{\bar{\rho} - 1}{\bar{\rho}} \boldsymbol{g} \tau_{cutoff} / \lambda \tag{36}$$

$$Re_p = \frac{|\boldsymbol{u} - \boldsymbol{v}| D_p}{\nu_g} \tag{37}$$

where ν_g is the kinematic viscosity of the gas and

$$\bar{\rho} = \frac{\rho_p}{\rho_g} \tag{38}$$

λ is a correction factor to the Stokes law and defined by [30]

$$\lambda = \begin{cases} 1 + \frac{3}{16} Re_p, & Re_p \leq 0.01 \\ 1 + 0.131 Re_p^{0.82 - 0.05 log_{10} Re_p}, & 0.01 \leq Re_p \leq 20 \\ 1 + 0.1935 Re_p^{0.6305} & 20 \leq Re_p \leq 260 \end{cases} \tag{39}$$

Note that a first approximation of the mean settling velocity is used with $\lambda = 1$. The particle time constant τ_{cutoff} for these particles used $\epsilon_{cutoff} = 0.02$ which is associated with the density difference between the gas density and particle density[29], and is calculated by [23]

$$\tau_{cutoff} = \frac{D_p^2}{8 \nu_g \epsilon_{cutoff}^2} \tag{40}$$

For the calculations shown in Table 6, $\nu_g = 15.34$ x 10^{-6} [m^2/s] and $\rho_g = 1.225$ [kg/m^3].

Though the particles can be described quite well individually, the particle bed as a whole has some inherent randomness associated with it, as the particles cannot be placed in the exact same position every realization. To better understand the particle bed randomness and any affects caused by the wall, CT images were taken by Kyle Hughes at the University of Florida's CCMT. Hughes poured a mock particle bed in the same fashion the particle beds at ASU are poured and put it inside the scanner. The results from these scans are shown in Figure 26. Initially, the mock particle beds were scanned to try to determine if there were any large inhomogeneities in the particle packing. It was determined after many pours and scans, that large voids or bridges, such as those formed in grain silos, do not regularly form during the particle bed emplacement. In fact there were no instances of voids or bridges in any of the test pours performed at CCMT. The question of whether the particle volume fraction is the same across the circular cross-section was not easily determined from these scans, as the wall of the cylinder caused the glass particles to be brighter near the walls. To further explore this topic, simulations of the particle bed pour were performed by Vowinckel and Meiburg at the University of California, Santa Barbara. The results of these simulations will be discussed in Chapter 4.1.

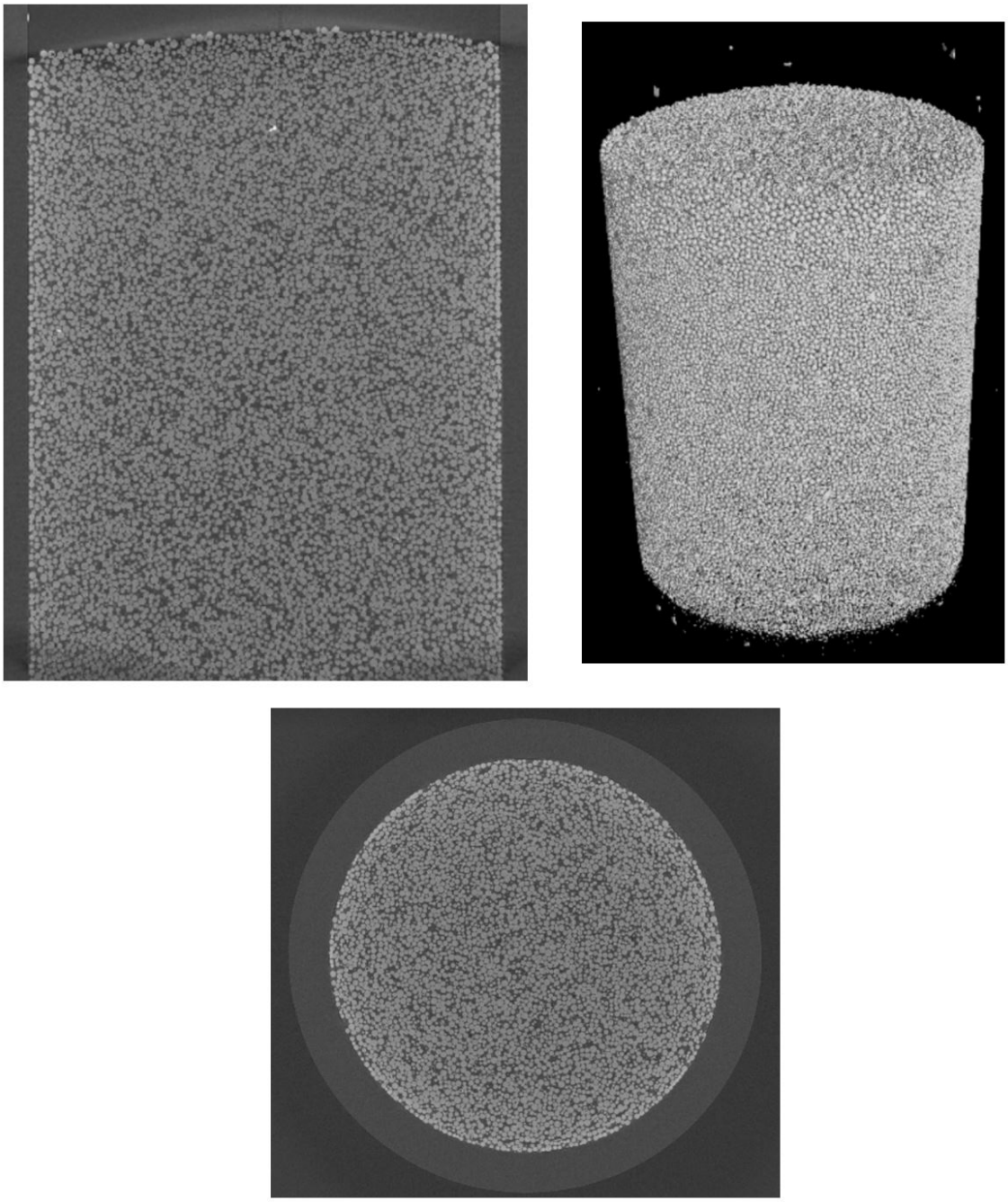

Figure 26: Pictured Are Three Ct Scans of a Mock Particle Bed Performed by Kyle Hughes from the University of Florida in 2017. Individual Particles Are Visible in These Scans. The Increase in Brightness near the Walls Was Determined to Be Caused by the Wall, and Not by an Increase in Particle Volume Fraction near the Wall. *Used with Permission from CCMT.*

2.2 Running the Experiment

The general process for running the experiment in the standard configuration is to ensure the any particles from prior experiments are removed from the shocktube, as to keep the particle size distribution as narrow as possible; pour the particles into the bottom of the shocktube; replace the polypropylene diaphragm; connect the glass segments and joints in place; reduce the pressure in the driven section (P_1) of the shocktube *via* the vacuum pump; and when the desired P_1 is achieved, trigger the power generator to send current through the Nichome wire which burns through the diaphragm. However, in addition to these general steps, there are many more small detailed steps required to ensure the experiment runs correctly. The first enumerated list below details the steps for the experiments run in the standard configuration, the shock velocity configuration, and the diaphragm timing configuration. The second enumerated list below details the steps for experiments run with the shocktube configured for Particle Image Velocimetry. A complete record of all experiments used in this research is shown in Table 7.

2.3 Experimental Procedure Checklist for Standard, Shock Velocity, and Diaphragm Timing Experiments

1. *Turn on the NI PXIe-1073
2. *Turn on BNC 565—Ensure it is set to #2 in saved settings (H enabled only)
3. *Plug all cabling into Phantom Camera—Yellow: Ethernet, Red: Power 1, BNC to Trigger
4. *Restart PC and open LabVIEW and PCC—LabVIEW: IEPE - Finite Input Reference Trigger with Hysteresis
5. Click CSR in PCC Software—CSR is Current Session Reference
6. Detach shocktube at diaphragm & remove cabling
7. Rebuild Diaphragm—Take extra care to press down tape tightly
8. Pour out old particles and air out shocktube
9. Shake/Blow out old particles from vacuum tank
10. Record mass & bed height of new particle bed
11. Reattach shocktube
12. Connect all 8 pressure sensors—Make sure the transducer faces are flush with inside of tube
13. Connect alligator clips from power supply

14. Plug in LED lights
15. Focus Phantom camera
16. Ensure settings in LabVIEW and PCC are correct—See experimental notebook
17. Close red release valve on vacuum plumbing—Ensure all other valves are open
18. Turn on blue snorkel/venting system—Should be placed near pump to reduce breathing hazards
19. Record P4 pressure from Omega Pressure gauge
20. Click RUN on BNC 535—Should see a circle blinking in upper left corner of screen
21. Click CAPTURE on PCC software—DO NOT CLICK TRIGGER
22. Turn on vacuum pump—Ensure all PPE is worn: respirator mask & impact glasses
23. Turn on Sorensen power supply—Leave in standby mode ONLY for now, 10V & 2.15A
24. When P1 is at desired pressure, turn off pump
25. Close valve directly below Omega gauge
26. Click Run Arrow on LabVIEW
27. Click OUTPUT 1 to apply voltage —Watch for P1 pressure at burst
28. Once diaphragm bursts, click OUTPUT 1—Can also turn off power supply at this time
29. Release all pressure from system
30. Record P1 and save video data
31. Turn off Omega pressure gauge
32. *Turn off camera, NI PXIe-1073, BNC 535

2.4 Experimental Procedure Checklist for PIV Experiments

1. *Turn on the NI PXIe-1073
2. *Restart PC and open LabVIEW—LabVIEW: IEPE - Finite Input Reference Trigger with Hysteresis
3. *Turn on LaserPulse Synchronizer
4. *Turn on BNC 565—Ensure it is set to #9 in saved settings (A enabled only)
5. *Plug all cabling into TSI Camera
6. *Turn on laser power supply, laser warning lights—Run pump, laser On, shutter Open, Q/Flash external
7. *Turn on PC and open Insight3G—Select Experiment, New Run A
8. Detach shocktube at diaphragm and remove cabling

9. Rebuild diaphragm—Take extra care to press down tape tightly
10. Pour out old particles and air out shocktube
11. Shake/Blow out vacuum tank and wash tube—Only need to wash tube in region of interest, use soap and water
12. Record mass & bed height of new particle bed
13. Reattach shocktube—All screws in P1 section should be quite tight
14. Connect 7 pressure sensors, exclude AI5—Make sure faces are flush with inside of tube
15. Connect alligator clips from power supply
16. Focus TSI camera, align optics —14.5 Hz, LPD: 190.001μs, ∇ t: 150μs, PIV Exp.: 250μs, no ext. trigger
17. Record 20 image pairs in Run A, save —1 Hz, synchronized, sequence, "full" laser power
18. Install Mask to block reflections—There may still be some faint reflections in the middle
19. Inject tracer particles from Laskin Nozzle—Slightly higher seeding density than "normal" PIV, plug AI5 port
20. Turn on blue snorkel/venting system—Should be placed near pump
21. Close red release valve on vacuum plumbing—Ensure all other valves are open
22. Record P4 pressure from Omega Pressure gauge
23. Turn on vacuum pump—Ensure all PPE is worn: respirator mask & impact glasses
24. Click RUN on BNC 535—Should see a circle blinking in upper left corner of screen
25. Turn on Sorensen power supply—Leave in standby mode ONLY for now, 10V & 2A
26. Ensure settings in LabVIEW are correct—See experimental notebook
27. When P1 is at desired pressure, turn off pump
28. Close valve directly below Omega gauge
29. Click LASER ON & CAPTURE in Run C—Correct Trigger and timing settings, synchronized, 5 image sequence
30. Click Run Arrow in LabVIEW
31. Click OUTPUT 1 to apply voltage —Watch for P1 pressure at burst
32. Once diaphragm bursts, click OUTPUT 1—Also turn off power supply
33. Release all pressure from system—Use red valve release and valve directly below Omega Gauge
34. Record P1 and save PIV data
35. Turn off Omega pressure gauge

36. *Turn off camera, NI PXIe-1073, BNC 535

NOTE: Each of these tasks listed, except for those marked with an *, needs to be performed every realization to ensure the uncertainty in the acquired data is as narrow as possible. The tasks marked with * need only to be performed once an experimental session—for example, once per day.

2.5 Table of Experiments

Run Name	z_b [m]	D_p [μm]	$P_0[kPa]$	Campaign
111317, 7	0.102	[44, 90]	5.6	Standard
111317, 8	0.101	[44, 90]	5.3	Standard
111317, 9	0.103	[44, 90]	4.1	Standard
111317, 10	0.101	[44, 90]	4.5	Standard
111617, 5	0.100	[44, 90]	5.1	Standard
111317, 2	0.100	[150, 212]	5.4	Standard
111317, 3	0.101	[150, 212]	4.7	Standard
111317, 4	0.102	[150, 212]	4.8	Standard
111617, 3	0.100	[150, 212]	4.8	Standard
111617, 4	0.100	[150, 212]	5.2	Standard
110617, 7	0.100	[212, 297]	4.3	Standard
110717, 2	0.103	[212, 297]	4.7	Standard
110717, 3	0.102	[212, 297]	5.1	Standard
111317, 1	0.101	[212, 297]	4.4	Standard
111617, 2	0.100	[212, 297]	4.5	Standard
111417, 1	0.198	[44, 90]	4.4	Standard
111417, 5	0.200	[44, 90]	4.2	Standard
111417, 7	0.200	[44, 90]	4.7	Standard
111417, 8	0.200	[44, 90]	5.9	Standard
111617, 6	0.198	[44, 90]	5.0	Standard
111417, 10	0.202	[150, 212]	4.9	Standard
111517, 1	0.200	[150, 212]	4.5	Standard
111517, 2	0.203	[150, 212]	4.6	Standard
111517, 3	0.202	[150, 212]	4.9	Standard
111617, 7	0.200	[150, 212]	5.1	Standard
111517, 5	0.199	[212, 297]	4.7	Standard
111517, 6	0.200	[212, 297]	4.6	Standard
111517, 8	0.200	[212, 297]	4.8	Standard
111517, 9	0.200	[212, 297]	4.9	Standard
111617, 1	0.200	[212, 297]	4.8	Standard
102717, 1	—	—	4.3	Diaphragm Timing
102717, 2	—	—	4.2	Diaphragm Timing
102717, 3	—	—	4.9	Diaphragm Timing
022118, 2	—	—	4.9	Shock Velocity
022218, 1	—	—	4.9	Shock Velocity
022218, 2	—	—	4.8	Shock Velocity

Continued on next page

Run Name	z_b [m]	D_p [μm]	$P_0[kPa]$	Campaign
030918, 3	0.1	[44, 90]	5	PIV t_{early}
030918, 4	0.1	[44, 90]	5	PIV t_{early}
030918, 5	0.1	[44, 90]	5	PIV t_{early}
030818, 2	0.1	[150, 212]	5	PIV t_{early}
030818, 3	0.1	[150, 212]	5	PIV t_{early}
030818, 4	0.1	[150, 212]	5	PIV t_{early}
030718, 3	0.1	[212, 297]	5	PIV t_{early}
030718, 4	0.1	[212, 297]	5	PIV t_{early}
030718, 5	0.1	[212, 297]	5	PIV t_{early}
031418, 1	0.15	[44, 90]	5	PIV t_{early}
031418, 3	0.15	[44, 90]	5	PIV t_{early}
031418, 4	0.15	[44, 90]	5	PIV t_{early}
031618, 1	0.15	[150, 212]	5	PIV t_{early}
031618, 3	0.15	[150, 212]	5	PIV t_{early}
031618, 4	0.15	[150, 212]	5	PIV t_{early}
031518, 4	0.15	[212, 297]	5	PIV t_{early}
032018, 1	0.15	[212, 297]	5	PIV t_{early}
032018, 3	0.15	[212, 297]	5	PIV t_{early}
031018, 1	0.1	[44, 90]	5	PIV t_{late}
031018, 2	0.1	[44, 90]	5	PIV t_{late}
031018, 3	0.1	[44, 90]	5	PIV t_{late}
030818, 5	0.1	[150, 212]	5	PIV t_{late}
030918, 1	0.1	[150, 212]	5	PIV t_{late}
030918, 2	0.1	[150, 212]	5	PIV t_{late}
030618, 2	0.1	[212, 297]	5	PIV t_{late}
030718, 1	0.	[212, 297]	5	PIV t_{late}
030718, 2	0.1	[212, 297]	5	PIV t_{late}

Table 7: Shown is a Complete Record of the Experiments Performed Used in the Research Presented.

3 GAS MOTION PRIOR TO 1st PARTICLE MOTION

3.1 Diaphragm Burst

The timing associated with the diaphragm burst is very important, as it is the event which begins the entire decompression process. The large diaphragm rupturing event is regarded as t = 0 for all the data presented. To study the exact timing of the diaphragm burst and the resultant expansion wave, a diaphragm timing experimental configuration was designed. Table 8 is a table of the timing associated with the diaphragm and expansion. Notice that for all measurements, the variability between three different realizations is quite small, even when the pressure ratios are not exactly the same. Take special notice of the last row at the bottom of the table. This is the length of time between the large diaphragm rupture event and the system trigger *via* the shock passing by pressure transducer P_0. This measurement did not vary at all within the uncertainty associated with the camera frame rate (0.1ms). This is very important because in the standard configuration, the exact moment the diaphragm bursts (t = 0) cannot be measured. It must be calculated from the pressure traces. Because the time between the large rupture event and the trigger is so precise, the t = 0 and all subsequent timing can be determined with a high-degree of confidence within the known uncertainty.

	# 1 $\frac{P_4}{P_1} = 24.03$	# 2 $\frac{P_4}{P_1} = 24.61$	# 3 $\frac{P_4}{P_1} = 21.30$
Duration of large rupture event [ms]	0.6	0.4	0.6
Duration of expansion [ms]	21.19	21.75	21.42
First tear to first pressure drop [ms]	9.255	9.165	9.165
Large rupture event to trigger [ms]	0.9	0.9	0.9

Table 8: Shown Is a Table Measured Timings Associated with the Diaphragm Burst of Three Realizations, Labeled #1, #2, and #3. The Duration of the Large Rupture Event Is the Time from When the First Hole in the Diaphragm Is Visible (See Figure 25) to the First Large Tear Caused by the Pressure Gradient. The Duration of the Expansion Is the Length of Time Between the First Measurable Pressure Drop (Occurring at Teflon Ring p_{123}) to When the Pressure Transducers Trace the Minimum Pressure Seen for That Experiment. The Time Between the First Tear and the Initial Pressure Drop Is the Time from the Beginning of the Large Rupturing Event to the Moment When the First Measurable Pressure Drop Occurs at p_{123}. The Large Rupture Event to Trigger Is the Time Between the Beginning of the Large Rupture of the Diaphragm Occurs to When the Shock Wave Triggers the Data Acquisition System After .01s of Buffer Data (Data Recorded on a Loop until the System Is Triggered).

3.2 Shock and Reflected Shock

Once the diaphragm ruptures at $t = 0$, a shockwave forms and travels upward (away from the diaphragm) and toward the top of the vertical shocktube. The shockwave is used to trigger the data acquisition system. The pressure transducer used to trigger during the standard setups is located on the Teflon ring P_{123} one glass cylinder above the diaphragm at z_4. There are three pressure transducers installed in this joint, so that any inconsistencies in the triggering signal caused by errors or irregular pressure variations can be easily identified and corrected for in post-processing. The shock is temporally resolved by three data points, and the triggering event was designed to be the center data point. To determine the robustness of the triggering mechanism , the shocks from five experimental realizations measured with three pressure transducers (Ai1, Ai2, and Ai3, located on ring P_{123}) are compared (see Figure 27).

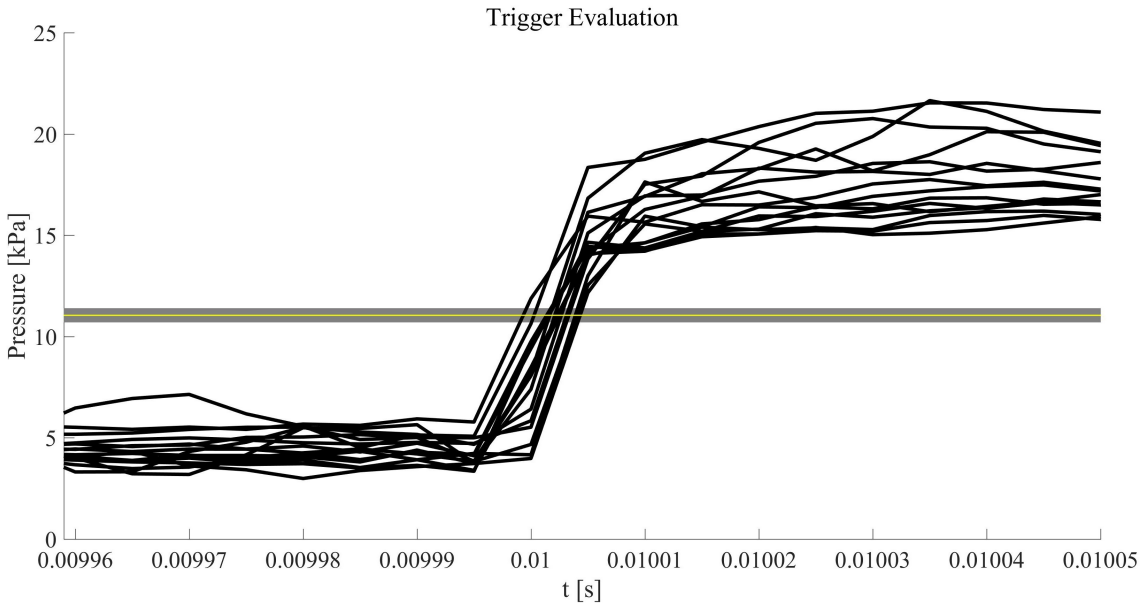

Figure 27: Shown Are the Traces from the Three Pressure Transducers (Ai1, Ai2, Ai3) over Five Realizations of the Experiment in the Standard Configuration in the Same Teflon Ring p_{123} at z_4. Notice That All Traces Align t = 0.01s (Which Corresponds to the Buffer of Data Being Recorded on a Loop until the Triggering Event Occurs) Exactly in the Center of the Shock. *Note: The Time Axis Has Not Been Altered at All in Post-processing. This Is in Contrast to the Other Pressure Trace Plots Shown, Where the Time Axis Is Translated to Make t_0 the Time When the Diaphragm Large Rupture Event Occurs.*) The Threshold for the Triggering Event Is 6kpa + P_1. The Horizontal Yellow Line Shows the Average Threshold and the Gray Surrounding Shows the Peak-to-peak Variance of the Threshold. This Means That the Triggering Mechanism Is Very Robust, Even for Varying Slopes of the Pressure Variations Across the Width of the Shock. This Also Demonstrates the *Flatness* of the Shock. It Is Important That the Shock Is Flat as It Travels Upward, Because If It Were Skewed, the System Could Not Be Considered to Be Axisymmetric During This Time Period.

Without altering the time domain in post-processing, not only was every included realization triggered by the center datapoint in the middle of the shock front, but all redundant pressure transducers sensed the center of the shock front at the exact same instant in time, down to 5μs. This is important because all pressure data from standard experiments can be directly compared without adding any temporal variability by altering the time domain in post-processing.

Though the purpose of this research was not to study the shock characteristics, it is important to understand all aspects of this experiment, including the shock dynamics away from the particle bed. A shock velocity campaign was designed to measure shock velocities at different locations

to ensure the shock velocity measurements made during the standard experiments are taken at an appropriate time during the shock's evolution—when the shock is neither accelerating or decelerating. The experimental setup for this campaign was altered from the standard configuration by moving the diaphragm Teflon joint down one segment. It was placed so that one glass segment was below the diaphragm, and three were above. This allowed for two accurate shock velocity measurements to be made using three sets of pressure transducers. From these two velocity measurements, any accelerations or decelerations in the shock velocity c_s can be determined. These measurements are shown in Table 9.

Realization	P_1 [kPa]	P_2 [kPa]	P_4 [kPa]	$\frac{P_4}{P_1}$	$\frac{P_2}{P_1}$	t_1[ms]	t_2[ms]	c_s[m/s]	**z**
#1	4.90	18.2	103.31	21.1	3.7	10.005	10.585	586.2	z_3 , z_4
			19.7		4.0	10.0585	11.155	596.5	z_4 , z_5
#2	4.9	16.2	103.26	21.1	3.3	9.995	10.57	591.3	z_3 , z_4
			20.2		4.1	10.57	11.145	591.3	z_4 , z_5
#3	4.84	16.3	103.24	21.3	3.4	9.995	10.575	586.2	z_3 , z_4
			18.5		3.8	10.575	11.15	591.3	z_4 , z_5

Table 9: Shown on the Left Is a Table of the Shock Measurements Made During the Shock Acceleration Campaign. Note That the Shock Velocities Are Nearly the Same Between p_{45} to p_{123} ($\boldsymbol{z_3}$ to $\boldsymbol{z_4}$) and p_{123} to p_0 ($\boldsymbol{z_4}$ to $\boldsymbol{z_5}$) Within the Uncertainty Associated with the Pressure Transducers Sampling Rate of 200kHz.

All experimental realizations in this campaign had an initial pressure ratio $\frac{P_4}{P_1} \approx 20$. This campaign determined that the pressure transducers are located in an ideal position along the longitudinal axis of the shock tube and that during the time of measurement, the shock is neither accelerating or decelerating within the bounds of the uncertainty associated with the pressure transducer sampling rate of 200kHz. The shock velocity measured between 0.33m above the diaphragm and 0.67m above the diaphragm was 587.9m/s averaged over three realizations. The shock velocity measured one glass segment higher, between 0.67m above the diaphragm and 1.01m above the diaphragm, was 593.3m/s averaged over those same three realizations. This spread is within the uncertainty associated with the pressure transducer sampling rate and the shock velocity ($\pm$ 2.5m/s).

Given a specific pressure ratio, it is expected that the shock strength $\frac{P_2}{P_1}$ reaches a certain threshold. The degree to which the shock wave reaches the expected threshold will be described as the "quality". A poor quality shock would be one that did not reach the expected threshold.

Similarly, a poor quality expansion wave would be one that does not cause the expected pressure drop or gas velocities. The quality and velocity of the shock are easily measurable quantities, while the gas velocities in the expansion region are not. Gas velocities in the expansion region need to be measured by setting up a different data acquisition system using Particle Image Velocimetry. For this reason, being able to determine if the quality of the expansion wave from another measure would be very valuable. As it turns out, a poor quality shock is associated with a poor quality expansion wave in the sense that when the P_2 value is low, the gas velocities in the expansion region are slow. In Figure 28, a lower gas velocity, as measured by PIV, occured in the same realization as a poor quality shock. Realizations with "poor quality" shocks were excluded from the statistical analyses used to describe the expansion wave and particle bed expansion, as it was expected that the expansion wave would be similarly "poor quality" and representative of the flows this experiment was designed to study.

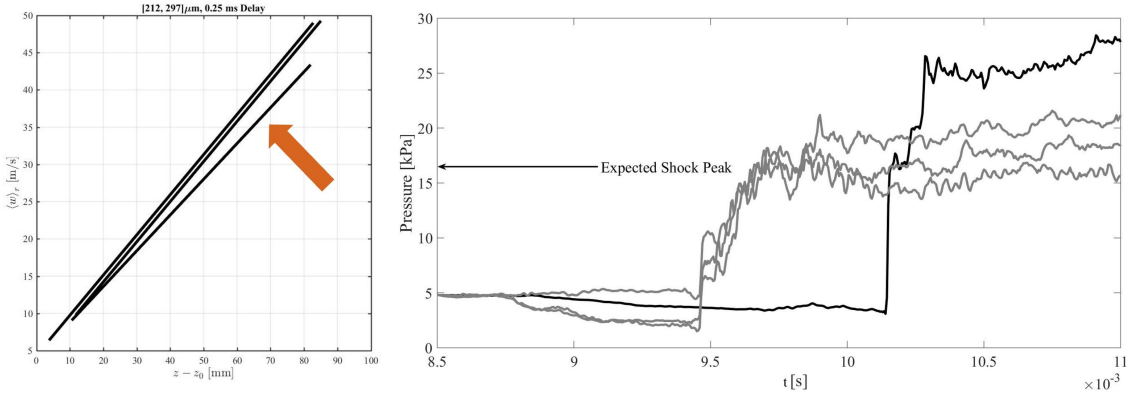

Figure 28: Shown on the Left Are the Gas Velocities Measured above the Bed Using Piv. The x-axis in This Figure Is the Distance from the Particle Bed Surface z_0. Notice That One of the Plots Has a Lower Slope than the Others. The Shock Pressure Traces from the Same Realization Are Shown on the Right. Notice That the Shock Front Failed to Reach the Expected Value of 16kPa.

When the shockwave comes into contact with the irregular joint at the top of the shocktube, it will partially reflect and the pressure transducers will read a second jump up in pressure after the initial shockwave passes by. This reflected wave causes the pressure in this corner to nearly double in approximately 0.1ms. The pressure increase as a result of the reflected shock is not perfectly doubled, because it is not a perfect reflection. A lot of the energy associated with the shock continues past the

joint and into the large-diameter vacuum tank. All the pressure transducers are sampled at 200kHz to appropriately resolve the shock and reflected shock. The pressure transducer located in Teflon ring P_0 records the dramatic increases in pressure caused by the reflection and a sample of the output can be seen below in Figure 29.

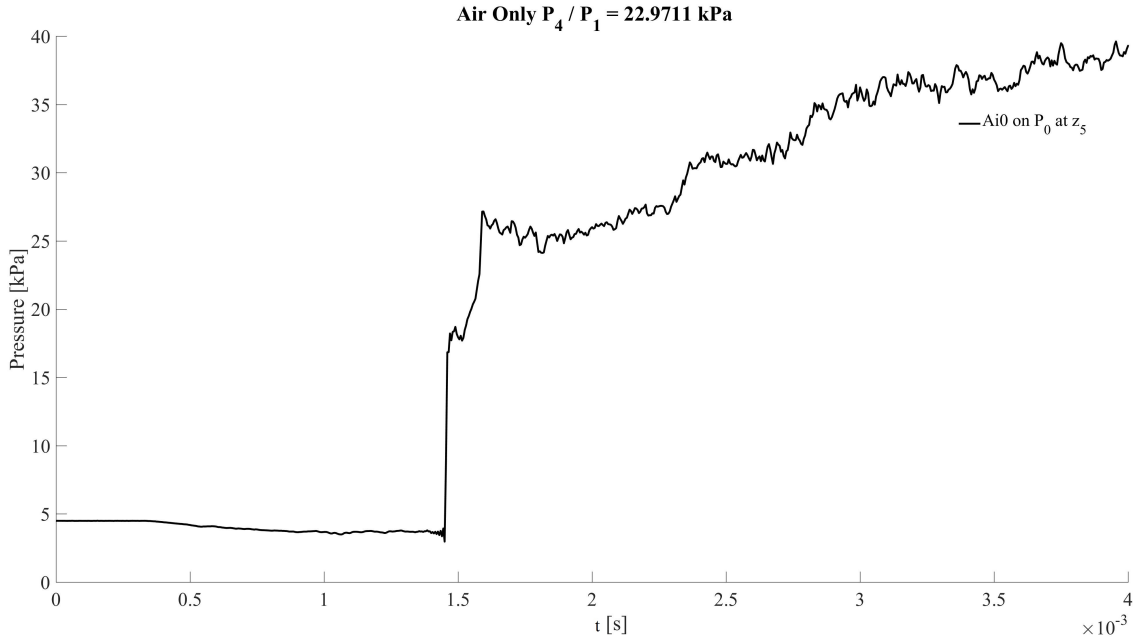

Figure 29: Shown Is the Pressure Trace Recorded from Pressure Transducer Ai0, Located on Ring p_0 at z_5. In This Plot, as with the Other Pressure Trace Plots, $t = 0$ Is the Rupture of the Diaphragm. Notice the Small Blip in the Dramatic Pressure Increase Right at 1.5ms Before the Pressure Makes a Second Jump to Approximately Double the Initial Reading. This Is the Due to the Initial Shockwave Reflecting off a Corner Inside an Irregular Joint at the Junction Between the Vertical Shocktube and the Vacuum Tank. After the Reflected Shock, the Pressure Trace Continues to Rise Slowly. The Pressure Fluctuations in This Time Period Were Not Studied in Depth, as the Focus of This Research Was to Study the Expansion Characteristics. The Shape of This Pressure Trace after the Reflected Shock May Be Due Secondary and Smaller Reflections in That Corner or Associated with the Relaxation of the Pressure Transducer (as They Are Designed to Measure Very High-frequency Pressure Fluctuations and Not Lower-frequency Fluctuations).

The pressure traces are not the only place to observe the effects of the reflected shockwave. As noted previously in Chapter 1.5, there is a dramatic temperature drop associated with the expansion wave as it travels down towards the gas-particle interface. This temperature drop can be estimated using measured values of P_3 and P_4 and equation (20). With a $T_4 = 296.15$K and

measured values of $P_3 = 20$kPa and $P_4 = 101.325$kPa, the expected temperature in region three is $T_3 = 184.42$K or -88.73°C. This dramatic temperature drop causes the water vapor capacity of the enclosed air to drop to nearly zero [22]. In turn, all the water vapor contained in region three is forced to condense and a condensation cloud is formed inside the glass cylinders. The amount of water vapor condensed out of the air is dependent on the humidity of the atmospheric air on the particular days the experiments are performed. The Experimental Volcanology Laboratory at ASU does not have humidity controls emplaced through the ventilation system, however the laboratory next door (a clean room) does. Based on the measurements from the laboratory next door, the relative humidity of the Experimental Volcanology Laboratory is expected to range between 45.5% and 47.3%. Arizona State University is based out of Tempe, Arizona, which has an intense monsoon season in the fall of every year due to a general change in wind direction, bringing a lot of moisture to the area. The outside humidity during this time can vary significantly (even over the course of a single day), possibly affecting the relative humidity in the Experimental Volcanology Laboratory. For these reasons, it is expected that the total amount of water vapor condensed out of the air contained within region three of the vertical shocktube will vary somewhat over the course of all the experiments presented.

The condensation cloud forms and comes into view of the high-speed camera approximately 2—3ms after the large rupture event of the diaphragm t_0. However, gases escaping the decompressing particle bed are relatively warm and humid, just as (or very close to) the atmospheric air is outside the shocktube. Because these gases are warm, the contained water is still in the gaseous phase, allowing the gas to be transparent in contrast to the white condensation cloud in the low-temperature gas above the bed. As the warm gases continue to escape the bed, the condensation cloud is pushed away from the bed and is forced to recess. An poorly-defined, but somewhat resolvable boundary is visible between the cloud and warm gas. As the cloud recession progresses, the reflected shock coming down from the top of the shocktube momentarily forces the condensation cloud boundary back down towards the particle bed, before it continues its recession caused by the degassing of the particle bed. This process can be seen by viewing highly-processed images collected from the high-speed camera as shown in Figure 30.

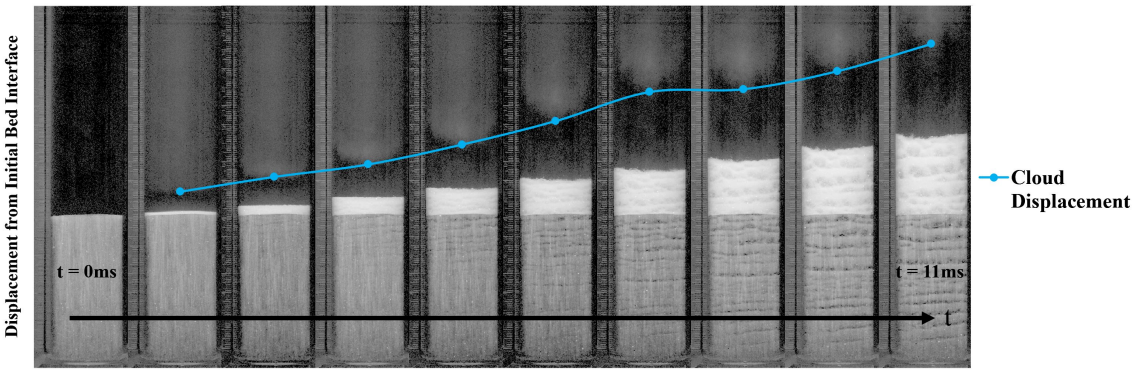

Figure 30: Shown Is a Plot Overlaid onto Captured Images Depicting the Effect of the Reflected Shock on the Condensation Cloud Droplets. As the Reflected Shock Comes down from the Top of the Shocktube, It Interrupts the Smooth Recession of the Condensation Cloud as Shown in the Overlaid Trendline approximately in the middle of this plot. After the Reflected Shock Passes the Cloud Interface, the Condensation Droplets Continue to Recess Away from the Particle Bed as More Warm Gasses Are Escaping the Particle Bed During Decompression. The Image Processing Used to Capture the Cloud Includes Several Steps. The First Is to Measure a Temporal Background—Meaning Creating a Background Frame with the Lowest Intensity Value (as Measured over All Frames) Is Determined at Every Pixel Location. This Temporal Background Image Is Then Subtracted from Every Subsequent Image and Then the Intensity Scale Is Weighted Toward the Lower Intensity Values. In This Way, Intensity That Would Otherwise Be Too Low to See Is Brightened Without Making the Pixels with Higher Intensity Values Look Overexposed. These Images are Associated with Filename 110617_7.

An important note regarding Figure 30 is the disruption in the smooth recession of the condensation cloud. Between t = 8ms and t = 9ms, the the upward motion of the cloud is momentarily paused and gets pushed slightly downward. The droplets in a condensation cloud are very small with a diameter $D_c < 1\mu m$ [22]. Equation (36) describes the mean settling velocity of a particle [23]. When applied to a 0.1μm water condensation droplet, the mean settling velocity is $8.04\frac{\mu m}{s}$ and the particle time constant $\tau_{cutoff} = 0.82\mu$s. In a 2009 study[24] designed to parameterize the response times of particles used to measure shock velocities in Particle Image Velocimetry experiments, Ragni found most response times for particles used to measure shock velocities have a $2\mu s \leq \tau_{cutoff} \leq 3\mu s$. This means that the condensed cloud may trace the shock velocity relatively well and acts as a good visual confirmation of the reflected shock timings. This makes the condensation cloud a valuable tool for determining the location of the reflected shock away from the pressure sensors, like at the gas-particle bed interface. This figure will be shown again in Chapter 4.1 as the cloud can be used to

illuminate some intricacies of the gas flow near the wall just above the gas-particle bed interface.

3.3 Expansion Wave

Just as the shock begins traveling upward just after the diaphragm ruptures, the expansion wave forms and travels downward toward the gas-particle bed interface. Also similarly to the shock, the expansion wave will reflect off the top of boundaries, like the particle bed, and move upward toward the diaphragm. The shape of the reflected expansion wave is not necessarily intuitive, as it does not have a sharp, square drop-off at its front like a reflected shockwave has. The expansion wave first impinges on a physical barrier (like the gas-particle interface or the bottom of a closed shocktube) and then a plateau begins to form, stretching in the direction away the physical barrier—in the context of this experiment, the plateau grows in the $+z$-direction. In the very first moments of the expansion wave impingement and subsequent reflection, the particles remain frozen until the forces exerted by the moving gases overcome the inertia of the particles. Figure 31 shows a simulated expansion wave reflection off the top of the particle bed. In this figure the growing plateau is very noticeable for the first few timesteps and then the pressure gradient at the front edge of the plateau dissipates until it no longer visible.

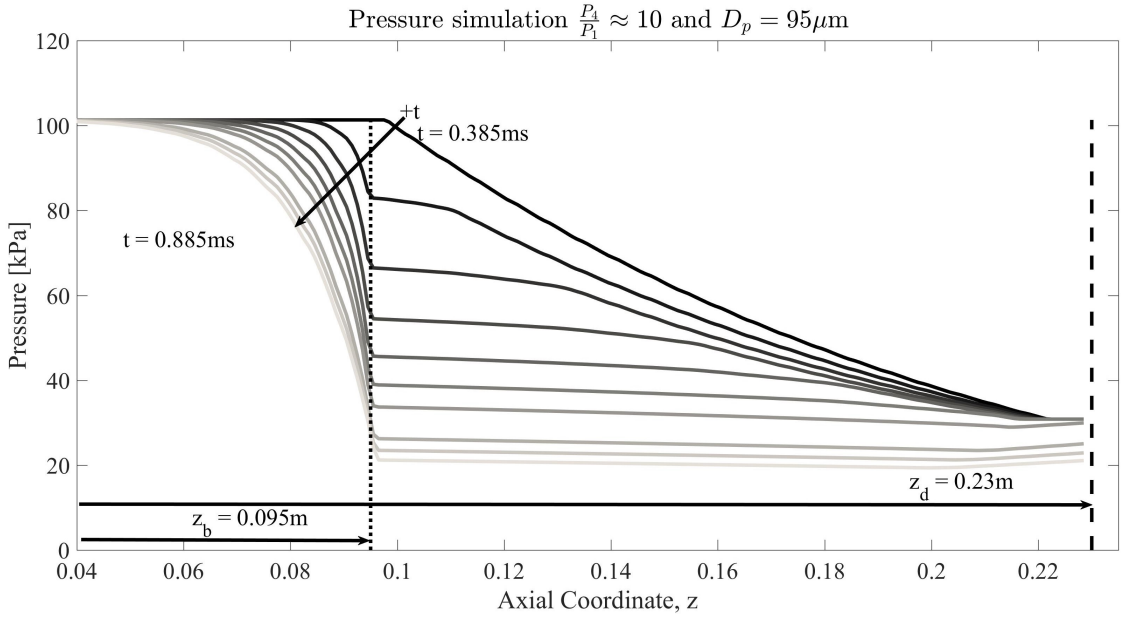

Figure 31: Shown Are Pressure Profiles Simulated by CCMT at Varying times in a Vertical Shocktube Setup Similar to the Experiment at Asu. Only the Driving Section, with Length Of 0.23m, Was Simulated and the Initial Bed Height z_b Was 95mm. The Particles Were 95μm in Diameter. Note the Expansion Wave Can Be Seen Reflecting off the Interface of the Particle Bed. The Reflected Expansion Wave Resembles a Plateau Growing in the $+z$ Direction. In This Simulation, Just as in the Experiments at ASU, t_0 Is the Diaphragm Rupture and z_0 Is the Bottom of the Particle Bed. *Used with Permission from CCMT.*

3.4 Timing Between Shockwave and Expansion Wave

In addition to the reflected expansion wave, there is also a transmitted expansion wave, which travels into the bed and decompresses the gas-particle mixture. Just as the expansion wave impinges on the surface of the particle bed, gas escapes from the open interstices in the first few layers of glass particles. In these very early times, the particles remain stationary until the forces associated expanding gas overcome the particles' inertia. Once this happens the bed begins to evolve, beginning with the gas-particle interface located at z_b.

A common theme throughout these experiments has been the importance of timing. Figure 32 is an example set of pressure curves showing what the data looks like and the z-locations where each trace comes from. This specific example is from experiments with an initial bed height of 0.2m, but the times of when the expansion wave impinged on the 0.2m tall particle beds and a when

the expansion wave *would* have impinged on 0.1m tall particle beds are both marked for reference. Note on the plot that t = 0 is the diaphragm rupture. The curves on the lower part of the figure come from the transducers above the diaphragm, in the shocked region. The traces from located on rings P_{123} and and P_0 are distinguished by arrows on the plot. The curves on the upper part of the figure come from the transducers in the expansion region below the diaphragm.

First the shock develops from the diaphragm burst and then travels upward, crossing the pressure transducer in ring P_{123} at $\boldsymbol{z_4}$. At the same time and also starting from the diaphragm, the expansion wave travels downward, first passing by the Ai4 and Ai5 pressure transducers in ring P_{45} at $\boldsymbol{z_2}$. Continuing forward in time, the shock travels upward, crossing the Ai0 pressure transducer on P_0 at $\boldsymbol{z_5}$. As the expansion wave continues traveling, it reaches the bottom two pressure transducers in ring P_{67} at $\boldsymbol{z_0}$.

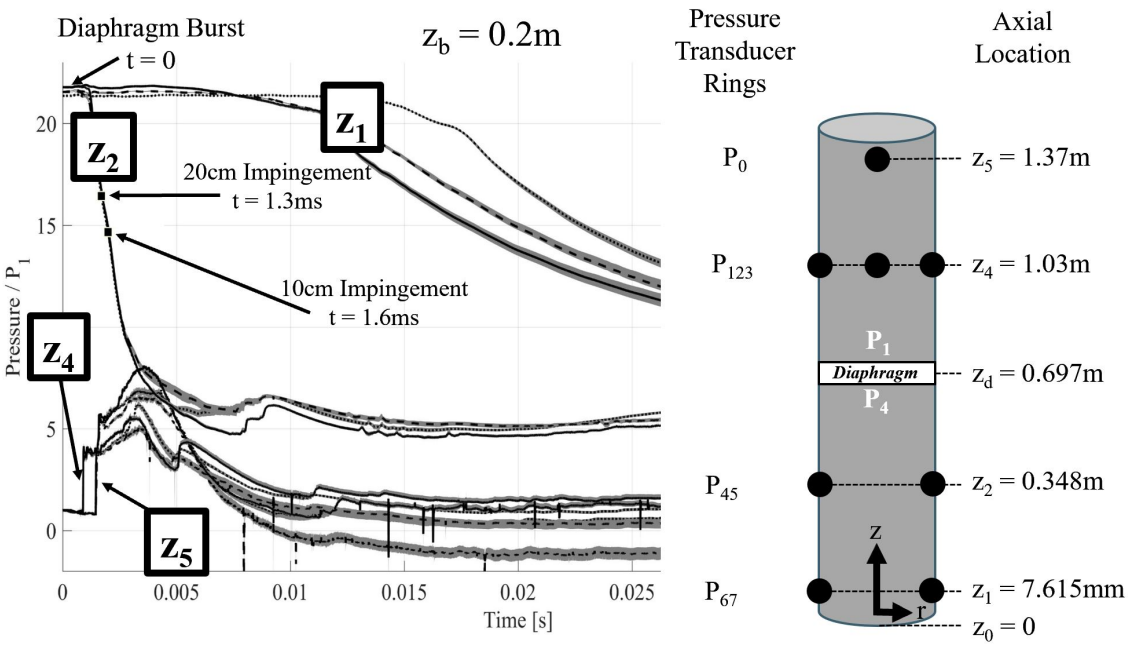

Figure 32: Shown on the Left Is the Timing Diagram for When the Expansion Wave Impinges on a 0.2m and 0.1m Tall Particle Bed. Also Shown Is the Relationship Between the Pressure Traces and the Locations of the Pressure Transducers on the Right.

4 BED MOTION DURING EARLY EXPANSION

4.1 Transient Interfacial Evolution and Wall Effects

As mentioned in Chapter 1, some wall effects were noted during early experiments performed at ASU. After a brief swelling period, where the bed seems to expand roughly homogeneously, the edges of the particle bed interface rise faster than the interior of the interface. See Figure 33 for a series of images showing the progression of the interface deformation caused by the wall effects and the cellular structure of particle-vacant regions forming below the interface. The first image, taken 2.5ms after any motion is seen in the particle bed, shows a roughly periodic wave-like pattern along the perimeter of the particle bed interface. The periodicity is synced to the periodicity of the first layer of the horizontal layers and particle-vacant regions below. This deformation accounts for approximately 12.5% of the total surface area. These wave-like features grow upward and inward and progress from smooth waves to sharp finger-like structures as the first layer of particle-vacant regions burst through the top layer of the gas-particle interface near the wall. As time goes on, more of the interface surface area is deformed as the gases continue to escape past the gas-particle boundary and the particle-vacant regions away from the wall begin to burst through the interface as well. By 5ms after motion begins in the particle bed, the sharp structures have taken over more than half of the surface area of the particle bed interface.

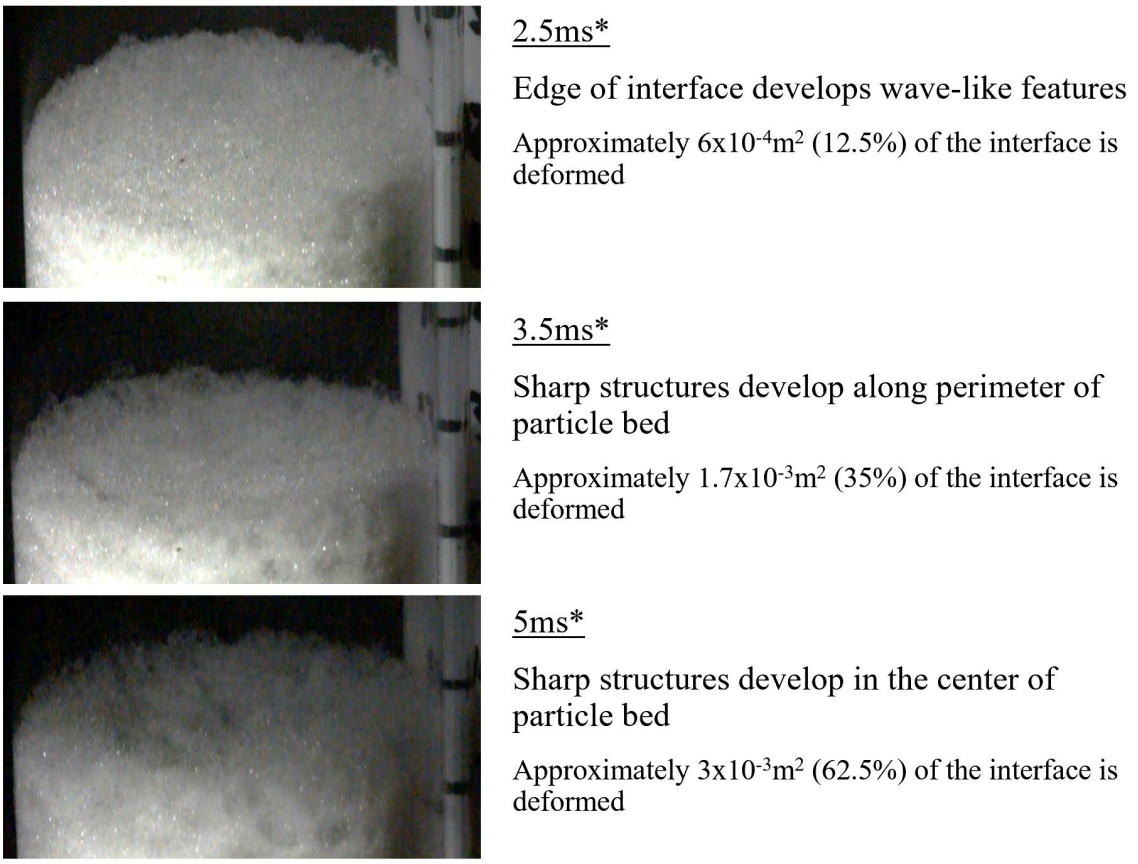

Figure 33: Shown Is a Time Progression of the Particle Bed Interface. Note That the Edges of the Particle Bed Rise Earlier than the Interior of the Interface. The Starred times Signify the Time from When Any Motion in the Particle Bed Is Seen at All to When the Associated Image Was Taken.

As evidenced by Figure 33, the walls have an effect on the gas velocity. Because the particles nearest the wall move upward first and continue to move upward at a faster rate for the early stages of the gas-particle interface deformation shown, it seems that the gases are escaping the particle bed nearest the wall faster and earlier than the gases contained within the rest of the bed. The most plausible explanation for this is that the gases experience less impedance nearest the walls than anywhere else in the bed. The glass spheres only make contact with the cylinder wall over a very small surface area (ideally a single point), meaning the majority of the volume between the wall and the first half particle diameter in the $-r$-direction is empty space and not particles. This is distinct from the interior of the bed, where the much more of the surface area of each particle is in

contact with other particles. To understand this particle-packing regime near the wall and determine how far in the $-r$-direction the wall affects the particle packing, a simulation was performed by Vowinckel and Meiburg at the University of California, Santa Barbara. In this simulation, particles settle under gravity between two infinitely long planes along the x-direction which are separated by 20 particle diameters. This method solves the ordinary differential equation for translational particle velocity $\boldsymbol{v}$ and angular velocity ω_p for each particle.

$$M_p \frac{d\boldsymbol{u}}{dt} = V_p(\rho_p - \rho_g)\boldsymbol{g} + \boldsymbol{F_c} \tag{41}$$

$$I_p \frac{d\boldsymbol{u}}{dt} = \boldsymbol{T_p} \tag{42}$$

T_p is the torque due to particle collisions and note that $V_p(\rho_p - \rho_g)\boldsymbol{g}$ is the body force due to gravity $\boldsymbol{F_b}$. In this simulation the collisional force $\boldsymbol{F_c}$ includes the force acting in the normal direction $\boldsymbol{F_n}$ and the force acting in the tangential direction $\boldsymbol{F_t}$ between both individual particles and particles and walls. $\boldsymbol{F_n}$ was calculated using a nonlinear spring-dashpot model and $\boldsymbol{F_t}$ was modeled by a linear spring-dashpot model capped by the Coulomb friction law.

Two simulations were performed, one with a total number of particles of 2,500, and another with 5,000 particles. In both cases, the size of the particles were 212-297μm. The primary results shown in Figure 34 show point-profiles of the averaged solid volume fraction in the three Cartesian directions ϕ_x, ϕ_y, and ϕ_z; where $\bar{\phi}$ is phase indicator that equals unity within a solid particle and zero outside a particle[25].

$$\begin{aligned}
\phi_x &= \frac{1}{L_y L_z} \int_{L_y} \int_{L_z} \bar{\phi} dy dz \\
\phi_y &= \frac{1}{L_x L_z} \int_{L_x} \int_{L_z} \bar{\phi} dx dz \\
\phi_z &= \frac{1}{L_x L_y} \int_{L_x} \int_{L_y} \bar{\phi} dx dy
\end{aligned} \tag{43}$$

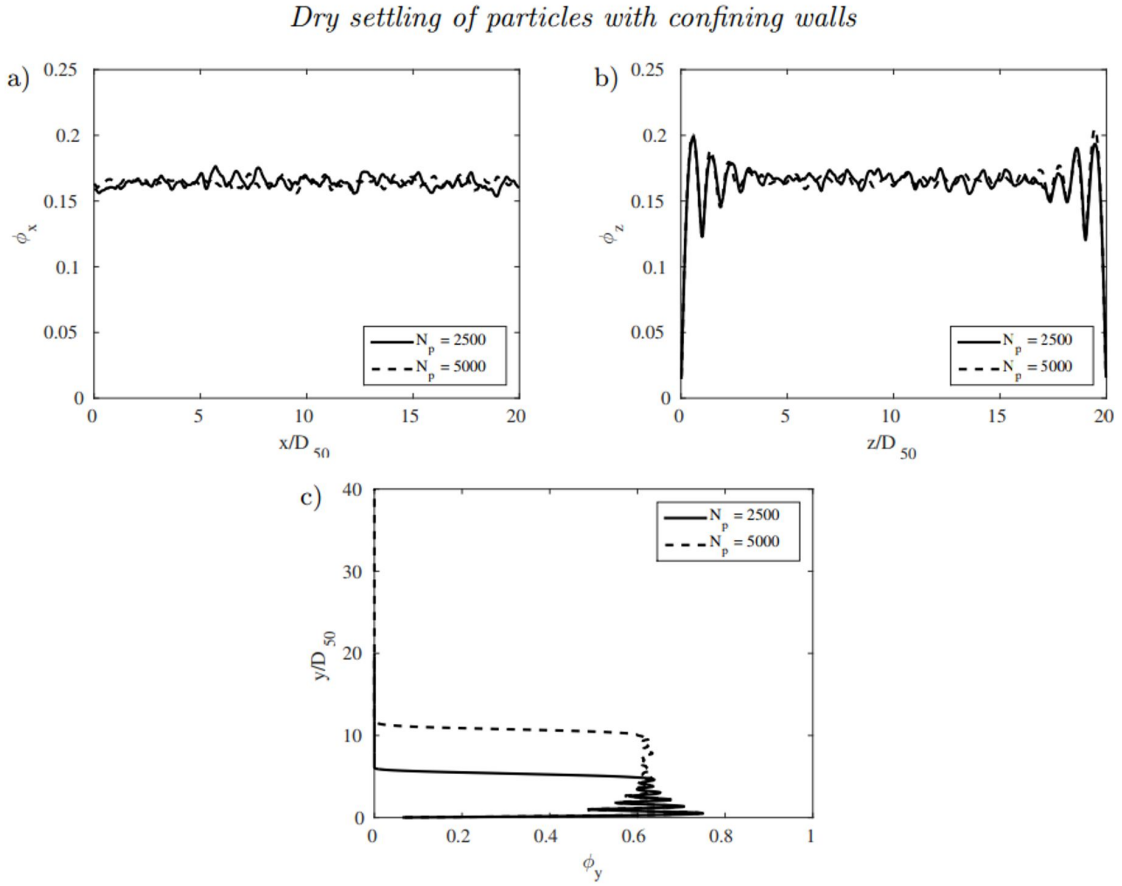

Point-profiles averaged into the different Cartesian directions. (a) averaged in y and z, (b) averaged in x and y, and (c) averaged in x and z.

Figure 34: Shown Are the Some Point Profiles Averaged in the Three Cartesian Directions. The Most Important Profile Relative to the Wall Effects Is Plot (b). This Is the Profile Looking Between the Two Infinitely Long Planes. The Profile in Plot (b) Shows a Large Variation in Solid Volume Fraction Between the Walls, Which Persists for Five Particle Diameters. The x-coordinate Noted in These Figures Is the Direction Aligned with the Infinitely Long Planes. The y-coordinate Is Aligned Vertically with the Height of the Particle Bed. The z-coordinate Is Aligned with the Width of the Particle Bed Between the Two Infinitely Long Planes. *Used with Permission from Vowinckel and Meiburg 2018[25].*

In Figure 34, the point-profiles averaged in the x and y-directions show a very distinct oscillation in solid volume fraction near the walls. The contact between the glass spheres and the wall occurs at a nearly perfect point, so the averaged solid volume fraction right at the wall is very low. This effect appears to persist for five particles diameters. This may explain why the perimeter

of the particle bed interface rise faster and earlier than the interior of the particle bed interface, as the lower solid volume fraction presents less impedance to the moving and expanding gas near the walls. This effect is seen in the high-speed images shown in Figure 35. The images shown in Figure 35 are highly-processed in a similar way to the images shown in Figure 30, but with the intensity stretched even further.

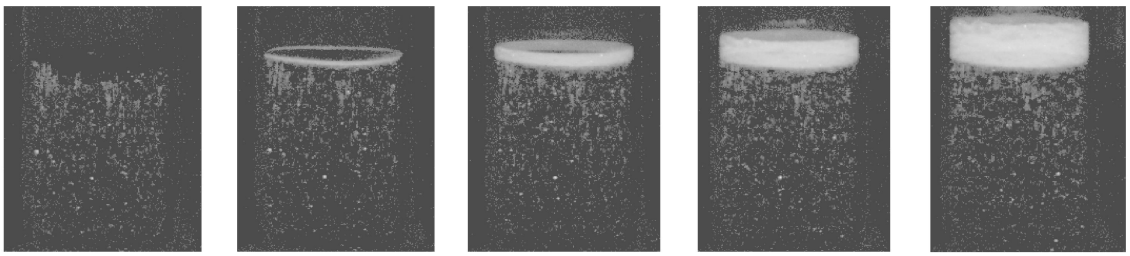

Figure 35: Shown Is a Series of Highly-processed Images Designed to Show the Growth of the Edge Effects over Time. The δt Listed in the Figure Is Equal to 1.6ms. The Bright and Intense Pixels in These Images Denote a Large Change from the Initial State of the Particle Bed at $t = t_0$. The Less Intense Pixels Show Any Low-level Fluctuating Noise Occurring Between the Current Frame and the Initial Frame.

The first frame in Figure 35 is essentially a background image and the low-level intensity seen is noise due to the shimmering particles. Every subsequent frame has the same background image subtracted from it, making any change in intensity from the first frame to the current frame appear as with bright white pixels. The second frame shows a bright white ring along the perimeter of the particle bed interface, because there is strong movement between the second frame and the first frame. As time progresses this ring grows in thickness as the particle bed also expands upward in general. The shapes of the bright white ring in the second and third frame show that not only do the particles near the perimeter of the interface rise earlier (seen in the comparison between the second frame and the frist frame) than those in the center of the interface, but they also rise faster and accelerate away from the center of the interface (comparing the third frame to the second frame shows that the white ring grows taller with the center of the interface remains undisturbed). Another feature to note is that the breakdown of the bright white region into horizontal layers is also seen starting in the fourth frame and continuing into the fifth frame.

In Chapter 3, a condensation cloud was mentioned. This condensation cloud develops due to the dramatic temperature drop, described in Figure 11. As the air cools due to the expansion, it loses the capacity to hold as much water. When the temperature drops enough, the water vapor condenses out of the air forming a cloud. This cloud is both helpful and hindering depending on the experimental configuration. In the standard setup, the cloud is very helpful as it helps visualize the reflected shock as it travels up and down in the shock tube. However, it has another use—it recesses away as the gas escapes the bed. When these experiments were performed without the particle bed in place, the cloud remained in place until it faded away as gases in region three re-warmed and the condensation droplets re-evaporated. The cloud was only seen to recesses as a consequence of the degassing particle bed. This means that if gases are escaping in a specific region, it could be evidenced in the shape of the cloud-escaped gas interface. The imagery of the recessing cloud shown in Figure 36 is as expected—showing the cloud being further pushed away near the walls than in the center of the glass cylinder. This creates a conically-shape interface on the cloud, which becomes more dramatic as time progresses—again, supporting the theory that the gases escape earlier and more rapidly near the perimeter of the particle bed interface.

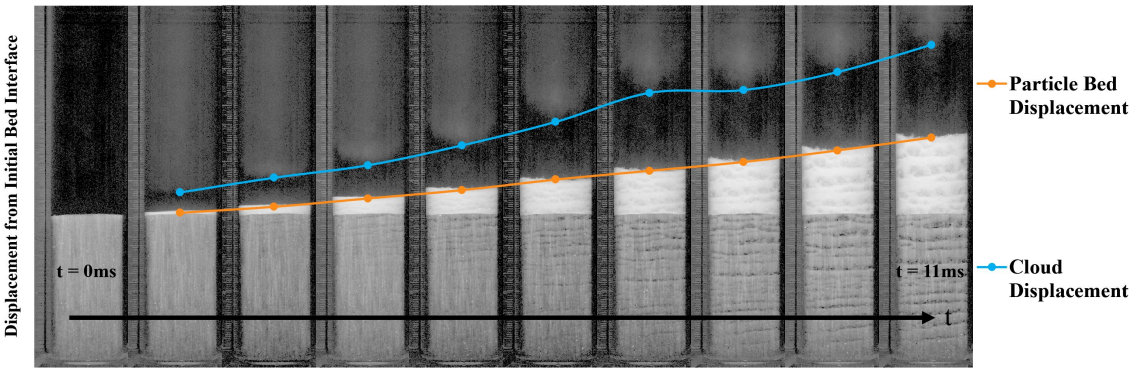

Figure 36: Shown Is the Recession of the Condensation Cloud Due to the Degassing of the Particle Bed. Also Note Transition Into Bulk Motion As Reflected Shock Doesn't Affect Particle Bed Height.

Note that there are two trendlines shown in Figure 36. The blue trendline was shown in Figure 30 and shows the recession of the cloud and how it is affected by the reflected shock. The orange trendline shows the location of the gas-particle interface as it rises in time due to the forces exerted on the particles from the expanding and moving interstitial gases. Tracking the interface

of the particle bed as it rises in time was a parameter CCMT had initially determined would be a good metric to help validate their simulation. A concern early on was that the reflected shock may interfere with the rise of the particle bed interface (as it certainly interferes with the gases above the bed), but because the reflected shockwave was not being simulated, there would be a notable difference between the simulated interface rise and the experimental interface rise. However, as shown by smooth orange trendline, the interface rise remains visibly unaffected by the reflected shockwave. The particle bed interface rises smoothly across all frames, and in particular between t = 7ms and t = 8ms—when the gases are seen to be affected by the reflected shockwave. Additionally, as listed in Table 6, the time constants τ_{cutoff} associated with the glass particles are quite long—especially compared to the τ_{cutoff} of the condensation droplets as noted in Chapter 3.2. For these reasons, it was determined that despite the presence of a reflected shockwave, the particle bed interface rise rates would still be a valuable way to compare the simulation and the experiments performed at ASU.

4.2 Early Bed and Gas Motion Compared with Simulations

To better understand the gas and particle behavior in the shocktube experiments, simple simulations were performed using Two Phase Euler Foam from the OpenFOAM[32] Computational Fluid Dynamics Toolbox. Two Phase Euler Foam is an Eulerian-Eulerian code commonly used to examine multiphase compressible flows, much simpler than the simulations being performed at CCMT. There is a brief write up discussing this code in Appendix A of this document. Shown in Figure 37 is simulated solid volume fraction and the z-component of the gas velocity data. Overlaid onto the surface colored by solid volume fraction are contour lines at approximately every 10%. Overlaid onto the gas velocity surface are streamlines of the gas. This data set was taken 7ms after the diaphragm rupture. Notice in these images, the paths the gases take while escaping the particle bed interface. As seen by the gas velocity-colored surface on the right hand side, there is very high velocity near the wall within the bed, and then the gas moves away from the wall once it escapes the particle bed interface, as seen by the black streamlines. Both of these slices were taken from the center of the simulated shocktube. *It is important to note that this code has not being rigorously validated for comparisons relating to this experiment. However, there is still value in making a comparison to see*

how well this experiment can be modeled with an Eulerian-Eulerian-type code.

This simulation was performed with a higher resolution in the radial direction than other simulations. It had a radial resolution of 100 (compared to 25 for the other simulations) and an axial resolution of 500. With higher resolution between the two sidewalls, the increased solid volume fraction near the walls is clearly visible. As the snapshots of the simulation in Figure 37 are from 7m after the diaphragm ruptures, they can be compared to the sixth frame shown in Figure 36. Notice in both figures the perimeter of the particle bed interface is higher near the walls.

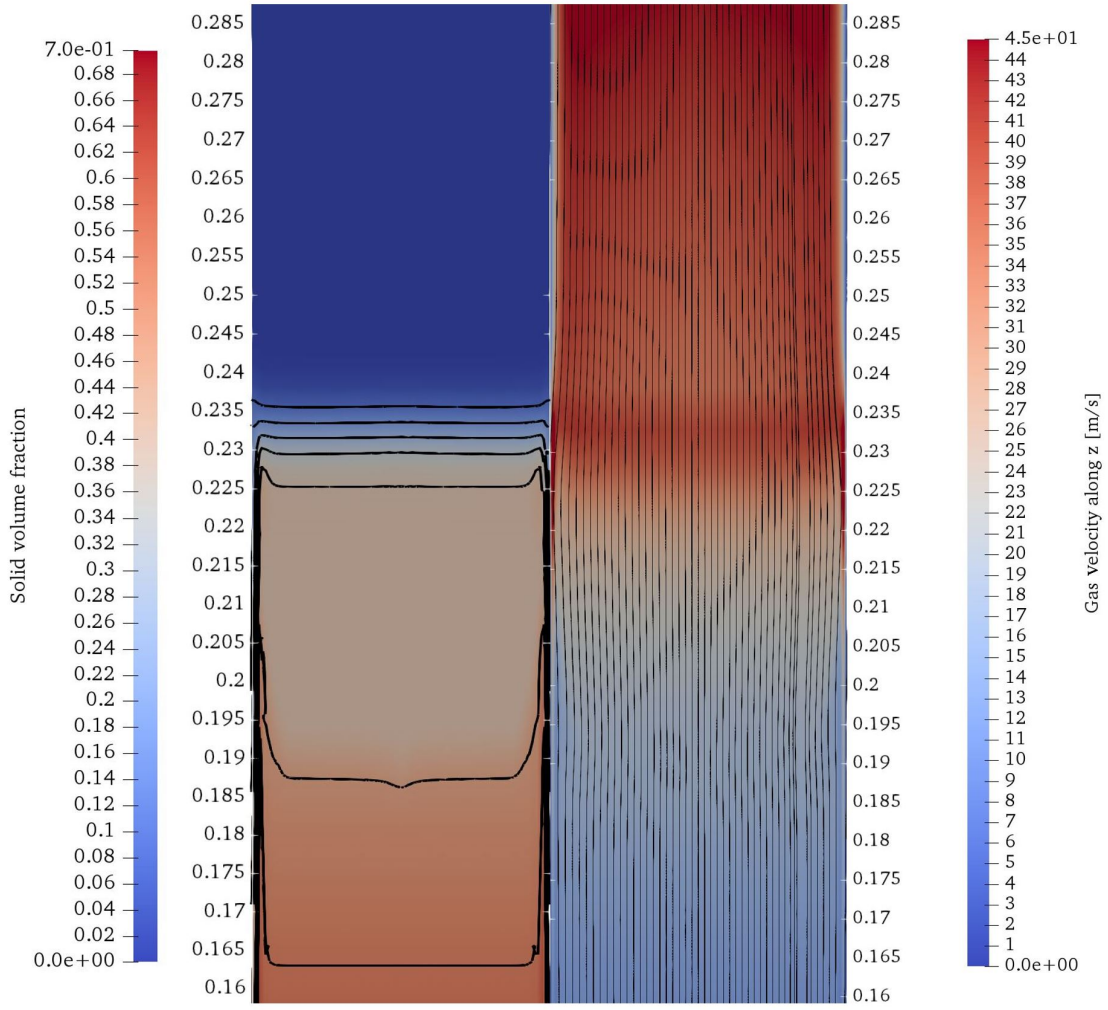

Figure 37: Shown Are the Simulated Values of the Solid Volume Fraction (Left) and the Gas Velocities (Right) 7ms after the Diaphragm Ruptures. This Simulation Was of an Experiment with a 0.2m Bed Composed of 297μm Diameter Particles and an Initial Pressure Ratio of 20. On the Left, Contour Lines at Approximately Every 10% of the Solid Volume Fraction Are Overlaid onto a Background of a Surface Colored by the Solid Volume Fraction. On the Right, Black Streamlines of the Gas Are Overlaid onto a Surface Colored by the Gas Velocities in the z-direction. Unique to This Specific Simulation Compared to Other Simulations Performed Is the High-resolution in the Radial Direction (100), Which Is Four times Greater than the Other Simulations.

4.3 Results

It was shown that the first particles to rise during the particle bed expansion process are those nearest the walls. The reason for this is that there is less impedance to the gas flowing between

the outer-most particles and the smooth glass wall, because the overall solid volume fraction near the wall is very low, as shown by the simulations performed by Vowinckel and Meiburg in 2018. As the gases are able to move more readily and rapidly near the wall, the drag forces exerted by those gases on the particles is much greater. This causes the perimeter of the particle bed interface to rise more quickly. As the particles begin to move, simple geometry requires the same low volume fraction must be maintained right at the wall, as the spheres can only come into contact with the wall at a point. Therefore, not only do the gases near the wall get a "headstart" so-to-speak on the gases closer to the interior of the bed, but gases located close to the wall will have higher velocities due to the reduced impedance caused by the particles' inertia.

The simulation compares well with the experimental data as shown between Figures 37 and 36. The gas are moving rapidly near the walls while within the particle bed and then move slightly away from the walls once they have escaped the gas-particle interface as seen in the black streamlines in Figure 37. Additionally, the solid volume fraction profile near the wall matches what is seen in the experiments. More in-depth comparisons between simulations and experiments will be shown in Chapters 5.2, 7.2, and 8.3.

5 PARTICLE BED INTERFACE RISE

5.1 Experimentally Measured Particle Bed Interface Rise Rates

A simple but elucidating comparison to make is the differences in rise rates of the particle bed interface when varying particle diameter and initial bed heights. To do this, the location of the particle bed interface needs to be determined from the high-speed video data. The frame rate of the camera was 10,000fps, which is fast enough to allow for good temporal resolution of the rapidly moving gas-particle interface. It was also slow enough to allow for good spatial resolution, as with any high-speed camera there is a trade-off between frame rate and spatial resolution. The camera resolution used for the data presented was 208($\mathbf{X}$) x 800($\mathbf{Y}$). With these parameters set, the calibration along the vertical image coordinate $\mathbf{Y}$ was 0.24mm per pixel. The intensity profiles along the centerline of the glass cylinders were measured to locate the general region where the particles are (high pixel intensity values) and where the particles are not (low pixel intensity values). The centerline (averaged over twenty pixels, which is approximately 10% of the width of the glass cylinder in the images) was used to avoid any distortions associated with refracted light through the curved glass. The first step in the data processing was to collect an intensity profile for every frame of every experiment presented.

The next step is to choose a threshold for determining what pixel intensity value represented the particle bed interface. The beds composed of larger particles appear brighter in the captured images than the beds composed of smaller particles do. Therefore, the threshold was calculated as a percentage of the maximum pixel intensity of the bed seen in the first frame captured at $t < 0$. Four different percentages were tested 15%, 25%, 35%, and 45%. Shown in Figures 38, 39, and 40, are the frames showing where each of the proposed intensity threshold percentages would place the particle bed interface for particle beds composed of [44, 90]μm, [150, 212]μm, [212, 297]μm, respectively.

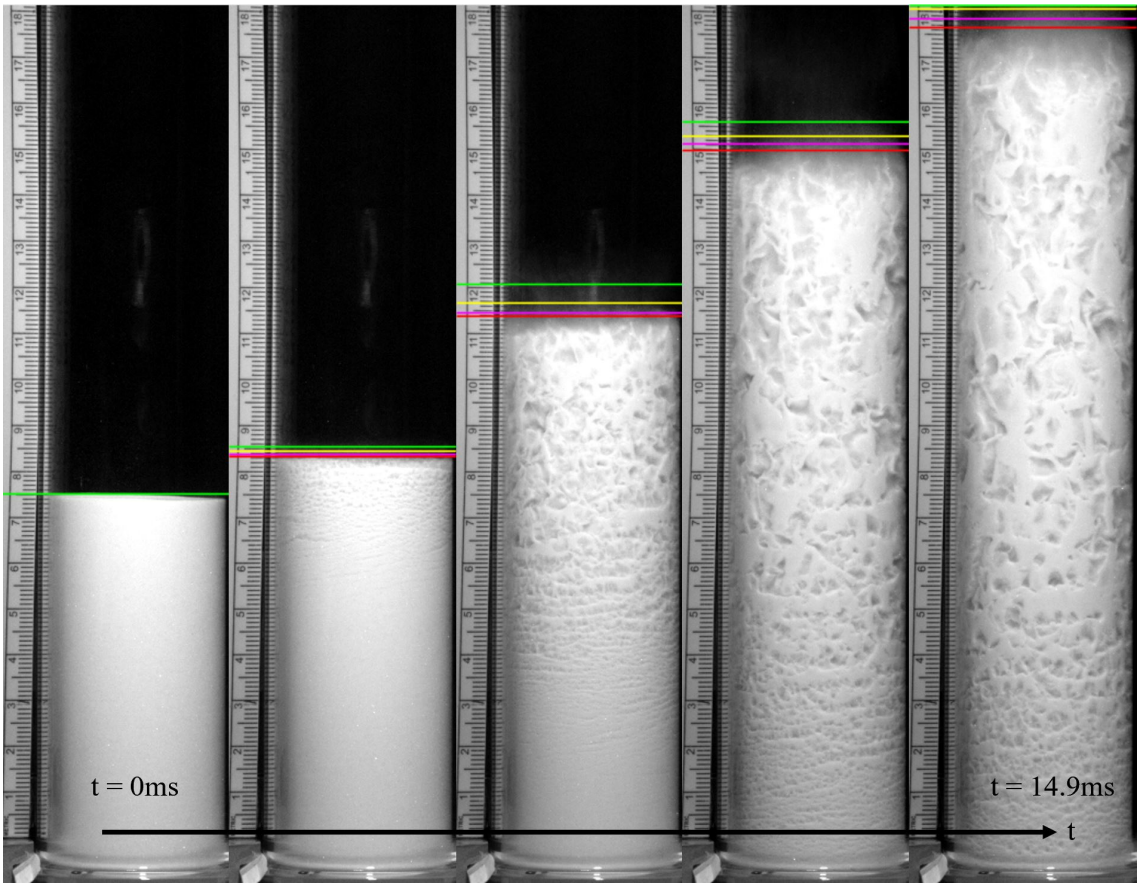

Figure 38: Shown Are Five Frames Taken at Progressively Later times During an Experimental Realization with a Particle Bed Composed of [44, 90]μm Diameter Particles at an Initial Bed Height of $z_b = 0.1m$. The Four Proposed Pixel Intensity Threshold Percentages Are Shown in Green (15%), Yellow (25%), Magenta (35%), and Red (45%). These Images are Associated with Filename 111317_7.

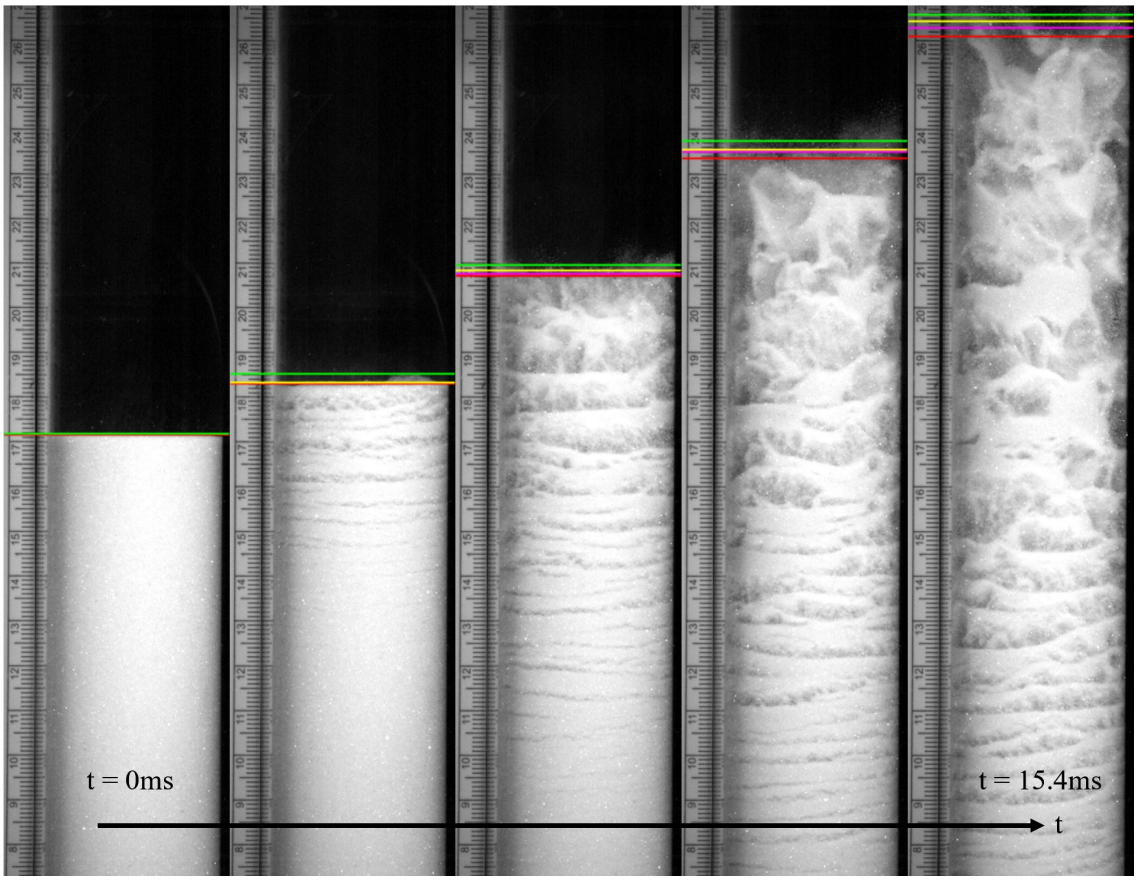

Figure 39: Shown Are Five Frames Taken at Progressively Later times During an Experimental Realization with a Particle Bed Composed of 150, 212]μm Diameter Particles at an Initial Bed Height of $z_b = 0.1m$. The Four Proposed Pixel Intensity Threshold Percentages Are Shown in Green (15%), Yellow (25%), Magenta (35%), and Red (45%). These Images are Associated with Filename 111517_1.

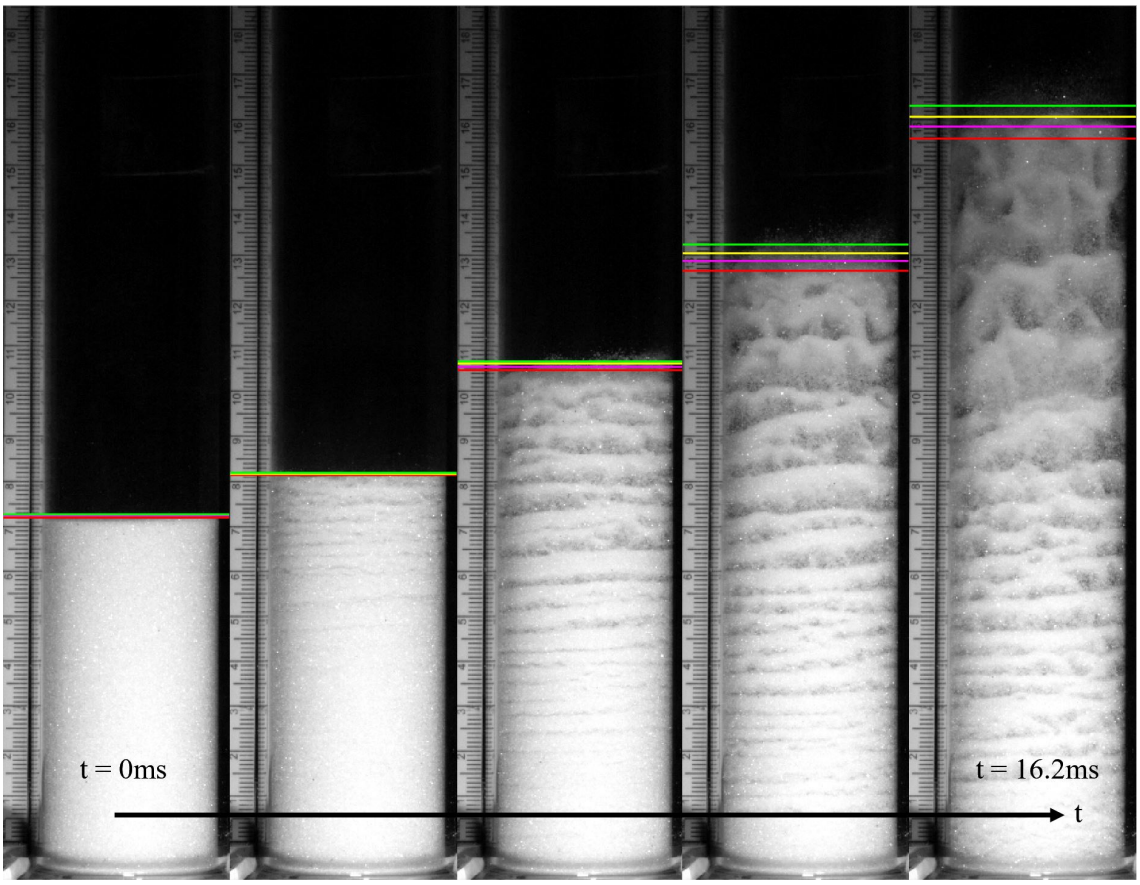

Figure 40: Shown Are Five Frames Taken at Progressively Later times During an Experimental Realization with a Particle Bed Composed of [212, 297]μm Diameter Particles at an Initial Bed Height of $z_b = 0.1m$. The Four Proposed Pixel Intensity Threshold Percentages Are Shown in Green (15%), Yellow (25%), Magenta (35%), and Red (45%). These Images are Associated with Filename 111617_2.

In early times, all four proposed intensity threshold percentages yielded particle interface locations that were within a few millimeters of each other. As the bed begins to further evolve, varying the threshold percentage has a much stronger effect and can place the gas-particle interface as much as a centimeter off. The percentage that seemed to place the interface the best was 35%. This corresponds to the magenta lines in Figures 38, 39, and 40. For all following data analyses a threshold of 35% of the maximum pixel intensity seen is used to locate the gas-particle interface.

Shown in Figures 41, 42, and 43, are the gas-particle bed interface displacements over time. Each line on these three plots is an ensemble average of five separate realizations all initiated

with a pressure ration $\frac{P_4}{P_1} \approx 20$. The shadowing behind each of the plots represents the estimated RMS as calculated by (44) where n = the number of experimental realizations. The x-axis on each of these figures is $t - t_i$, where t_i marks the estimated time that the expansion wave impinges on the gas-particle interface. Note the slow ramp-up in the early times and then the rapid transition into a linear regime. In each of these figures, it can also be noted that the taller beds rise faster than the shorter beds.

$$\text{estimated RMS} = 2.5 \times (n)^{\frac{1}{2}} \tag{44}$$

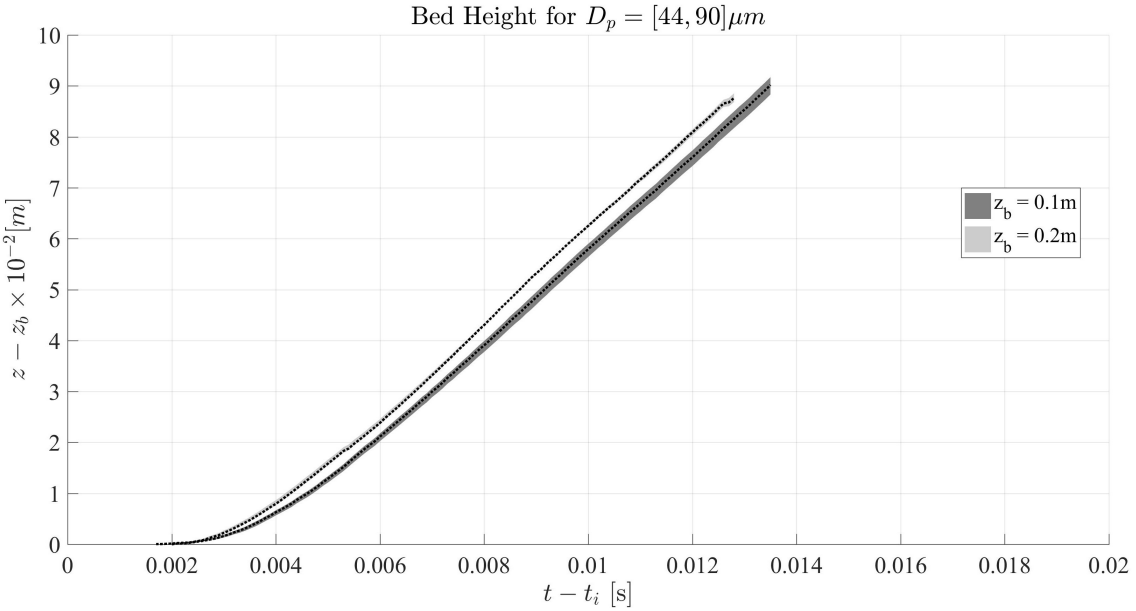

Figure 41: Shown Plotted Is the Ensemble Average of Particle Bed Interface Displacement over Time for Two Experiments Composed of Five Realizations Each. Both Experiments Used Particle Beds with $44\mu m \leq D_p \leq 90\mu M$, but with Different Initial Bed Heights z_b of 0.1m and 0.2m. The Coloring of the Shadowing Behind Each Plot Denotes the Bed Height. The Width of the Shadowing Is Equal to the Estimated RMS.

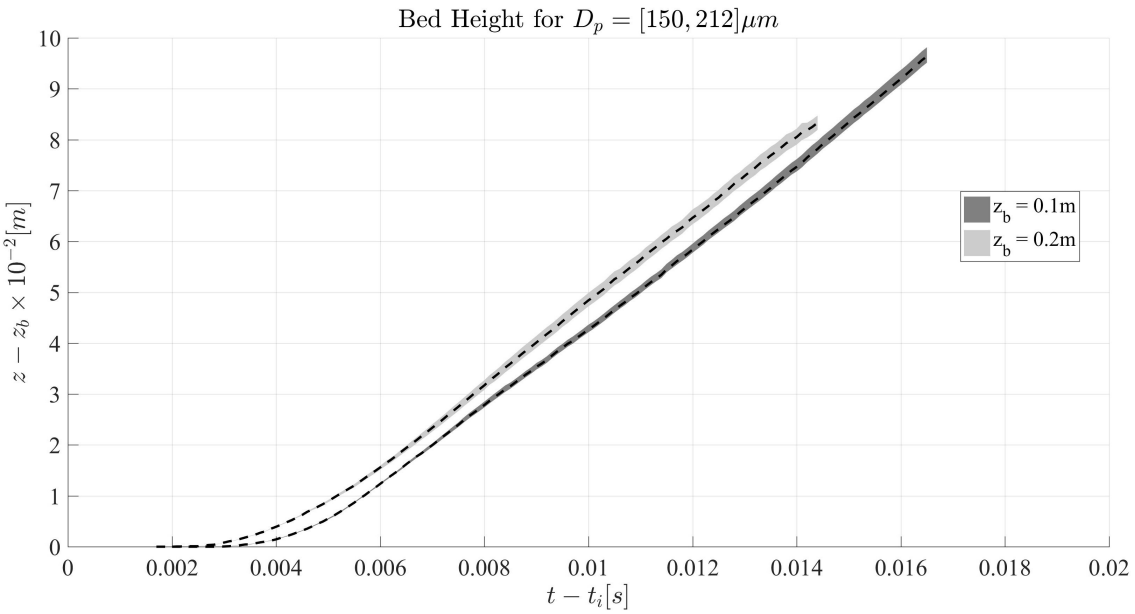

Figure 42: Shown Plotted Is the Ensemble Average of Particle Bed Interface Displacement over Time for Two Experiments Composed of Five Realizations Each. Both Experiments Used Particle Beds with $150\mu m \leq D_p \leq 212\mu$m, but with Different Initial Bed Heights z_b of 0.1m and 0.2m. The Coloring of the Shadowing Behind Each Plot Denotes the Bed Height. The Width of the Shadowing Is Equal to the Estimated RMS.

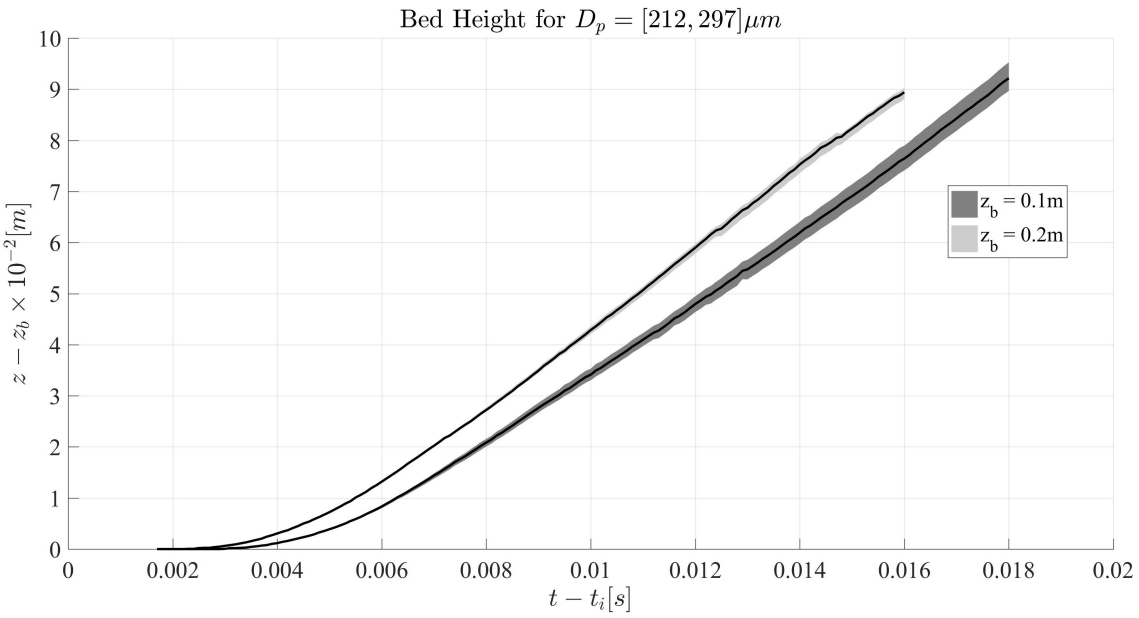

Figure 43: Shown Plotted Is the Ensemble Average of Particle Bed Interface Displacement over Time for Two Experiments Composed of Five Realizations Each. Both Experiments Used Particle Beds with $212\mu m \leq D_p \leq 297\mu m$, but with Different Initial Bed Heights z_b of 0.1m and 0.2m. The Coloring of the Shadowing Behind Each Plot Denotes the Bed Height. The Width of the Shadowing Is Equal to the Estimated RMS.

Initial bed height z_b is not the only factor that affects the gas-particle interface rise. Additionally, the diameter of the particles composing each bed also affect the displacement of the interface over time. Shown in Figures 44 and 45 are plots of ensemble averages of the gas-particle bed interface displacement over time for beds composed of all three size ranges with $z_b = 0.1$m and for $z_b = 0.2$m. Just as with the plots comparing initial bed height, the x-axis on each of these figures is $t - t_i$, where t_i marks the estimated time when the expansion wave impinges on the gas-particle interface. For both beds of $z_b = 0.1$m and $z_b = 0.2$m, the rise rates are affected by the composition of the particle bed. The beds composed of smaller particles rise more quickly than the beds composed of larger particles.

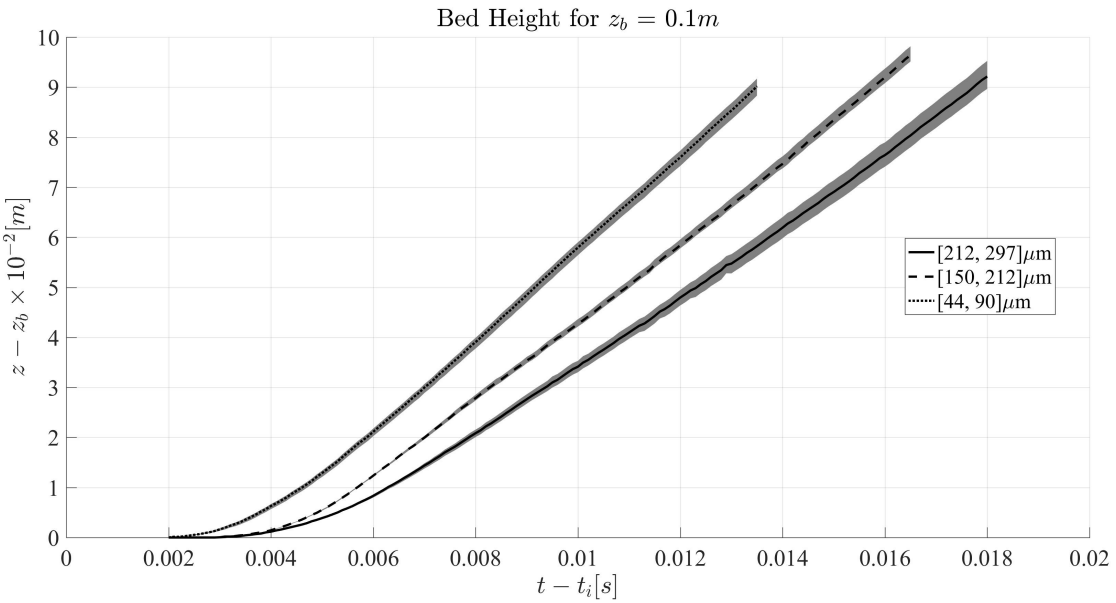

Figure 44: Shown Plotted Is the Ensemble Average of Particle Bed Interface Displacement over Time for Three Experiments Composed of Five Realizations Each. All Three Experiments Used Particle Beds with an Initial Bed Height of $z_b = 0.1$m, but with Three Different Particle Size Ranges $44\mu m \leq D_p \leq 90\mu m$, $150\mu m \leq D_p \leq 212\mu m$, and $212\mu m \leq D_p \leq 297\mu m$. The Line Style Denotes the Different Particle Size Ranges as Noted in the Legend. The Width of the Shadowing Is Equal to the Estimated RMS.

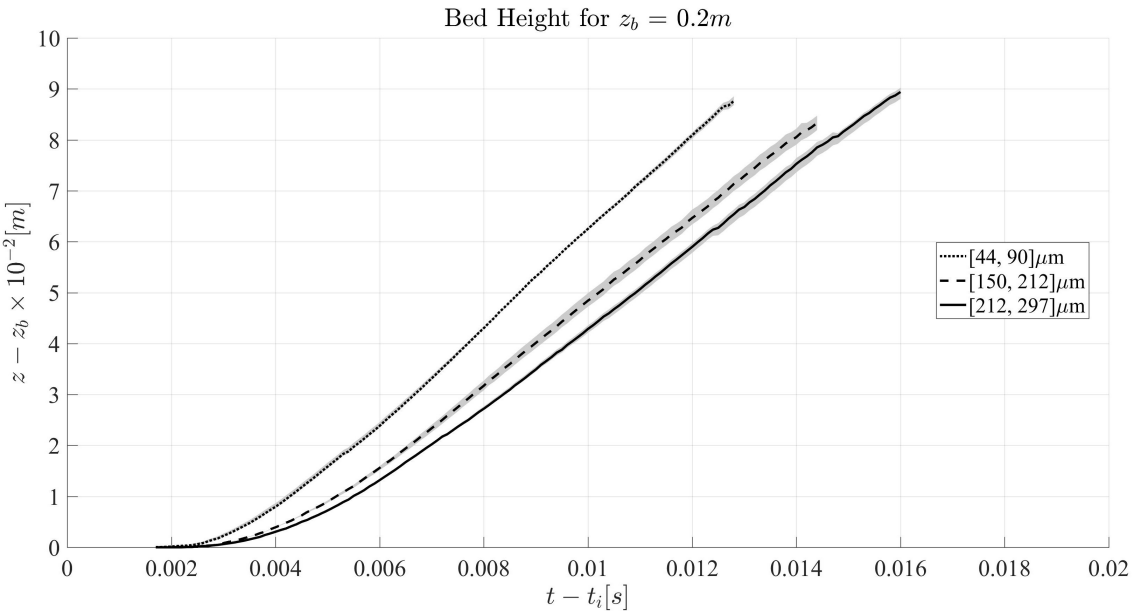

Figure 45: Shown Plotted Is the Ensemble Average of Particle Bed Interface Displacement over Time for Three Experiments Composed of Five Realizations Each. All Three Experiments Used Particle Beds with an Initial Bed Height of $z_b = 0.2$m, but with Three Different Particle Size Ranges $44\mu m \leq D_p \leq 90\mu m$, $150\mu m \leq D_p \leq 212\mu m$, and $212\mu m \leq D_p \leq 297\mu m$. The Line Style Denotes the Different Particle Size Ranges as Noted in the Legend. The Width of the Shadowing Is Equal to the Estimated RMS.

One factor that may come into play that has not been mentioned yet is the natural variation of solid volume fraction associated with the varying bed height and the varying particle sizes. Under a random pour, solid volume fraction is expected to be between 60% and 70% [26]. This was observed to be the case for all realizations in each of the five experiments presented in this chapter. See Table 10 for the averaged solid volume fraction calculations from the measured mass of each particle bed. Interestingly, the average solid volume fraction ψ increases as the particle size increases, but also decreases with bed height.

$D_p[\mu m]$	$z_b[m]$	ϕ_p
$44\mu m \leq D_p \leq 90\mu m$	0.1	0.6384
	0.2	0.6199
$150\mu m \leq D_p \leq 212\mu m$	0.1	0.6684
	0.2	0.6476
$212\mu m \leq D_p \leq 297\mu m$	0.1	0.6842
	0.2	0.6733

Table 10: Shown Is a Table Noting the Varying Solid Volume Fraction of Particle Beds of Varying Initial Bed Height and Particle Size.

In the experiments performed, careful measures were taken to make sure the particle beds were as consistent as possible. These included taking care to measure the mass of the particle beds carefully, pouring the particles into the bottom of the shocktube slowly over approximately 45 seconds, and careful bed height measurements once the particles were emplaced. If the mass was measured to be within six percent of the mass of the beds within the same experiment, it was considered acceptable. If the measured bed height was within 3mm of the target height, it was considered acceptable. For all experiments performed in this study, the variation in volume divided by the variation in mass was between 0.0006 and 0.002. The experiments with values on the lower end of that spectrum were performed after a new, more accurate scale was purchased.

5.2 Particle Bed Interface Rise Compared with Simulations

Although there was not a reliable way to alter the solid volume fraction evenly throughout the bed in experiments, it can easily be altered in a simulation. In order to determine whether it was simply the varied solid volume fraction causing the changes seen in the interface rise rate in experiments or if it had to do specifically with the particle size and the resulting size of the interstices, simple simulations of the shocktube experiments were performed using Two Phase Euler Foam from OpenFOAM[32].

A brief look at the effects of initial solid volume fraction was done by performing a simulation of the expanding particle bed and comparing the gas-particle interface rise rates for beds of differing heights and particle size, but with the same initial volume fraction. A second set of simulations were done with varying the simulated initial volume fraction to match the values shown

in Table 10. The results of these simulations are plotted together in Figure 46.

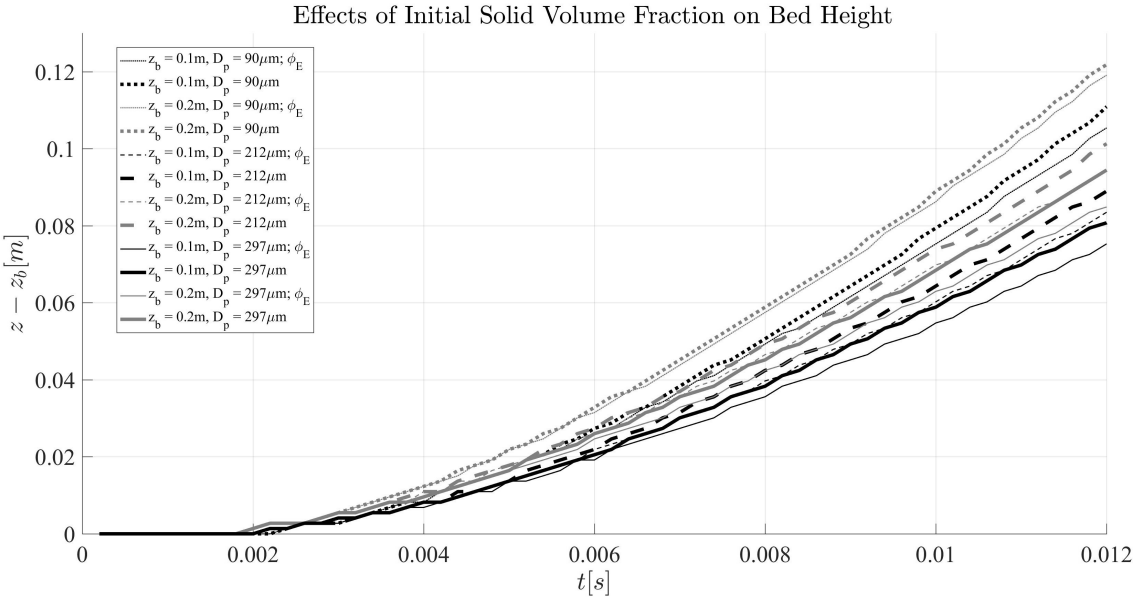

Figure 46: Shown Is a Comparison Between the Simulated Bed Rise Rates with a Generic Solid Volume Fraction ϕ_p =0 .60 Marked by Thick Lines and the Rise Rates from Simulations Where the Real Experimental Value for the Solid Volume Fraction Was Used, Called ϕ_e, Marked by Thin Lines. These ϕ_e Values Are Equal to the ϕ_p Values Found in Table 10. Note That in Early times There Is Very Little Difference Between the Two Sets of Curves.

In Figure 46, it can be seen that altering the initial solid volume fraction of the bed does not have a large effect on the interface displacement over time. Around t = 8ms, the beds composed of larger particles seem to be affected much more by the varied ϕ_p value than the beds composed of the smaller particles. The two plots for the mid-size 150μm particles begin to drift apart midway through the simulation—though the difference in the ϕ_p values was only 0.04, while the smallest 44μm look nearly unaffected by nearly the same change in ϕ_p. It seems that the larger simulated particles are more affected by variations in initial solid volume fraction than smaller simulated particles. However, one of the most important takeaways from this figure is that even when the ϕ values are kept constant while the particle diameter is varied, the bed rise rates still vary. This means that, according to the simulation, it is not just the variation in the bulk solid volume fraction (though the solid volume fraction is affected by the particle size in the loose random pack of the

dense particle bed) that causes the beds composed of smaller particles to rise more quickly; but that it is also the variation in the actual particle size and subsequently the size of the interstices between the particles. If there was a way to perfectly align the solid volume fractions for the dense particle beds composed of different ranges of particle sizes this could be tested experimentally. As it is now, with the current shocktube setup, trying to alter the solid volume fraction would introduce more variability in the experiment, making it a less valuable tool for code validation.

Shown in Figure 47 are the simulated bed displacements over time. The initial solid volume fraction values used for these simulated particle beds were matched to the values shown in Table 10. In Eulerian-Eulerian codes, it is not easy to simulate a range of particle sizes, so single particle sizes were used. The upper bound of the particle ranges were used for this comparison, meaning the simulations labeled as 212μm in Figure 47 were meant to show the upper bound of the mid-range size particles [150,212]μm. The solid volume fraction used to determine the gas-particle interface was 0.1. Figure 48 shows contour lines of the solid volume fraction at every multiple of 0.025 overlaid onto a centerline slice through simulated volume at t = 10ms after the diaphragm rupture. Though the simulation is presented as a horizontal shocktube, the direction of gravity has been modified to be along the axial coordinate of the shocktube, just as in the experiment at ASU. Note that these plots follow the same trends seen in the experimental data, in that the simulated beds with $z_b = 0.2$m rise faster than the simulated beds with $z_b = 0.1$m and the simulated with smaller diameter particles rise faster than the simulated beds with larger particles.

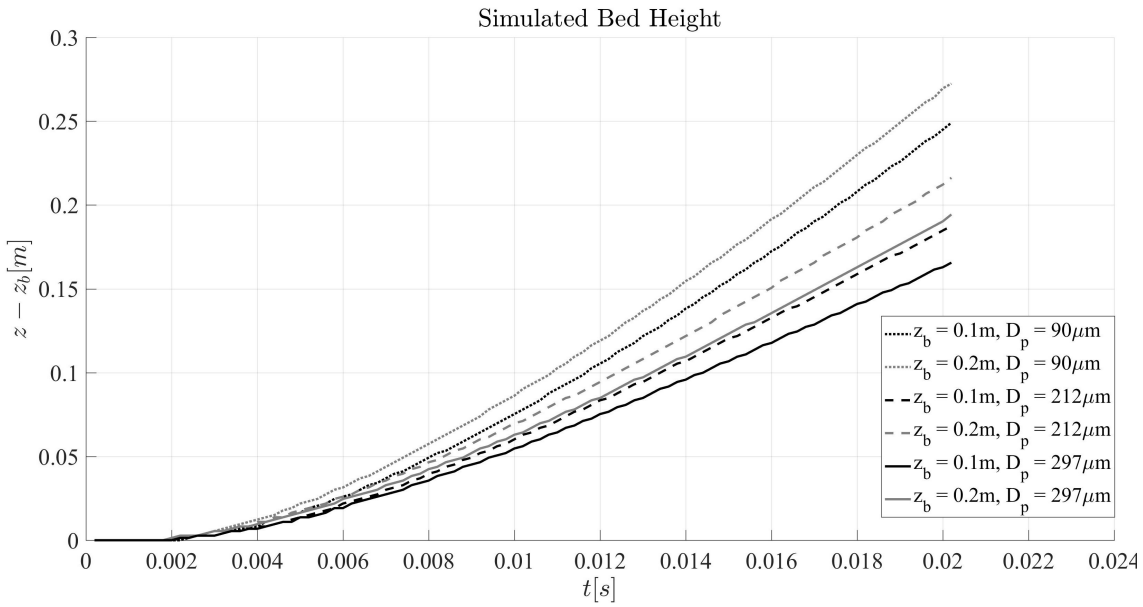

Figure 47: Shown Are the Simulated Bed Heights over Time from Six Simulations Designed to Mimic the Experiments Performed at ASU. The Trends Seen in the Simulations Match the Trends Seen in the ASU Experiments in Terms of the Taller Beds Rising More Quickly than the Shorter Beds and the Beds Composed of Smaller-diameter Particles Rising Faster than the Beds Composed of Larger-diameter Particles.

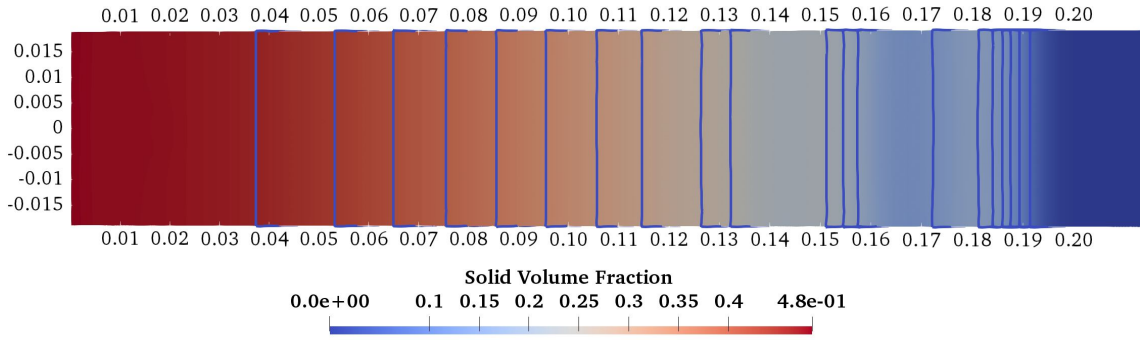

Figure 48: Shown Is a Slice along the Centerline of the Two Phase Euler Foam Simulated Shocktube with a Bed Composed of [44, 90]μm Particles and an Initial Bed Height $z_b = 0.1$m 10ms after the Diaphragm Ruptured. The Coloring Denotes the Solid Volume Fraction and the Overlaid Contours of Solid Volume Fraction Are Separated by 0.025. Interestingly, the Simulation Did Show the Particle Bed Expanding Non-homogeneously, as There Are Layers Visible in This Figure. The Initial Solid Volume Fraction of the Bed in This Simulation Has Been Matched to the Experimental Data Shown in Table 10.

In order to help determine whether these simulated results are representing the real physics involved in the experiment. Experimental data was overlaid onto the simulated bed rise rates. This comparison is shown in Figure 49. Note that in early times the simulation seems to match the experimental data relatively well. However, at approximately t = 8ms, the simulation predicts a much faster interface rise rate than is seen in experiments. This could partially be explained by the difficulty in choosing an appropriate solid volume fraction value to marking the particle bed interface. In the simulation data shown, a solid volume fraction threshold of 0.1 was used. This corresponds to the medium-blue color in the color scaling of Figure 48. When higher solid volume fractions were used to define the top of the simulated particle bed, the interface selection would jump up and down rapidly. This was due to the fact that the simulated particle bed evolution involves layering and particle-vacant regions, somewhat similar to the data captured from experiments show. Associated with this topic is the diffuse expanding particle bed interfaces, as seen in Figures 38, 39, and 40. Notice that the boundary between the top of the particle bed and the region above is somewhat blurred and diffuse, especially between the third and fourth frames shown in each figure. This time period $t \approx 8ms$ corresponds to when the simulated rise rates depart from the experimental rise rates. For time $t < 8ms$, the simulation seems to do a good job at simulating the effects seen in the experiment.

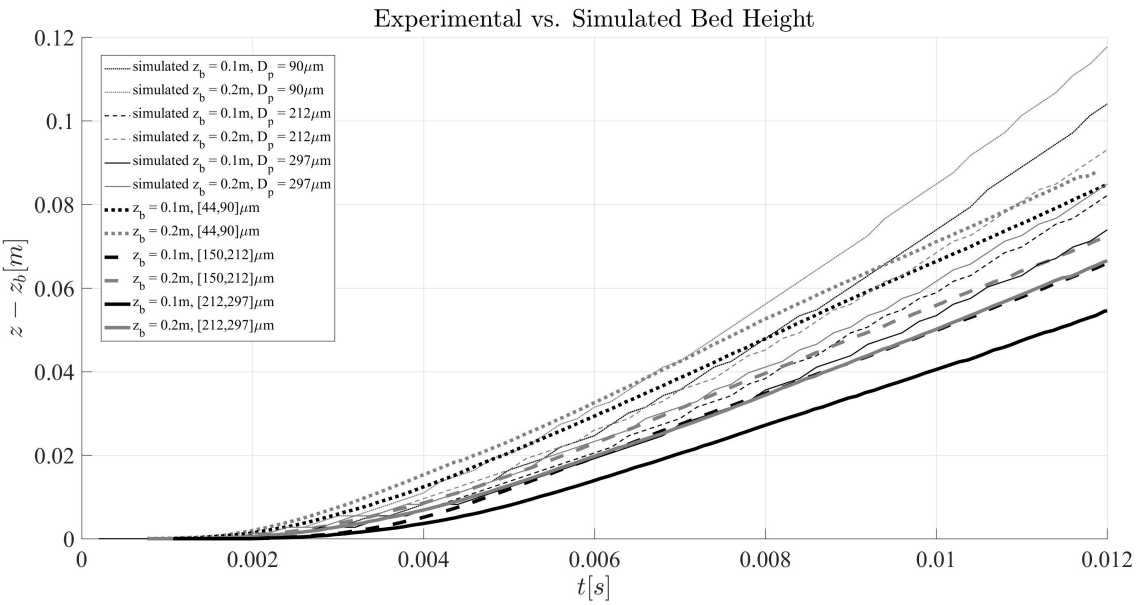

Figure 49: Shown Plotted Are Simulations of Particle Bed Interface Displacements over Time for Three Different Particle Sizes $90\mu m$, $212\mu m$, and $297\mu m$; and Two Different Bed Heights $z_b = 0.1$m and $z_b = 0.2$m. The Initial Solid Volume Fraction of the Beds in These Simulations Have Been Matched to the Experimental Data Shown in Table 10.

5.3 Results

Figure 50 shows a comparison between the exponential trendlines of normalized particle bed interface velocities (calculated from experimentally measured gas-particle interface displacements) for each type of particle bed. When all the velocities are plotted in this way, it can be seen that—in all cases—the taller beds rose more quickly than the shorter beds and beds composed of smaller particles rise faster than beds composed of larger particles.

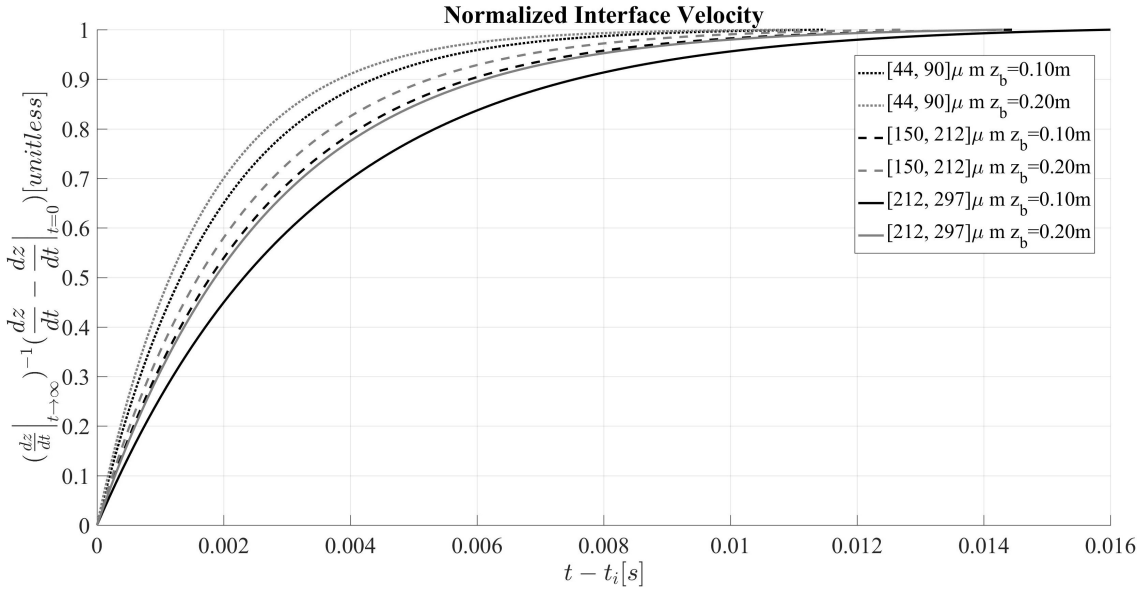

Figure 50: Shown Is a Comparison of the Exponential Trendlines of the Normalized Interface Rise Velocities. Three Particle Size Groups Are Shown: [44, 90]μm Marked with Dotted Lines, [150, 212]μm Marked with Dashed Lines, and [212, 297]μm Marked with Solid Lines. The Black Lines Are from Beds with $z_b = 0.1$m and Gray Lines Are from Beds with $z_b = 0.2$m. Because the Expansion Wave Impinges on Beds of Different Bed Heights at Different times, the Time Axis at the Bottom of the Figure Shows $t - t_i$, Where t_i Is the Time When the Expansion Wave Impinges on the Particle Bed.

Additionally, it has been noted that in all experimental realizations and in all simulations that the taller beds rise faster than the shorter beds. This most likely can be attributed to the fact that the taller beds contain more gas overall. As it is the expanding gases contained within the interstices of the particle bed that drive the particles upward, it is reasonable that more gases would yield a more rapid expansion of the particle bed.

Lastly, while the solid volume fraction ϕ_p certainly has an effect on the gas-particle interface rise rates, it is not the sole factor in what causes the variation of the bed rise across experiments with different particle sizes. It is reasonable the that actual size of the particles does matter, so that even if the particle beds could be formed with the exact same ϕ_p, but varied D_p, the interface rise velocities would still vary, because the it requires more energy to move a larger and more massive particles. This is also supported by what was shown in the simulations performed using Two Phase Euler Foam.

6 BULK MOTION IN PARTICLE BEDS

6.1 Examination of Bulk Motion in Particle Beds

In the first few moments of the bed motion, the bulk of the bed appears to swell somewhat homogeneously and the bed height is increased by a few millimeters. Then the perimeter of the gas-particle interface rises, and as seen in Figure 35, the bed then begins to break down into horizontal void cracks. These features were first seen by Anilkumar in 1989. These cracks are shown in higher resolution in Figure 51. One important thing to note about these horizontal void cracks is that they do not appear to slice cleanly through the bed. There may certainly be similar structures in the interior of the bed, however.

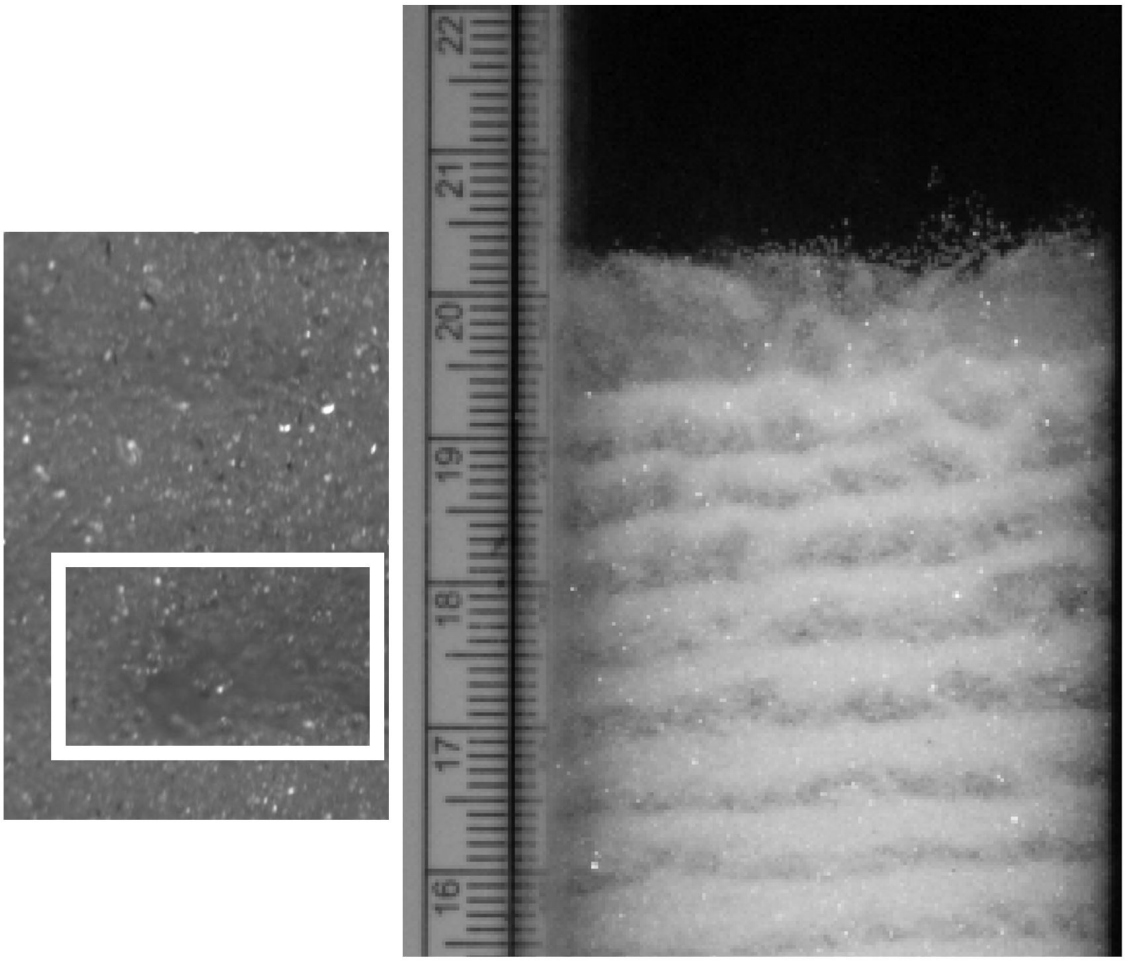

Figure 51: Shown on the Right Is a Closeup Image of the Horizontal Void Cracks That Develop Within the Expanding Particle Bed Composed of [212, 297]μm Particles With an Initial Bed Height of $z_b = 0.2$m. Important to Note Is That the Horizontal Voids Do Not Slice Clean Through the Particle Bed.

The horizontal layers and the subsequent breakdown of those layers looks different for different particle sizes. The biggest difference seen between bed expansions for varying particle sizes is the timeline. For beds composed of smaller particles, the timeline is somewhat accelerated. The horizontal layers form very rapidly and then breakdown into a cellular structure very soon afterward. In contrast the horizontal layers formed in beds composed of larger particles are somewhat stable for a period of time, before they breakdown into the cellular-like structures. Figures 52, 53, and 54, show a time progression of the particle bed expanding, breaking down into layers, and further

breaking down into the cellular-like structure of particle-vacant regions.

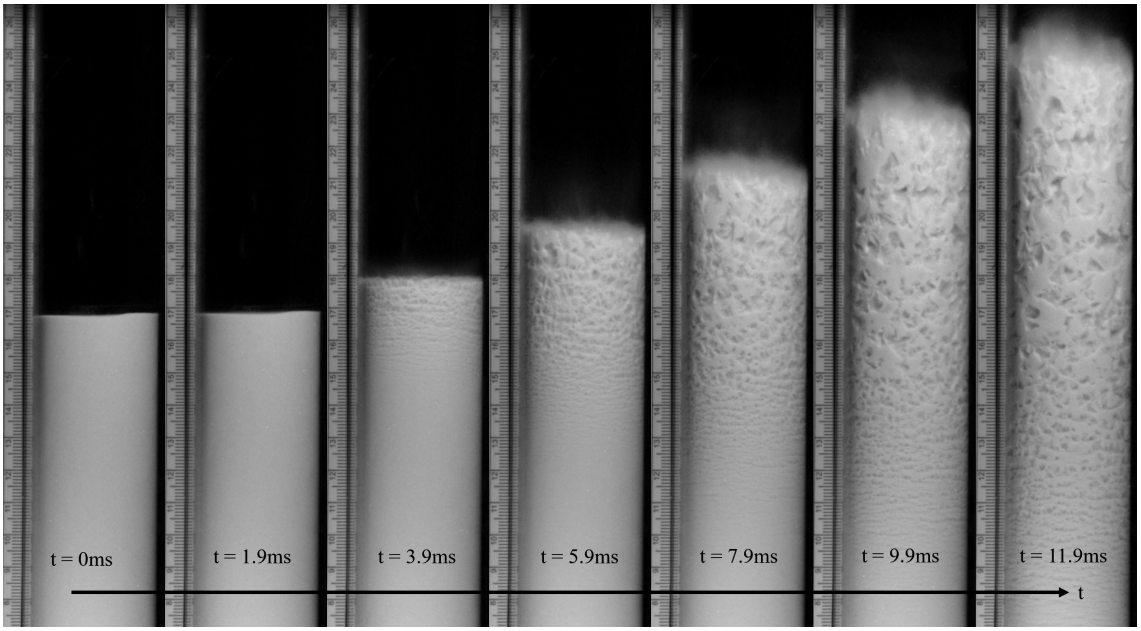

Figure 52: Shown Is a Time Progression of the Particle Bed Expansion with a $z_b = 0.2$m and Particles [44, 90]μm. Note at t = 3.9ms, Several of the Top Horizontal Layers Have Already Formed and Broken Down. Also Note the Interface Becomes Somewhat Difficult to Precisely Define at Approximately t = 7.9ms. These Images are Associated with the Filename 111617_6.

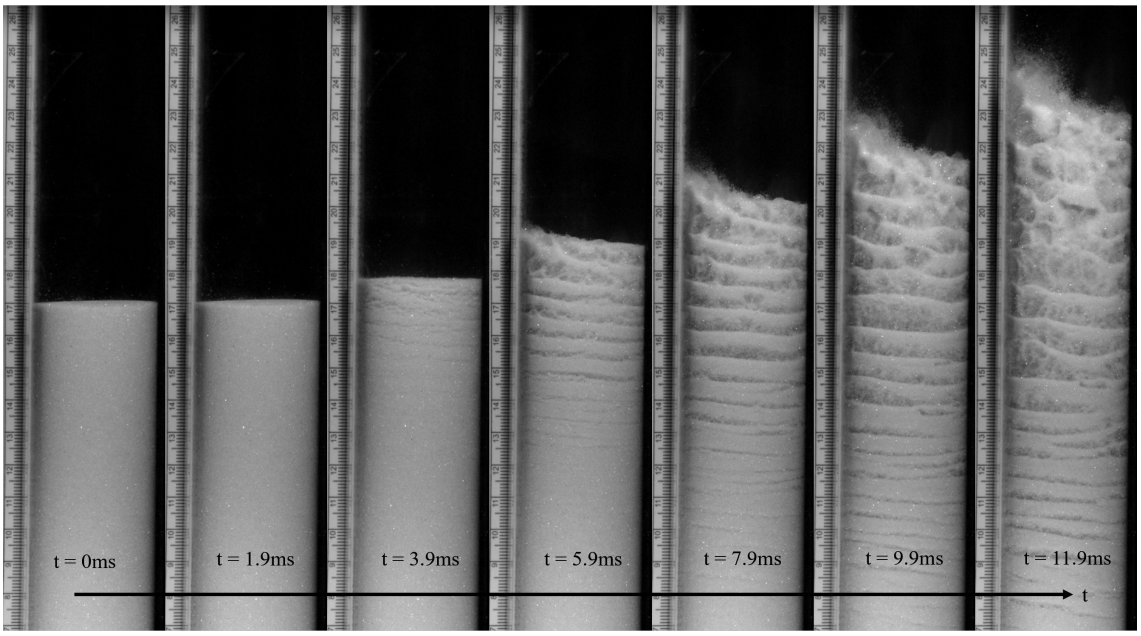

Figure 53: Shown Is a Time Progression of the Particle Bed Expansion with a $z_b = 0.2$m and Particles [150, 212]μm. Similar to the Bed Composed of [44, 90]μm Particles, There Is a Breakdown of the First Few Horizontal Layers Seen Early on at t = 3.9ms. The Horizontal Layers in This Time Progression Are Much More Well-defined and Stable than Those Seen in Figure 52. Though the Interface Somewhat Slants off to the Side, It Still Remains Somewhat Distinct from the Clear Gas Above. These Images are Associated with the Filename 111617_7.

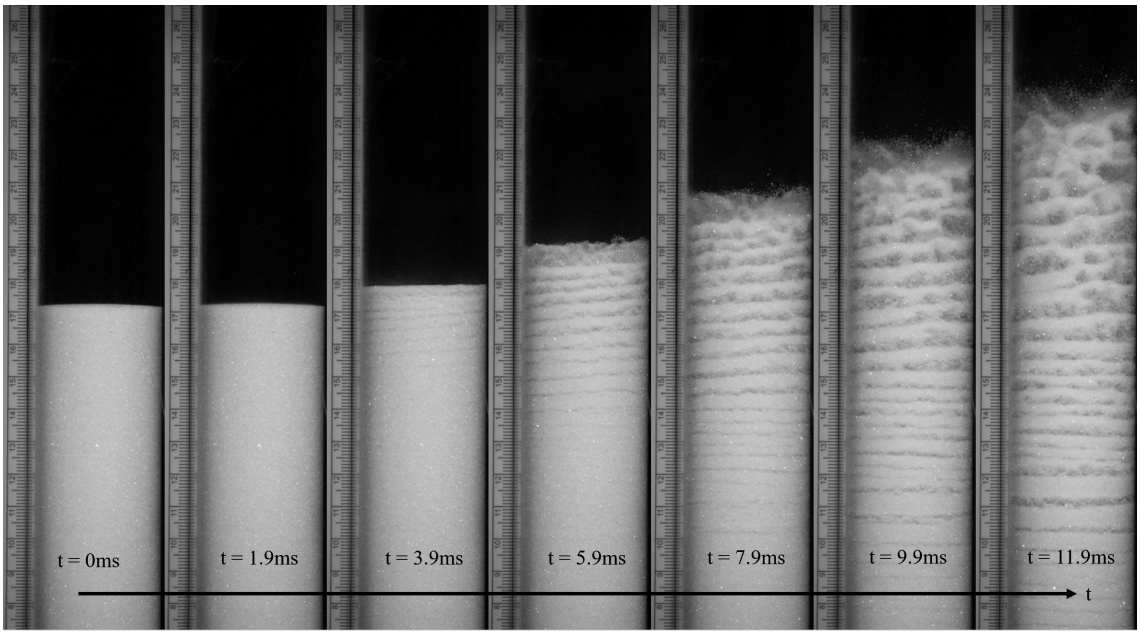

Figure 54: Shown Is a Time Progression of the Particle Bed Expansion with a $z_b = 0.2$m and Particles [212, 297]μm. The Particle Bed Shown Contains the Largest Particles Used Throughout All the Research Presented. The Beds Composed of These Large Particles Breakdown into Stable Horizontal Layers, Which Persist and Remain Well Defined for Approximately 6ms, as Seen in This Progression. These Images are Associated with the Filename 111617_1.

The images shown in Figures 52, 53, and 54, reveal how dynamic, beautiful and complex, this rapid decompression event really is. The imagery is somewhat reminiscent of the photographs NASA's Hubble Space Telescope captures of giant, expanding nebulae in the deep reaches of space—like the Crab Nebula photograph as shown in Figure 55. As time goes on, the particle flow in the glass cylinders becomes less structured and the cellular pattern is diminished as large pockets of gas rapidly rise, disturbing everything in its path.

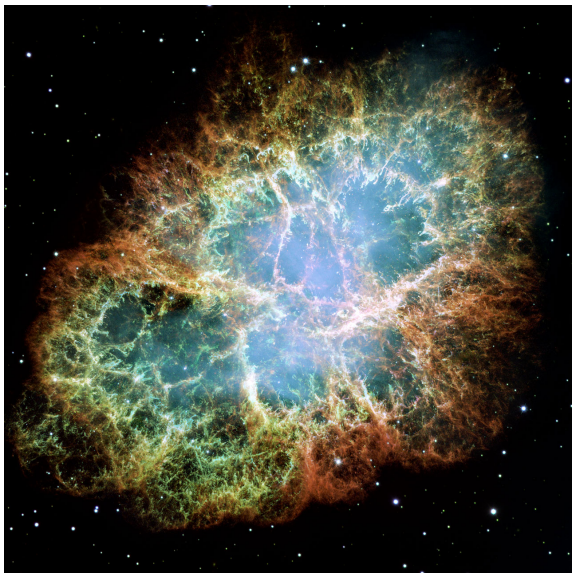

Figure 55: Shown Is an Image Captured by NASA's Hubble Space Telescope of the Crab Nebula. It Is Interesting That the Structures Seen in the Expanding Particle Bed Somewhat Resemble Those Seen in This Image. *This Image Is in the Public Domain under Nas5-26555, but Is Credited to NASA's Hubble Space Telescope Program and STScI.*

Due to the minimal image intensity difference between the void regions and the particle regions, and the imperfect boundaries between the two, it is difficult to track these features from frame to frame automatically. For this reason, a simulated streak image of the high-speed videos was created to examine the evolution of the horizontal void cracks. Shown in Figures 56, 57, and 58, are images of a 0.2m particle bed composed of [44, 90]μm diameter particles, [150, 212]μm diameter particles, [212, 297]μm diameter particles, respectively. Each section has a different average intensity, due to the curved cylindrical glass and the planar array of LED lights used to illuminate the particle bed. The particle bed was sectioned into sixths width-wise, corresponding to about twenty pixels for each section. The intensity for these twenty pixels was then averaged and plotted as a single column in the streak images. Every column in the streak images represents one frame in the high-speed video. The independent axis on the bottom of each streak segment is time, starting at the diaphragm rupture. The inner four of those six sections are shown in each of the figures below.

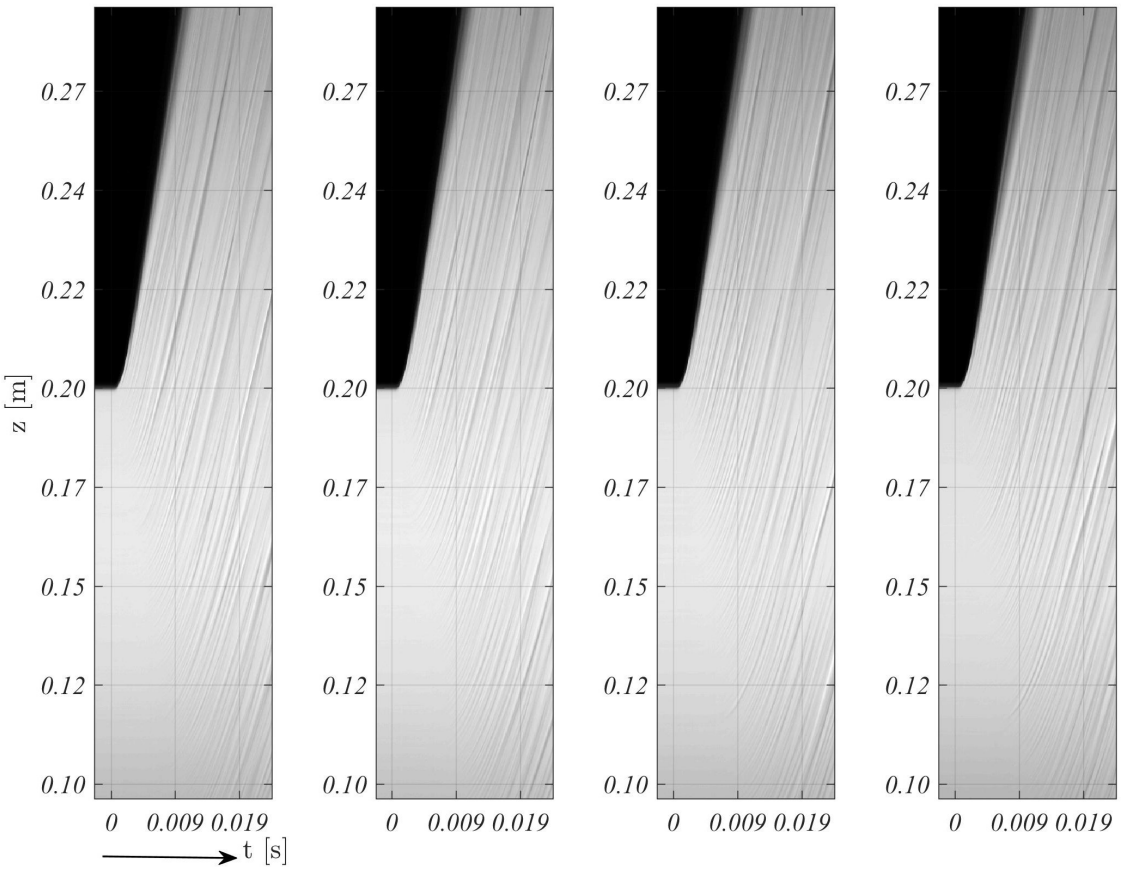

Figure 56: Shown Are Streak Images from a Particle Bed Composed of [44, 90]μm Diameter Particles and an Initial Bed Height of $z_b = 0.2$m. Each Column in the Streak Images Shown Corresponds to a Frame in the High-speed Video Data. The Four Regions Shown Represent Twenty Pixels of the Shocktube, Meaning a Total of Two Thirds of the Entire Width of the Shocktube Is Represented from Left to Right. The Outer Sixth of the Shocktube on Either Side Are Not Shown, as the Intensity Is Not as Bright on the Edges of the Shocktube Due to the Curvature of the Glass.

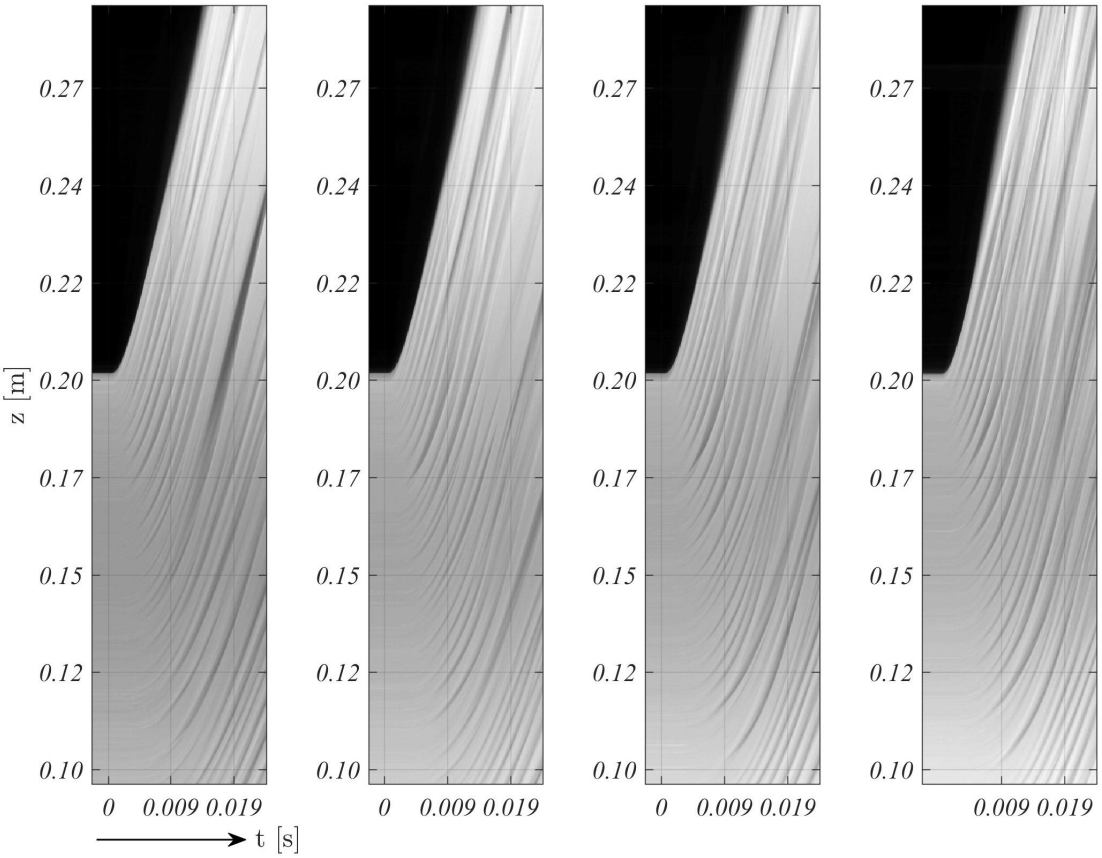

Figure 57: Shown Are Streak Images from a Particle Bed Composed of [150, 212]μm Diameter Particles and an Initial Bed Height of $z_b = 0.2$m. Each Column in the Streak Images Shown Corresponds to a Frame in the High-speed Video Data. The Four Regions Shown Represent Twenty Pixels of the Shocktube, Meaning a Total of Two Thirds of the Entire Width of the Shocktube Is Represented from Left to Right. The Outer Sixth of the Shocktube on Either Side Are Not Shown, as the Intensity Is Not as Bright on the Edges of the Shocktube Due to the Curvature of the Glass.

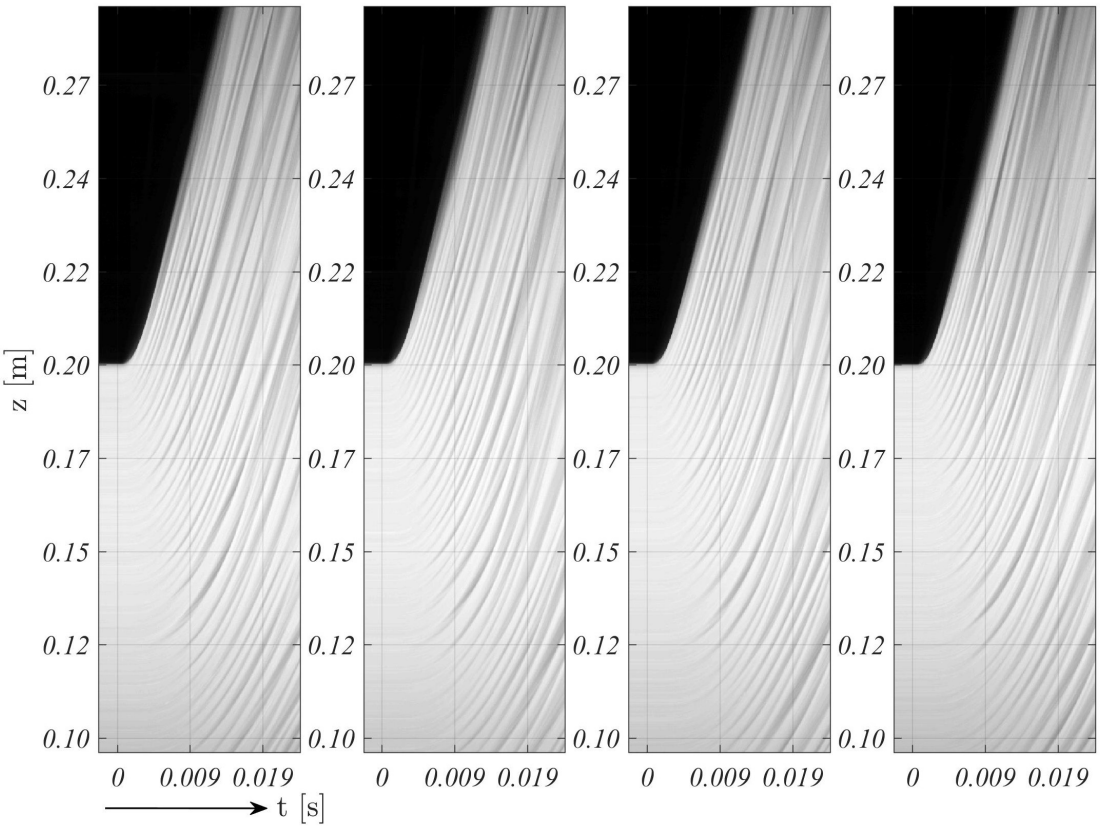

Figure 58: Shown Are Streak Images from a Particle Bed Composed of [212, 297]μm Diameter Particles and an Initial Bed Height of z_b = 0.2m. Each Column in the Streak Images Shown Corresponds to a Frame in the High-speed Video Data. The Four Regions Shown Represent Twenty Pixels of the Shocktube, Meaning a Total of Two Thirds of the Entire Width of the Shocktube Is Represented from Left to Right. The Outer Sixth of the Shocktube on Either Side Are Not Shown, as the Intensity Is Not as Bright on the Edges of the Shocktube Due to the Curvature of the Glass.

There are some important differences between the streak images from beds composed of larger particles and smaller particles. The streaks from the larger-diameter particle bed are much more well-defined than those from the smaller-diameter particle bed. Additionally, the cracks in the beds composed of larger particles appear to be more stable than those composed of smaller particles. The streaks in Figure 56 fade in and out, meaning that the horizontal layers are breaking down into the honeycomb pattern. The streaks shown in Figure 58 persist for a long time. In both cases the

streaks widen in time, although this is much more dramatic in the particle beds composed of the larger diameter particles.

In his research, Ergun noted that particle-vacant regions in some fluidized beds would travel at different rates than the particle bed interface. Figures 59 and 60 are the zoomed in second frames from Figures 56 and 58 showing the [44, 90]μm particles and [212, 297]μm particles, respectively. The lines within the bed created by the streak images and the top of the particle bed seem fairly parallel for the bed composed of the [212, 297]μm particles in Figure 60. Figure 59 showing bed composed of the smaller [44, 90]μm particles has streaks that are close to parallel with the interface, but when examining the streaks near the top of the interface, the interface itself appears to be rising a slightly faster rate than the streaks below.

Another takeway from all of the streak images shown is that the transition from horizontal layers to the breakdown of those layers is very fast for the beds composed of small particles. Note in Figures 56 and 59 that the streaks appear and disappear multiple times during the timeline of the streak images. This is in contrast to the streaks seen in Figures 58 and60, where the same streak can be traced throughout the entire time shown in the streak images. Not only do these streaks persist, but they remain fairly well-defined.

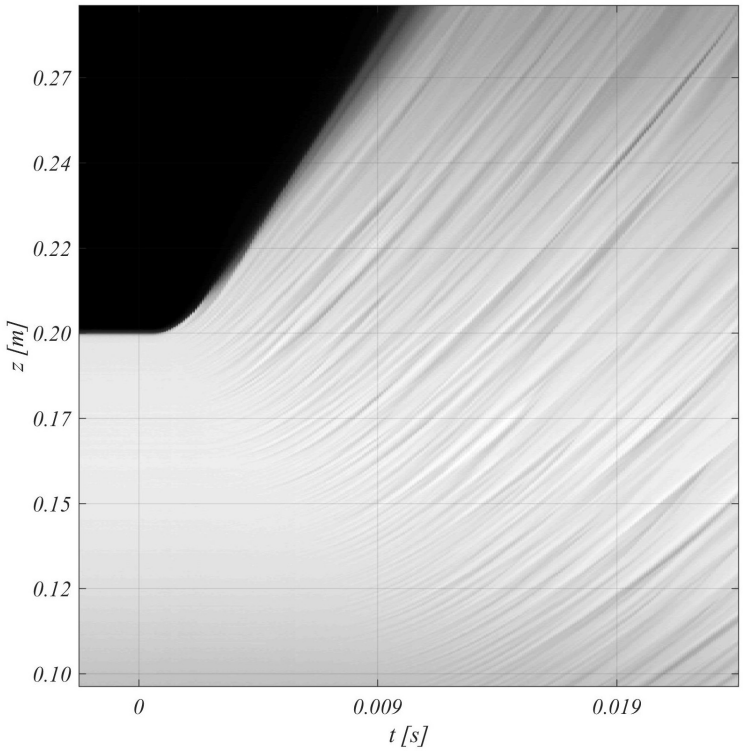

Figure 59: Shown Are Zoomed in Streak Images from the Second Frame Shown in Figure 56, Which Has [44, 90]μm Diameter Particles and a z_b 0.2m. The Slopes of the Streaks Are More Visible in This Zoomed in Image. Note That the Slope of the Streaks Is Slightly Lower than the Slope of the Top Interface. This Is More Clear near the Top of the Particle Bed.

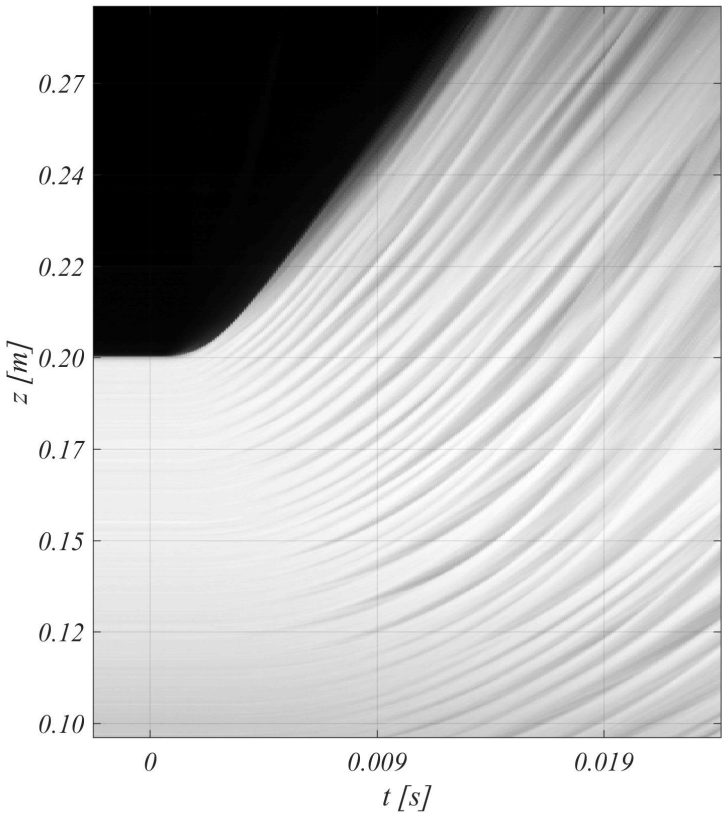

Figure 60: Shown Are Zoomed in Streak Images from the Second Frame Shown in Figure 58, Which Has [212, 297]μm Diameter Particles and a z_b 0.2m. The Slopes of the Streaks Are More Visible in This Zoomed in Image. Note That the Slope of the Streaks Is Nearly Constant and Even with the Top of the Particle Bed Interface. This Means That the Horizontal Layers Travel Upward at Nearly the Same Velocity as the Interface.

6.2 Results

The bulk motion of the particle bed during rapid decompression is very dramatic and complex. Through high-speed imaging, some of the intricacies are revealed. The beds composed of the smaller-diameter particles are on an accelerated timeline as evidenced by the time series of images shown in Figure 52 compared to Figure 54. In the beds composed of smaller particles, the horizontal layers appear rapidly, but then rapidly breakdown into the cellular structure. Soon after the cellular structure breaks down to form a more chaotic and non-uniform pattern. The structures seen in the beds composed of the larger particles are much more stable. These horizontal layers

persist long into the evolution of the particle bed. The horizontal layers break down into roughly similarly-sized and similarly-spaced particle-vacant regions before cellular pattern is significantly stretched and eventually lost.

These findings may relate back to the time constant shown for each particle size in Table 6. The time constant for the larger-diameter particles used is over 45 times that of the smaller-diameter particles. Smaller time constants mean the particles respond more readily to changes in the flow. Additionally, the difference in size ranges between the smallest and largest particles used spread across two different particle groups, as defined by Geldart and discussed in Chapter 1.3. The smaller-diameter particles are classified as Group A, which are described as creating fluidized beds that promote mixing and gas exchange between the "bubbles" and the rest of the particle bed. The figures shown in this chapter tell a very similar story as the horizontal layers and the cells in the beds composed of small-diameter particles are rapidly formed and rapidly break down. The larger particles within the [212, 297]μm size range fall into Group B. These particles are described as not promoting mixing as the bed is fluidized, as there is little gas exchange between the particle-vacant regions and the rest of the bed. Although, Geldart found no evidence of the horizontal layers or "slugs" breaking down into smaller structures, which is different than what was observed in the experiments performed at ASU, many of the findings by Geldart are still relevant to this experiment. It is possible that an adjusted Geldart-type grouping could be made for dense particle beds in a rapid decompression regime.

7 PRESSURE FLUCTUATIONS

7.1 Experimentally Measured Pressure Fluctuations

The dynamic pressure changes that occur in the vertical shock tube experiment are recorded using pressure transducers. Six distinct experiments, each with five realizations, were performed. The varying parameters amongst the six experiments was particle diameter and initial bed height. The particle diameters compared were 44-90μm, 150-212μm, and 212-297μm. The two initial bed heights examined were 0.1m and 0.2m. All experiments in this study were performed with a pressure ratio $\frac{P_4}{P_1} \approx 20$.

The first comparison to be made is between the two different bed heights for a particle bed composed of 44-90μm particles, shown in Figure 61. The most obvious difference between the two experiments is that the expansion wave takes longer to travel to the bottom of the shock tube when the bed is twice as high. Additionally, the expansion wave decompresses the region above the particle bed more rapidly when the bed is taller. For both the pressure measurements shown in this section and the bed rise measurements shown in Chapter 5, the shadow behind each of the ensemble averaged plots is the estimated RMS spread. The RMS for all cases was calculated by dividing the peak-to-peak spread of the data by 2.5 x $\sqrt{n}$, where n is the number of realizations per experiment. In all cases presented, n = 5.

When reviewing the following plots, it may be useful to refer to Figure 32 as a key for which location each pressure trace was recorded. Additionally, the light gray shadowing denotes to experiments with $z_b = 0.1m$ and the dark gray shadowing denotes experiments with $z_b = 0.2m$.

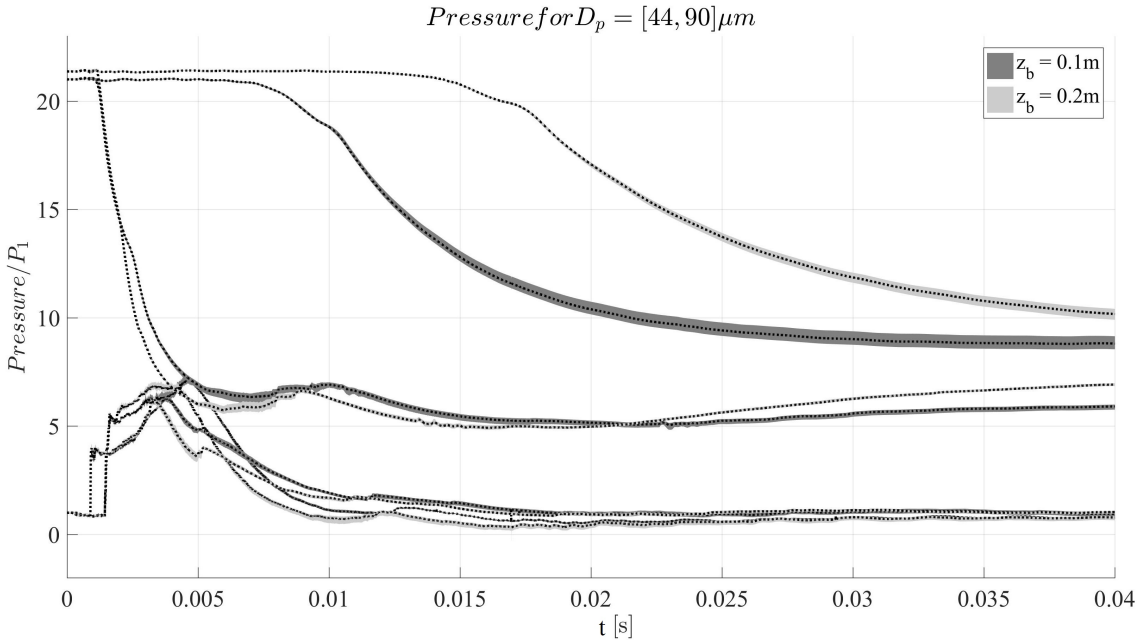

Figure 61: Shown Are the Ensemble Averages of the Pressure Traces from Five Realizations of a Both A 0.1m and 0.2m Bed Composed of [44,90]μm Particles.

Figure 62 shows the comparison between two different bed heights for a particle bed composed of 150-212μm particles. The same dramatic difference between the time the expansion wave hits the bottom of the 0.1m bed vs the 0.2m bed is seen. However, this effect is slightly decreased compared to the separation between the two lines seen in the experiments performed with the 44-90μm particles.

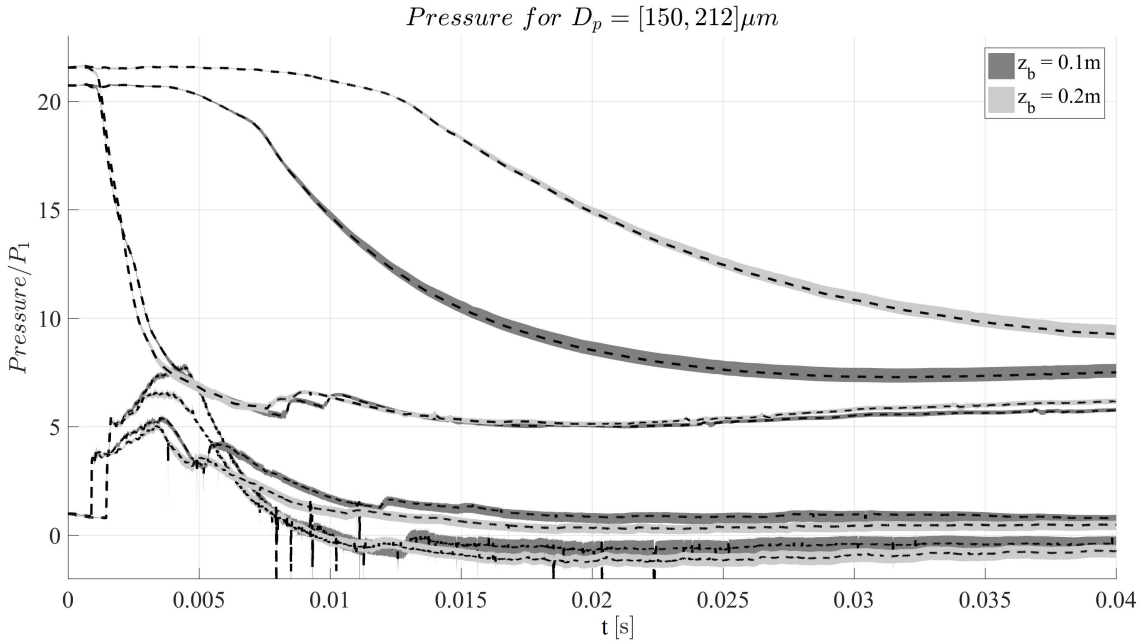

Figure 62: Shown Are Ensemble Averages of the Pressure Traces from Five Realizations of a Both a 0.1m and 0.2m Bed Composed of 150-297μm Particles.

Just as the same features are seen in Figures 61 and 62, they are seen in Figure 63. Again, difference in arrival time of the expansion wave to the bottom of the particle bed is even less dramatic for the largest particle diameter.

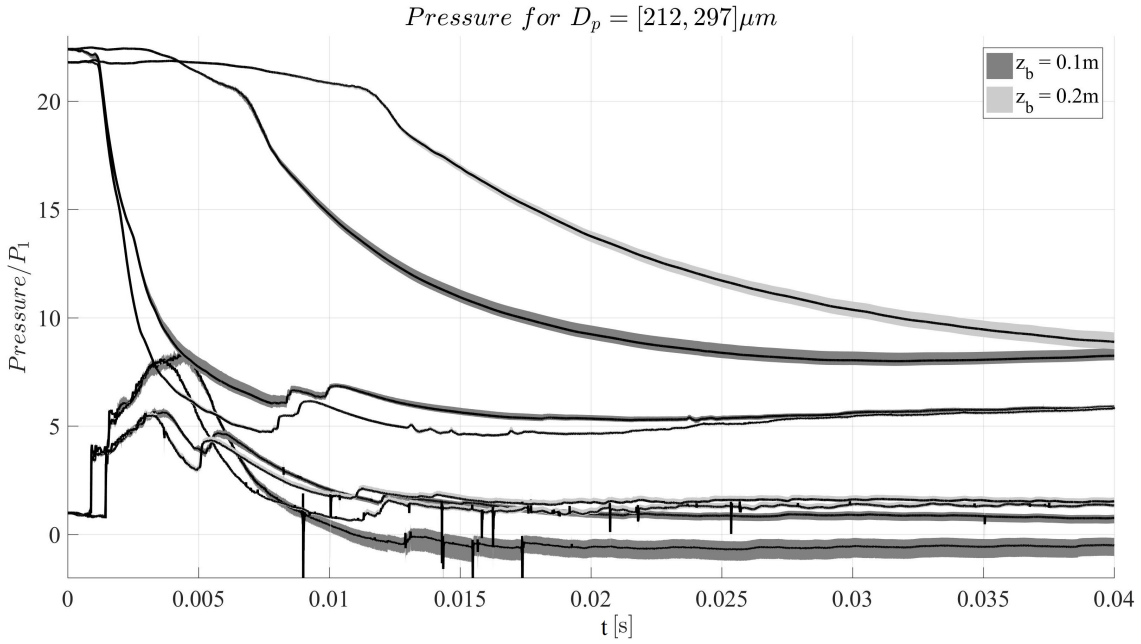

Figure 63: Shown Are Ensemble Averages from the Pressure Traces from Five Realizations of a Both a 0.1m and 0.2m Bed Composed of [44, 90]μm Particles.

Figures 64 and 65 show the effects of changing the particle diameter and keeping the initial bed height fixed. The effect seen is that the expansion wave takes longer to travel through the bed composed of smaller particles than through the bed composed of larger particles. The $\frac{P}{P_1}$ varies in these pressure traces because of the difficulty controlling P_1 during the experiment. To see the comparison mentioned, examine the points where the profiles created from the pressure transducers on Teflon ring P_{67} initially begin to dip.

Note that the effect of the particle diameter is increased when the initial bed height is increased. The separation between the pressure traces in the expansion region is magnified for the 0.2m bed compared to the 0.1m bed.

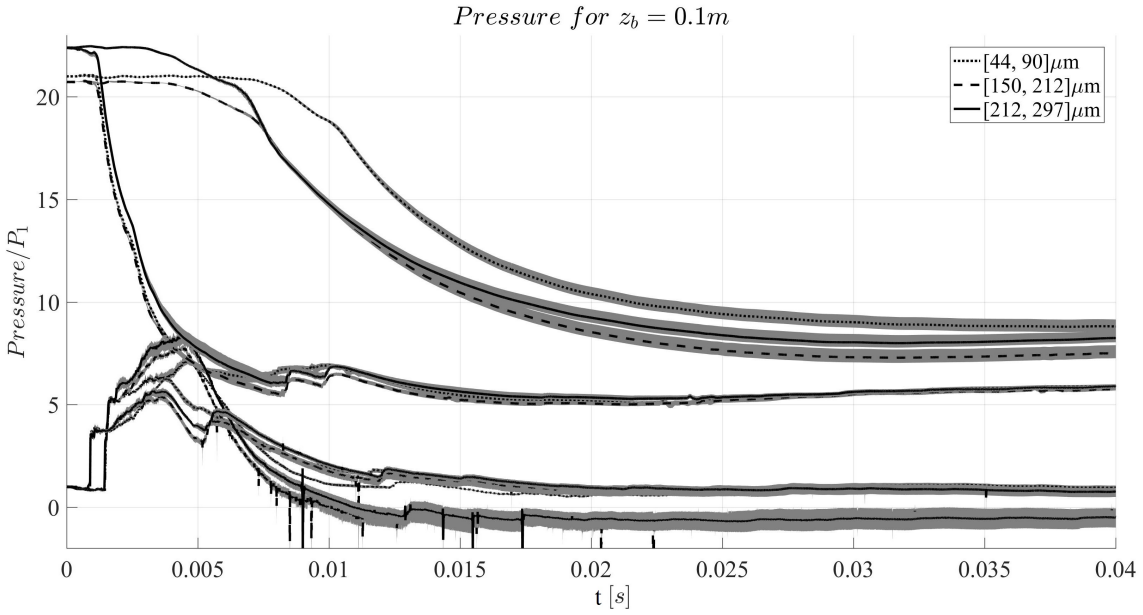

Figure 64: Shown Are Ensemble Averages from the Pressure Traces from Five Realizations of Three Experiments Using All Three Different Particle Sizes. All Initial Bed Heights in This Comparison Were 0.1m.

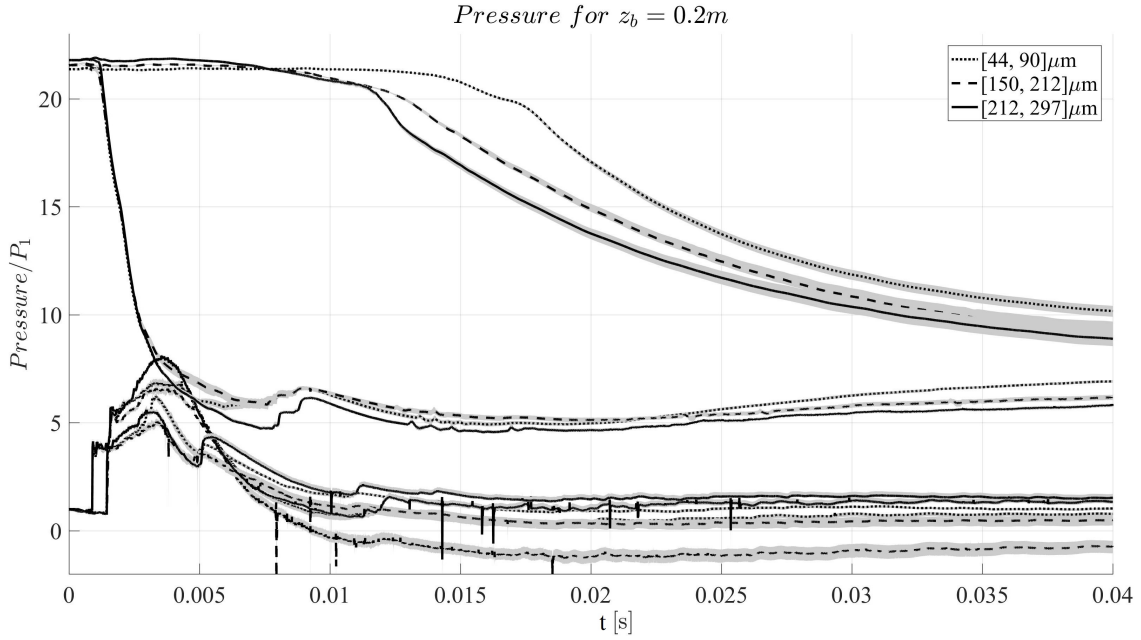

Figure 65: Shown Are Ensemble Averages from the Pressure Traces from Five Realizations of Three Experiments Using All Three Different Particle Sizes. All Initial Bed Heights in This Comparison Were 0.2m.

7.2 Pressure Fluctuations Compared with Simulations

Using Two Phase Euler Foam, a series of comparisons were made between the experimentally measured pressure fluctuations and simulated pressure fluctuations. From the simulated pressure data, artificial pressure transducers were made to sample the pressure at the same locations as the pressure transducers are located on the vertical shocktube. These locations are listed in Table 5. Figures 66—71 show the comparisons between the experimentally measured pressure fluctuations and the simulated pressure fluctuations. Each plot has three lines, shown in black or gray (depending on the initial bed height z_b) are ensemble averages of the experimentally measured pressure fluctuations and the two pressure traces shown in blue are from simulations with beds each composed of the upper limit and lower limit of the particle size ranges in the experimental particle beds.

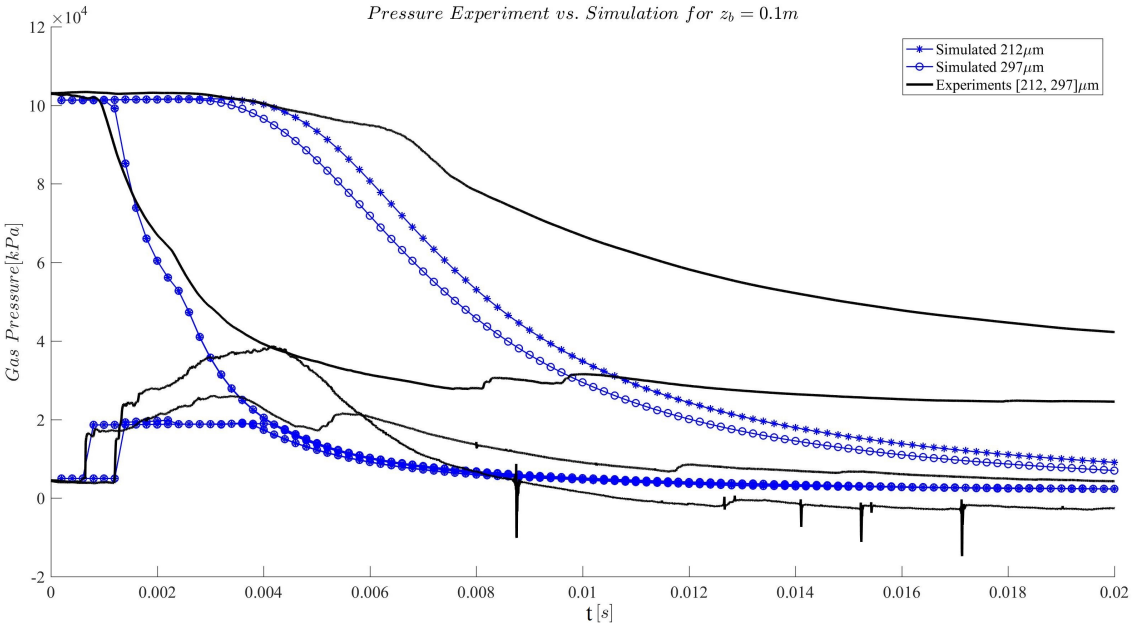

Figure 66: Shown Is a Comparison Between Simulations and the Ensemble Averages of the Experimentally Measured Pressure Fluctuations for Experiments with Particle Beds Composed of $[212, 297]\mu$m Diameter Particles; Both with $z_b = 0.1m$. Shown in Blue Are Two Simulations with Particles Sized 212μm and 297μm.

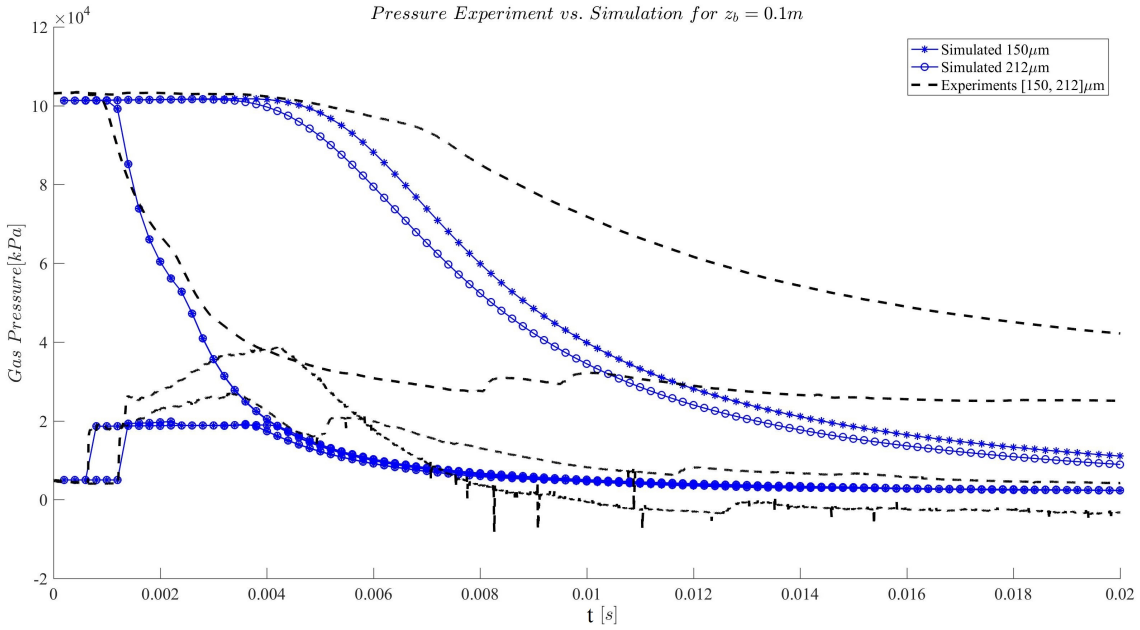

Figure 67: Shown Is a Comparison Between Simulations and the Ensemble Averages of the Experimentally Measured Pressure Fluctuations for Experiments with Particle Beds Composed of $[150, 212]\mu$m Diameter Particles; Both with $z_b = 0.1m$. Shown in Blue Are Two Simulations with Particles Sized 150μm and 212μm.

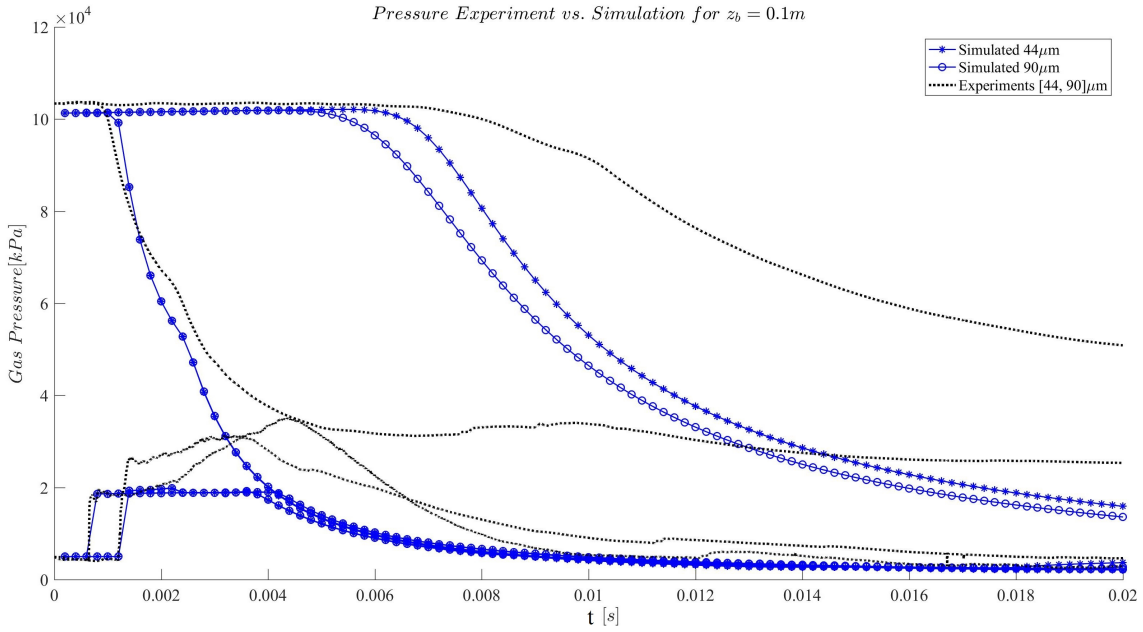

Figure 68: Shown Is a Comparison Between Simulations and the Ensemble Averages of the Experimentally Measured Pressure Fluctuations for Experiments with Particle Beds Composed of $[44, 90]\mu$m Diameter Particles; Both with $z_b = 0.1m$. Shown in Blue Are Two Simulations with Particles Sized 44μm and 90μm.

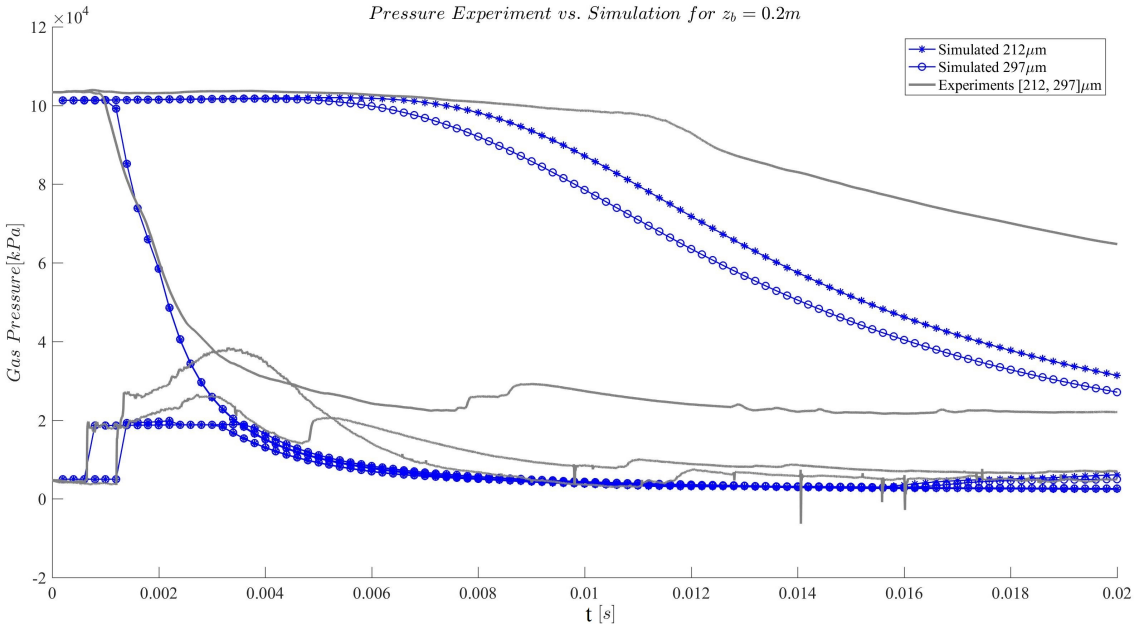

Figure 69: Shown Is a Comparison Between Simulations and the Ensemble Averages of the Experimentally Measured Pressure Fluctuations for Experiments with Particle Beds Composed of $[212, 297]\mu$m Diameter Particles; Both with $z_b = 0.2m$. Shown in Blue Are Two Simulations with Particles Sized 212μm and 297μm.

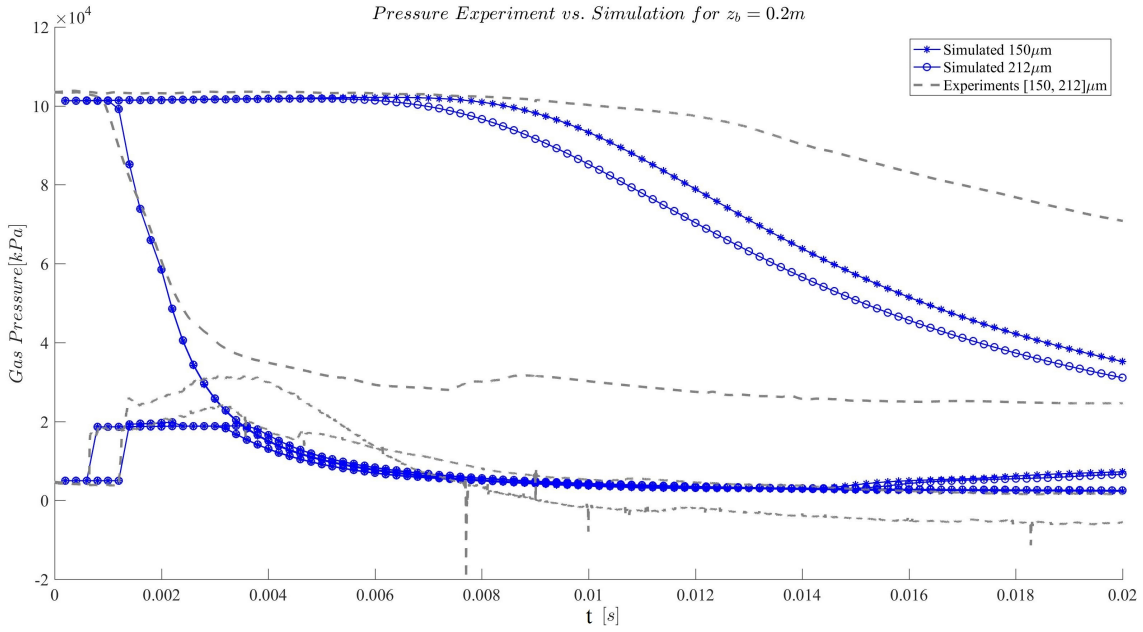

Figure 70: Shown Is a Comparison Between Simulations and the Ensemble Averages of the Experimentally Measured Pressure Fluctuations for Experiments with Particle Beds Composed of $[150, 212]\mu$m Diameter Particles; Both with $z_b = 0.2m$. Shown in Blue Are Two Simulations with Particles Sized 150μm and 212μm.

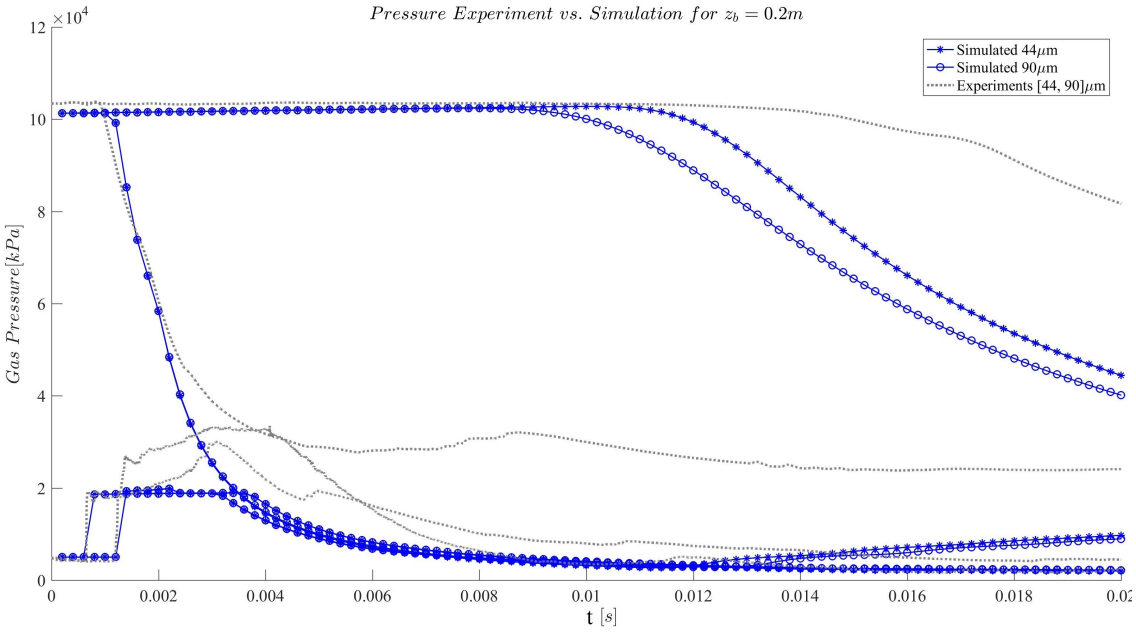

Figure 71: Shown Is a Comparison Between Simulations and the Ensemble Averages of the Experimentally Measured Pressure Fluctuations for Experiments with Particle Beds Composed of $[44, 90]\mu$m Diameter Particles; Both with $z_b = 0.2m$. Shown in Blue Are Two Simulations with Particles Sized 44μm and 90μm.

Performing the simulations shown in Figures 66—71 helped elucidate the relaxation nature of the pressure transducers. Notice in each plot the timing associated with the significant events (pressure drop seen at P_{45} and P_{67} as well as the shocks seen at P_{123} and P_0) between the simulation and the experiments match very well. However, the experimental pressure traces begin to deviate from the simulated pressure traces once the rate of change in the pressure decreases—for example, just after the pressure drop is seen on P_{67}. The pressure transducers are very accurate for measuring high-frequency pressure changes, but they have a relaxation behavior that makes them less accurate for measuring pressure changes occurring at lower frequencies. From looking at experimental data alone, it was unclear when the pressure transducers' relaxation behavior began to affect the analog voltage output. Because the simulated pressure traces match the magnitudes and timings of the beginning of all significant events associated with the expansion and shock during experiments during the high-frequency changes (when the pressure transducers are the most accurate), it is

reasonable to attribute some of the discrepancy between the simulations and experiments during low-frequency pressure fluctuations to the relaxation behavior of the pressure transducers; the trace of the ground truth pressure fluctuations most likely lies in between the experimental and simulated traces.

Figures 66—71 show the higher expansion wave velocity associated with larger particle diameter, as seen in Figures 65 and 64. The separation between the pressure traces of simulations with particles in the size range $[44, 90]\mu$m appears to be greater than the separation between the pressure traces in the other size ranges, even though the actual difference between 44μm and 90μm is less than the difference between the bounds of the other two size ranges.

To test whether the varied expansion wave velocity associated with varied particle size could simply be attributed to varied solid volume fraction, simulations were performed using the exact same solid volume fraction of 60% for 0.1m and 0.2m beds composed of all three particle size ranges. The results are plotted in Figure 72. If the varied solid volume fraction associated with varied particle diameter (discussed previously in Chapter 5.2), was the sole reason the variations in expansion wave velocity occur, then the simulated pressure traces for each bed height should lie directly on top of one another.

Also elucidated by the simulations is the moderate reflection of the expansion wave on the gas-particle interface. Though the experiments show a more dramatic reflection occurring seen approximately 2.5ms after the diaphragm rupture, a mild reflection is still seen in the simulations as well. Characterizing the reflection more, based on bed height may be a topic for future research. As it is seen in Figure 65, the reflection does not appear to be dependent on particle diameter.

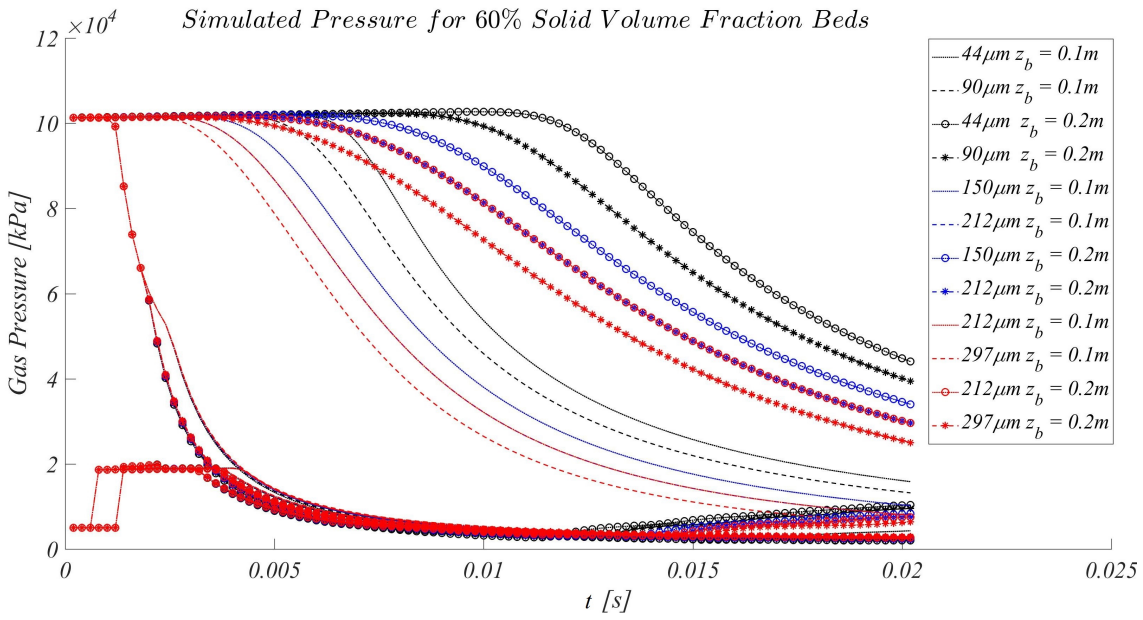

Figure 72: Shown Are the Simulated Pressure Traces for Eight Simulations with Different Particle Diameters. The Solid Volume Fraction ϕ_p Was Set to 60% for All Runs to Test Whether Varied Solid Volume Fraction Was the Sole Cause of Varied Expansion Wave Velocity. The Simulated Pressure Traces in This Figure Show That the Expansion Wave Velocity Does Not Exclusively Depend on Solid Volume Fraction.

Figure 72 shows that the expansion wave velocity is not exclusively dependent on the solid volume fraction ϕ_p, but is also dependent on the actual particle diameter D_p. As expected, in all cases the expansion wave travels more slowly through taller beds. Additionally, the effect the height of the particle bed has on the expansion wave velocity is magnified for beds composed of smaller-diameter particles.

7.3 Results

The expansion waves takes longer to travel through a taller bed, as a taller bed impedes the gas expansion for a longer period of time. Also, the pressure above the particle bed interface drops more rapidly when the interface is closer to the diaphragm (i.e. the initial bed height is taller). As for the comparisons between the different particle sizes, the expansion wave travels more slowly through beds composed of smaller particles. The smaller the particles, the smaller the interstices between the particle and the open channels allowing the gas to move freely. This magnifies the effect

a taller bed has on expansion wave velocity.

8 GAS MEASUREMENTS *VIA* PIV

The expanding interstitial gas is the driving force for the bed expansion. The gases expand within the interstices of the particle bed and also escape out of the gas-particle bed interface. Particle Image Velocimetry is an optical velocity measurement technique that is well-suited to measure the velocity of the gases escaping the bed. The fourth and final experimental configuration was designed for making these measurements. The region of interest was just above the bed after the expansion wave impinged on the gas-particle bed interface.

8.1 PIV Setup

The forth experimental configuration was designed to take PIV measurements of the gas velocities. The setup was very similar to the standard configuration, except a TSI PowerView 11MP PIV camera was used in place of the Vision Research v641 high-speed camera. Also, one of the pressure transducers at z_2 was removed. In place of the pressure transducer Ai5 at z_2, a hose connected to a Laskin nozzle was inserted to seed the driving gas with small-diameter oil droplets. Once the seeding density was adequate, the hose was removed and the port was sealed prior to rupturing the diaphragm. The oil droplets have an estimated diameter of less than 1μm, and therefore traced out the gas velocities very well. Table 6 lists a few of the characteristics of the oil droplets. Figure 73 is a photograph with overlaid annotations depicting the PIV experimental setup.

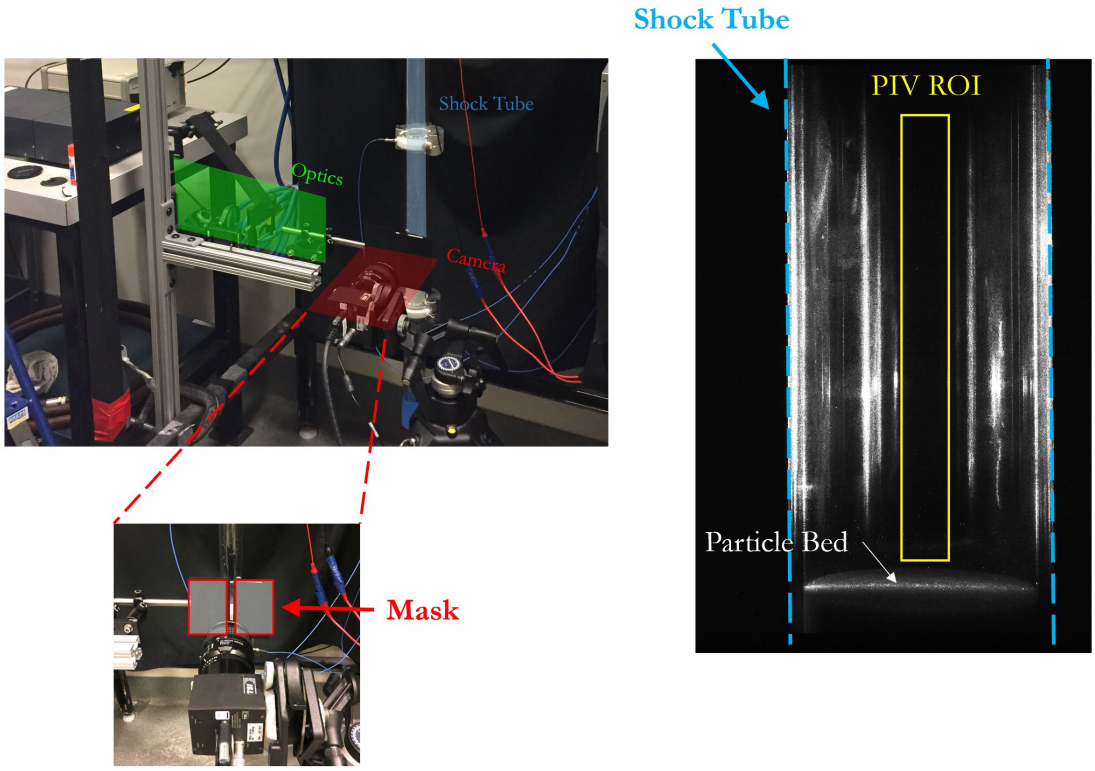

Figure 73: Shown Is the Forth Shocktube Configuration, a PIV Setup. The Optics Creating a Vertical Laser Light Sheet Are Shown on the Green Plane, the Shocktube Is Shown in the Light Blue Plane, and the Imaging System Is Shown in the Red Plane. Note the Region of Interest (ROI) Depicted in the Right-most Image. This Region Has the Fewest Reflections, Which Were Blocked out Using the Masking System Shown in the Bottom-most Image, and Reduced Optical Distortions Relating to the Curvature of the Glass Cylinder. The Laser Light Sheet Travels Through the Center of the Shocktube and Can Be Seen Hitting the Bed in the Right-most Image.

Figure 73 shows a vertical laser light sheet oriented to illuminate the center of the vertical shock tube. Due to the cylindrical shape of the shocktube and the thickness of the laser light sheet (2mm), there were several bright reflections along the sidewalls of the shocktube. To remove the reflections from the PIV images, a mask was emplaced, blocking the reflections from the camera view. A plane in the center of the shocktube was the region of interest or ROI for these PIV experiments. Taking optical data from the center of the shocktube allows for reduced optical distortions associated with the cylindrical shape of the shocktube, therefore reducing overall error in the gas velocity measurements.

Several parameters were varied for the PIV campaign, including bed height and expansion

penetration depth. See Figure 74 for a visual description of those parameters where each vertex is an experiment. Note that some of the vertices are blocked out. This is because the condensation cloud occludes the measurement region for the experiments with a taller bed in later times.

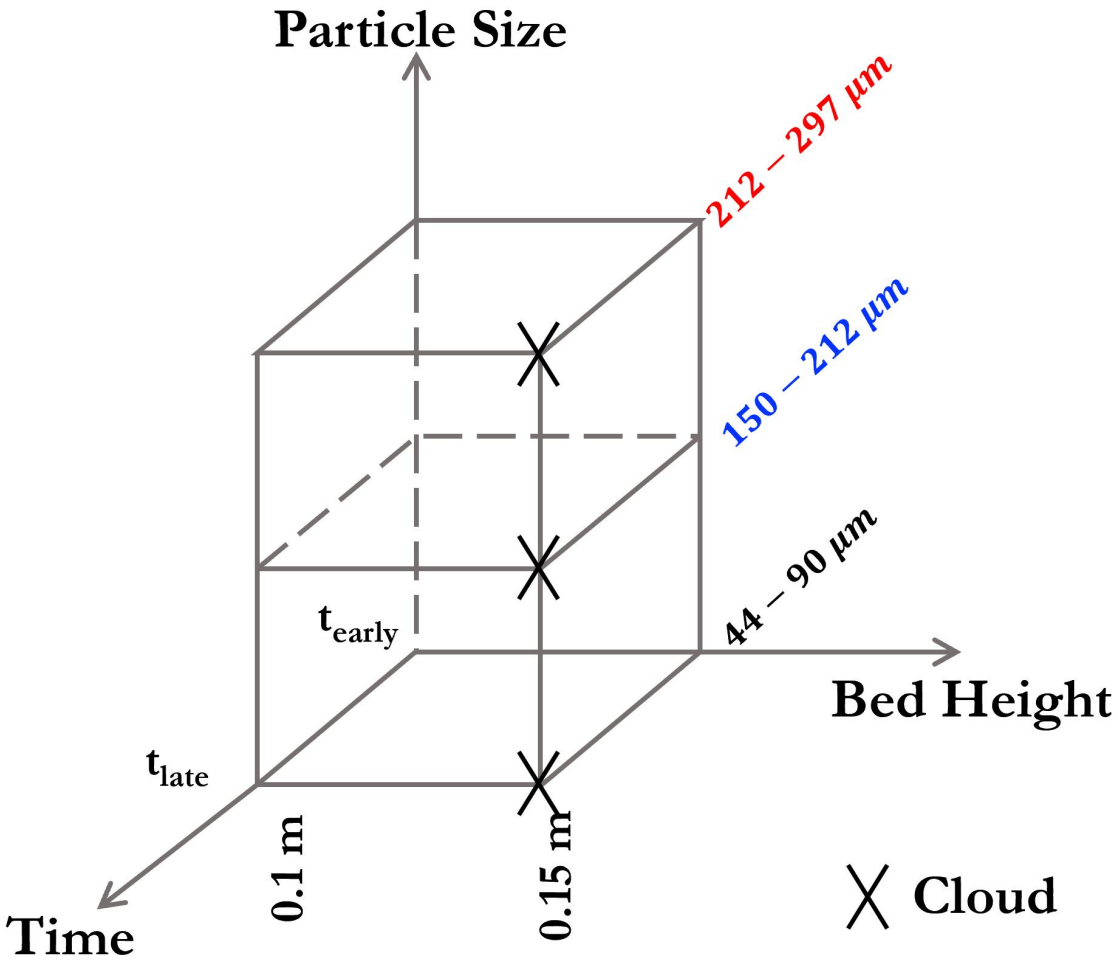

Figure 74: Shown Is a Graphical Description of the Parameters Varied During the PIV Campaign.

The data acquisition times needed to be matched with the bed impingement time to make more meaningful comparisons between experiments of varying bed heights. Two times were chosen, t_{early} and t_{late}. At t_{early}, the expansion wave has just impinged on the particle bed surface. t_{late} is one millisecond after t_{early}, when the expansion wave has propagated approximately 40mm to 90mm into the particle bed, depending on the particle diameter. These penetration depth estimates

were determined from simulations using Two Phase Euler Foam. While performing experiments, it was determined that the comparison between a 0.1m initial bed height and a 0.2m initial bed height could not be made for the gas velocities due to the triggering constraints associated with the PIV system and the condensation cloud. The triggering system could not send out a signal quickly enough to initialize the data acquisition for a 0.2m bed. As such, the comparison would have to be made between a 0.1m bed and a 0.15m bed. While the timing to trigger these experiments was achievable, the condensation cloud made optical measurements in this region at later times impossible. As noted previously, the pressure drop associated with taller beds is more dramatic than for shorter beds. In turn, this likely means the temperature drop is also more dramatic for taller beds, and the condensation cloud appears earlier compared to the shorter beds. The cloud completely blocks the measurement plane from view of the camera as seen in Figure 75. Also shown in the same figure, is a very late time image showing the rising particle bed blocking the field of view, which is the source of another experimental constraint.

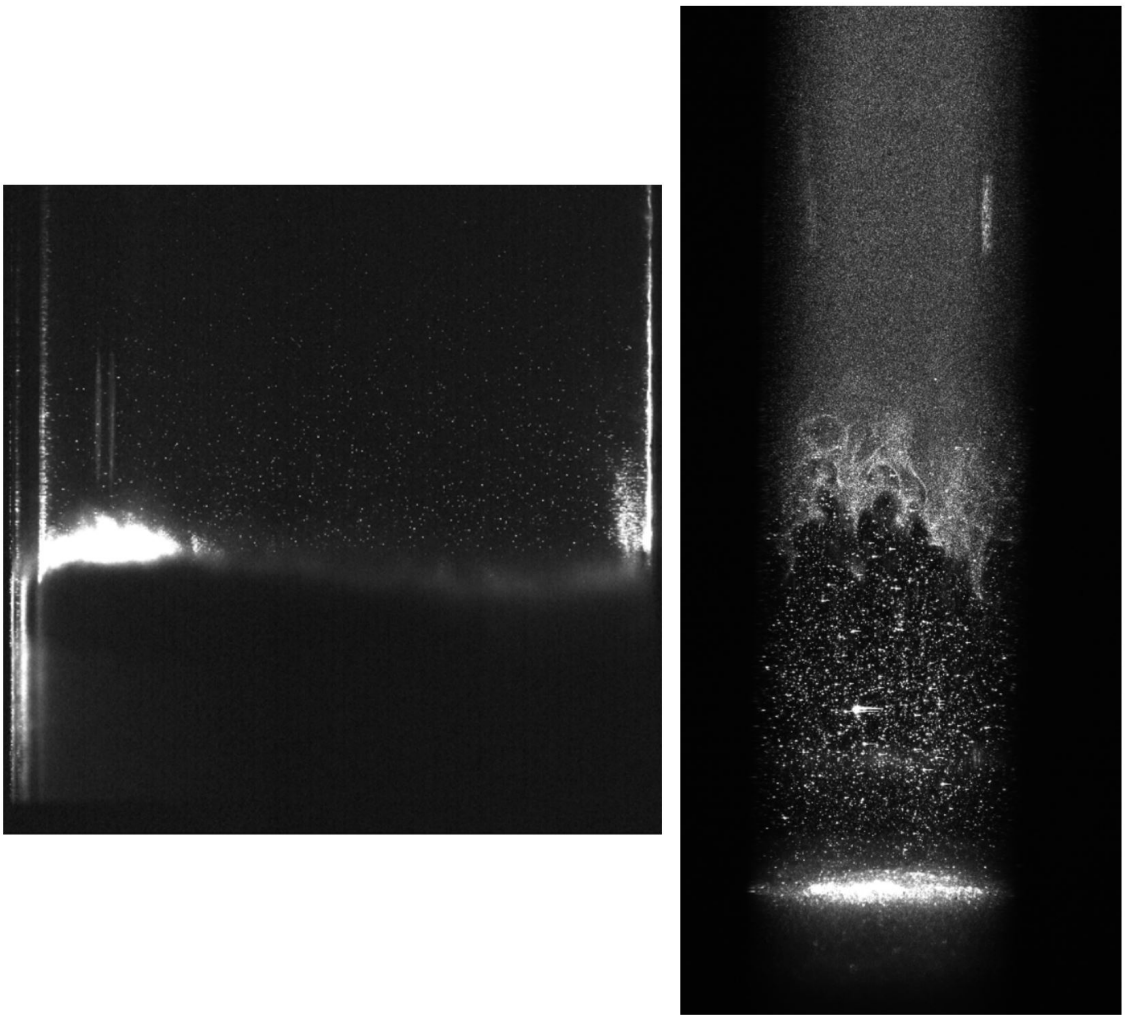

Figure 75: Shown Are Two Images Depicting Some of the Difficulties with Measurement Access Associated with the PIV Experiments. The Image on the Left Shows the Rising Particle Bed Blocking the Laser Light Sheet and the Field of View from the Camera. The Image on the Right Shows the Condensation Cloud Blocking the Measurement Region. This Image Is Also Very Interesting, Because the Effects of the Gas Jetting out of the Particle Bed and Deforming the Cloud Front Are Visible.

8.2 Experimental PIV Measurements

Figure 76 shows a comparison of the gas velocity measurements at early and later times measured above beds composed of varying particle diameters and initial bed heights. An additional constraint of the Particle Image Velocimetry experiments is related to the oil droplet seeding. Only

the gas above the particle bed is seeded, meaning when the gases within the particle bed interstices (which are not seeded) begin to escape, the oil droplets are pushed away from the surface of the particle bed and replaced with unseeded gases. Because only velocities from seeded gases are measurable with the PIV setup, it was not possible to measure the gas velocities right at the surface of the particle bed. Measurements begin approximately 10mm above the particle bed. However, because the velocities were measured to follow a linear trend, a linear extrapolation was used to determined the predicted velocity of the gases right at the particle bed interface. These extrapolated data points are shown at $z - z_b = 0$. The dependent axes in Figure 76 is the ensemble averaged velocity ω along the axial coordinate z minus the extrapolated velocity at $z - z_b = 0$, denoted as ω_0.

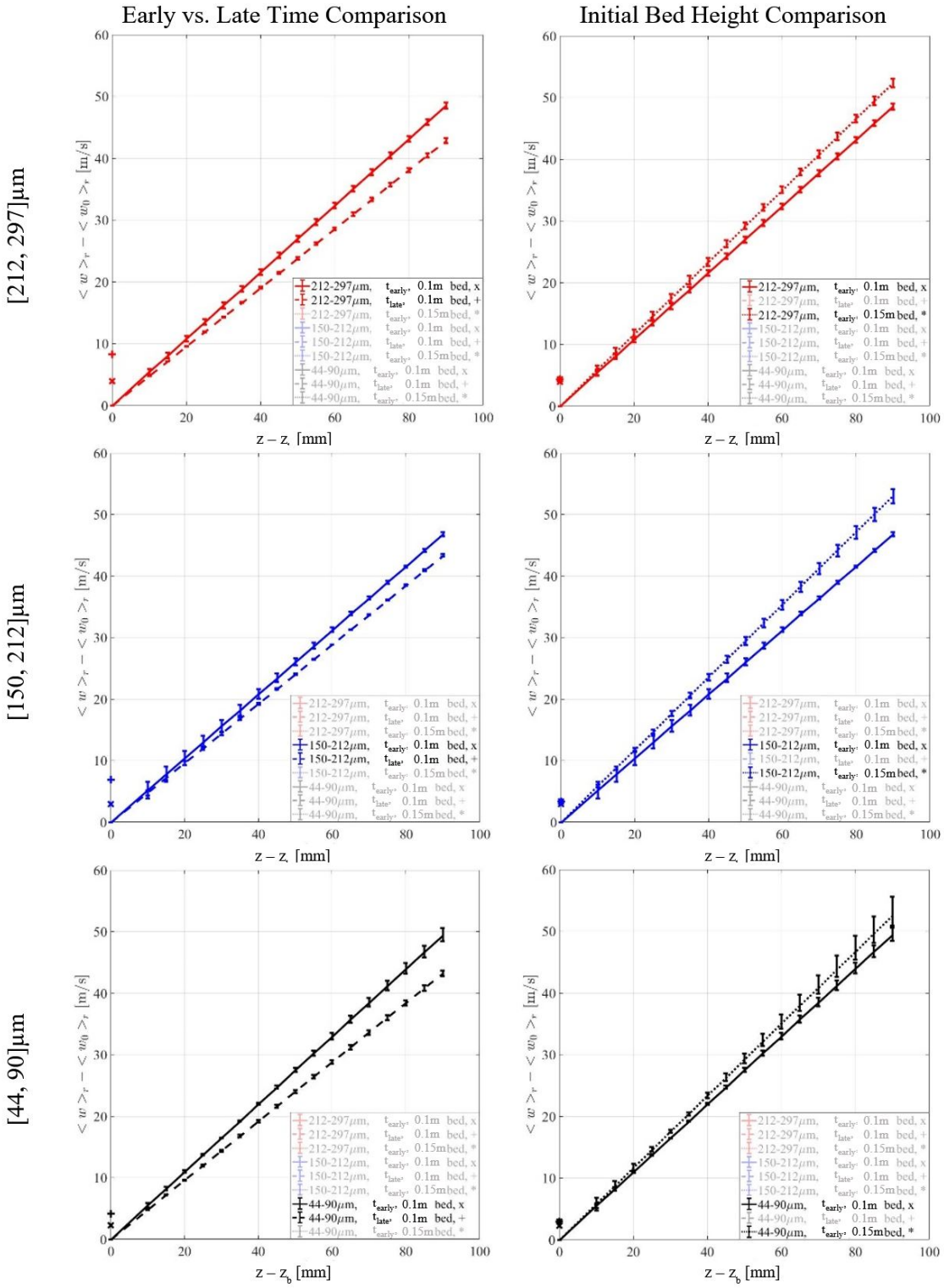

Figure 76: PIV Gas Velocity Data. Each Plot Shown Is an Ensemble Average of Three Independent Realizations.

Note in beds composed of all particle sizes used, the overall gas velocity is higher for later times (shown by the extrapolated velocity value ω_0 plotted at $z - z_0 = 0$, but the slope of the gas velocity at later times is lower. The slope of the gas velocity along z is a measure of the gas dilation or expansion due to the reduced pressure. At earlier times, the gas dilation is stronger. However, the gas has had less time to accelerate in earlier times—making the overall velocities lower. To show each of these data plots in more detail, the individual gas velocity comparisons between early times and later times for each particle size are shown in Figure 77—Figure 79 and the gas velocity comparisons as measured above a the 0.1m bed and above a 0.15m bed are shown in Figure 80—Figure 82.

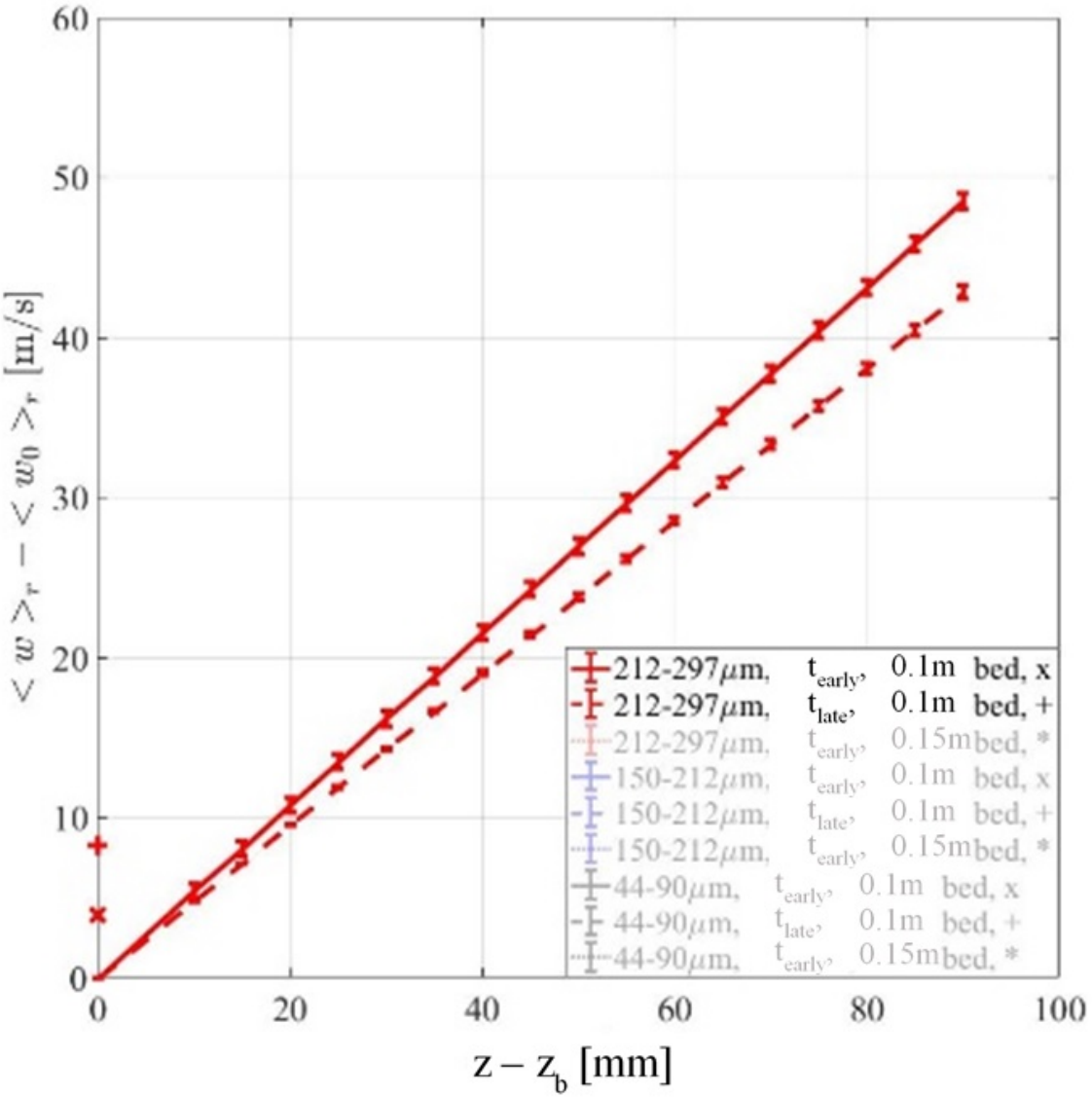

Figure 77: Shown Are Plots of PIV Gas Velocity Data as Measured above a 0.1m Bed Composed of Particles with Diameters Ranging [212, 297]μm at Early and Late Times. Each Plot Is an Ensemble Average of Three Independent Realizations..

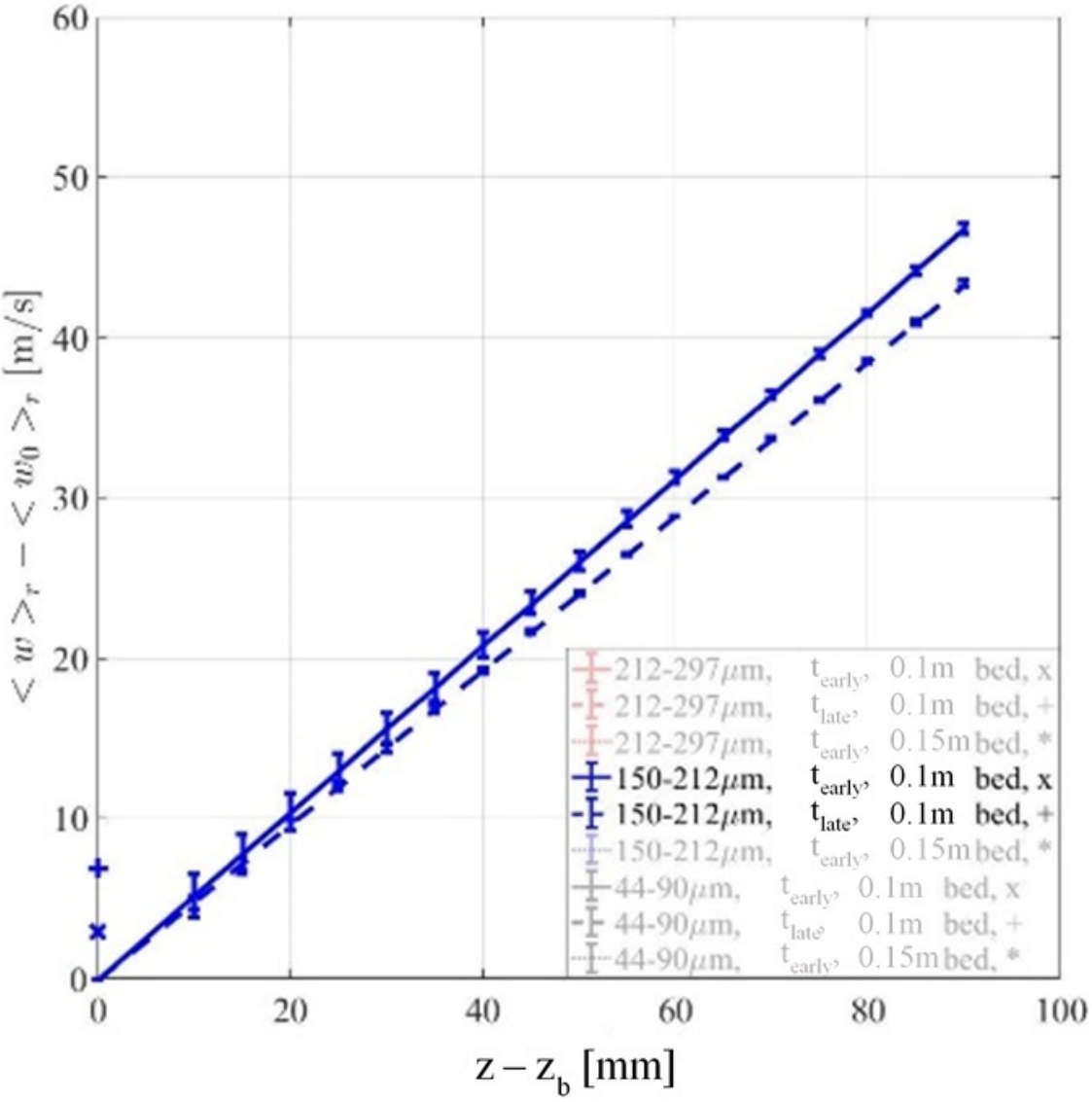

Figure 78: Shown Are Plots of PIV Gas Velocity Data as Measured above a 0.1m Bed Composed of Particles with Diameters Ranging [150, 212]μm at Early and Late Times. Each Plot Is an Ensemble Average of Three Independent Realizations.

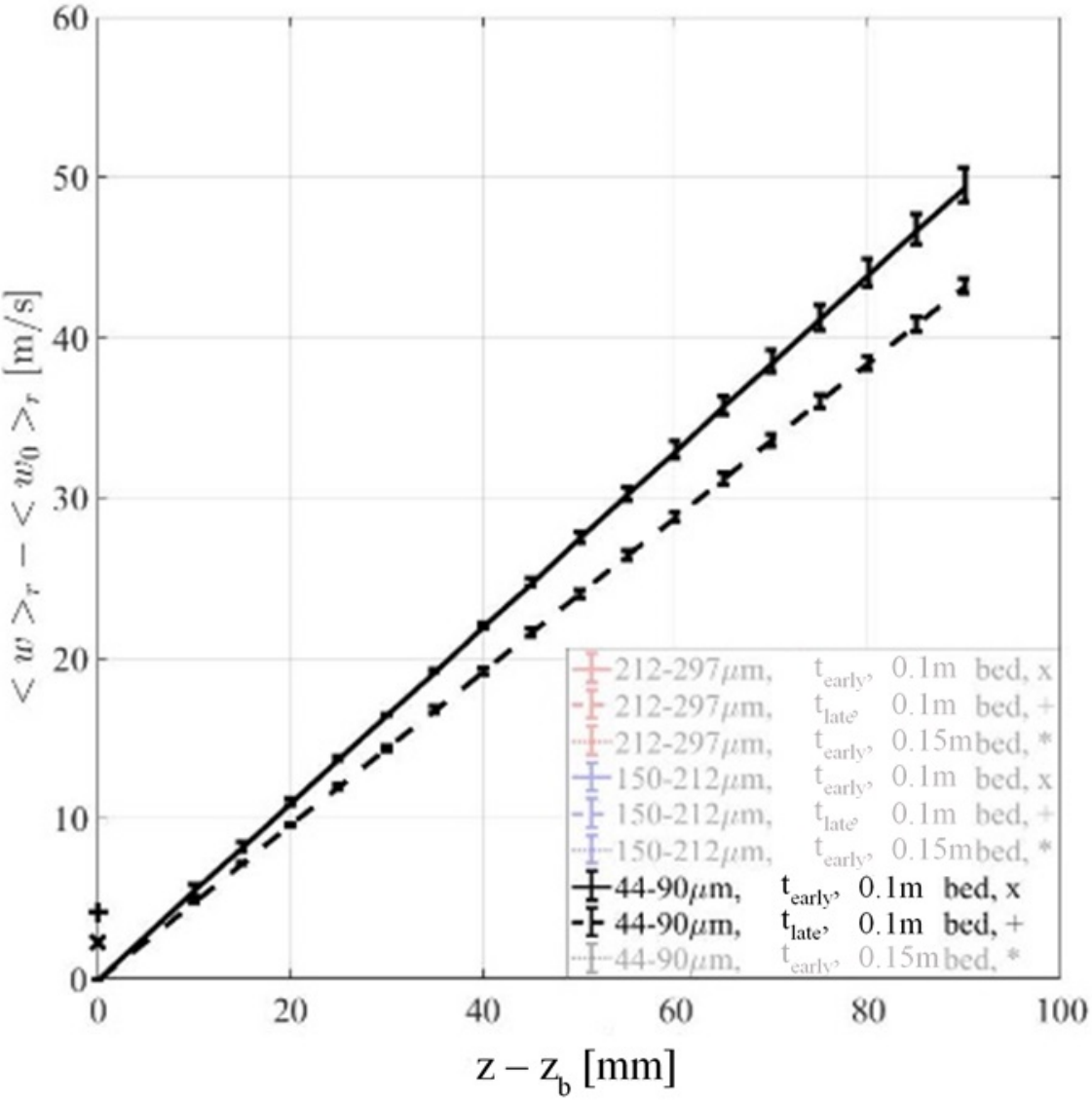

Figure 79: Shown Are Plots of PIV Gas Velocity Data as Measured above a 0.1m Bed Composed of Particles with Diameters Ranging [44, 90]μm at Early and Late Times. Each Plot Is an Ensemble Average of Three Independent Realizations.

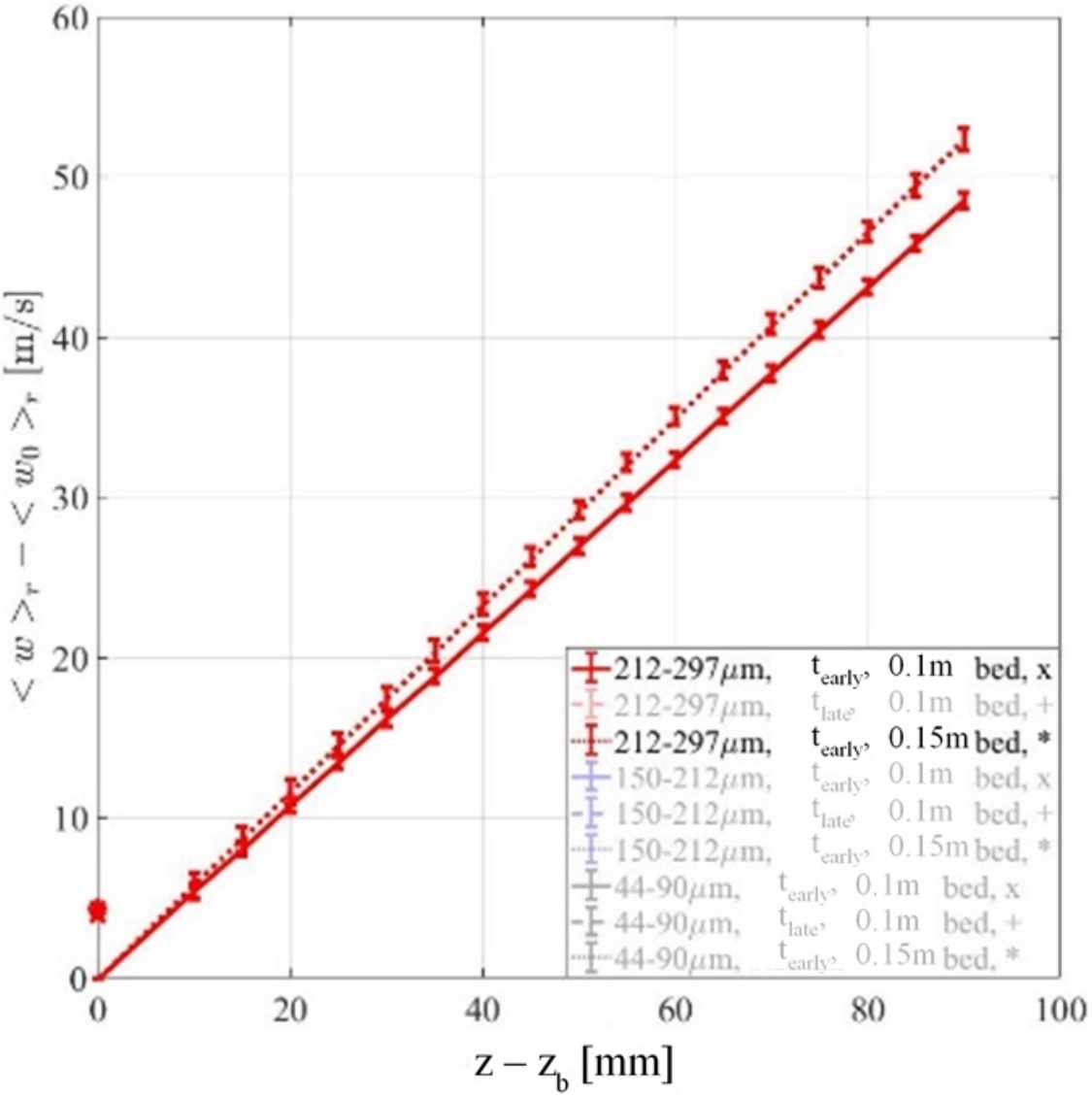

Figure 80: Shown Are Plots of PIV Gas Velocity Data as Measured above a 0.1m Beds and 0.15m Beds Composed of Particles with Diameters Ranging [212, 297]μm at Early Times. Each Plot Is an Ensemble Average of Three Independent Realizations.

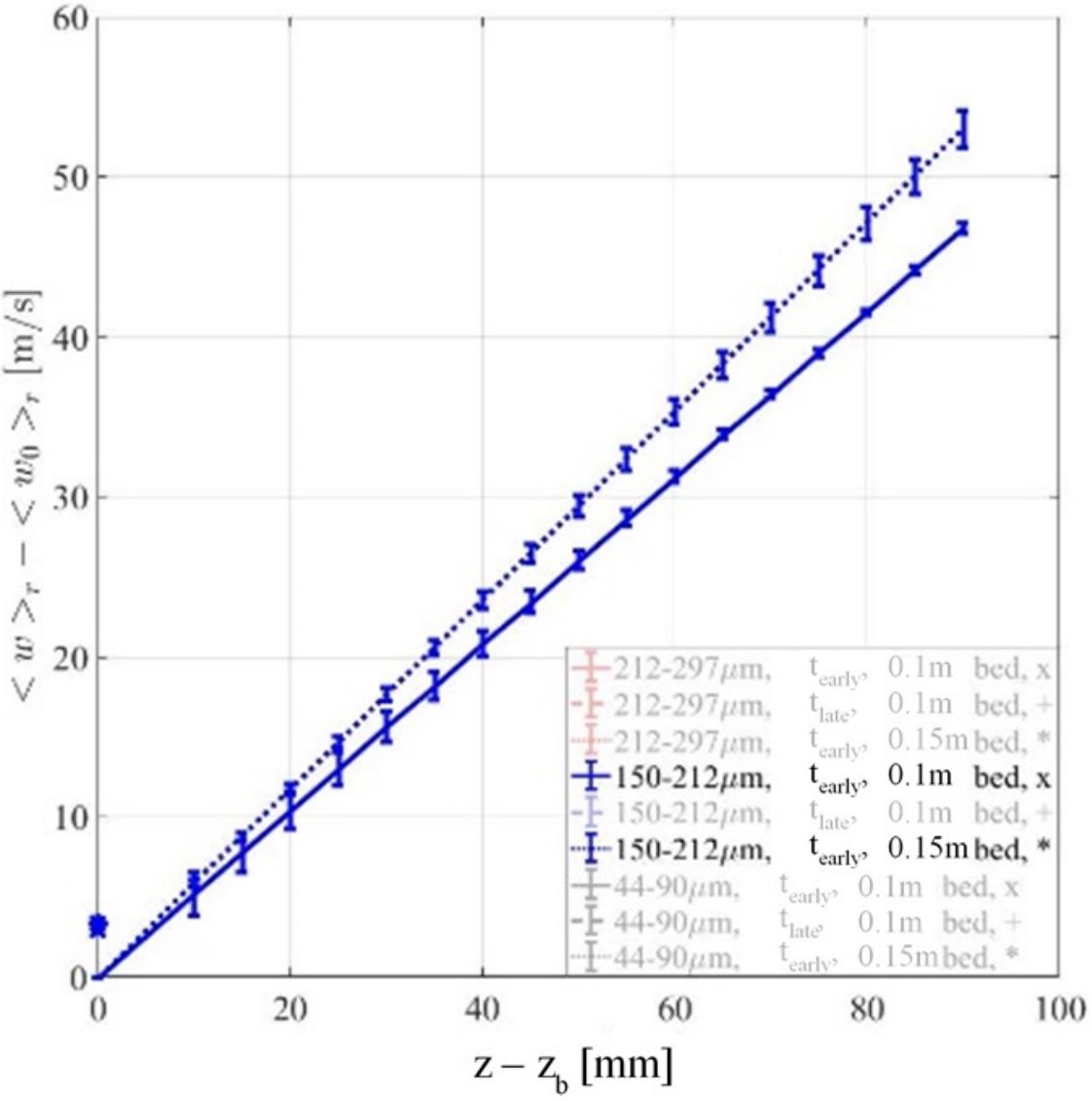

Figure 81: Shown Are Plots of PIV Gas Velocity Data as Measured above A 0.1m Beds and 0.15m Beds Composed of Particles with Diameters Ranging [150, 212]μm at Early Times. Each Plot Is an Ensemble Average of Three Independent Realizations.

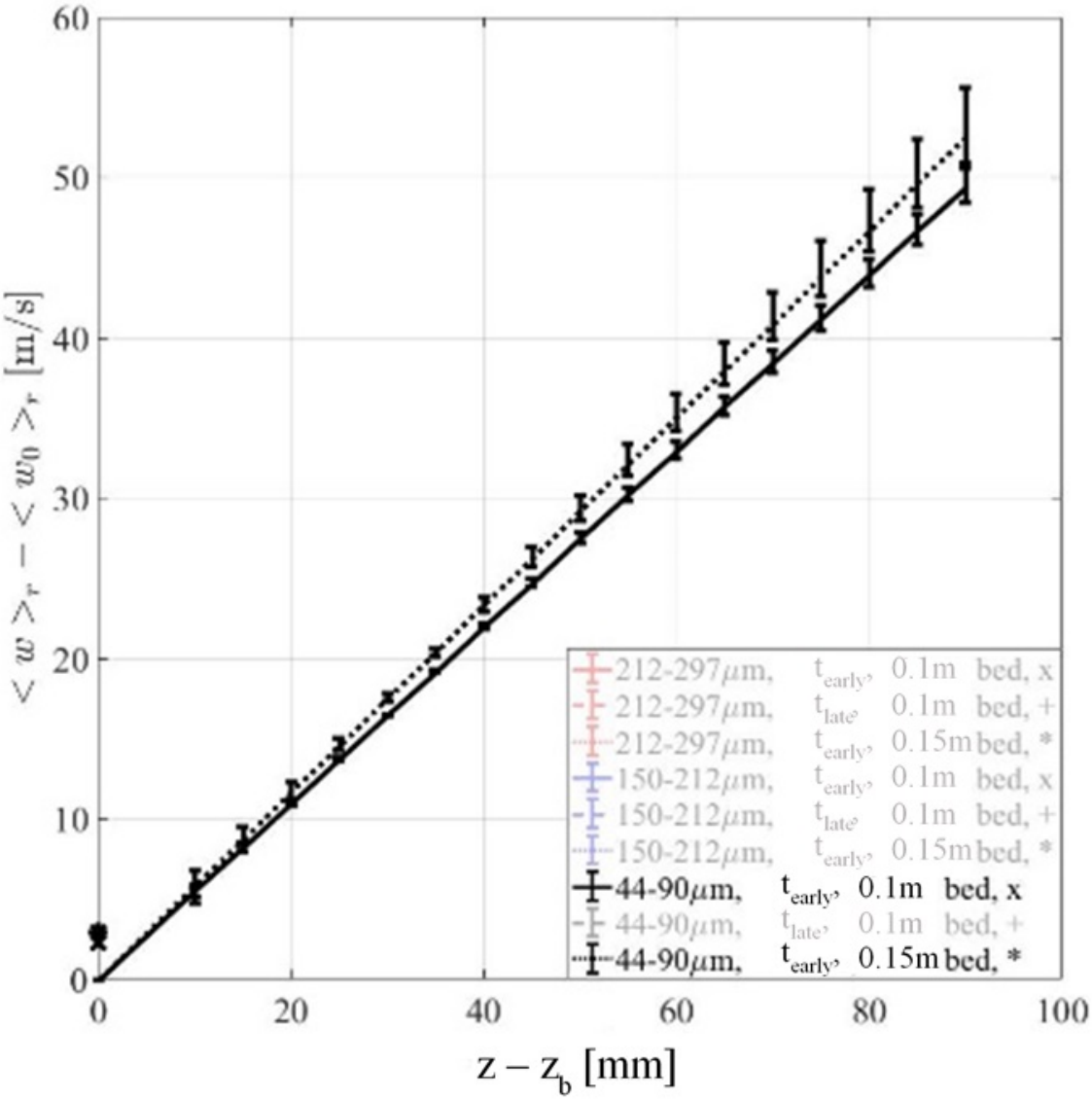

Figure 82: Shown Are Plots of PIV Gas Velocity Data as Measured above a 0.1m Beds and 0.15m Beds Composed of Particles with Diameters Ranging [44, 90]μm at Early Times. Each Plot Is an Ensemble Average of Three Independent Realizations.

Shown in Figure 83 is a comparison chart showing the gas velocities above 0.1m beds and 0.15m beds for varying particle diameters and the effects of time delay on the shorter 0.1m beds. Each plot is an ensemble average of three independent realizations. In early times, the gas velocity profiles from gases above 0.1m beds do not collapse as the others do. It is suspected that

some small inherent variability in the triggering mechanism, the expansion wave passing Ai4 at z_2, may contribute to the data sets not aligning perfectly. However, in all cases the extrapolated gas velocities at $z - z_b = 0$ are ordered by descending particle size. The gases escaping the particle bed and the gases above the bed are faster for experiments using larger-diameter particles. This coincides with the findings from Chapter 7 that the expansion wave travels faster through beds composed of larger particles, and so must the gas.

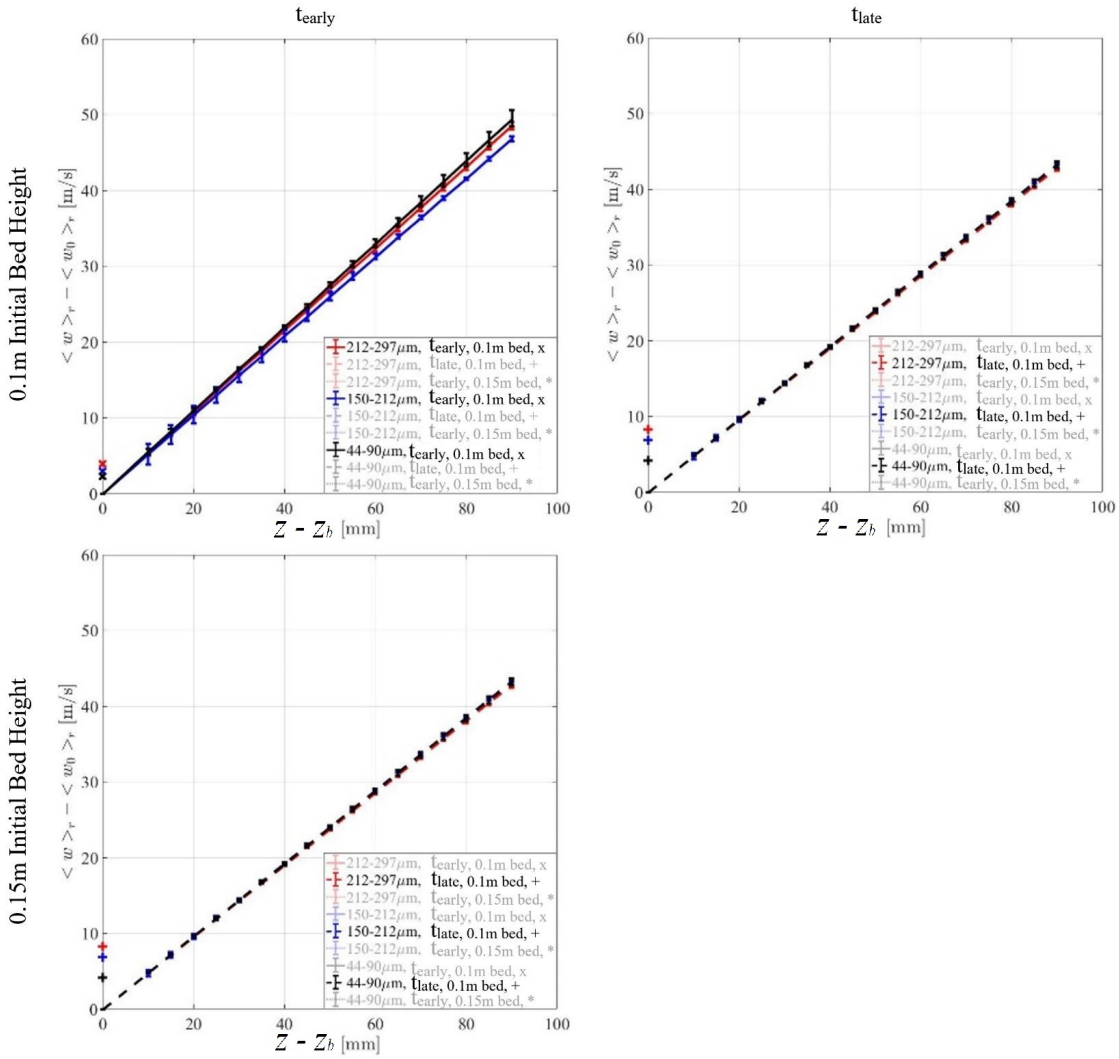

Figure 83: Shown Is a Comparison Chart of PIV Gas Velocity Data from 0.1m Beds and 0.15m Beds for Varying Particle Diameters and the Effect of Time Delay on the 0.1m Beds. Each Plot Is an Ensemble Average of Three Independent Realizations.

Shown in Figure 84 —Figure 86 are the individual plots from Figure 83 to visualize the data in more detail.

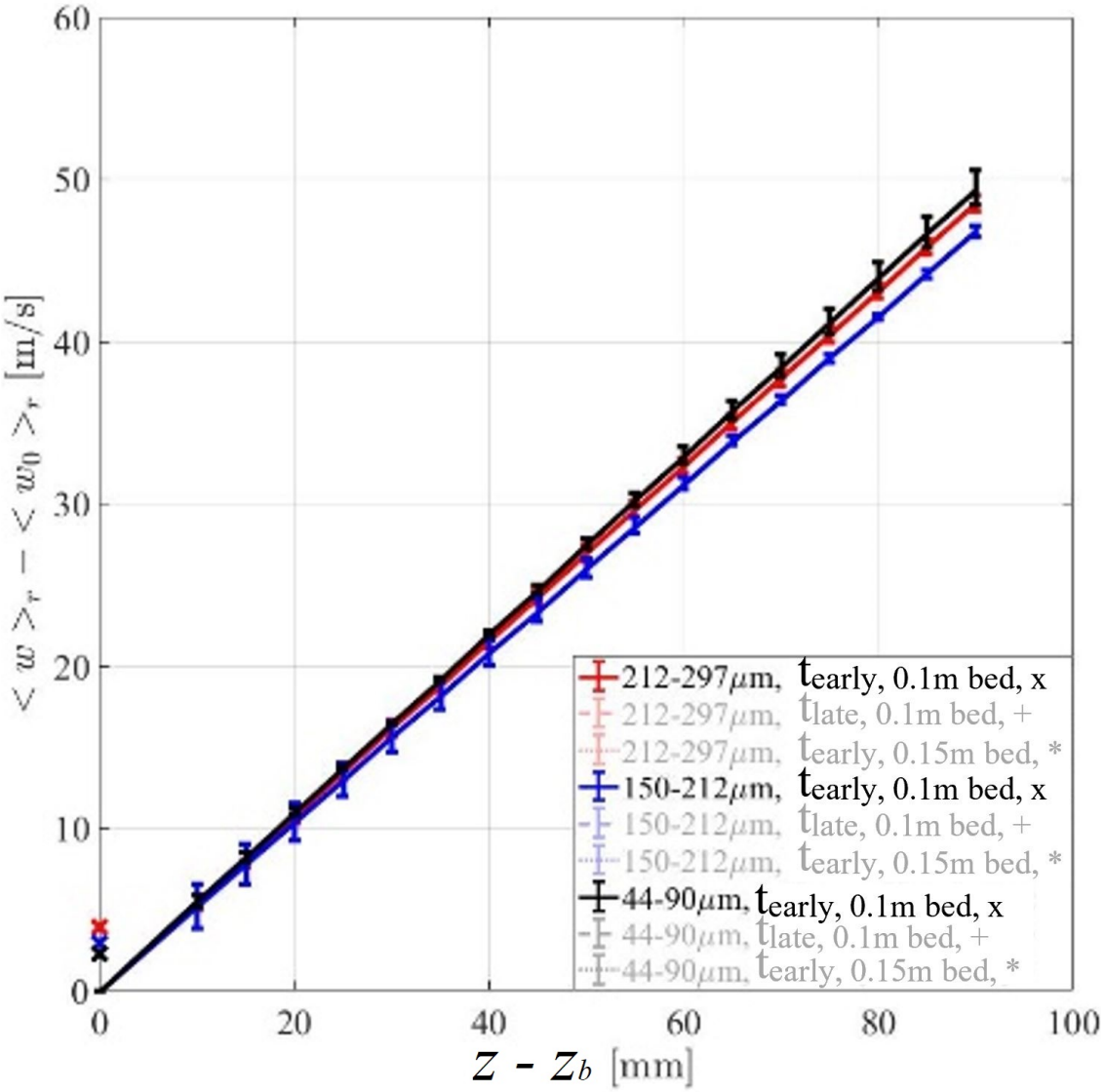

Figure 84: PIV Gas Velocity Data Taken above Beds with $z_b = 0.1m$ at $t = t_{early}$. Each Plot Is an Ensemble Average of Three Independent Realizations. Note That While the Overall Plots Do Not Collapse, the Extrapolated Velocities at $z - z_b = 0$ Are Aligned by Descending Particle Diameter.

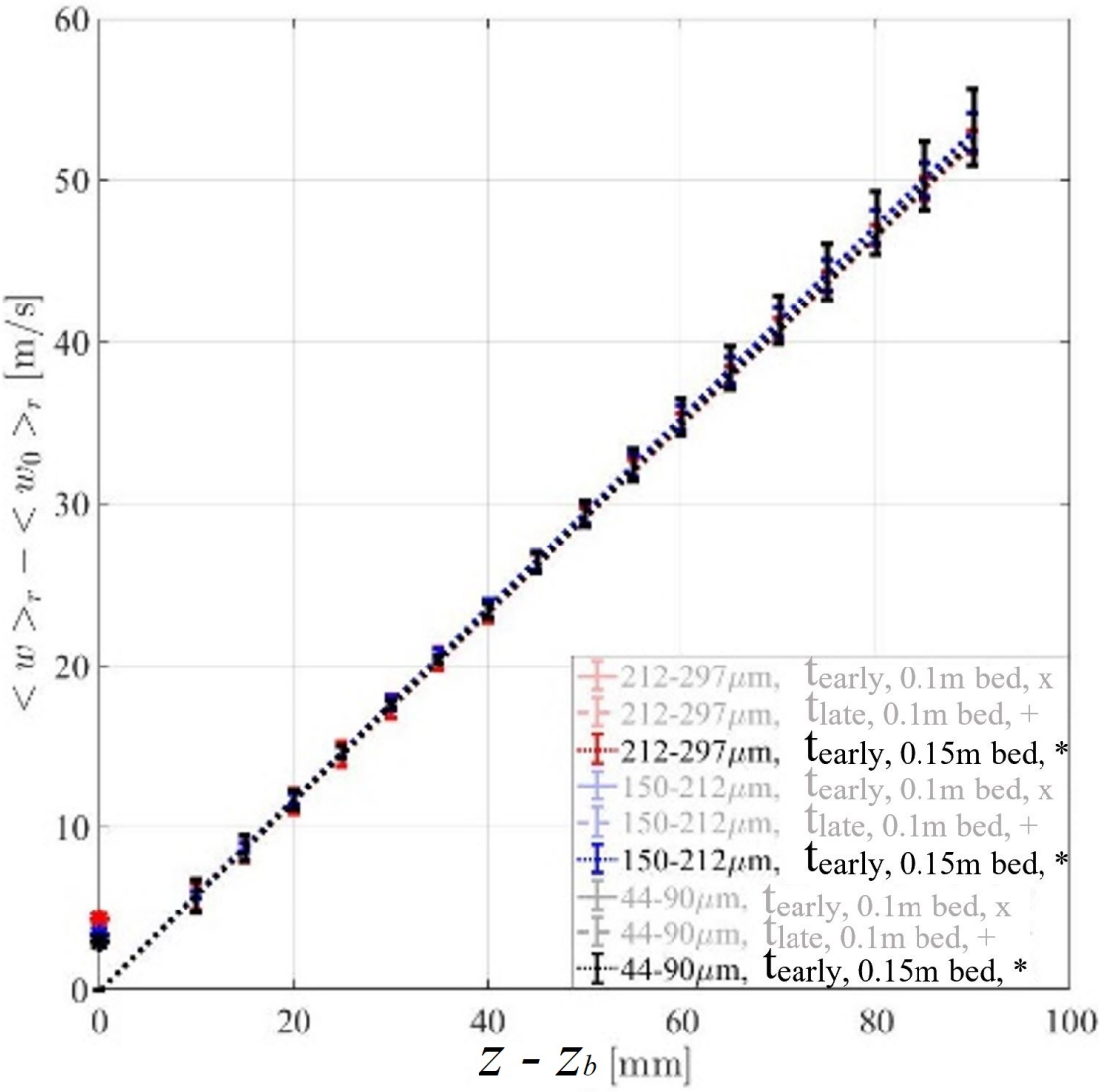

Figure 85: PIV Gas Velocity Data Taken above Beds with $z_b = 0.15m$ at $t = t_{early}$. Each Plot Is an Ensemble Average of Three Independent Realizations. All Three Plots from the Three Different Particle Diameter Ranges Collapse on Top of One Another. In Addition, the Extrapolated Velocities at $z - z_b = 0$ Are Aligned by Descending Particle Diameter, as All the Other Comparisons Show.

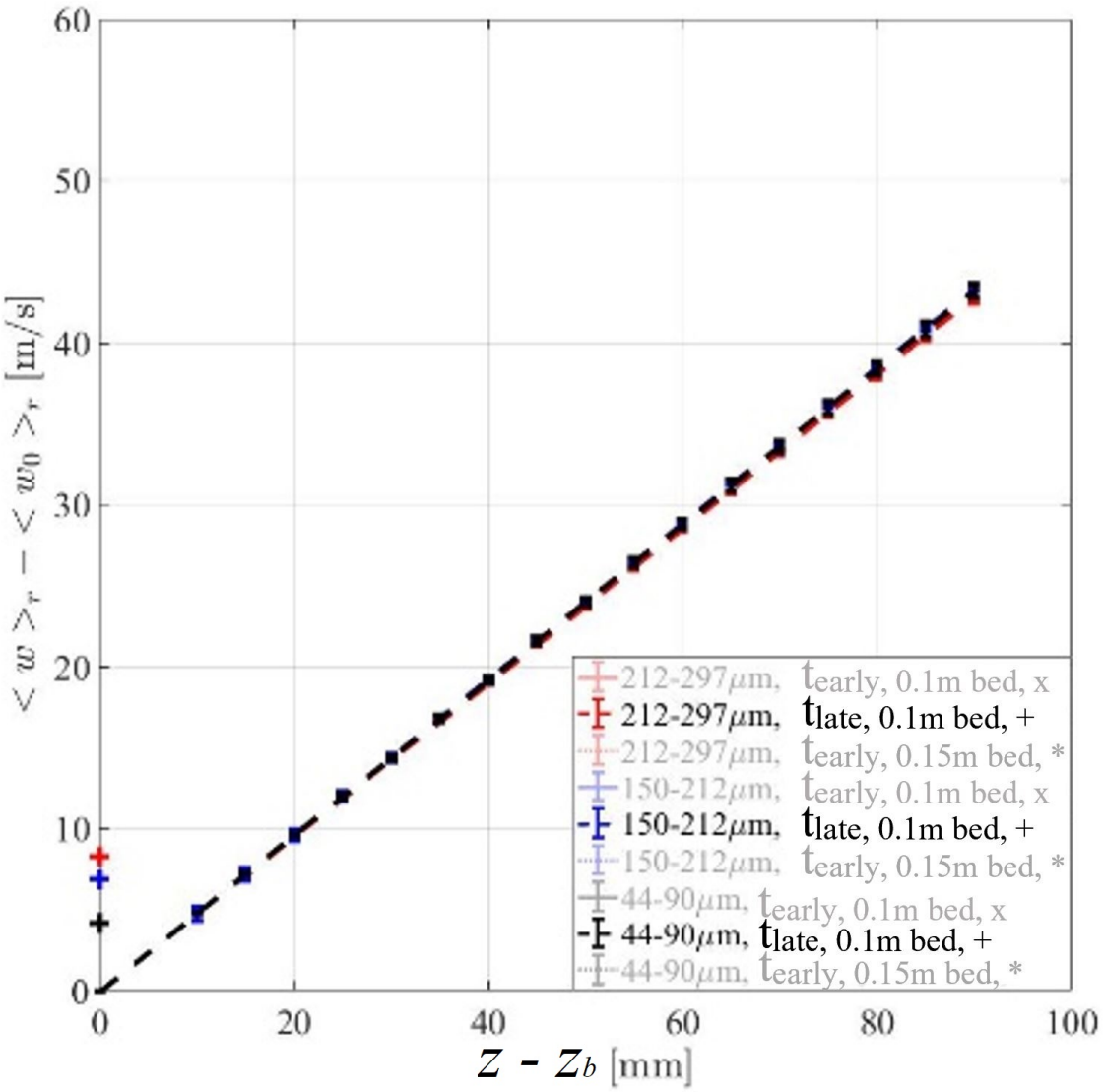

Figure 86: PIV Gas Velocity Data Taken above Beds with $z_b = 0.1m$ at $t = t_{late}$. Each Plot Is an Ensemble Average of Three Independent Realizations.

Shown in Figure 87 are the linearly extrapolated gas velocities at $z - z_b = 0$ at $t = t_{early}$. Notice that for all particle diameters, the gas velocities at z_b are higher for particle bed interfaces closer to the diaphragm (taller beds). When the particle bed is taller, the particle bed interface is closer to the diaphragm and the expansion wave impinges on the interface earlier. Also, recall that t_{early} and t_{late} are chosen so that the expansion wave impinges on the particle bed interface at

the same time. t_{early} is chosen so that the data is taken just as the expansion wave is impinging on the gas-particle interface, regardless of the initial particle bed height z_b. t_{late} in all cases is one millisecond later than t_{early} for the same bed height when the expansion wave has penetrated between 40mm and 90mm of the particle bed, depending on the particle diameter. Therefore, the varying velocities shown in Figure 87 are not due to the data being taken at different times relative to the moment when the expansion wave impinges on the gas-particle interface, but due to the difference in $z_d - z_b$. Additionally, particle beds composed of larger-diameter particles have higher gas velocities at the interface and above the bed as a whole. This effect is also seen in Figure 88.

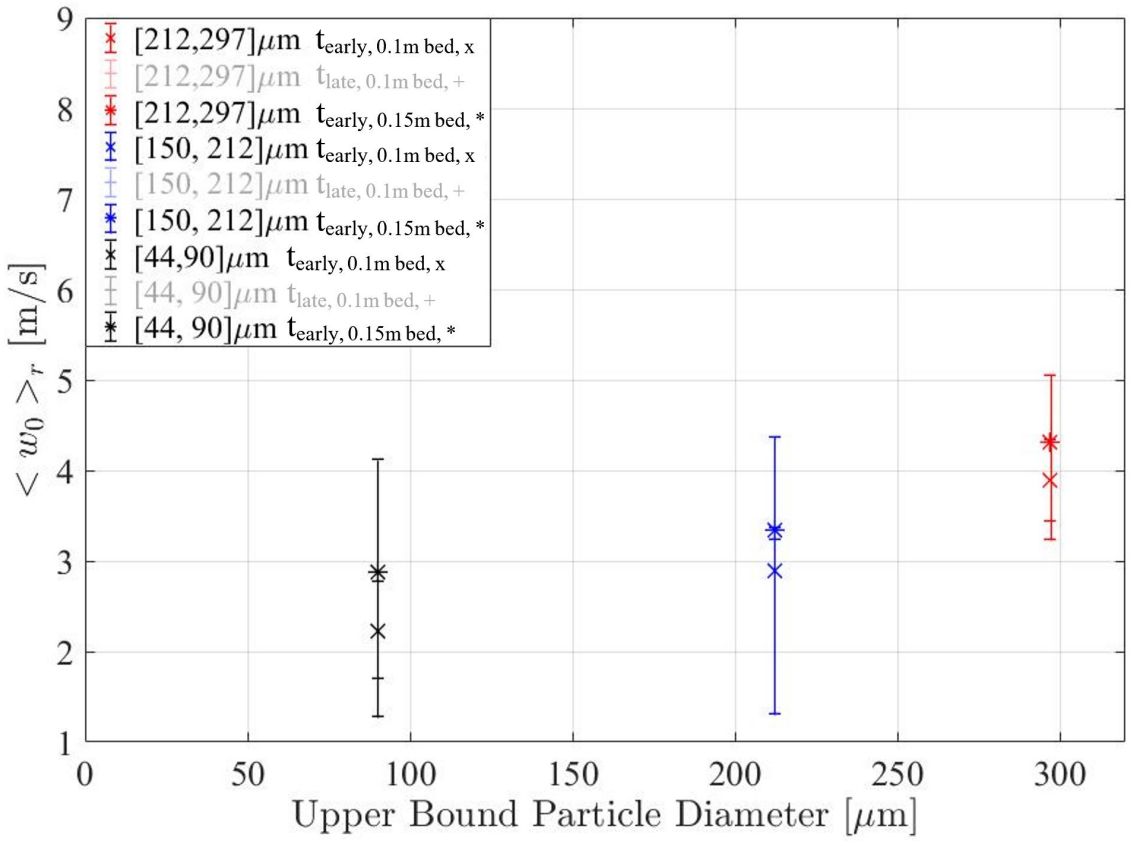

Figure 87: Shown Are the Linearly Extrapolated Gas Velocities at $z - z_b = 0$ at Early Times. t_{early} Is When the Expansion Wave Has Just Impinged on the Particle Bed Interface at z_b.

Shown in Figure 88 are the linearly extrapolated gas velocities at $z - z_b = 0$ for beds with $z_b = 0.1$m at t_{early} and t_{late}. Notice for all particle sizes, gas velocities at earlier times are lower than

gas velocities at later times. This is due to the gas having less time to accelerate by the time the data is taken. Data could not be taken at t_{late} for beds with $z_b = 0.15$m, because the condensation cloud blocked the camera view of the oil droplets.

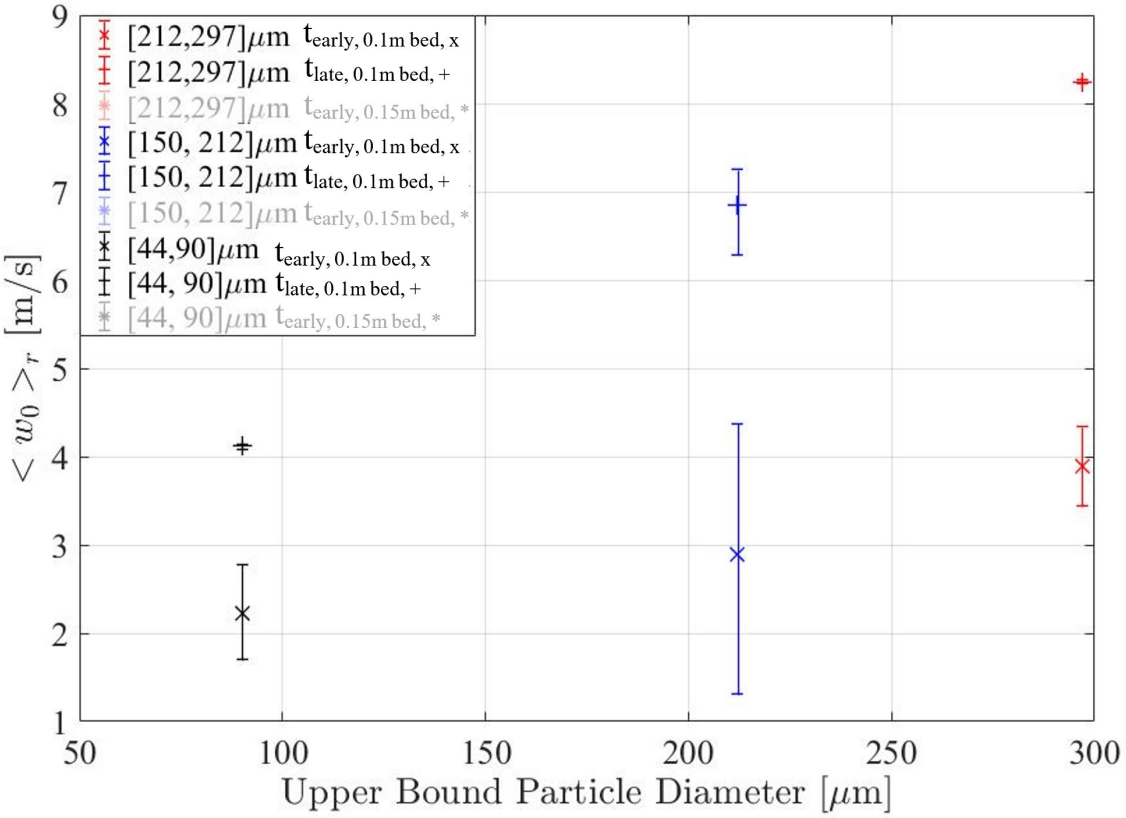

Figure 88: Shown Are the Linearly Extrapolated Gas Velocities at $z - z_b = 0$ for Both t_{late} and t_{early}. Note That $t_{late} = t_{early} + 1ms$.

8.3 PIV Experiments Compared with Simulations

Using Two Phase Euler Foam, part of the OpenFOAM[32] Computational Fluid Dynamics Toolbox, several shocktube experimental measurements were simulated, including gas velocities the above the bed. Simulations of 38mm diameter 1.37m long shocktube were run with a resolution of 500 in the radial direction and 1000 in the axial direction. The simulated shocktube was rectangular, however all the values were taken from the center, away from the sidewall effects. In all simulations performed, the initial pressure ratio was $\frac{P_4}{P_1} = 20.265$. To compare with the gas velocities, experiments

with all three particle size ranges with initial bed heights of $z_b = 0.1m$ were used. In the simulations, the experimentally measured solid volume fraction was used as a parameter for each particle size range. As shown in Figures 89 - 95, the simulation has predicted gas velocities slightly higher than what was measured, however the almost all simulated values are less than $5\frac{m}{s}$ greater than the experimentally measured gas velocities. The Eulerian—Eulerian code does not easily simulate a range of particle diameters, as is used in the experiments, so the simulated particles were monodisperse. For this reason, simulations using particles at the boundaries of each experimental particle size range were performed. For example, to better understand the gas velocities above a bed composed of particles ranging from 212μm to 297μm, two simulations were performed; one with 212μm diameter particles and one with 297μm diameter particles. Similar simulations were performed for all three particle size ranges. The experimentally measured gas velocities are plotted alongside two simulated gas velocities with particles at the boundaries of the experimental particle size distributions.

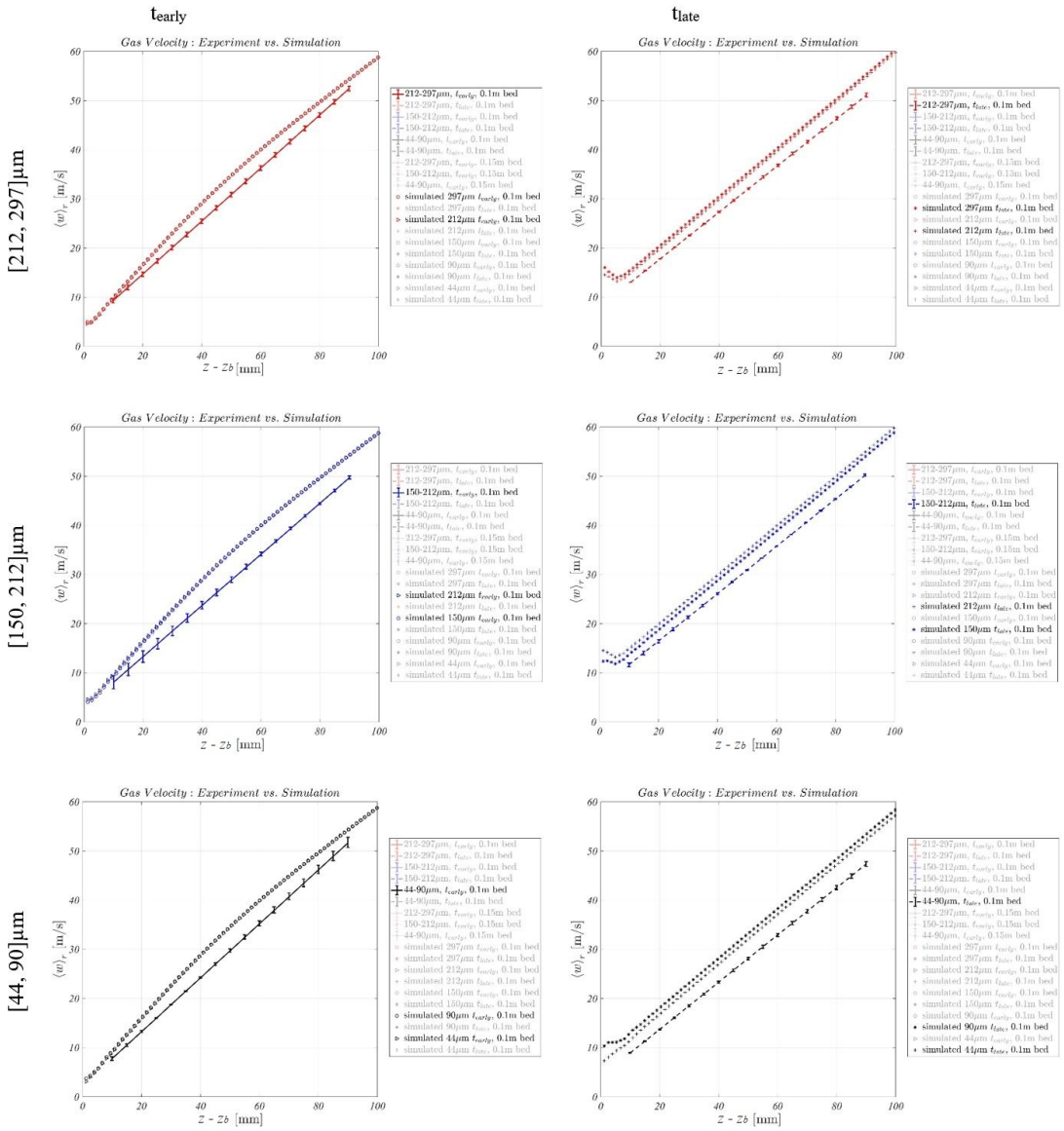

Figure 89: Shown Is a Comparison of the Simulated Gas Velocities and the Experimentally Measured Gas Velocities Using PIV. The Left Column Shows Simulated and Experimentally Measured Gas Velocities Just after the Expansion Wave Has Impinged on the Gas-particle Interface Located at $z_b = 0.1m$. The Right Column Shows the Gas Velocities One Millisecond Later. The Minimum and Maximum Particle Sizes Within Each Particle Size Range Were Simulated.

Figures 90—95 are the individual plots shown in the comparison chart in Figure 89 to be viewed in more detail.

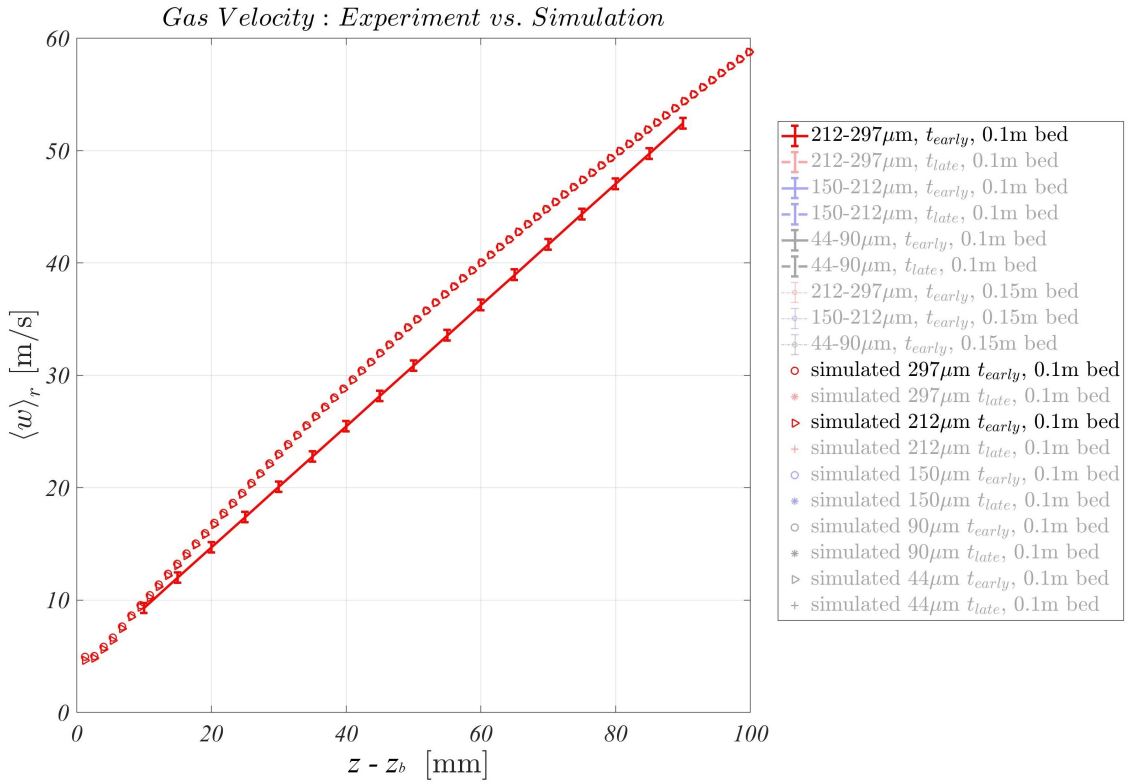

Figure 90: Shown Is a Comparison of the Simulated Gas Velocities above a Bed Composed of 212μm Particles and a Bed Composed of 297μm Particles along with the Experimentally Measured Gas Velocities above a Bed Composed of [212, 297]μm Particles. All Three Data Sets Were Taken at $t = t_{early}$ and with an Initial Bed Height of $z_b = 0.1m$.

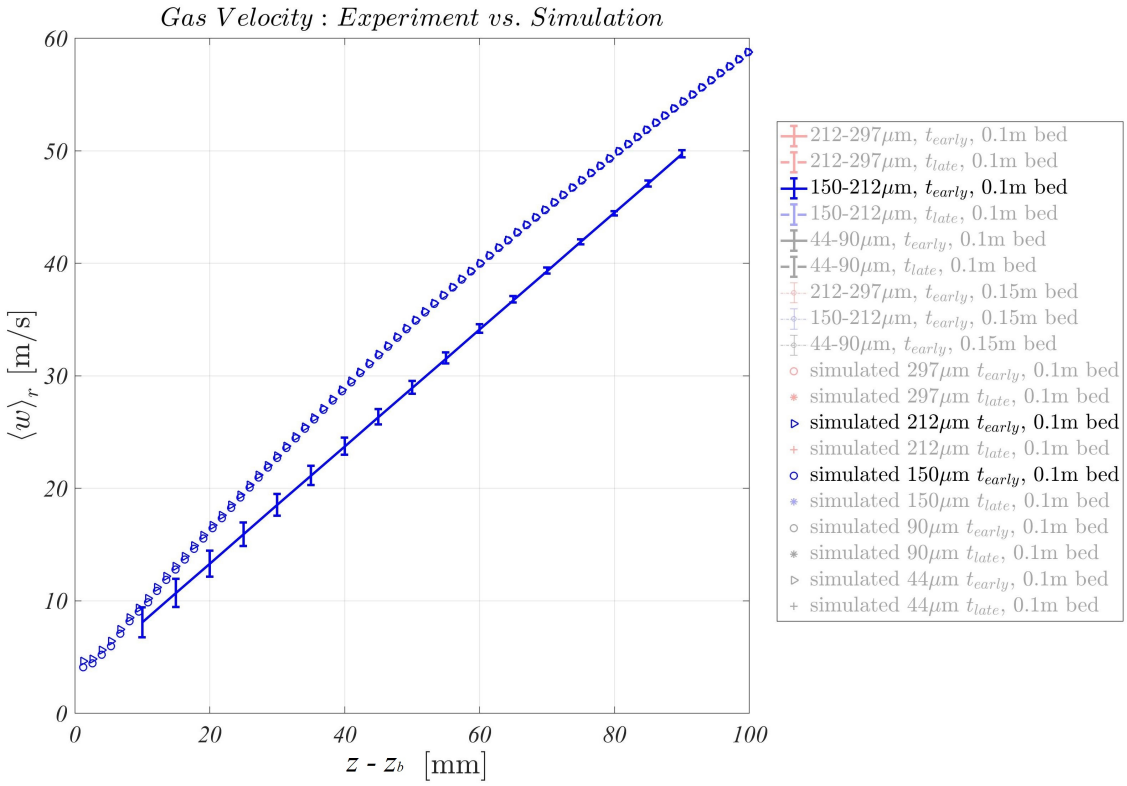

Figure 91: Shown Is a Comparison of the Simulated Gas Velocities above a Bed Composed of 150μm Particles and a Bed Composed of 212μm Particles along with the Experimentally Measured Gas Velocities above a Bed Composed of [150, 212]μm Particles. All Three Data Sets Were Taken at $t = t_{early}$ and with an Initial Bed Height of $z_b = 0.1m$.

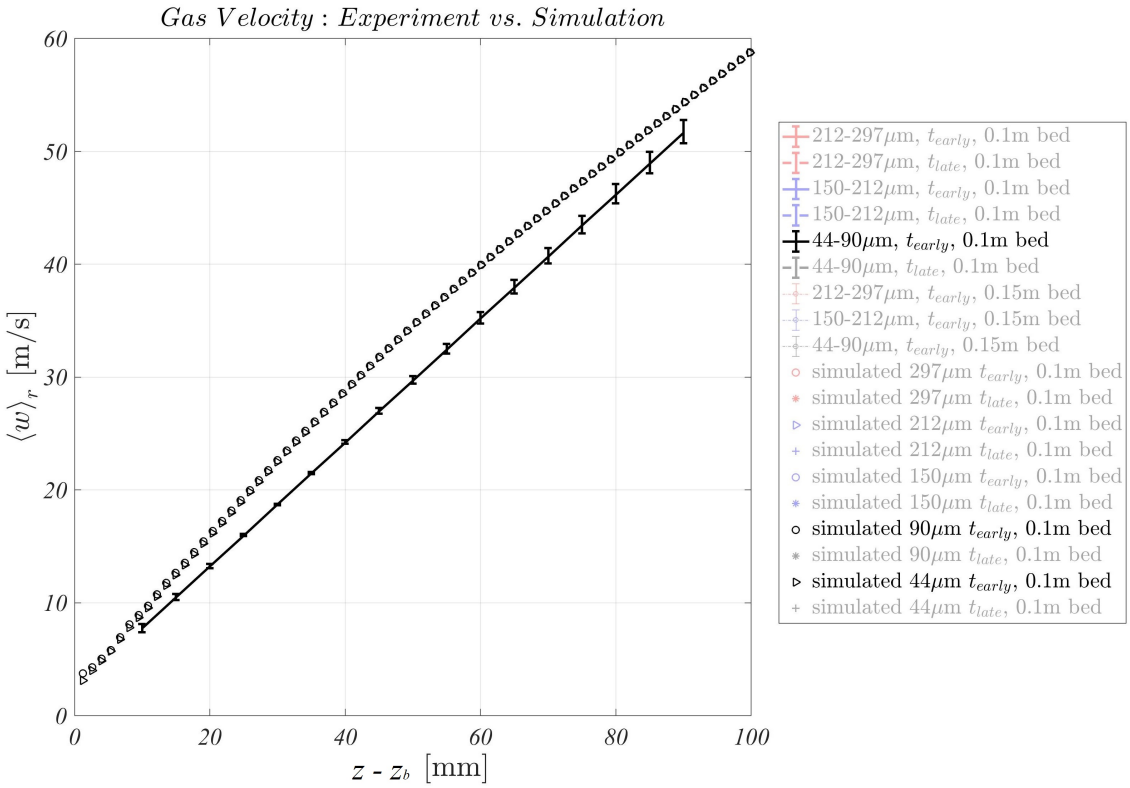

Figure 92: Shown Is a Comparison of the Simulated Gas Velocities above a Bed Composed of 44μm Particles and a Bed Composed of 90μm Particles along with the Experimentally Measured Gas Velocities above a Bed Composed of [44, 90]μm Particles. All Three Data Sets Were Taken at $t = t_{early}$ and with an Initial Bed Height of $z_b = 0.1m$.

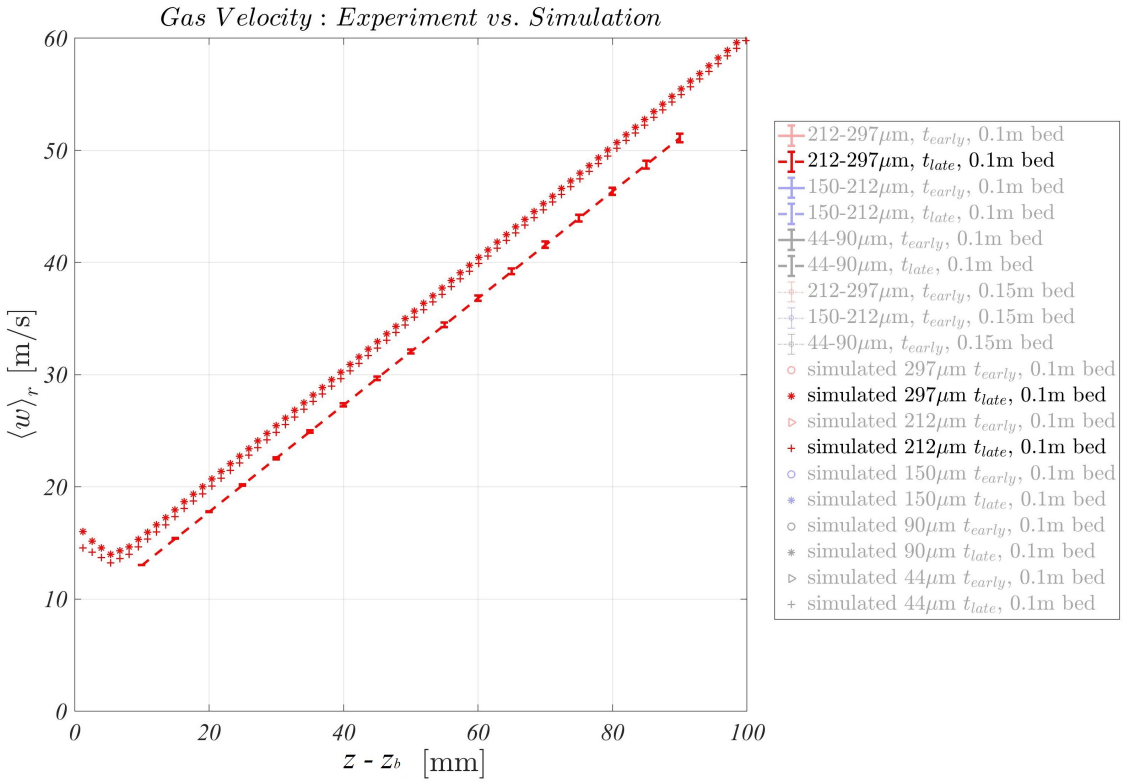

Figure 93: Shown Is a Comparison of the Simulated Gas Velocities above a Bed Composed of 212μm Particles and a Bed Composed of 297μm Particles along with the Experimentally Measured Gas Velocities above a Bed Composed of [212, 297]μm Particles. All Three Data Sets Were Taken at $t = t_{late}$ and with an Initial Bed Height of $z_b = 0.1m$.

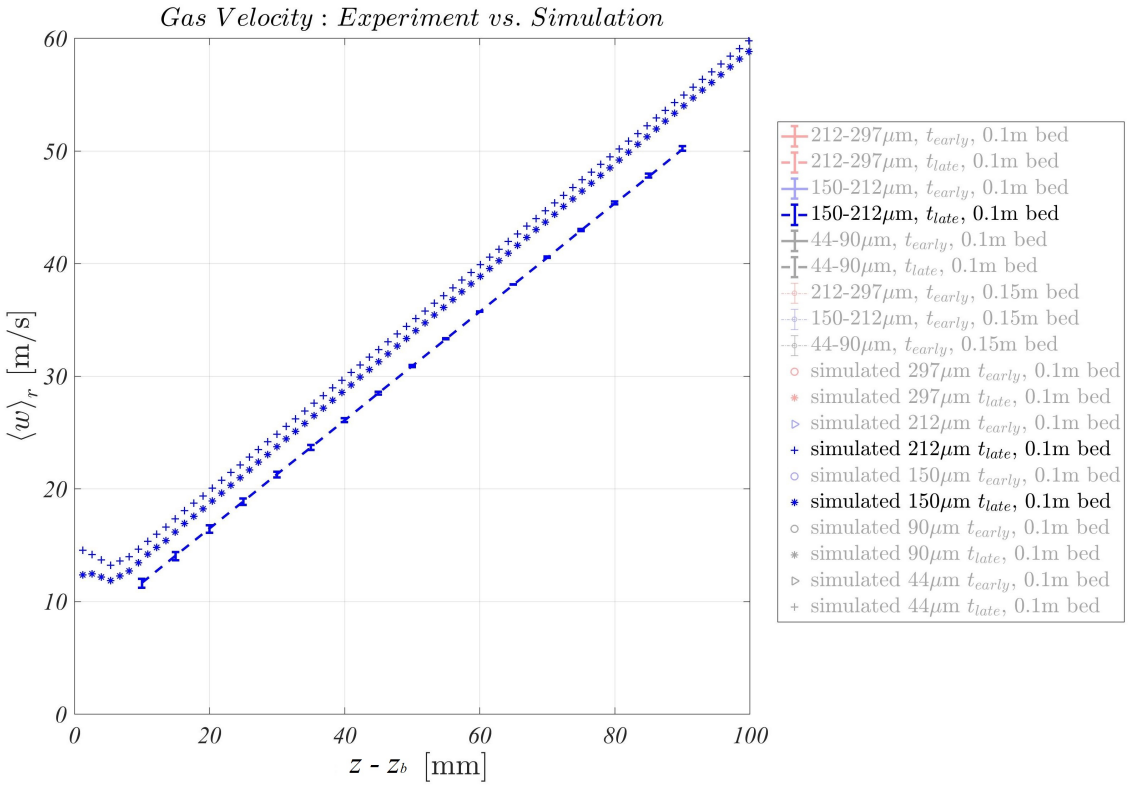

Figure 94: Shown Is a Comparison of the Simulated Gas Velocities above a Bed Composed of 150μm Particles and a Bed Composed of 212μm Particles along with the Experimentally Measured Gas Velocities above a Bed Composed of [150, 212]μm Particles. All Three Data Sets Were Taken at $t = t_{late}$ and with an Initial Bed Height of $z_b = 0.1m$.

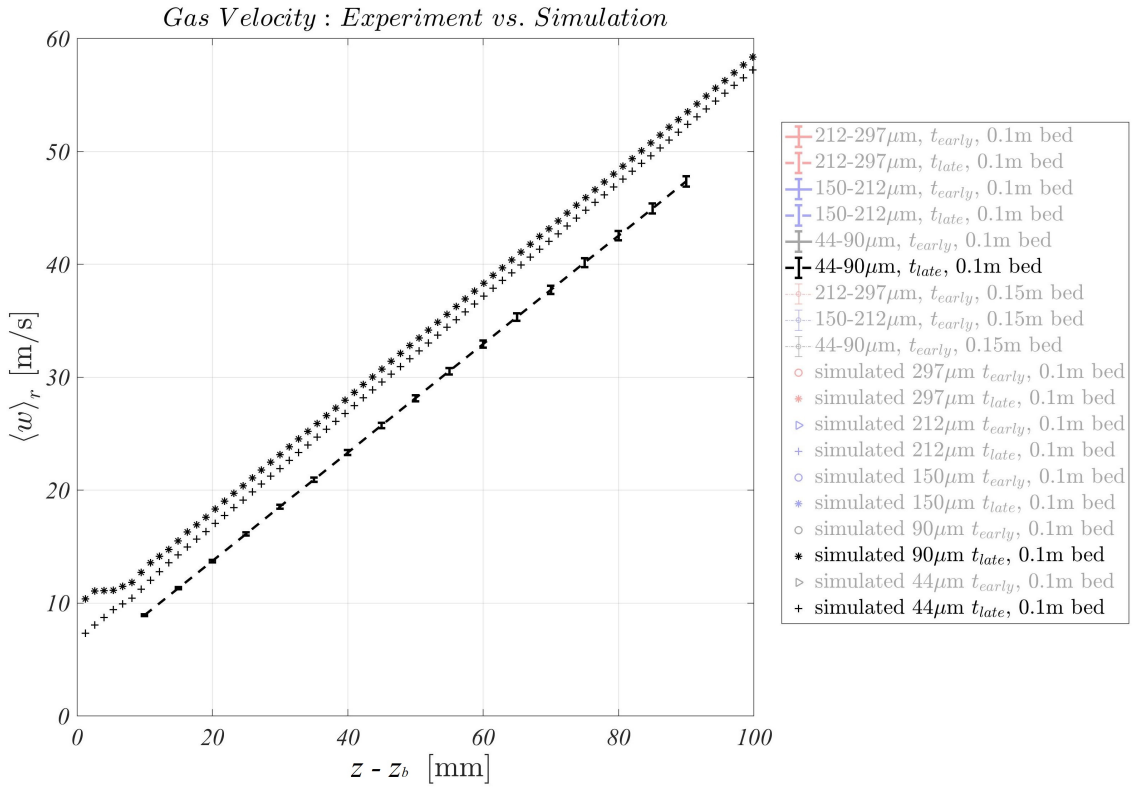

Figure 95: Shown Is a Comparison of the Simulated Gas Velocities above a Bed Composed of 44μm Particles and a Bed Composed of 90μm Particles along with the Experimentally Measured Gas Velocities above a Bed Composed of [44, 90]μm Particles. All Three Data Sets Were Taken at $t = t_{late}$ and with an Initial Bed Height of $z_b = 0.1m$.

The minimum and maximum particle sizes for each size range were simulated showing that in early times, the particle diameter does not have much effect on the gas velocities, as the expansion wave has only just impinged on the gas-particle bed interface. One millisecond later at $t = t_{late}$, the simulated gas velocities above particle beds composed of larger-diameter particles are higher. This effect seems to be magnified as the particle size decreases.

Another way to visualize gas velocity data in a shocktube is with an x-t diagram. In the case of the vertical shocktube at ASU, a z-t diagram is used, as the axial coordinate is z and aligned vertically. Shown in Figure 96 are the gas velocities over time and space in the shocktube. The black contour lines are plotted every $50m \cdot s^{-1}$. In this figure, it is clear that the gas velocities

continue to increase rapidly in the expansion region, far away from the particle bed interface. The gas velocities near $250m \cdot s^{-1}$ just below the diaphragm, located at z = 0.697m. However, this is outside the measurements of the PIV experiments, which only extend 0.1m above the particle bed.

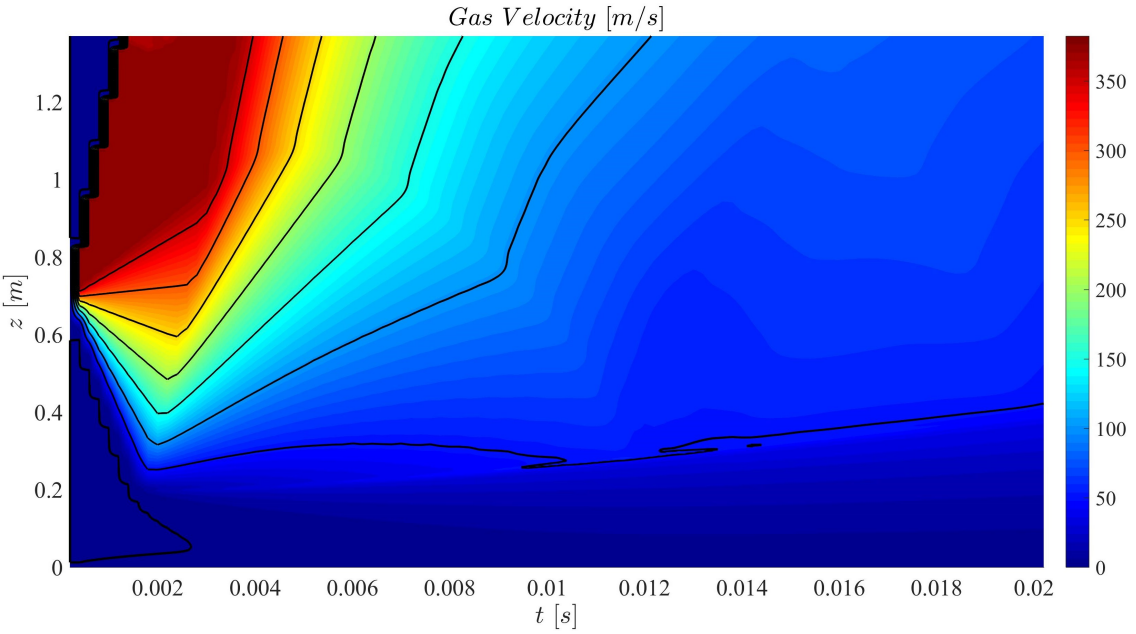

Figure 96: Shown Is a z-t Diagram of the Simulated Gas Velocity Data from an Experiment with a 0.2m Bed Composed of 297μm Diameter Particles. The Black Contour Lines Are Plotted Every $50m \cdot s^{-1}$. The Jaggedness of the Contours and Colored Surface near the Location of the Shock (Shown as Dark Red) Is Due to the Low Temporal Resolution of the Simulation. Data Was Saved from the Simulation Every 0.2ms.

8.4 Results

Higher gas velocities are associated with particle beds composed of larger particle diameters. Similar to the pressure trace comparisons, the higher velocities can be expected given the larger interstices (less flow impedance). Additionally, when the gas-particle interface is closer to the diaphragm, as is true for taller beds, the gas velocities tend to be higher. When gas velocity measurements were taken at later times, the gas dilation (slope of the velocity curve) was less significant, but the overall gas velocities were faster, as the gases had been accelerating for longer.

The simulations using Two Phase Euler Foam, which is an Eulerian-Eulerian computational

fluid dynamics code matched reasonably well with the experimental gas velocity measurements. When the shocktube experiment was simulated with a monodisperse particle bed, it was shown that just as the wave impinges, the particle diameter has minimal effect on the gas velocities. However, as the particle bed begins to degas, the gas velocities above beds with larger particles are higher. This is seen in the experimental data as well. In Figures 84 and 85, there is only a very slight difference in gas velocities due to different particle size ranges—plotted at $z - z_b = 0$. However, note in Figure 88 and Figure 86 that the gas velocities one millisecond after the expansion wave impinges on the gas-particle interface are higher for experiments with particle beds composed of larger-diameter particles.

All the datasets and comparisons seem to be telling the same story. The gas-particle interface rise rate data comparisons show that, in all cases, taller beds and beds composed of smaller-diameter particles expand faster. Smaller particles have less inertia, requiring less force exerted by the gas to move, thus the beds composed of these small particles rise more quickly. Additionally, the beds composed of smaller-diameter particles have a lower overall solid volume fraction ϕ_p, meaning there is more gas available in the bed to expand and exert a drag force on the particles. Interestingly, the taller beds have lower overall ϕ_p than shorter beds composed of the same particle sizes; meaning, again, there is more gas available to expand and exert forces on the particles. In the simulated experiments, it was shown that while even a slightly lower solid volume fraction is sufficient to cause the particle bed to expand more quickly, it is not the only factor.

Simple simulations were performed to investigate whether particle size and bed height were sufficient on their own to cause variation in gas-particle interface rise rates while keeping the initial solid volume fraction for all beds the same ($\phi_p = 0.6$). It was shown that both are sufficient to cause variation in bed rise rates. When the initial solid volume fraction for shorter beds and taller beds was the same, the taller beds expanded more quickly. Additionally, when initial solid volume fraction for beds composed of smaller-diameter particles and larger-diameter particles was the same, the beds composed of smaller-diameter particles still expanded more quickly. This shows that while ϕ_p does have an effect on bed expansion rates, it is not the only reason for the trends discussed and shown in Figure 46. Though the Two Phase Euler Foam simulations provide valuable insight, conclusions cannot be drawn from them solely, as they have not been rigorously validated with the vertical shocktube experiment.

Also related to solid volume fraction, the particle bed density is lower near the walls, due to geometry of sphere-packing near the glass wall of the cylinder. When the solid volume fraction is lower, the gas experiences a lower impedance to flow. This causes the gases near the wall to have higher velocities. This corresponds to faster gas escape near the walls and earlier particle bed interface motion near the walls, as seen in the gas-particle interface deformation imagery in Figure 33. The cloud recession data also supports this as shown in Figure 36.

The experimental and simulated data both show that the expansion wave travels more

quickly through particle beds composed of larger-diameter particles. As for particle-diameter-related comparisons, beds that rise more quickly are associated with slower moving expansion waves (for beds of the same initial height z_b). Of course, the expansion wave moves more slowly through taller beds than shorter beds.

As for gas velocities measured above the particle bed using Particle Image Velocimetry, higher gas velocities are associated with beds composed of larger-diameter particles. This relationship pairs nicely with finding that the expansion wave travels more quickly through beds composed of larger-diameter particles. Gas velocity measurements were taken for shorter beds ($z_b = 0.1$m) at the time the expansion wave was predicted to have impinged on the gas-particle bed interface (t_{early}) and one millisecond later (t_{late}). Depending on the particle-diameter, the expansion wave had traveled between 40mm and 90mm into the particle bed. At t_{early}, gas velocities measured right at the particle bed interface were very close to one another for all particle diameters. This was expected, as the particles had barely had any time to affect the gas flow at that point. At t_{late}, there is a clear relationship between particle size and gas velocities, as the beds composed of larger-diameter particles were also associated with higher gas velocities. The simulated gas velocity measurements mimicked these same trends as seen in Figure 89.

Performing simulations was very helpful for understanding some of the complexities of the decompression experiments, especially relating to solid volume fraction and pressure fluctuations. While OpenFOAM is an Eulerian-Eulerian code, without particles *per se*, many quantities measured from these simulations still mimicked the experimental measurements surprisingly well, including pressure fluctuations and gas velocities above the bed. However, a more rigorous validation must be performed of the Two Phase Euler Foam simulation to make more meaningful comparisons. An Eulerian-Lagrange simulation with solid particles and collision dynamics may match the data collected from ASU more closely.

Initially, this experiment was motivated by providing simple validation data for the codes and models being developed at the Center for Compressible Multiphase Turbulence at the University of Gainesville. The simulation is still being developed there and a paper will be written detailing that comparison at a later date. Presently, the simulated particle bed decompression data from CCMT matches reasonably well with the experimental data collected from the vertical shocktube at

ASU. Interestingly, the simulation predicts the particle-vacant regions similar to those seen in the high-speed images of the ASU experiment.

10 FUTURE RESEARCH

10.1 Additions and Improvements

To complete the story of the rapidly decompressed particle beds, it will be necessary to explore various non-dimensionalizations to try to collapse the different curves presented. Additionally, a more complete description of the horizontal void crack and honeycomb pattern of voids needs to be developed. Comparing the data to available more complex simulations will also be very informative.

Should more data be required to accomplish these goals, a fourth particle diameter range of 90-150μm is available. A comparison with a third bed height may also be useful. For some experiments, it might be worthwhile to include a second pressure ratio. It is possible that varying the pressure ratio may reveal some different regimes or dominating effects.

Once the computational codes being developed at CCMT, very meaningful comparisons between experiments and simulations will be performed. The simulation that will be performed by CCMT will also be compared to a high resolution Two Phase Euler Foam simulation.

10.2 Future Publications

Several publications are planned for this data presented. The first being a physics paper describing the flow regimes and structures seen in the vertical shock tube experiments. This will include the gas motion prior to the 1st particle motion, the bed motion during early expansion, the bulk motion of the particle bed, the pressure fluctuations, and the particle bed interface rise. The second paper planned is a paper specifically discussing the PIV experiments and the incipient bed motion. This paper will be written in collaboration with Dr. Liuyang Ding and Dr. Blair Johnson. A third paper is planned to compare ASU's experimental data to the simulated data from CCMT. The last paper planned is one that will go into depth describing the formation of the horizontal void cracks and possibly the honeycomb-like pattern seen in the particle bed evolution. This paper would be written in collaboration with Dr. K.P. Chen at ASU.

References

[1] Chojnicki, K., Clarke, A., Phillips, J. (2006). A shock-tube investigation of the dynamics of gas-particle mixtures: Implications for explosive volcanic eruptions. Geophysical Research Letters, 33(15). DOI 10.1029/2006GL026414.

[2] Wagner, J.L., Beresh, S.J., Kearney, S.P., Trott, W.M., Castaneda, J.N., Pruett, B.O., and Baer, M.R., (2012). A multiphase shock tube for shock wave interactions with dense particle fields. Experiments in Fluids, 53, 1507 - 1517. DOI 10.1007/s00348-012-1272-x.

[3] Frost D.L., Gregoire, Y., Goroshin, S., and Zhang, F,. (2012). Particle Jet Formation During Explosive Dispersal. Physics of Fluids, 24. DOI 10.1063/1.4751876.

[4] Grady, D.E., (1982). Local intertial effects in dynamic fragmentation. Journal of Applied Physics, 53, 322 - 325. DOI 10.1063/1.329934.

[5] Milne, A.M., Parrish, C., and Worland, I., (2010). Dynamic fragmentation of blast mitigants. Shock Waves, 20, 41 - 51. DOI 10.1007/s00193-009-0235-5.

[6] Hughes, K., (April 2017). Simulation-Driven Experiments of Macroscale Explosive Dispersal of Particles. Presentation presented at the Center for Compressible Multiphase Turbulence at the University of Florida. Gainesville, FL.

[7] Anilkumar, A.V., (1989). Experimental studies of high-speed dense dusty gases. Doctoral Dissertation. California Institute of Technology. CaltechETD:etd-08312006-130447.

[8] Cagnoli, B., Barmin, A., Melnik, O. and Sparks, R.S.J., (2002). Depressurization of fine powders in a shock tube and dynamics of fragmented magma in volcanic conduits. Earth and Planetary Science Letters, 204, 101 - 113. DOI 10.1016/S0012-821X(02)00952-4.

[9] Cantwell, B.J. (2011) *Fundamentals of Compressible Flow.* Retrieved from `https://web.stanford.edu/~cantwell/AA210A_Course_Material/AA210A_Course_Notes/`.

[10] Zwick, D., Balachandar, S., (2019) Dynamics of Rapidly Depressurized Multiphase Stock Tubes. Journal of Fluid Mechanics (in process).

[11] Ling, Y., Balachandar, S., Parmar, M., (2016). Inter-phase heat transfer and energy coupling in turbulent dispersed multiphase flows. Physics of Fluids, 28, 033304. DOI 10.1063/1.4942184.

[12] Ling, Y., Wagner, J. L., Beresh, S. J., Kearney ,S. P., Balachandar, S., (2012). Interaction of a planar shock wave with a dense particle curtain: Modeling and experiments. Physics of Fluids, 24, DOI 10.1063/1.4768815.

[13] Gidaspow, D. (1994) Multiphase flow and fluidization: continuum and kinetic theory descriptions. Academic Press.

[14] Holdich, R. G., (2002) Fundamentals of Particle Technology. Midland Information Technology and Publishing.

[15] Shallcross, G.S., Capecelatro, J., (2018). A parametric study of particle-laden shock tubes using an Eulerian-Lagrangian framework. AIAA Aerospace Sciences Meeting. DOI 10.2514/6.2018-2080

[16] Geldart, D., (1973). Types of gas fluidization. Powder Technology, 7, 285-292.

[17] Zwick, D., Blachandar, S., (2018). An Eulerian-Lagrange approach for multiphase flow simulation on spectral elements. International Journal of High Performance Computing Applications (Submitted)

[18] Dechsiri, C., (2004). Particle transport in fluidized beds: experiments and stochastic models. Doctoral Dissertation. Groningen: s.n.

[19] Ergun, Sabri. (1952). Fluid flow through packed columns. Chemical Engineering Progress, 48, 89-94.

[20] Kehoe, P. W. K., J. F. Davidson, (1970) Proc. of Chemeca, 70, Butterworths, Melbourne, Australia, 97.

[21] Wen, C.Y., Yu, Y.H., (1966). A generalized method for predicting the minimum fluidization velocity. American Institute of Chemical Engineers, 12(3), 610-612.

[22] Wallace, J.M., Hobbs, P.V., (2006). Atmospheric Science: An Introductory Survey. University of Washington, Elsevier Publishing.

[23] Adrian, R.J., Westerweel, J., (2011). Particle Image Velocimetry. Cambridge University Press.

[24] Ragni, D., Schrijer, F., van Oudheusden, B.W., Scarano, F., (2009). Particel tracer response across shocks measured by PIV. Experiments in Fluids, (50), 53-67.

[25] Vowinckel, B., Meiburg, E., (2018). Dry settling of particles with confining walls. In submission process.

[26] Song, C.; Wang, P.; Makse, H. A. (2008). A phase diagram for jammed matter. Nature. 453, (7195): 629–632.

[27] Kahler, C.J., Sammler, B., Kompenhans, J., (2001). Generation and Control of Particle size distributions for Optical Velocity Measurement Techniques in Fluid Mechanics. 4th International symposium on PIV, Gottingen, Germany, September 17-19, 2001.

[28] D. Zwick, Scalable highly-resolved Euler-Lagrange multiphase flow simulation with applications to shock tubes, PhD thesis, University of Florida, 2019.

[29] Mei, R., Velocity fidelity of flow tracer particles. Experiments in Fluids, 22, 1-13.

[30] Clift, R., J., Burckhardt, C.B., and Lin, L.H., (1978). Bubbles, Drops and Particles. San Diego, CA: Academic.

[31] Manni, A., (2014). An introduction to twoPhaseEulerFoam with addition of a heat exchange model in 23x version [PowerPoint slides]. Retrieved from http://www.tfd.chalmers.se/ hani/kurser/OS_CFD_2014/Alessandro%20Manni/SlidesAM.pdf.

[32] Weller, H.G., Tabor, G., Jasak, H., Fureby, C., (1998). A tensorial approach to computational continuum mechanics using object-oriented techniques, Computers in Physics, 12(6).

[33] van Wachem, B.G.M., Derivation, Implementation, and Validation of Computer Simulation Models for Gas-Solid Fluidized Beds, PhD thesis, TU Delft, 2000.

[34] Baila,P.P., (2008) A twoPhaseEulerFoam tutorial. Chalmers University of Technology, TME 050. Retrieved from http://www.tfd.chalmers.se/~hani/kurser/OS_CFD_2008/PraveenPrabhuBaila/Report_twoPhaseEuler.pdf

APPENDIX A

TWO PHASE EULER FOAM

A Two Phase Euler Foam

As mentioned in Chapter 4.2, Two Phase Euler Foam has not been rigorously validated for simulating the vertical shocktube experiment at ASU. It has been determined that to make the most meaningful comparisons, higher-resolution simulations would need to be run. Additionally, there are still a few unanswered questions in regards to the simulated gas and particle interactions near the shocktube wall. Nonetheless, this is a good starting point for comparing the experiments performed at ASU to simulations and will be valuable when the compared with the outputs of the finalized simulation prepared by the Center for Compressible Multiphase Turbulence at the University of Florida.

Two Phase Euler Foam is one of the solvers in the OpenFOAM[32] Computational Fluid Dynamics toolbox. It is used for simulations involving two compressible fluid phases, including a dispersed phase. This code has commonly been used to describe fluidized beds and flows associated with volcanic eruptions. It is an Eulerian-Eulerian code, meaning it treats the solid or dispersed phase as a fluid and does not track particles, greatly reducing the computational cost. A requirement of this type of code is that the solid volume fraction plus the fluid volume fraction must equal exactly one. The code is solved by using Multidimensional Universal Limiter with Explicit Solution, which uses the Flux Corrected Transport technique iteratively and computes a flux between higher and lower order scheme solutions, including a weighting factor. The velocities are calculated as mixture velocities and relative velocities.

The momentum equations are solved for both phases individually and a physical definition for the particle stress tensor is used to allow for mathematical closure. To accomplish this, flows are separated into three different regimes relating to the degree of solid volume fraction: Kinetic regime for dilute solid volume fraction, Collisional regime for slightly higher solid volume fraction, and a Frictional regime for a high solid volume fraction. The Frictional regime is used for a solid volume fraction greater than or equal to 60%. For the case of the simulations of the shocktube experiment at ASU, all runs were performed with a solid volume fraction of sixty percent or higher, putting these simulations in the Frictional regime[31].

The averaged momentum equation solved by Two Phase Euler Foam is [34]

$$\frac{\delta \alpha_\phi \overline{U}_\phi}{\delta t} + \nabla \cdot (\alpha_\phi \overline{U}_\phi \overline{U}_\phi) + \nabla \cdot (\alpha_\phi \overline{R}_\phi^{eff}) = -\frac{\alpha_\phi}{\rho_\phi} \nabla \overline{p} + \alpha_\phi g + \frac{\overline{M}_\phi}{\rho_\phi} \tag{45}$$

The averaged continuity equation is

$$\frac{\delta \alpha_\phi}{\delta t} + \nabla \cdot (\overline{U}_\phi \alpha_\phi) = 0 \tag{46}$$

The volumetric continuity equation is

$$\nabla \cdot \overline{U} = 0 \tag{47}$$

where

$$\overline{U} = \alpha_a \overline{U}_a + \alpha_b \overline{U}_b \tag{48}$$

In both (45), (46), and in the following equations, the subscript ϕ denotes the phase (a or b), α is the phase fraction, and $\overline{R}_\phi^{eff}$ is the combined Reynolds (turbulent) and viscous stress. $\overline{M}_\phi$ is the averaged inter-phase momentum transfer term, which includes drag, lift, and virtual mass forces. In these simulations, Basset and history forces are not calculated.

The drag is formulated using the Gidaspow Ergun-Wen-Yu model[13], which uses Ergun[19] if $\beta < 0.8$ and the Wen-Yu correction[21] is added for $\beta \geq 0.8$

$$\beta' = \begin{cases} 150 \frac{\alpha^2 \nu_b}{\beta^2 \rho_b d_a^2} + 1.75 \frac{\rho_b \alpha}{\beta d_s} U_r & \text{Ergun (1952)} \\ \frac{3 C_{Ds} \alpha \beta \rho_b U_r}{4 d_a} \beta^{-2.65} & \text{Wen and Yu (1966)} \end{cases} \tag{49}$$

where

$$C_{Ds} = \begin{cases} \frac{24}{Re}(1 + 0.15(Re)^{0.687}) & Re < 10^3 \\ 0.44 & Re \geq 10^3 \end{cases} \tag{50}$$

Formulated implicitly from the volumetric continuity equation, the pressure equation is as follows

$$\frac{\delta \alpha_a}{\delta t} + \nabla \cdot (\overline{U} \alpha_a) + \nabla \cdot (\overline{U}_r \alpha_a (1 - \alpha_a)) = 0 \tag{51}$$

where $\overline{U}_r$ is the relative velocity between phases a and b.

Kinetic theory of granular flow is used to determine the granular viscosities and pressure. Granular flow temperature Θ replaces thermodynamic temperature and is calculated using

$$\Theta = \left(\frac{(-K_1\alpha_s + \rho_s)tr(\overline{D}_s) + \sqrt{(K_1\alpha_s + \rho_s)^2 tr^2(\overline{D}_s) + 4K_3\alpha_s[2K_3 tr(\overline{D}_s^2) + K_2 tr^2(\overline{D}_s)]}}{2\alpha_s K_4} \right)^2 \quad (52)$$

where the subscript s denotes quantities associated with the solid phase, $\overline{D}_s$ is the strain tensor rate for the solid phase and $K_1 - K_4$ are calculated from van Wachem[33].

The simulations of the shocktube experiment at ASU used a rectangular domain with a resolution of 500 along the axial coordinate, z, and 25 along the width of the shocktube. The physical dimensions used in the simulation mimicked the real shocktube at ASU with a length of 1.37m and a width of 38mm. Three high-resolution runs were performed to determine if the solution changed when the resolution was altered. It was determined that the standard 500 x 25 resolution was sufficient enough for basic comparisons. In each case a high-pressure P_4 of 101,325Pa and a low-pressure P_1 of 5,000Pa was used. For each particle size and bed height, two simulations were performed. One with a standard solid volume fraction of $\phi_p = 0.60$ and a second with a solid volume fraction value representing the experimentally measured ϕ_p values as listed in Table 10. A full record of the simulations used in the present research is shown in Table 11.

z_b [m]	Particle Diameter [μm]	[ϕ_p]	Axial Resolution	Radial Resolution
0.1	44	0.6	500	25
0.1	44	0.6384	500	25
0.1	90	0.6	500	25
0.1	90	0.6384	500	25
0.1	150	0.6	500	25
0.1	150	0.6684	500	25
0.1	212	0.6	500	25
0.1	212	0.6684	500	25
0.1	212	0.6842	500	25
0.1	297	0.6	500	25
0.1	297	0.6842	500	25
0.2	44	0.6	500	25
0.2	44	0.6199	500	25
0.2	90	0.6	500	25
0.2	90	0.6199	500	25
0.2	150	0.6	500	25
0.2	150	0.6476	500	25
0.2	212	0.6	500	25
0.2	212	0.6476	500	25
0.2	212	0.6733	500	25
0.2	297	0.6	500	25
0.2	297	0.6733	500	25
0.1	44	0.6384	1,000	25
0.2	297	0.6733	500	100
0.2	297	0.6733	1,000	100

Table 11: Shown is a Table of the Simulations Performed Using Two Phase Euler Foam.

Resolution can have large effects on the results of a simulation. Tests were performed to see how well the simulations converged when the resolution was changed. Figures 97 through 101 show the variations caused by changing the simulation resolution. Note that there are no large-scale differences seen in any of the figures, especially in the figures showing pressure comparisons. The most notable differences are seen in the bed height tests. When the resolution is changed along the axial direction, the first layer of particles lifts off sooner. Note that the plots have a jagged feature as seen in Figure 97. This jagged feature is caused when the threshold setting for selecting the location of the gas-particle interface is slightly lower than desirable for tracking the interface. However, for determining the variations in the simulation due to resolution, it is valuable to use a lower threshold, because the timing when the first layer lifts off the bulk of the particle bed becomes evident. The

location of the gas-particle interface is determined by searching from the top of the shocktube down for the first instance when the solid volume fraction (or in the case of using real experimental data, the pixel intensity) reaches the defined threshold value. That location is where the gas-particle interface is said to be for each time step (or video frame). When the first layer of the particle bed lifts off, it is dense at first, but then as it spreads out in the axial direction, it becomes less dense. Initially, the measured location of the gas-particle interface is at the top of the first layer that lifts off. The top of the first layer remains the measured location of the particle bed interface until the solid volume fraction is reduced below the threshold; at which point the algorithm no longer recognizes that top layer as the gas-particle interface. Once this occurs, the bulk of the bed is recognized as the top of the particle bed.

Interestingly, when the resolution is increased in both the radial and the axial directions, it causes a slight variation in the particle bed interface rise rate as seen in Figure 98. When the resolution is increased in both directions, the simulated interface rise is faster. This in combination with what is seen in Figure 97 means that further high-resolution tests should be performed to make the comparisons between the simulations and experimental data more meaningful.

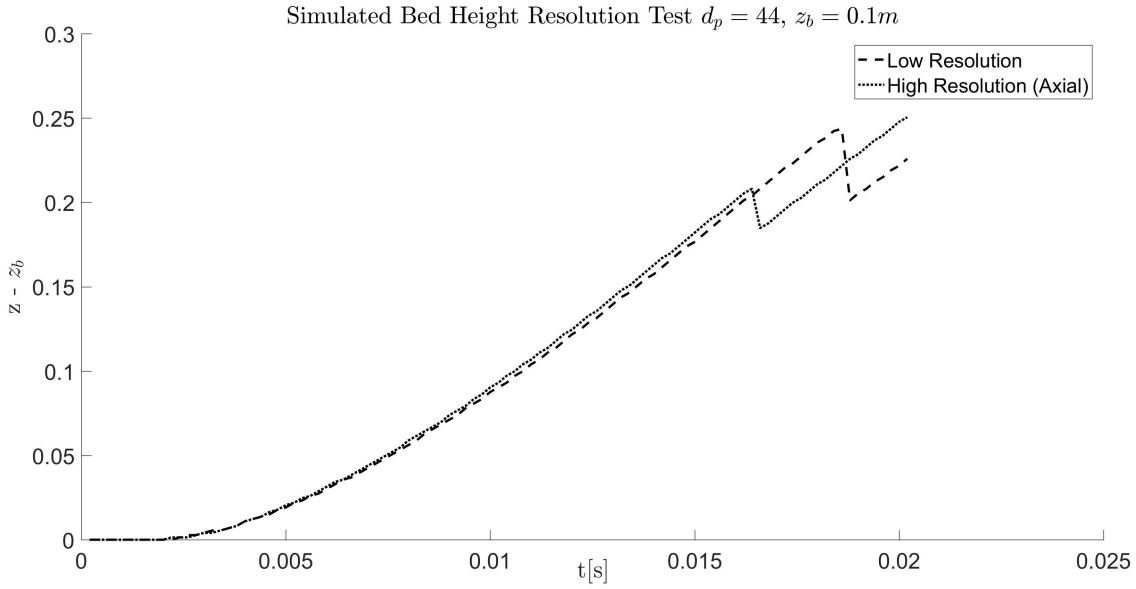

Figure 97: Shown is a Comparison of Two Two Phase Euler Foam Bed Height Datasets Calculated Using Two Different Resolutions. These Simulations are of a 0.1m Bed Composed of 44μm Spheres.

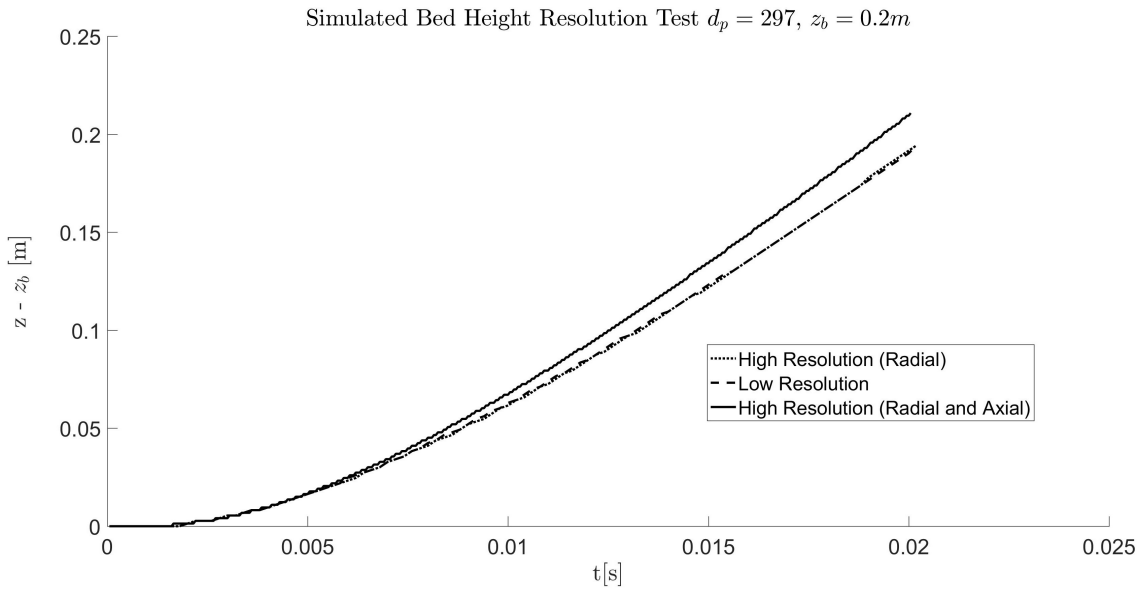

Figure 98: Shown is a Comparison of Two Two Phase Euler Foam Bed Height Datasets Calculated Using Two Different Resolutions. These Simulations are of a 0.2m Bed Composed of 297μm Spheres.

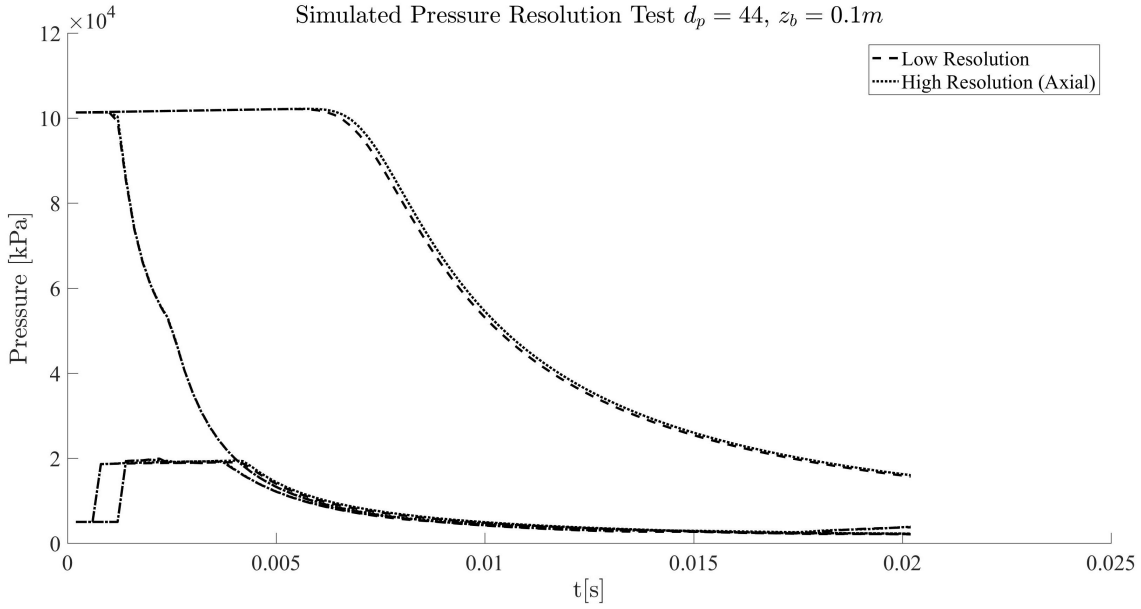

Figure 99: Shown is a Comparison of Two Two Phase Euler Foam Pressure Datasets Calculated Using Two Different Resolutions. These Simulations are of a 0.1m Bed Composed of 44μm Spheres.

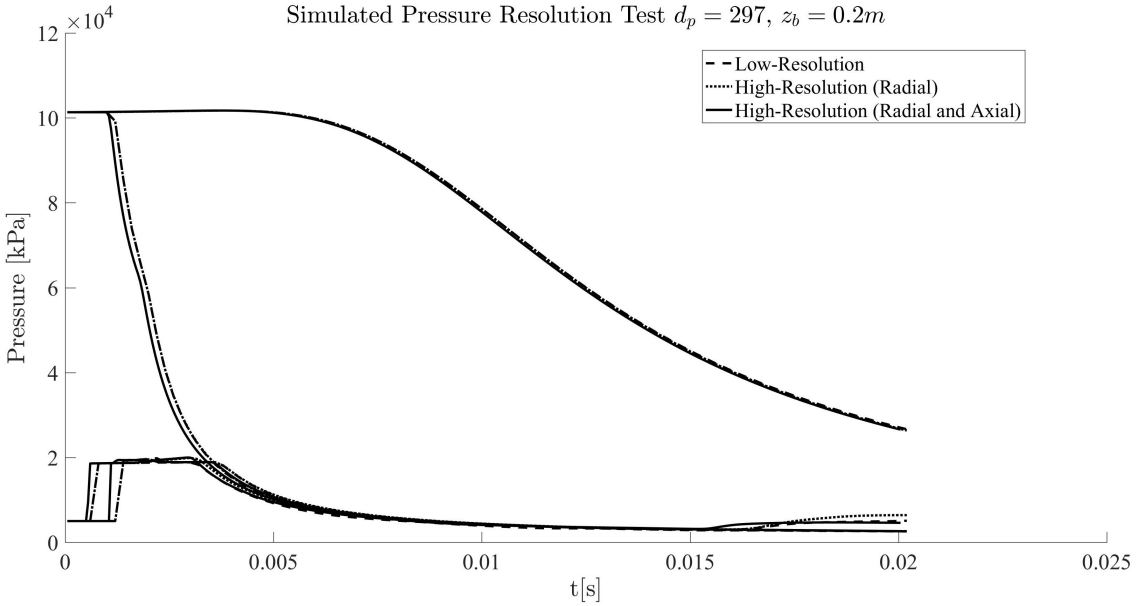

Figure 100: Shown is a Comparison of Two Two Phase Euler Foam Pressure Datasets Calculated Using Two Different Resolutions. These Simulations are of a 0.2m Bed Composed of 297μm Spheres.

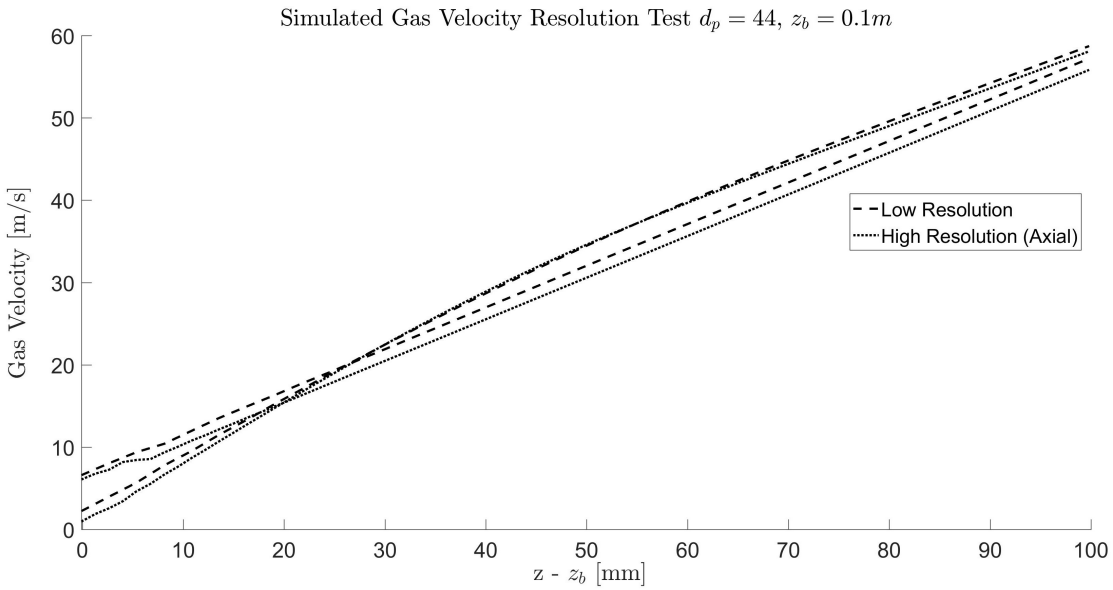

Figure 101: Shown is a Comparison of Two Two Phase Euler Foam Gas Velocity Datasets Calculated Using Two Different Resolutions. These Simulations are of a 0.1m Bed Composed of 44μm Spheres.

APPENDIX B

NON-INTRUSIVE CALIBRATION TECHNIQUE

B Non-intrusive Calibration Technique

This research was motivated by the need to perform camera calibrations in enclosed measurement volumes. The process involved camera calibrations can be quite lengthy and tedious. In experiments with enclosed measurement volumes, calibration becomes even more difficult. Typically, the experiment must be partially or fully disassembled to insert a calibration target, reassembled to take calibration images, disassembled to remove the calibration target, and then finally reassembled again to perform the experiment. Throughout this process, standard calibration techniques require the assumption that the experimental setup does not change at all (windows put back in exact same place, etc.)—an assumption that may not hold true for many complex experimental setups. The deviation from this assumption is exacerbated when experiments have curved or thick optical components (for example curved glass cylinders or thick viewing windows), where small variations in placement can cause large shifts due to the refraction of light.

This new technique was invented so that the experimenter may perform camera calibrations from outside an enclosed measurement region. The following is a conference paper on a non-intrusive image calibration technique designed for enclosed Particle Image Velocimetry experiments. It was presented at the Particle Image Velocimetry Meeting in 2015 and was funded in part by the Extreme Fluids Team at Los Alamos National Laboratory.

11TH INTERNATIONAL SYMPOSIUM ON PARTICLE IMAGE VELOCIMETRY - PIV15
Santa Barbara, California, September 14-16, 2015

Non-intrusive calibration technique

Heather Zunino[1], Ronald Adrian[1] and Liuyang Ding[1]

[1] School for Engineering of Matter, Transport and Energy, Arizona State University, Tempe, AZ, United States
heather.zunino@asu.edu

ABSTRACT

Many Particle Image Velocimetry (PIV) experiments have complicated and delicate optical setups. Common camera calibration techniques require assumptions regarding unknown camera parameters (*e.g.* optical axis angle, distortions, etc.)—reducing the accuracy of the calibration. Additionally, slight accidental movements to these experimental setups after calibration may cause significant errors—particularly for tomographic PIV [3]. Therefore, a rigorous and non-intrusive method is highly desirable. A new method of camera calibration for PIV experiments satisfying these conditions, is discussed.

1. Introduction

A common method for calibrating optical systems is to place a machined calibration grid with well-known markers into the region of interest. The grid is carefully translated a known distance into the test section and the grid is imaged at several z-locations. A generalized mapping function is used to map from image space to physical space [1]. This method will be hereafter referred to as the *traditional* method of calibration.

This traditional method requires the experimenter to assume certain camera parameters. For example, many calibration techniques assume the camera lens causes only negligible image deformation and the optical axis angle (relative to the laser light sheet) is perfectly known. While these assumptions have been previously required for calibrating PIV cameras, it is widely known they are not true.

Additionally, it is assumed that after the camera calibration is performed, the experimental setup does not change. If the experimenter is required to open up a closed test section, traverse a calibration target across the test section, remove the calibration setup, and close the test section, there are many opportunities for accidental relative motion to occur between the test section and the optical setup. These small movements will foster errors in the calibration.

A new camera calibration method is developed which accomplishes the following:

1. The calibration is performed without the need to insert a target into the region of interest.
2. The calibration is accomplished without the requirement of target displacement.
3. The calibration is capable of accounting for lens distortion and distortions caused by windows and other optical media (i.e. water in the test section).

2. Method

Described in this section is a technique to calibrate the optical system for PIV experiments without placing any calibrating materials inside the test section. Additionally, the specific geometry of the optical system is unknown, therefore this method must be independent of camera angles, lens orientation, etc. The method will be described for experiments with closed flows. However, a window enclosing the test section is not needed. It is possible to do this by using a transparent calibration plate with markings on both sides (shown in Figure 1) and the following calibration steps:

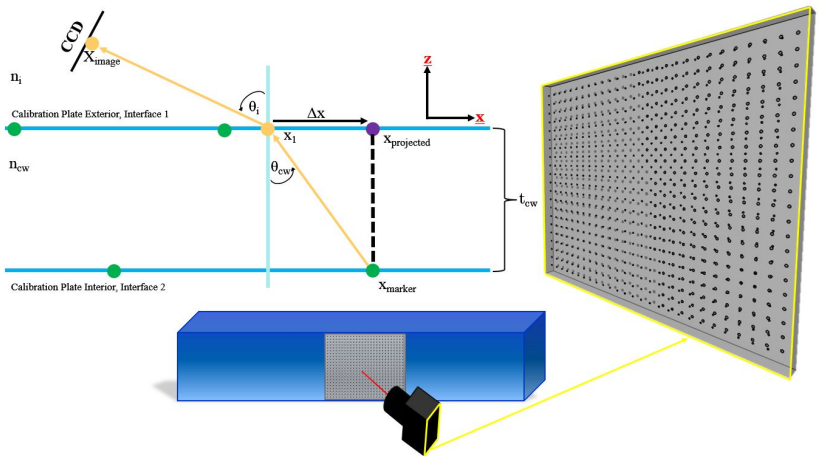

Figure 1: Small (1mm diameter) circular dots are milled onto a transparent window. The dots are milled very accurately in a grid arrangement using a highly-calibrated CNC machine. The grid of dots on the front and back are offset by 2.5mm. This allows for all dots to be seen from either side of the window, with no overlap. To increase visibility of the dots on the camera images, the edges of the transparent window may be lined with small LED lights. To see an illuminated image of this calibration window, see Figure 4. Also shown is a representation of light ray refraction in one direction through the two-sided calibration plate. The green dots represent physical markers, x_1 is where the physical marker, x_{marker}, appears on the exterior surface of the calibration plate. $x_{projected}$ is the x location where x_{marker} *would* appear on the front surface given no distortions due to lens aberrations, refraction, etc. The subscripts i and cw stand for incident and calibration window, respectively.

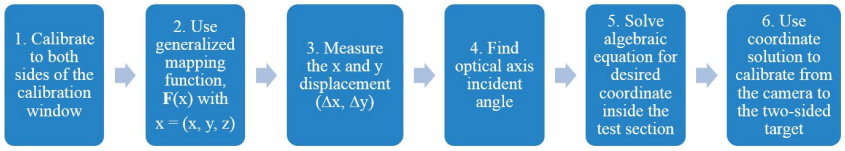

Figure 2: Listed are the steps to perform the new *ex situ* calibration method.

1. To calibrate to the front and back sides of the calibration window, cross-correlate a template of the markers and a calibration image, followed by a peak-finding algorithm to find the coordinates of each marker image.
   (a) To obtain sub-pixel coordinates, define a coordinate axis on the object plane and the image plane. Locations of the markers may be measured relative to the defined origin.
2. Use a generalized mapping function $\hat{\mathbf{F}}(\mathbf{x})$, where $\mathbf{x} = (x, y, z)$.
   (a) $\hat{\mathbf{F}}(\mathbf{x}) = \mathbf{a_0} + \mathbf{a_1}x + \mathbf{a_2}y + \mathbf{a_3}z + \mathbf{a_4}x^2 + \mathbf{a_5}xy + \mathbf{a_6}y^2 + \mathbf{a_7}xz + \mathbf{a_8}yz + \mathbf{a_9}z^2 + \mathbf{a_{10}}x^3 + \mathbf{a_{11}}x^2y + \mathbf{a_{12}}xy^2 + \mathbf{a_{13}}y^3 + \mathbf{a_{14}}x^2z + \mathbf{a_{15}}xyz + \mathbf{a_{16}}y^2z + \mathbf{a_{17}}xz^2 + \mathbf{a_{18}}yz^2$
   (b) The 36 coefficients are determined by a least squares fit to a 3D set of calibration points. These coefficients will be used to map between real space and image space [2].
   (c) The z-coordinate is determined by the experimental setup (i.e. the location of the light sheet).
3. Measure the x and y displacement $(\Delta x, \Delta y)$ between the images of the interior markers and the projections of where they should appear on the exterior surface (from a perfectly perpendicular viewing arrangement, the only varying coordinate would be in the z-direction), to find the incident angle Θ_i of incoming light (See Figure 1).

Light from the marker on the interior surface of the window reaches the exterior surface of the window at x_1. It is necessary to find the incident angle Θ_i in order to calculate the position of a particle in the wind tunnel that would appear at x_1. It is possible to calculate Θ_i by first finding Θ_{cw}, the angle of refraction through the window, and then using Snell's Law to find Θ_i. This step requires the test section to be well-known (thickness, material properties, etc.).

4. Because $x_{projected}$ and x_{marker} have the same x values, the x-displacement between $x_{projected}$ and x_{marker} is the same x-displacement between x_1 and $x_{projected}$. By measuring this Δx, the distance between x_1 and x_{marker}, it is possible to find the tangent of Θ_{cw}.

   By using simple right triangle relations, Θ_{cw} can be found

$$\Theta_{cw} = \arctan \frac{\Delta x}{t_{cw}} \tag{1}$$

   The incident angle is easily found by incorporating Snell's Law

$$\Theta_i = \arcsin\left(\left(\frac{n_{cw}}{n_i}\right) \sin\left(\arctan\left(\frac{\Delta x}{t_{cw}}\right)\right)\right) \tag{2}$$

   Using the previous equations, the camera can be calibrated to the depth corresponding to the interior of the window. Note that the above equations are for a single coordinate x; for two-dimensional corrections, these calculations must be performed in the y-direction as well. To calibrate for a particle inside the test section at some specified depth z_L, additional calculations are needed.

5. In order to project this calibration inside the test section in x and y, it is useful to re-define x and y as a composite coordinate ξ. The primed coordinates represent the apparent location of a physical calibration dot at the first interface. Note that $\xi_1 = \xi_1'$. The subscripts ts, f, p, L, stand for test section, fluid, projected, and laser, respectively. For a graphical representation of this concept, see the 3D light ray trace diagram in Figure 3. The numbered subscripts of each coordinate represent a different plane (subscript 1 corresponds to the exterior calibration window plane—closest to the CCD chip, subscripts 2, 3, and 4, correspond to the interior calibration window plane, the interior test section plane, and the laser light sheet plane, respectively).

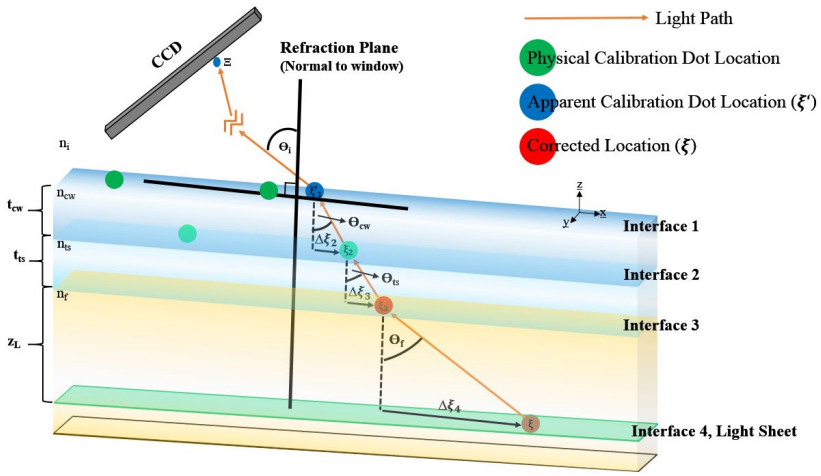

Figure 3: Three-dimensional light ray trace of transparent calibration window from physical location in test section, to the image location on the CCD.

Again, using Snell's Law relations, the unprimed coordinates can be found easily. ξ_2 is simply the physical location of the marker on the interior side of the calibration window. This location is known from the experimental setup and the chosen origin. From there, the coordinates of the images the marker can be found at each interface. The equation for the coordinates at the third interface (the inside of the test section) is as follows

$$\xi_3 = \xi_2 + t_{ts} \tan \Theta_{ts}. \tag{3}$$

Then, continuing to ray trace into the test section and using (3), the solution for the final coordinate is

$$\xi = \xi_3 + z_L \tan\Theta_f = \xi_2 + t_{ts}\tan\Theta_{ts} + z_L \tan\Theta_f. \tag{4}$$

It is important to remember (4) includes the shift associated with the light ray refraction through the calibration window. If the calibration window will be removed during the experiment, this shift must also be removed from the final correction equation.

Using Snell's Law and (1),

$$n_f \sin\Theta_f = n_{ts}\sin\Theta_{ts} = n_{cw}\sin\Theta_{cw} = n_i \sin\Theta_i = n_{cw}\sin(\ \arctan\frac{\Delta x}{t_{cw}}\ ). \tag{5}$$

The unknown location ξ can be solved in terms of the physical location ξ_2 and the test section characteristics. Plugging (5) into (4) yields the following equation

$$\xi = \xi_2 + t_{ts}\tan[\ \arcsin(\ \frac{n_{cw}}{n_{ts}}\sin(\ \arctan\frac{\Delta x}{t_{cw}})\ )\ ] + z_L \tan[\ \arcsin(\ \frac{n_{cw}}{n_f}\sin(\ \arctan\frac{\Delta x}{t_{cw}})\ )\ ]. \tag{6}$$

6. Using this equation, it is possible to find the position ξ if $\xi_1^{'}$ is known, and given Ξ.

$$\xi = F(\xi_1^{'}\xi)(\xi_1^{'};\Xi) \tag{7}$$

Additionally, to obtain Ξ, calibrate from camera to the dual-layer target.

$$\Xi = \mathbf{F}_{\xi_1^{'}\Xi}(F_{\xi\xi_1^{'}}(\xi)) \tag{8}$$

3. Experiment

To test this new calibration method, experiments were performed. In addition, experiments using the traditional calibration method were also performed in order to compare the new and traditional methods. Shown in Figure 4 is an image of the calibration window on the exterior of a six inch deep wind tunnel test section. The camera was not focused to the calibration window, but to the laser light plane in the center of the test section (three inches from the interior of the $\frac{1}{4}$ inch thick test section window). For this reason, the f-number was set at 32—to allow for the greatest depth of field.

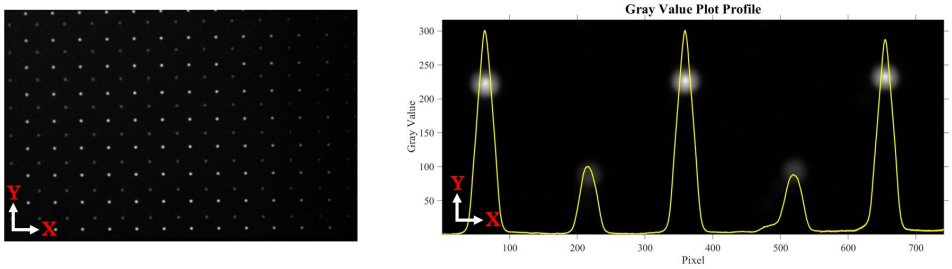

Figure 4: *Left*: Shown is the unfiltered image of the transparent 2-sided calibration window placed outside of the test section. The image was taken taken by a camera focused in the center of a 6" deep test section at an f-number of 32. The calibration window is illuminated by LED lights lining the outer edges. *Right*: Shown is a plot profile of the intensity averaged over the Y image coordinate and overlaid onto a zoomed-in section of the image on the left.

As shown in Figure 4, the grid of dots are illuminated differently. The markers on the front side of the calibration window are fainter than the markers on the back side. Also shown in Figure 4 is the approximate Gaussian intensity distribution over each dot. It is important to differentiate between the front and back dots in order to correctly calculate the $\Delta\xi_1$, as depicted in Figure 3.

To find the center of each dot, the image was convolved with a Gaussian filter. Then the Gaussian kernel was correlated with the filtered image. The center of each correlation peak is a Gaussian shape. By finding the center of the Gaussian curve for each dot, the sub-pixel image locations were found. During image processing, the experimenter can differentiate between the correlation peaks corresponding to the dots on the front of the calibration window and those on the back by thresholding the correlation peak values. However, a simpler method is to mask out one set of dots at a time and find the pixel coordinates of the front dots separately from the back dots. This is the method discussed below.

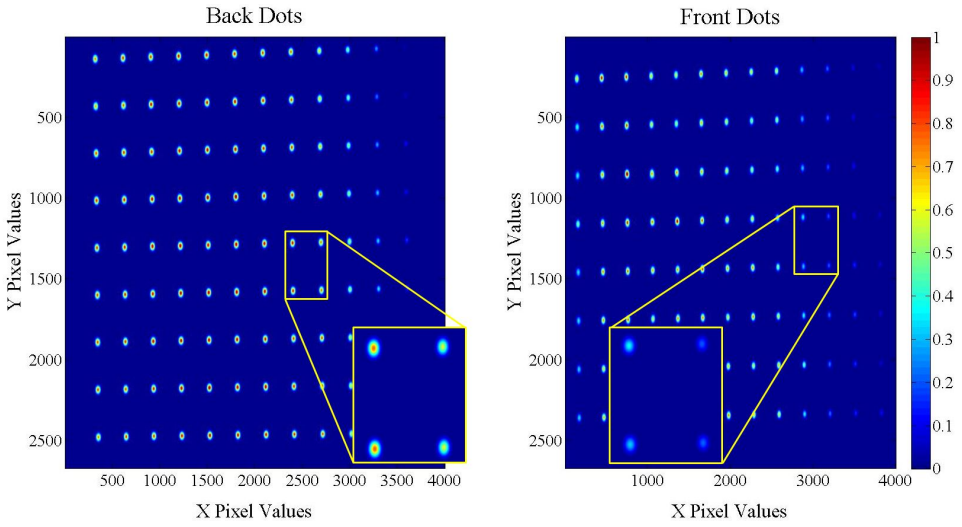

Figure 5: Shown is correlation map of the Gaussian kernel with the filtered front and back calibration grid images. The warmer areas are associated with higher correlation.

When the correlation peaks were found, they were mapped onto the original images as seen in Figure 6.

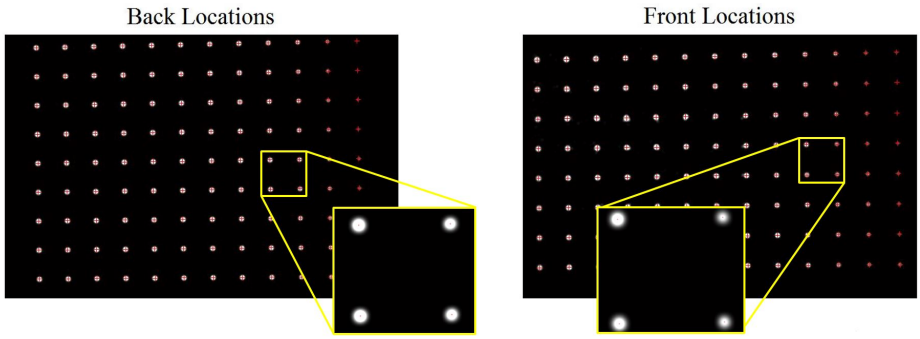

Figure 6: Displayed as red crosses are the locations found by finding local maxima in the correlation map shown in Figure 5 The maxima are overlaid onto a filtered image of the calibration window.

To test the mapping function, physical coordinates ξ within the test section were used as inputs to retrieve the associated image coordinates Ξ. Shown in Figure 7 is the comparison between the reference image coordinates and the image coordinates outputted by the mapping function.

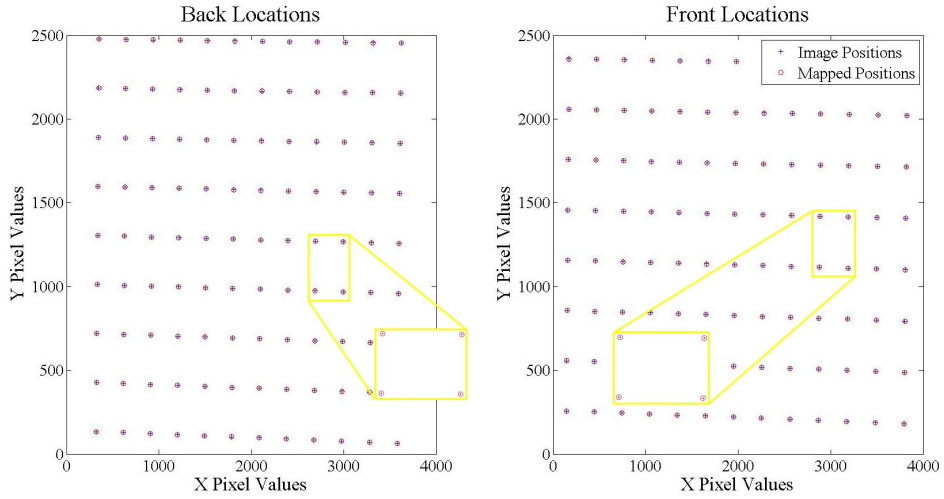

Figure 7: Shown is a plot depicting the accuracy of the mapping function used. Reference image positions are displayed as blue crosses. The red circles are the image positions outputted by the mapping function given physical coordinates. The maximum error ($\sim$ 1 pixel) appears near the edges of the image.

With the projected locations, the known spacing of the milled dots, and the characteristics of the test section, everything needed for (6) is known. See Figure 8 for a visual representation of the calculations traced throughout a square test section.

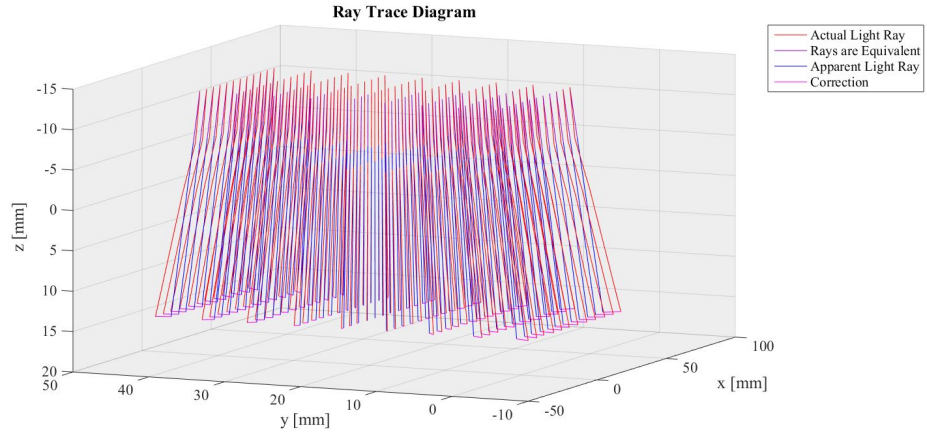

Figure 8: Shown is a ray trace diagram. The apparent (blue rays) and the actual (red rays) light ray path are calculated using right triangle relations and (6), respectively. The correction between the apparent and actual light rays at the laser light sheet location z_L are shown in magenta.

4. Results

This method is suited for large scale flows with test sections which are difficult to traverse a calibration plate through. This method is also useful for experiments where the experimenter cannot remove the calibration target from the test section without moving the cameras or other optical components. Additionally, the experimenter may want to employ the new proposed method, if relative motion is expected to occur between the imaging system and the flow during experimental realizations (e.g. shock tubes and other experiments with energetic flows), as this may be accounted for if the calibration window remains installed during the experiment.

This method is not as well-suited for very small scale flows when the experimenter can easily employ the traditional method. When this method is used, the camera is focused in the center of the test section. Therefore, the calibration markers are very out of focus compared to images obtained from the traditional method—where the camera is actually focused on the calibration markers located at the laser light sheet plane. As for the new method, the camera is still focused at the light sheet, but the calibration window is placed over 80mm (3") closer. This means the diameters of the images of the calibration markers are much larger. This effect is reduced as the projection distance ($+z$ into the test section) is reduced. When the new calibration method was projected into the test section 15.24mm, the average residual calculated in real space was 0.1217 in the x-direction and 0.1236 in the y-direction. The x and y rms values were 0.1531 and 0.1538 respectively. This is between 21 and 25 times worse than the ideal traditional method. However, there are many factors to be considered.

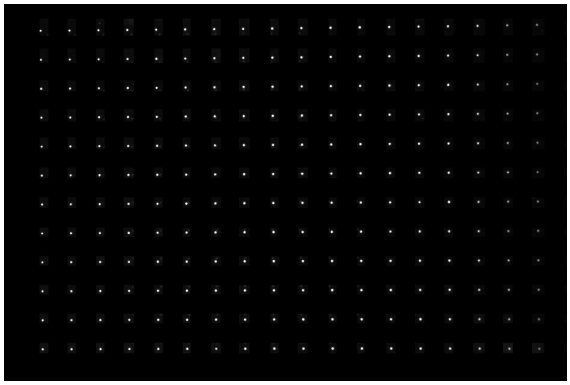

Figure 9: Shown is the image used to compare the new calibration method to the traditional calibration method. Note that twice the number calibration markers are visible in this image compared to the image used for the new method (see Figure 4), as the calibration plate is further away. Additionally, the calibration marker images are three times smaller than the calibration marker images used for the new method.

When calibrating a camera, finer resolution of the target plane (many, highly refined calibration points) yields higher accuracy in the mapping function. As seen in Figure 9, twice the number of calibration markers are visible when the calibration target is inside the test section when compared to when the calibration window is placed outside the test section. This yields a more finely resolved mapping function. Another source of error associated with the new method is the large marker images. The marker images used for the new method are about three times larger than those used for the traditional calibration method. It is also important to recall this comparison is made from ideal conditions for the traditional calibration method, because the calibration equipment was inserted into an open test section. Any errors associated with moving the calibration equipment out of the test section were not included.

5. Summary

A new technique for the calibration of PIV cameras has been developed and demonstrated. It is *ex situ*, in the sense that the calibration target can be outside the object region—making it possible to perform calibrations completely outside the domain of interest. This method accounts for unknown camera placement and orientation; and distortions caused by the camera lens without invoking a camera model. Distortions due to intervening media are accounted for geometrically.

This method is suitable for experiments with larger scale flows, where the flow will traverse several pixels in image space between frames. Additionally, this method may be used when access to the region of interest is difficult or not permitted.

REFERENCES

[1] Adrian RJ and Westerweel J "Particle Image Velocimetry" Cambridge University Press (2010)

[2] Soloff MD and Adrian RJ "Distortion compensation for generalized stereoscopic particle image velocimetry" Measurement Science and Technology 8 (1997) pp. 1441–1454

[3] Wieneke B "Volume self-calibration for 3D particle image velocimetry" Experiments in Fluids 45 (2008) pp. 549–556